LEABHARLANN CHOLÁISTE NA TRÍONÓIDE, BAILE ÁTHA CLIATH | TRINITY COLLEGE LIBRARY DUBLIN
Ollscoil Átha Cliath | The University of Dublin

Terms and Conditions of Use of Digitised Theses from Trinity College Library Dublin

Copyright statement

All material supplied by Trinity College Library is protected by copyright (under the Copyright and Related Rights Act, 2000 as amended) and other relevant Intellectual Property Rights. By accessing and using a Digitised Thesis from Trinity College Library you acknowledge that all Intellectual Property Rights in any Works supplied are the sole and exclusive property of the copyright and/or other IPR holder. Specific copyright holders may not be explicitly identified. Use of materials from other sources within a thesis should not be construed as a claim over them.

A non-exclusive, non-transferable licence is hereby granted to those using or reproducing, in whole or in part, the material for valid purposes, providing the copyright owners are acknowledged using the normal conventions. Where specific permission to use material is required, this is identified and such permission must be sought from the copyright holder or agency cited.

Liability statement

By using a Digitised Thesis, I accept that Trinity College Dublin bears no legal responsibility for the accuracy, legality or comprehensiveness of materials contained within the thesis, and that Trinity College Dublin accepts no liability for indirect, consequential, or incidental, damages or losses arising from use of the thesis for whatever reason. Information located in a thesis may be subject to specific use constraints, details of which may not be explicitly described. It is the responsibility of potential and actual users to be aware of such constraints and to abide by them. By making use of material from a digitised thesis, you accept these copyright and disclaimer provisions. Where it is brought to the attention of Trinity College Library that there may be a breach of copyright or other restraint, it is the policy to withdraw or take down access to a thesis while the issue is being resolved.

Access Agreement

By using a Digitised Thesis from Trinity College Library you are bound by the following Terms & Conditions. Please read them carefully.

I have read and I understand the following statement: All material supplied via a Digitised Thesis from Trinity College Library is protected by copyright and other intellectual property rights, and duplication or sale of all or part of any of a thesis is not permitted, except that material may be duplicated by you for your research use or for educational purposes in electronic or print form providing the copyright owners are acknowledged using the normal conventions. You must obtain permission for any other use. Electronic or print copies may not be offered, whether for sale or otherwise to anyone. This copy has been supplied on the understanding that it is copyright material and that no quotation from the thesis may be published without proper acknowledgement.

Rheological and Local Fluid Dynamics in Foams

by

Maria Dolores Alonso Craus,
Physics Department, Trinity College Dublin, Ireland

A Thesis Submitted to
The University of Dublin
for the Degree of

Doctor of Philosophy

DEPARTMENT OF PHYSICS
TRINITY COLLEGE
UNIVERSITY OF DUBLIN

October 2004

TRINITY COLLEGE
0 5 MAY 2005
LIBRARY DUBLIN

THESIS
7587

Declaration

This thesis has not been submitted as an exercise for a degree at any other University. Except where otherwise stated, the work described herein has been carried out by the author alone. This thesis may be borrowed or copied upon request with the permission of the Librarian, Trinity College, University of Dublin. The copyright belongs jointly to the University of Dublin and Maria Dolores Alonso Craus,
Physics Department, Trinity College Dublin, Ireland .

Signature of Author........................Lole A. Craus..............................

Maria Dolores Alonso Craus,
Physics Department, Trinity College Dublin, Ireland
May, 2004

A mis padres (mi pasado),
Víctor (mi presente)
y a la siguiente generación en nuestra familia (mi futuro).

A mis padres (mi pasado),
Víctor (mi presente)
y a la siguiente generación en nuestra familia (mi futuro)

Acknowledgment

First and most, I thank my supervisor, *Prof. Denis Weaire.* Thanks for giving me a great opportunity, an excellent working atmosphere and for pointing the right direction when needed. A mention also to *Colette*, for providing nice lunches and conversation.

My examiners, *Prof. Jan Cilliers* and *Prof. Charles Patterson* have helped with their critical corrections to improve the material presented here.

I have also to thank all the people in the "Foam Physics Group" at Trinity. Thanks for making me wiser through discussion. Particular mention has to be given to: *Dr. Stefan Hutzler*, for the pre-prints, article copies and experimental tips. *Dr. Simon Cox*, because my English and my math intuition has improved a lot thanks to his patient corrections. *Drs. Nic* and *Claire Pittet*, for lodging me when I came to Dublin and help at my first steps with Evolver. *Dr. Norbert Kern*, for reading and commenting pre-pre-prints of this thesis (and we both know that's hard work).*Dr. Geoff Bradley*, for help with the four-fold calculations and all the music borrowed. *Wiebke*... out of words... du bist wunderbar! *Finn, Aengus, Gary* and *Paul* because it's always refreshing to hear new ideas. *Daniel Pardal* suggested the Stokes experiments using coarsening foam. All the *secretarial* and *technical staff* in Physics. Special thanks to *Jeanette Cummins* for sorting out my arrival in Dublin.

Part of this project was made on a very nice and productive visit to the Instituto Tecnico Superior in Lisboa (Lisbon). I have to thank the warm welcome I had on those fifteen days and I am "obrigadissima" to *Prof. Fátima Vaz* for providing this opportunity and for all her support.

Thanks to all the people that has made my years in Dublin nice and worth remembering: the people at Howth Road (*Blandine, Christine* and *"la" Jose*) and Castelnock Manor (*Bee,*

Donagh, Eduardo, Johnny and *Tom*); the mates at work (*Connor, Gemma, Judith, Joanne, Joe, Lorenzo, Marco, Nikos, Simon E., Sonja, Svetjlana* and the others) and the friends (*Fran, Isabel, "el" Jose, Juan, Liza...*). Finally, to all the people that I have forgotten because memory is fragile.

This work was supported by the Irish H.E.A (PRTL199) and the Trinity College Postgraduate Awards. During the period of this research, the Foams group was supported by the EU (Marie Curie programme), Enterprise Ireland (Basic Awards and ESA/Prodex). I would also like to thank H.E.A., Trinity Physics Department and the Trinity Postgraduate Travel Fund for providing the funds that made the trip to Lisbon, and therefore the cluster experiments, possible.

Y ahora, la parte en español:

A mis padres *Carmen* y *Ricardo* les debo TODO lo que soy. Os quiero.

A mis hermanos *Ricardo* y *Carolina*, que me han soportado y (finalmente) aceptado como la pedante que soy. A mis suegros *Pilar* y *Tomás* por haberme ofrecido la mejor canguro del mundo para Luna. También tengo que agradecer al resto de la familia, (la de sangre y la política), haber aguantado mis cambios de humor y la distancia durante toda la realización de esta tesis.

Gracias a *Eva* y *Ricardo*, por servirme como punto de referencia (y a sus respectivas parejas *Sergio* y *Bea*, por sanearles mentalmente de sus "vis-a-vis" conmigo). A todos los amigos de la Facu: hacer Físicas no hubiera sido ni la mitad de divertido e interesante sin vosotros. Gracias a *Alberto, Mayte* y *Miguel* que han sobrevivido al esfuerzo de leerse todos o parte de los capítulos de esta tesis.

Su, sin tus cafés y tus "lunch" no habría sobrevivido los últimos meses en Trinity. La siguiente eres tú.

Javi y *Silvia (Chivi)* las guindas de esta tesis se deben a que hay amigos que creen en mi más que yo y eso eleva la autoestima. Gracias por presentarme íntimamente a Bessel.

Gracias *Luna*, por dejar a mamá dedicar parte de un tiempo que era exclusivamente tuyo al trabajo.

Víctor, tú me empujas en dirección a mis sueños. El resto de lo que te podría decir ya lo sabes.

List of publications

Published:

- *The Stokes experiment in a foam.*

  Cox S. J. , Alonso M. D. , Hutzler S. and Weaire D.

  Foams, Emilsions and their Applications Proceedings Eurofoam 2000, 282-289 MIT Publishing Bremen(2000)

- *The Fluid Dynamics of Foams.*

  Weaire D. , Hutzler S. , Cox S. J. , Kern N. , Alonso M. D. and Drenckhan. W.

  J. Phys.:Condens. Matter **15**, S65 (2003)

- *Minimum energy configurations of small bidisperse bubble clusters.*

  Vaz M. F. , Cox S. J. and Alonso M. D.

  J. Phys.:Condens. Matter **16 (23)**, 4165-4175 (2004)

In preparation:

- *Drainage driven instabilities in a tilted tube.*

  Alonso M. D. , Cox S. J. , Hutzler S. and Weaire D.

- *Convective rolls in foams.*

  Weaire D. , Alonso M. D. , Cox S. J. , Rioual F. , and Hutzler S.

Abstract

This thesis explores the physics of foams, particularly those that are wet (i.e. have a high liquid fraction). The properties which are measured here relate to structure, drainage and rheology.

We have performed the first published Stokes experiment in a foam [41]. and compared results with estimates derived from the Herschel-Bulkley model for rheology.

The first extensive, systematic experiments on drainage driven instabilities reveal aspects hitherto unreported, including hysteresis and the existence of a cylindrically symmetric case. We offer a preliminary theoretical analysis of the case in which the column is tilted.

Other new results relate to the structure of finite 2D clusters [93].

Summary

The main focus of this work is on some particular problems that arise when an aqueous foam becomes wet. These problems are related to the flow of the foam itself (rheological properties) and the flow of liquid through the foam (drainage).

We start by making a general introduction of foam in Chapter 1. The main terms and definitions used in this thesis are covered, paying particular attention to the drainage of a liquid through the foam and the characteristics of flow in different materials.

In a version of the Stokes experiment, we have dropped spherical beads of known diameter and weight into a column of foam (Chapter 2). Only some of these beads can overcome the yield stress of the foam and sink immediately. The experimental results are compared with a model that considers foam as a Herschel-Bulkley fluid.

The following chapters (Chapters 3 to 5) study the important phenomenon of convective instabilities produced by forced drainage in foam. We have studied these instabilities in vertical cylindrical tubes, in Hele-Shaw cells and in tilted tubes. We have studied the relation of these instabilities with the liquid fraction in the foam, giving some experimental curves to describe how they vary. An interpretation of the convective instabilities in terms of the yield stress of the foam and inhomogeneous liquid fraction is proposed as a model for the system. This leads to satisfactory predictions for the tilted tube, and a preliminary analysis of the more difficult case of instability in a vertical tube.

Drainage experiments are also conducted in 2D foams. During these experiments using 2D foams, an interest arose in finite clusters of 2D bubbles. Some results on the minimal energy configuration of these clusters are included in Appendix B. Some further appendices include details on experimental foam formation and explanations of computational packages used on development. Reference is made to an additional internal technical report

on related research not included in this thesis.

Nunca perseguí la gloria
ni dejar en la memoria
de los hombres mi canción.
Yo amo los mundos sutiles,
ingrávidos y gentiles,
como pompas de jabón.
Me gusta verlos pintarse
de sol y grana, volar
bajo el cielo azul temblar
súbitamente y quebrarse.

Antonio Machado (spanish poet 1875-1939).

Life is what happens to you
when you are busy making other plans.

John Lennon.

Contents

1 **Basic notions** **1**

1.1 Motivation . . . 1

1.2 Definition of a foam . . . 3

1.2.1 Term definitions . . . 3

1.3 Foam structure . . . 4

1.3.1 Young-Laplace law . . . 4

1.3.2 Plateau rules . . . 5

1.3.3 The many bubble problem . . . 6

1.3.4 Topological changes . . . 7

1.3.5 Osmotic pressure . . . 8

1.4 Drainage . . . 9

1.4.1 Free drainage, forced drainage and pulsed drainage . . . 10

1.4.2 The growth of Plateau borders . . . 11

1.4.3 The drainage equation . . . 12

1.5 Rheology . . . 15

1.5.1 Flow properties of materials . . . 15

1.5.2 Mathematical models for viscoplastic flows, including foam . . . 18

1.5.3 Shear modulus and yield stress on foam . . . 20

1.6 Coarsening and collapse . . . 21

I Rheological Properties **23**

2 **The Stokes experiment in a foam** **24**

2.1 Motivation 24

2.2 The Stokes experiment in a foam 25

  2.2.1 Stokes experiment in Newtonian fluids 25

  2.2.2 Stokes experiment in a foam 27

  2.2.3 Outlook of the chapter 28

2.3 Materials and methods 29

2.4 Experimental results 31

  2.4.1 Experiments in forced drainage 31

  2.4.2 Experiments with coarsening foams 35

2.5 Analysis of the results 38

  2.5.1 Creep correction and data treatment 38

  2.5.2 A link to the rheology of the foam 41

2.6 Numerical modelling 46

2.7 Conclusion 50

3 Drainage induced convective motion in foam **52**

3.1 Motivation 52

3.2 Theorical background of the convective motion 53

  3.2.1 The nature of the transition to convective motion 53

  3.2.2 Previous results on convective motion 55

3.3 Materials and methods 56

3.4 Drainage driven convective motion in a vertical tube 57

  3.4.1 Description of the drainage driven convective rolls 57

  3.4.2 General description of results for the convective rolls 62

  3.4.3 Influence of the liquid input in the convective rolls 65

  3.4.4 Examples of hysteresis on the convective rolls 65

  3.4.5 Domains of the drainage driven convective motions in a foam . . 69

  3.4.6 Onset of the convective rolls 71

  3.4.7 Velocity of the bubbles in the convective rolls 76

3.5 Interpretation of the results: towards a model 78

  3.5.1 The ingredients of the theory 79

3.5.2 The driving force at the wall 82
3.5.3 The threshold condition 83
3.5.4 Towards a more complete theory 88
3.5.5 Discussion 91
3.6 Summary 93

4 Convective instabilities in 2D **95**
4.1 Motivation 95
4.2 Experimental set-up 96
4.2.1 Results 97

5 Convective motion in a tilted tube **101**
5.1 Motivation 101
5.2 Materials and methods 102
5.3 Experimental results for the tilted tube 104
5.4 Analysis of results 107
5.5 Theoretical Comparison 109
5.6 Conclusions for the tilted tube 109

A Measurements of local liquid fraction related to convective motions in foam **112**
A.1 Motivation 112
A.2 Surface liquid fraction measurements 113

B Minimal configurations of bidisperse bubble clusters **117**
B.1 Motivation 117
B.2 The minimal problem in 2D bubble clusters 120
B.2.1 Contributions to the energy in 2D clusters 121
B.2.2 The broken bond method 122
B.2.3 Estimates of the energy on monodisperse clusters 123
B.2.4 Estimates of the energy on polydisperse clusters 123
B.3 Experimental methods 124
B.3.1 Materials and methods 126

B.3.2 Experimental results 127

B.4 Evolver calculations 137

B.5 Analysis of results 141

B.6 Conclusions and Outlook 143

C The channel-dominated form of the foam drainage equation 145

D Experimental foam production 147

E Fluent 151

F Surface Evolver 153

G The foam drainage equation in a tilted tube 158

List of Figures

1-1 Some of the main challenges at present in the physics of foams. The figure is reproduced from [4] with the kind authorisation of the authors. 2

1-2 A soap film, containing amphiphilic molecules. These are chemicals formed by two parts. One of them attracts liquid molecules and the other repels them. The physical chemistry inside the films can be very complicated, including dynamic effects such as Marangoni convection which are beyond of the scope of this thesis. 4

1-3 Plateau rules for dry films. 5

1-4 In the T2 process in 2D a three-sided cell vanishes. It is similar in 3D with tetragonal bubbles. 7

1-5 The T1 changes in 2D and 3D dry foams. In 2D foams, a four-fold unstable vertex is broken. For 3D foams an elementary rearrangement exists that it is similar to the T1 two-dimensional process (shown right up). However, the most common form of rearrangement that is observed in three-dimensional foams is the multiple process shown right down. 8

1-6 The Plateau Borders (left) increase their volume when the foam becomes wet. Four of them join in a junction (right), following the Plateau rules represented in Fig. 1-3, in the dry limit. 11

1-7 Different response under shear stress for some characteristic types of fluids in which viscosity is independent of time. A/Newtonian flow, viscosity (η) is a constant, corresponding with the slope of the line in this case. B,C/ Shear-thinning and shear-thickening fluids start flowing as soon as a shear stress is applied, but in both cases a change occurs in viscosity while the stress is acting. In shear-thinning fluids that change acts to decrease in the viscosity of the material. The case of shear-thickening fluids is the opposite one, there is an apparent increase in viscosity. D/ Viscoplastic fluids start flowing at a certain shear stress different to zero. This threshold is the yield stress. 19

1-8 Sketched stress-strain relation for a liquid foam. Note the three different regions of behaviour (elastic solid, plastic solid and liquid). The diagrams of simulations in two-dimensional foams (which can be found in [34]) have a quite similar look. One can see a linear elastic relation for low stresses and a fluctuating behaviour of stress for larger strains, due to topological changes in a finite sample. Reproduced from [1]. 20

2-1 The Stokes experiment in a Newtonian fluid. w is the weight force and β the buoyancy. The drag force F_v is proportional to the velocity v of the falling sphere. Asymptotically, the equilibrium between forces causes the sphere to fall at constant velocity. This is what is known as terminal velocity. In our case the terminal velocity is reached almost immediately. 26

2-2 The density of the spheres is crucial in the Stokes experiment on a foam. We can vary two parameters to obtain the right density values: the sphere radius and weight. The radii of the spheres have to be chosen amongst those that make the continuum approach reasonable and minimise boundary effects. If the spheres are too heavy, it is difficult to time their descent and they can destroy the foam. On the contrary, when they are too light, their weight is not enough to overcome the initial force F_0 associated to yield stress S_y. The foam will not yield and the spheres will stay on top of the foam. The right densities of the spheres to perform forced drainage Stokes experiments are within a very narrow margin ($0.7 \times 10^3\ kg/m^3 \leq \rho \leq 0.9 \times 10^3\ kg/m^3$). With spheres made of plastic of densities smaller than $\rho = 0.6 \times 10^3\ kg/m^3$, we perform the experiments using coarsening foam. These values are taken for foams with a $B_r \leq 0.5\ mm$. 30

2-3 Stokes experiment using different bubble sizes. The graph at the top presents the terminal velocity of the spheres of different bubble sizes. The empty circles are experimental velocities obtained for each bubble size. We also include the average of velocities for each bubble size within a margin of confidence of 65%. The data are consistent with a linear fit, if we ignore the last point on the right (see text). The graph below shows the ratio of sphere radius to bubble radius for the different bubble radii used in this experiment. The breakdown is reached approximately when $B_r \approx a/2$ in this case ($a = 5\ mm$). 33

2-4 The velocity of spheres of radii $a = 2.5\ mm$, $3\ mm$ and $4\ mm$ and $\rho = (0.9 \pm 0.1) \times 10^3\ kg/m^3$ falling in a foam undergoing forced drainage. While the $a = 4\ mm$ sphere has a positive velocity for all the flow rates, the other ones do not move through the foam at low flow rates. This shows the existence of a yield stress in foams. The solid lines are linear fits to the data. The scale also includes the approximate values of average liquid fraction that correspond to the flow rates, estimated using Archimedes principle (Appendix D). 34

2-5 The sphere is dropped into a fairly dry foam compared with Fig. 2-4 (liquid fraction less than 0.01) at time zero and its position recorded. The radii of the spheres are between $2.5\ mm < a < 3.1\ mm$ and the cylindrical tube diameter is $40\ mm$. All the lines show a transition from creep (slow motion) to accelerated motion. Local inhomogeneities in the foam structure apparently cause the sphere to 'hesitate' in its descent during the accelerated motion, returning to the slow creep (Data in Trial 2 and Trial 6). 36

2-6 Original data for Trial 1. There is a transition between the motion produced by creep and the accelerated motion as the foam coarsens. 38

2-7 We convert the original data from Fig. 2-6 to a log plot. The log plot helps to difference the regions of slow creeping motion and fast accelerated motion, as they both have different dependences of position versus time. The full black dot represents t_0, the time at which the motion changes from creep to acceleration. In this case, we obtain $t_0 = 40.50\ min$. 39

2-8 We use the value of t_0 obtained from Fig. 2-7 to fit all the data in Fig. 2-6 with $t \leq t_0$ to a straight line. The value obtained in this case for the creep correction is $0.34t + 2.0$. This line represents the creep motion. 40

2-9 We obtain a corrected set of data from the original data in Fig. 2-6 by subtracting the creep correction (Fig. 2-8) from the position and the value of t_0 (Fig. 2-7) from the time. 40

2-10 Using the correction described in Figs. 2-6 to 2-9 for the original data from the Stokes experiment on a coarsening foam, we obtain a set of different lines, described by the power law in Eq. 2.6. 41

2-11 In order to obtain the values of the constant k in Eq. 2.6, we take logarithms on each side of the equation (Eq. 2.8). In this way, we obtain the values for k stated in Table 2.2. The line corresponds to the proposed value $k = 3.1$. Note that the second creep region on the data of Trial 2 (the flat part shown in Fig. 2-10) has been avoided when fitting this set of points. 42

2-12 The yield stress decreases due to coarsening (increase in bubble size with time) while the applied stress is roughly constant (neglecting the small change in buoyancy). Until the yield stress falls below the applied stress there is no motion, apart from that due to creep. 43

2-13 The foam flows past a stationary sphere. We sketch a cross-section showing the position of the yield surface (dotted line) around the sphere. The size of the yielded region between the yield surface and the sphere increases with velocity v and decreases with yield stress S_y. We measure this yielded region, δa, in the radial direction across the cylinder, as shown in the figure. 46

2-14 Streamlines (A) and viscosity values (B) for the Stokes experiment in a foam. The flow velocity is $v = 0.03\ cm/s$ Parameters are $m = 1, S_y = 0.01\ N/m^2$ and $K_p = 0.01\ Ns/m^2$ for a sphere of radius $a = 4mm$ in a tube of diameter $D = 40\ mm$. We attribute the non-spherical contour on the viscosity in (B) to the interaction with the boundary in the calculation. 47

2-15 The numerically calculated width (across the cylinder) of the yielded region as a function of free stream foam velocity. Parameters are $m = 1, S_y = 0.01\ N/m^2$ and $K_p = 0.01\ Ns/m^2$ for a sphere of radius $a = 4mm$ in a tube of diameter $D = 40mm$. Also shown is a fit to $\delta a \sim \sqrt{v}$, the value predicted in Eq. 2.12 for $m = 1$. Note that the sphere produces a yielded region around it even at a zero velocity. 48

2-16 In a numerical calculation, we vary the exponent m in Eq.(2.1) to find the corresponding variation of the force on the sphere with the velocity. For $F \sim v^n$, we see that n is an increasing function of m; the values are given in Table 2.3. Parameters are $K_p = 0.01\ Ns/m^2$ and $S_y = 0.01\ N/m^2$ for a sphere of radius $a = 4mm$ in a tube of diameter $D = 40mm$. 49

3-1 At some critical liquid fraction (or flow rate) uniform drainage is unstable. Convective rolls occur either "side-by-side" as shown, or in a cylindrical form. . . . 54

3-2 Schematic mechanical analogy: the observation of hysteresis suggests that the system is more analogous to the one represented in (b) than to (a), close to the threshold of convection. 54

3-3 The setups for Hutzler *et al.* and Vera *et al.* experiments. A list of the principal differences is included. 55

3-4 This sketch shows co-existence of both types of convective instabilities in a column of foam: the one that does not have cylindrical symmetry on top and the cylindrically symmetric at the lower part. In some cases, only the symmetry-breaking instability is observed. This happens when the tube is short or the bubble size of the foam is relatively big. The cylindrically symmetric instability has not been found on its own during any of the experiments. 57

3-5 Three consecutive snapshots of the **SCR**. The pictures are separated by 2 seconds. The positions of two particular bubbles are marked to indicate the motion, one in yellow, moving upwards and the other in red, moving downwards. If we plot the position of the bubbles in relation to time, the velocity of the motion is approximately uniform. Downward motion is faster than upward motion. This is due to the different relative volumes of wet and dry foam. N.B.: The tubes are accurately vertical but the camera was slightly misaligned. 58

3-6 Three consecutive snapshots of the continuous motion stage for **CSI**. The pictures are separated by 2 seconds. The coloured bubble indicates the motion. Again, a plot of the position of the bubble in relation to time, shows a quite uniform velocity of the motion. 60

3-7 Three consecutive snapshots of **CSI** for the non-continuous motion. The pictures are separated by 2 seconds. The red bubble moves downwards but then seems to stop for a while, as we can deduce by the plot of position versus time. The yellow bubble does not move at all during the making of the film. 61

3-8 Typical domain of co-existence for the two types of instability in the same tube. The x-axis shows liquid fraction values and the y-axis the fraction of the length of tube occupied by the convective flows. Let us recall that **SCR** develops at the top of the tube and **CSI** in the rest of it, as seen in Fig. 3-4. The different regions of existence of **SCR** and **CSI** appear shaded. **SCR** develops at the top of the tube, increasing in length until **CSI** appears in the rest of the tube. Data is taken increasing the flow rate (solid line) until both motions are fully developed on the tube. After that, we decrease the flow rate (dotted line). This shows hysteresis (the area shaded in black) in the onset of **CSI**. An example of the experimental data is shown in Fig. 3-11, where the shaded regions have been omitted. For most of the experimental data, we have only measured values decreasing the flow. . . 63

3-9 Bubble velocities (y-axis) in the **CSI** related to liquid fraction (x-axis). This diagram also shows hysteresis in the behaviour of the bubbles as flow rate is varied (see experimental values in Fig. 3-20). 64

3-10 The figure shows the influence of the three different positions available for the wetting input in the convective rolls. We compare tubes with foam length 30 cm and (A) 1.6 cm diameter, (B) 2.0 cm diameter and (C) 3.2 cm diameter. The bubble radius is $B_r = 0.16\ cm$. We increase the flow rate to obtain domains of the convective rolls (explained in Fig. 3-8) but the shading of the different regions is omitted for clarity. The tube with 1.6 cm diameter was too narrow to allow us to take data of the "Off-centred" position. The values for the centred input cannot be compared with further experiments due to the hysteresis, explained in Section 3.4.4 (see Fig. 3-11). 66

3-11 Typical co-existence pattern for the two types of instability in cylindrical tubes. The input of surfactant solution is centred for tubes (A) 1.6 cm diameter, (B) 2.0 cm diameter and (C) 3.2 cm diameter and foam length 30 cm. The bubble radius is $B_r = 0.13\ cm$ in the three samples. **SCR** first develops at the top of the tube, increasing in length until **CSI** appears in the rest of the tube. We have increased the flow rate first and decreased it afterwards. This shows the hysteresis (the area shaded in black at Fig. 3-8) in the onset of **CSI**. The values for the onset critical liquid fractions are in accordance with the values obtained in Fig. 3-15. 67

3-12 The velocity of the bubbles in **CSI** when the liquid fraction is increased until the motion is fully developed and decreased afterwards. The bubble radius is $B_r = 0.15\ cm$ and the tube diameter is $2.0\ cm$ with foam length $30\ cm$. The plot is similar to the sketch in Fig. 3-9. Each velocity point is the average of six measurements. 68

3-13 A plot of the values of the domains of the two convective rolls (see Fig. 3-8) for a centred input. The same tube diameters used in Fig. 3-11 are shown together to compare them when we decrease the flow rate. These diameters are $1.6\ cm$, $2.0\ cm$ and $3.2\ cm$ with foam length $30\ cm$. The bubble radius is $B_r = 0.13\ cm$ Relatively wide tubes present a bigger **SCR** domain. There is also a tendency to get lower onset values for **CSI** with higher tube diameter. This dependence of critical onset liquid fraction with tube diameter will be confirmed later (see Fig. 3-17). Again, the domain regions (Fig. 3-8) are not shaded for the sake of clarity. 69

3-14 The domain of existence of the convective motions (see Fig. 3-8 for interpretation of this diagram) is also dependent on bubble size. The graphs correspond to a tube of $2.0\ cm$ diameter and foam length $30\ cm$. The bubble radii are (A) $0.27\ cm$ and (B) $0.15\ cm$. An increase in the bubble size leads to an increase in the domain of **SCR**, with the subsequent decrease of **CSI**. Therefore, for big bubble sizes or relatively short tubes, **SCR** is the only instability that would be observed. This affirmation has been checked several times during the experiments and will affect the way in which we investigate the dependence of the onset of the rolls with bubble size. The onset critical liquid fraction values seem to be lower at bigger bubbles attending to the preliminary result in this plot. We can confirm this from extended data in Figs. 3-15 and 3-20. 70

3-15 Dependence of the critical liquid fraction for the onset of the convective rolls upon inverse bubble radius. Values for four different tube *diameters* (A $1.1\ cm$, B $2.0\ cm$, C $3.1\ cm$ and D $3.4\ cm$) are shown. The length of the tubes is $30\ cm$. The dashed-dotted line marks the inverse bubble radius below which the motion observed at the tube is **SCR**. The solid lines are fits to Eq. 3.3. 72

3-16 Dependence of the critical liquid fraction at the onset of the convective rolls with inverse bubble radius. Values for three different tube *lengths* (A 15 cm, B 30 cm and C 35 cm) are shown. The diameter of the tubes is 2.0 cm. The graph marked as B is the same graph shown in Fig. 3-15-B. The dashed-dotted line marks the inverse bubble radius below which the motion observed at the tube is **SCR**. The solid lines are fits to Eq. 3.3. 73

3-17 A comparison of the slopes for all the tubes (A) in Fig. 3-15 and (B) in Fig. 3-16. The slope a decreases with tube diameter and increases with tube length. This corresponds with the qualitative observations deduced from these figures. 74

3-18 Comparison of the data obtained for **CSI** to the values reported by Hutzler et al. [63] for the onset of **SCR**. We compare tubes with (A)-1.1 cm diameter and (B)-15 cm length to (C)-the original data (1.5 cm diameter and length 12 cm). Our results are in accordance to the previous ones for larger bubbles (as both measure the onset of **SCR** at that range) but there is a departure of the points for smaller bubbles. The data from Hutzler et al. appears to level off at a value around $\phi_l = 0.2$, which is lower than the values obtained in Figs. 3-15 and 3-16. 75

3-19 This diagram shows the average velocities of the **CSI** bubble motion for four sections of a relatively long tube, over a narrow range of liquid fractions above threshold. The tube has 2.0 cm diameter and 52 cm length and the bubble radius is 0.13 cm. Each of the sections covers 5 cm in the tube. Section 1 is at the top of the tube, close to the area where **SCR** ends. Sections 2 and 3 are at the middle part of the tube (as sketched in the graphic). Section 4 is at the bottom part of the tube. The values at the middle sections are similar (each data point is the average of seven measurements). 76

3-20 Velocity of the bubbles in **CSI**. We found there is linear dependence on the excess liquid fraction over its critical value. This dependence is found for several bubble radius B_r using a tube 2.0 cm diameter and 35 cm long. 77

3-21 A blow up of Fig. 3-20 showing the detail of the lines fitted to the data. This graphs also allow to determine values for the critical liquid fraction at the onset of the motion in an alternative way to the values obtained in Figs. 3-15 and 3-16. . 78

3-22 A four-fold vertex at the surface of the container, reproduced from [74]. 82

3-23 Schematic illustration of forces/stresses involved in the equilibrium of a small element of foam under steady drainage. Dashed lines indicate the direction of shear strain or strain rate, for positive S. 84

3-24 Estimated values of the threshold for the convective motion from the "surface-driven" theory. We plot $\phi_l^c(x)$ with $x = \frac{l_0}{d}$. The theory gives a critical liquid fraction, ϕ_l^c, much higher than the experimental values shown in Fig. 3-18, but with a very similar overall shape. 86

3-25 A blow up from Fig. 3-24 showing the quadratic dependence when $d \to \infty$ (Eq. 3.17). 87

3-26 The radial dependences of S and ϕ_l^c as from Section 3.5.3, without taking in account the elastic dilatancy. 88

3-27 The solutions sketched in Fig. 3-26 change when we introduce the effect of elastic dilatancy in our considerations. Recall that dilantacy predicts $\Delta\phi_l \propto S^2$ 88

3-28 A slice of the tube is represented by a cylindrical shell of thickness dr and height dh. Position is represented by the radial coordinate r. Liquid fraction and other variables are functions of r. 89

3-29 Examples of solutions of Eq. 3.23 for (A)-$\phi_l^0 \approx 0.08$; (B)-$\phi_l^0 \approx 0.15$. We approach $\rho = \rho_w \phi_l^0$. The values of the constants are estimated using [37, 68, 66, 53] 91

3-30 Schematic diagram of the anticipated form of $v(r)$ from a dynamic theory. . . . 92

4-1 An sketch of the 2D experimental setup. The separation between the plates is around 0.5 mm. The reservoir is refilled constantly with surfactant solution and spread evenly with the help of a piece of porous material. The foam undergoes convective motions similar to the ones described on the 3D case. The symmetry axis in the convections is marked by the dot-dashed line. 96

4-2 The patterns found for the 3D convective motions can be reproduced in the 2D experiment. There are some differences between the 2D and the 3D case. A - **CSI**, in which bubbles move downwards at the wall and upwards in the rest of the foam appears in all the experiments with homogeneous wetting conditions. B - However, to reproduce the **SCR**, in which bubbles on one side move downwards and the ones at the opposite side move upwards, we need to force an inhomogeneous input. We do not find coexistence of the different convective patterns in the 2D setup. 98

4-3 A liquid channel a 2D foam. The snapshots are separated by 0.02 seconds. Two adjacent columns of bubbles separate to allow a great amount of water passing through. After the water has drained through the bubbles, the foam returns to its original equilibrium state. This occurs very seldom. 99

4-4 There is a clear layer of fluid in contact with the wall at high liquid fractions. The bubbles are deformed in a quite particular way that reminds us of an 'S'. 100

5-1 A sketch of the convective roll in a tilted tube. The dashed central line is a reference showing the central axis of the tube. The black arrows show the sense of the motion of the bubbles. Fluid draining on the foam moves preferably in the vertical direction, due to the gravity force attraction. 102

5-2 As the angle is tilted in the tube, the water is driven to the wall. The width of the wet region reduces. It may be possible that eventually, an angle would be reached at which the dry foam will float on a thin layer of bubbly liquid. In practice, it is impossible to do the experiment at angles close to the horizontal orientation. . . 103

5-3 Division of the sections in the tube. As we tilt the tube to the right, sections 1 and 2 will fall below the axis (wet foam) and sections 4 and 5 above it (dry foam). . . 104

5-4 Average velocity of surface bubbles (six per point) at five different sections of the tube sketched in Fig. 5-3. Each set of data is for a different angle of inclination. Flow rate is fixed at $0.408\ ml/s$ and the bubble radius is $1.79\ mm$. The change of sign in velocity in section 3 start at angles $\approx 15^o$. Bubbles in position 2, slow their downwards motion as well at those angles. The width of the wet side decreases when the tube is tilted, as it is marked by the solid lines. The speed of bubbles in sections 4 and 5 is fairly constant at each angle, which is consistent with the plug flow observed visually. Error bars have been omitted for clarity. 105

5-5 The figure shows the velocity of the bubbles that move upwards in relation to the angle of tilt. Every curve is labeled with the fixed flow rate at which it was taken. Small increases in the tilt angle lead to an increase in the speed of the bubbles at first. This effect levels off. At low flow rates, the velocity reaches a stable level and at higher flow rates, the bubbles moving upwards start to slow down showing non-continuous motion. We ignore the points after this slow down deliberately to fit the motion (this only affects to the data at flow rates higher than $1.16\ ml/s$. For the other sets, all the data up to 25^o is considered). The points for each different flow rate can be fitted to the function $f(\theta) = a\ tanh(b\theta - c)$. This set of data is for foam with a bubble radius $r = 1.56\ mm$ in a 2 cm diameter tube. 106

5-6 The values for the limit velocity reached by the convective roll in a tilted tube (parameter a in Fig. 5-5). vary linearly with flow rate. This set of data is for foam with a bubble radius $r = 1.56\ mm$ in a 2 cm diameter tube. 107

5-7 The values for the flow rate related to critical angle at the onset of the tilt convective motion in radians ($\theta_c = \frac{c}{b} * \frac{2\pi}{360^o}$ see Fig. 5-5 for clarification.). This set of data is for foam with a bubble radius $r = 1.56\ mm$ in a 2 cm diameter tube. The data fits to Eqs. 5.2 and 5.3 (the approximation for small angles) in Section 5.5. . 108

A-1 Four pictures of the same bubble showing the growth of the Plateau borders when the liquid fraction is increased. The values of liquid fraction are, respectively (A)-$\phi_l = 0.048$; (B)-$\phi_l = 0.075$; (C)-$\phi_l = 0.089$ and (D)- $\phi_l = 0.097$ for a bubble radius 1.3 mm. The convective instability, **CSI**, is triggered at a slow velocity in picture (D) (see movie `wallmotion.mpg` in CD). Two black dots at the bottom of the pictures are one millimetre apart and serve also as a check for the camera focus. We have measured only the evolution of the Plateau Border width marked by the red line. Results are shown in Fig. A-2. 113

A-2 Apparent width of the Plateau Borders at the surface of the foam. The bubble radius is 1.3 mm. The foam is static when the liquid fraction is lower than 0.09 (dots) and moves in convective motion (**CSI**) at higher liquid fractions (squares). The solid line represent the values corresponding to Eq. A.1 and the dashed line is a best fit to the equation $\delta = constant * \phi_l^{1/2}$ 114

A-3 A four-fold vertex at the surface of the container. The width of the Plateau border at the container wall is twice the width of an internal Plateau border. Reproduced from [74]. 115

A-4 The experimental results in Fig. A-2 are sensibly lower than the ones expected from Eq. A.1. We attribute this difference in the measurements to optical reasons. The values we measure δ_{exp} are different to the real width of the Plateau borders δ_w. 116

B-1 A bidisperse bubble cluster has bubbles of two different areas. 117

B-2 What is the minimum perimeter that can enclose cells of a given area or volume? A/ For an infinite plane, the best option available has been proved to be the honeycomb. In 3D the problem is known as the Kelvin problem and space partition remains debatable. B/ Kelvin conjectured a solution with a unit cell composed by two equal cells (tetrakaidecahedrons), which are truncated octahedra slightly deformed. C/ Weaire and Phelan have calculated that the structure shown in the picture has lower energy than the Kelvin partition of space. The Weaire-Phelan unit cell is composed of eight bubbles of two different shapes but equal volume. 118

B-3 One candidate for minimum energy in (2-2) clusters. Experimental picture of the cluster (left). Simulations can be done the Surface Evolver (right). 119

B-4 Bubbles come together because sharing a common film lowers their surface energy. This energy is proportional to the total length of the film that encloses the bubbles. The bubbles are supposed to keep a constant area A. 120

B-5 When the bubbles sizes are different, the number of configurations that a cluster with the same topology can access grows. We can see on the sketch that the configuration on the left, does not change if we swap the elements between them. The ones at the right, that have different tiles, are not the same, even if all share the same topology. Greater polydispersity leads to a greater number of configurations. 125

B-6 A picture of the experimental set-up. A Plexiglas top plate covers the bottom left part of the vessel. It can be tilted to separate the bubbles by submerging them into the pool. One of the nozzles used for foam production (described in Appendix D) can be seen at the top left. The top plate is covering a cluster in the centre of the vessel. 126

B-7 Stable experimental clusters formed by 4 bubbles. $A_M/A_m \approx \frac{4}{3}$. The reference line corresponds to 5 mm in real size. Two different clusters are found. The statistics of the two clusters occurrence (see Fig. B-13) show a preference for the second configuration experimentally. This configuration is not symmetrical (the two small bubbles are in contact). 128

B-8 Stable experimental clusters formed by 6 bubbles where $A_M/A_m \approx \frac{4}{3}$. The reference line corresponds to 5 mm in real size. Fifteen candidates are found. The ones that appear more often experimentally (see Fig. B-13 for the complete statistical values) are marked in the picture as S1, S2 and S3. 129

B-9 Stable experimental clusters where $A_M/A_m = 2$. The reference line corresponds to 5 mm in real size. Two different clusters are found. The statistic study of occurrence of these clusters (see Fig. B-14) shows a preference to the symmetrical configuration (number 1), where the two small bubbles are separated. 130

B-10 Stable experimental clusters for 6 bubbles where $A_M/A_m = 2$. The reference line corresponds to 5 mm in real size. We find the same candidates as for $A_M/A_m = \frac{4}{3}$ (Fig. B-8) , except cluster 13. A statistical study of the clusters shows that the most frequent ones are numbers 2, 6 and 5. 131

B-11 The two stable experimental clusters for 4 bubbles where $A_M/A_m = 4$. The reference line corresponds to 5 mm in real size. The cluster labelled number 1 is statistically more probable than number 2 (see Fig. B-15). 132

B-12 Stable experimental clusters with six bubbles with area ratio $A_M/A_m = 4$. The reference line corresponds to 5 mm in real size. The three statistically most favourable clusters (see Fig. B-15) are marked in the picture. 133

B-13 Statistics that show the probability to find the clusters on experimental trials. In this case, $A_M/A_m = \frac{4}{3}$. 134

B-14 Statistics that show the probability to find the clusters on experimental trials, when $A_M/A_m = 2$. 135

B-15 Statistics that show the probability to find the clusters on experimental trials. In this case, $A_M/A_m = 4$. 136

B-16 The $(2, 2)$ cluster number 2 for the area ratio $A_M/A_m = \frac{4}{3}$. The experimental picture is shown together with the Evolver simulated shape. This cluster appears experimentally more often than expected, giving its calculated energy. 139

B-17 The $(3, 3)$ cluster number 13. A/ Experimental picture at a ratio $A_M/A_m = \frac{4}{3}$. B/ Evolver calculated shape for the same ratio and topology. C and D/ Evolver calculated shapes for the same topology and ratios $A_M/A_m = 2$ (C) and $A_M/A_m = 4$ (D). The cluster does not appear experimentally for these ratios. The length of the edges at the small bubbles at the calculated shape (D) suggest that the cluster may be prone to have a $T1$ and become a new configuration. 140

B-18 Cluster $(3, 3)$ number 7 becomes the one with less calculated energy at an area ratio $A_M/A_m = 4$. 141

B-19 The calculated energy of all clusters is presented here and compared with the lower bound calculated for polydisperse clusters and round boundary, Eq. B.8, and the lower bound calculated for bidisperse clusters and hexagonal boundary, Eq. B.9. The values are close to the theoretical equations, even if the number of bubbles N is quite small. However, some of the calculated energies of our clusters are below the possible lower bounds. This was expected, as Eq. B.8 and Eq. B.9 are deduced for clusters with a large number of bubbles. The experimental values included correspond to the minimum energy clusters obtained in Table B.1. The experimental values for $E/\gamma_{foam}\sqrt(SA_i)$ are around 10% below the energies predicted by the theoretical lines. These lower energies can be attributed to the experimental set-up, in which the bubbles are in contact to the surfactant liquid pool. 142

D-1 Foam produced by several different methods. The dispersion in bubble size is less for the blowing production methods. Reproduced from [1, 113]. 147

D-2 Experimental set-up to obtain monodisperse foams. Once produced, the foam can be introduced into different geometries to carry out 3D or 2D experiments. . . . 148

D-3 Experimental set-up to obtain monodisperse foams. Once produced, the foam can be introduced into different geometries to carry out 3D or 2D experiments. . . . 150

F-1 Images of a Plateau border at different stages of an Evolver calculation. A- Starting topology for the Plateau border. B- One level of refinement after 500 iterations. C- Two levels of refinement after 500 iterations. D- Three levels of refinement after 500 iterations. 155

F-2 The diagram shows the method followed in our calculations of flow induced deformation in tetrahedral junctions. First, the channel shape is calculated using the Surface Evolver. The surface is meshed using the preprocessor included in the Fluent package, Gambit and we simulate flow conditions inside the channel. The flow produces a force at the walls of the channels which can be introduced as a new boundary condition in the Surface Evolver. At that point, we compare the result of our calculation with the surface obtained at the previous step. If their energies differ by less than 0.01%, we consider the result converged. 157

G-1 The tilted tube changes its orientation with respect to gravity. The axis X1 and X2 are tilted an angle θ to get the new set of axis in which Z is parallel to the axis of the tube. M is the matrix that rotates the system X1-X2 into the new system Y-Z. 158

List of Tables

2.1 A table of different models used to fit experiments (Ex) and computations (C) in 2D and 3D systems on foam (F), Foam concentrates (FC) and emulsions (Em). The main models used are Power Law (PL) (Eq. 1.17, with exponent n), Bingham (B) (Eq. 1.15) and Herschel-Bulkley (H-B) model (Eq. 2.1 with exponent m). The Bingham model is a particular case of the Herschel-Bulkley model with exponent $m = 1$. The last two assume a finite yield stress of the foam. 28

2.2 Values for t_0 (Fig. 2-7) and the creep correction line (Fig. 2-8) applied to the experimental data in Fig. 2-5 to obtain the corrected values in Fig. 2-10. The last column gives the individual values of k obtained from the slopes on the log-log plot in Fig. 2-11. 43

2.3 Comparison of the theoretical and numerical estimates of the exponent of velocity, n, in the force equation (2.9). We also give the corresponding value of the exponent m in the Herschel-Bulkley relation, Eq.(2.1). We select values of n_{theory} between 0.4 and 0.67. The value of $m(n_{\text{theory}})$ is found from Eq. (2.13) and used in our numerical calculations to verify the value of n_{theory}. The values we find from the computations, n_{numeric}, are rather lower in all cases. 49

B.1 Surface Evolver energies for the area ratios $A_M/A_m = \frac{4}{3}$, $A_M/A_m = 2$ and $A_M/A_m = 4$. 138

F.1 Final energies for the iterated Plateau border for several levels of refinement. The column on the right is a power law extrapolation based on the previous and actual values obtained for the energy. The energy value converges to 1.35340 at the sixth level of refinement. 156

Chapter 1

Basic notions

1.1 Motivation

This thesis deals with some aspects of **the physics of foams** [1]. The basic knowledge of physical properties for dry static foam is sufficient to picture a quite complete theory (see Fig. 1-1). This theory has been gained using a variety of different approaches that combined *experiments, mathematical modelling* and *computations*. There has been a preference to use 2D geometries in experiments and simulations for the sake of simplicity. But with the availability of more computational power and tools, 3D geometries have provided new insight into the foam structure. The Surface Evolver [2] (Appendix F) calculations on minimal bubble areas [3] can be mentioned as an example of the latest developments.

Areas in which we have a good understanding about foams include the structure, electrical conductivity profiles and elastic deformation of the foam and how these properties change with the addition of amounts of liquid small enough for the foam to remain close to the dry limit. Some aspects, as drainage of liquid through the foam and foam flow properties, are fairly well understood but subtle questions related to these fields remain under debate: one example is the choice of boundary conditions to represent the Plateau borders when calculating the drainage equation on a foam. This problem will be explained in some detail at Section 1.4.

Wet foam physics and dynamics still pose us interesting questions that have not been explained (Fig. 1-1).

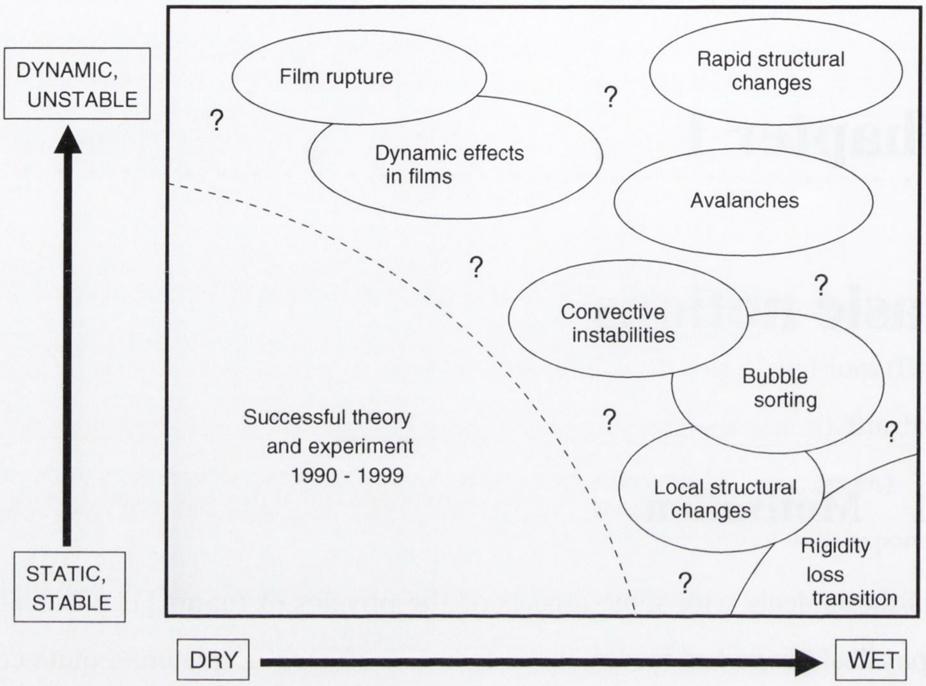
DYNAMIC, UNSTABLE
STATIC, STABLE
DRY
WET
Film rupture
Dynamic effects in films
Rapid structural changes
Avalanches
Convective instabilities
Bubble sorting
Local structural changes
Rigidity loss transition
Successful theory and experiment 1990 - 1999
?

Figure 1-1: Some of the main challenges at present in the physics of foams. The figure is reproduced from [4] with the kind authorisation of the authors.

This thesis deals with some of these unexplained effects in wet foams. This chapter is dedicated in full to a *review of what is already known and relevant* to what follows.

Firsly, it is necessary to define what is a foam, and introduce the main laws that govern foam behaviour. These rules will be grouped in four aspects: *structure, drainage, rheological properties* and *coarsening and rupture*:

STRUCTURE Foam structure conforms to simple geometrical rules. We will describe the laws for the equilibrium of a single bubble (Laplace law) and consider how two bubbles become in contact (Plateau rules). When many bubbles come together, statistical measures of the behaviour of the foam are also needed.

DRAINAGE We use the term drainage to describe the motion of a liquid through the foam. As we will see, foam is composed of a certain amount of liquid and this liquid plays an important role in the behaviour and properties of the system (rheology included). We have performed experiments in which a source of liquid is added at the top of the foam. Therefore, we should describe how this liquid percolates into the heart of the foam and the difference that the liquid makes in its properties.

RHEOLOGY Foams behave both as a solid and as a liquid, depending on external conditions. This behaviour is common to foams and many other materials, that are currently known as *plastic* materials. The capacity of foam to flow above a certain stress, makes possible the Stokes experiment, in Chapter 2. The existence of a yield stress is also an important aspect of the explanation of the convective instabilities described in Chapters 3 to 5.

COARSENING AND RUPTURE We all know from experience that bubbles do not last forever. This is a factor to be taken into consideration when experiments are made. The concepts of coarsening and collapse will be defined and the methods to minimise their effect during experiments will be noted.

1.2 Definition of a foam

Bikerman [5] says in his books devoted to the subject that 'foams are agglomerations of gas bubbles separated from each other by thin liquid films'. Weaire and Hutzler [1] refer to a foam as 'a two-phase system in which gas cells are enclosed by liquid'. Both definitions share the reference to two different phases, gas and liquid.

We are going to restrict ourselves to aqueous foams, which are gas-liquid mixtures. Other colloids, such as emulsions (liquid-liquid mixtures) and solid foams (often solidified liquid foams) share many properties with aqueous foams.

1.2.1 Term definitions

Bubbles or cells The bubbles or cells are any of the gas volumes that compose a foam. Each of the bubbles is partly surrounded by walls, which are called films.

Films The films or **lamellae** enclose some liquid. They are commonly stabilised by additives called **surfactants** (see Fig. 1-2). The surfactant (surface active constituent) also lowers the surface tension of the films.

Edges or Plateau borders The edges are the lines formed by three films coming in contact. They are also known as Plateau borders after Joseph Plateau, who described the rules that soap films follow to join together. Plateau borders will expand and thicken into channels when liquid is added to a dry foam.

Vertices or nodes A vertex is the point where several edges join. The term node is also used to refer the same point.

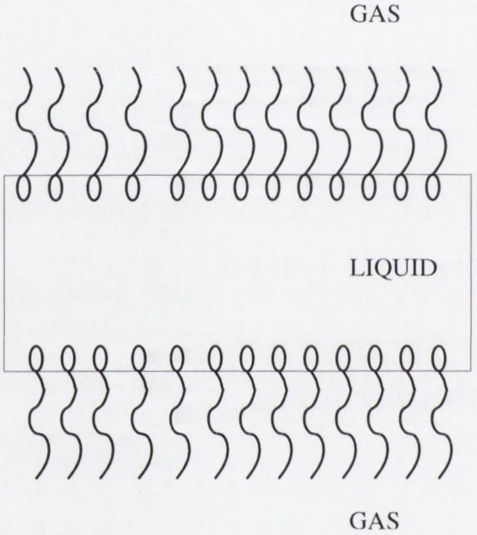

Figure 1-2: A soap film, containing amphiphilic molecules. These are chemicals formed by two parts. One of them attracts liquid molecules and the other repels them. The physical chemistry inside the films can be very complicated, including dynamic effects such as Marangoni convection which are beyond of the scope of this thesis.

1.3 Foam structure

1.3.1 Young-Laplace law

The interface in a 3D bubble obeys the *Laplace law* [1]:

---

[1] Sometimes also referred as Young-Laplace

$$\triangle p = 4\gamma/r = 2\gamma_{foam}/r, \tag{1.1}$$

where $\triangle p$ stands for the pressure difference between the inside and the outside of the bubble, γ is the surface tension or surface energy per unit area and r is the local radius curvature of the surface, related to the principal curvatures by $2/r = 1/r_1 + 1/r_2$. The factor 4 takes in account that the film is formed by two layers. Note that when the surface tension is renamed to be $\gamma_{foam} = 2\gamma$, the formulation in Eq. 1.1 is equivalent to the most usual form of the Laplace law in an air bubble immersed in water [1].

1.3.2 Plateau rules

In the XIX century, the Belgian scientist Joseph Plateau described the *main rules of equilibrium for soap films* (Fig. 1-3). These laws are valid for dry foams, but they can be adapted to some extent to wet foams, as we will describe in Section 1.4.

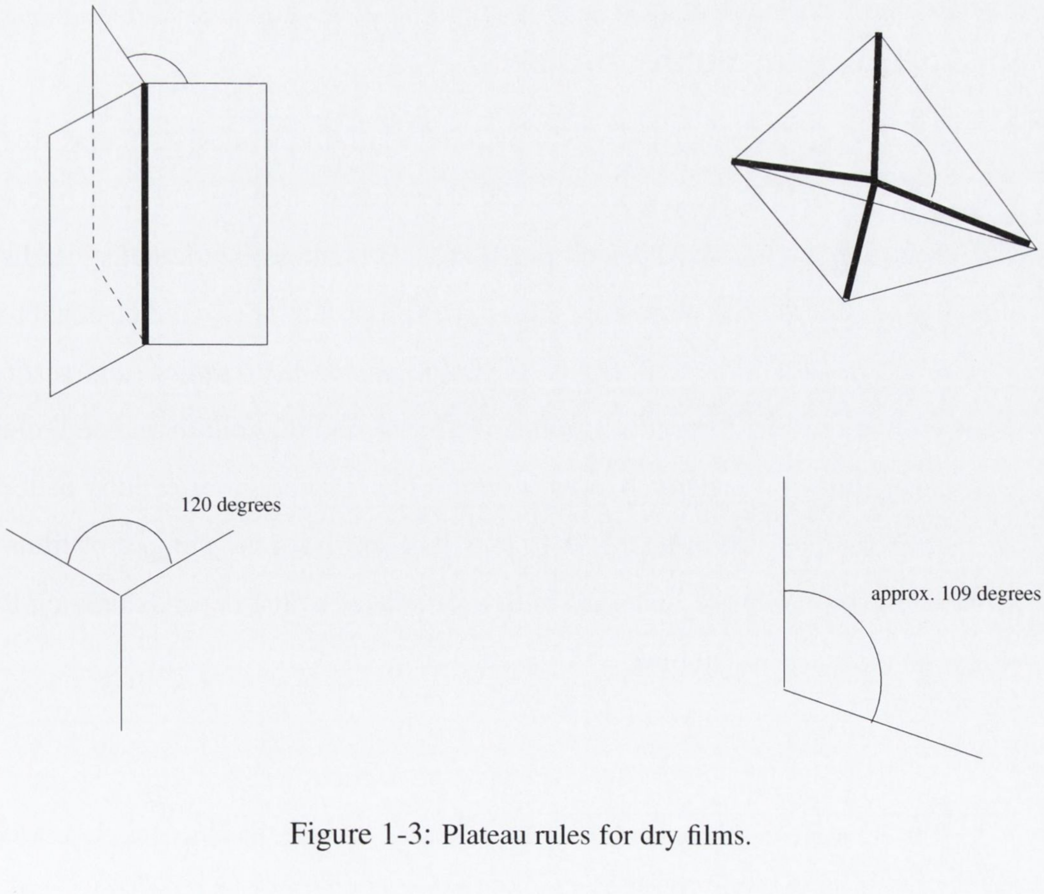

Figure 1-3: Plateau rules for dry films.

- The first equilibrium law says that
  - in a dry foam films can only intersect three at a time and with an angle of 120°.
  - only four edges can intersect in every vertex with perfect tetrahedral coordination. This implies a characteristic angle called sometimes Maraldi angle with value $\theta = cos^{-1}(-1/3)$.
- The second equilibrium rule says that a Plateau border joins the films at which it is attached at a zero angle (the surface normal is the same at both sides of the intersection).

These laws can be adapted to a 2D foam, where edges intersect three at a time at 120°. Plateau was completely blind when he described these laws, and he gained all the experimental data that needed for his theory using descriptions of other people and by visualising them in his mind.

1.3.3 The many bubble problem

The laws we have described previously are *local* equilibrium rules. As foams are formed by a large number of bubbles, a more extended theory, that describes the rules of coordination of multiple bubbles has also been proposed [1]. An example are the statistical distributions of bubble area $p(A_b)$ and number of edges $p(n)$ proposed for two dimensional foam [2].

In a 2D dry foam, $\bar{n} = 6$ that is, *the average cell has 6 edges (and vertices)*. This result will be used in Appendix B when we try to find the minimum configuration for a bi-disperse cluster. It is derived directly from Euler's theorem for cellular patterns, which we state in its 2D form in Eq. 1.2. Euler's theorem links the number of films F, edges E and vertices V in these materials with a parameter ψ that depends only on the surface where the cells are constrained:

$$F - E + V = \psi. \tag{1.2}$$

---

[2] For three dimensional foam, the distributions of bubble volume and number of faces are defined in a way equivalent to these. For experimental convenience, the two dimensional case is studied more often.

1.3.4 Topological changes

Among the most interesting phenomena in the structure of a foam are the *topological changes* that occur both in 2D and 3D foams. The most elementary changes are the so-called *T1* and *T2* processes, in a nomenclature due to Weaire and Kermode [6]. Other changes are combinations of these ones.

A T2 change consists of the shrinking and disappearance of a three-sided cell (2D) or a tetrahedral bubble (3D) as is sketched in Fig. 1-4.

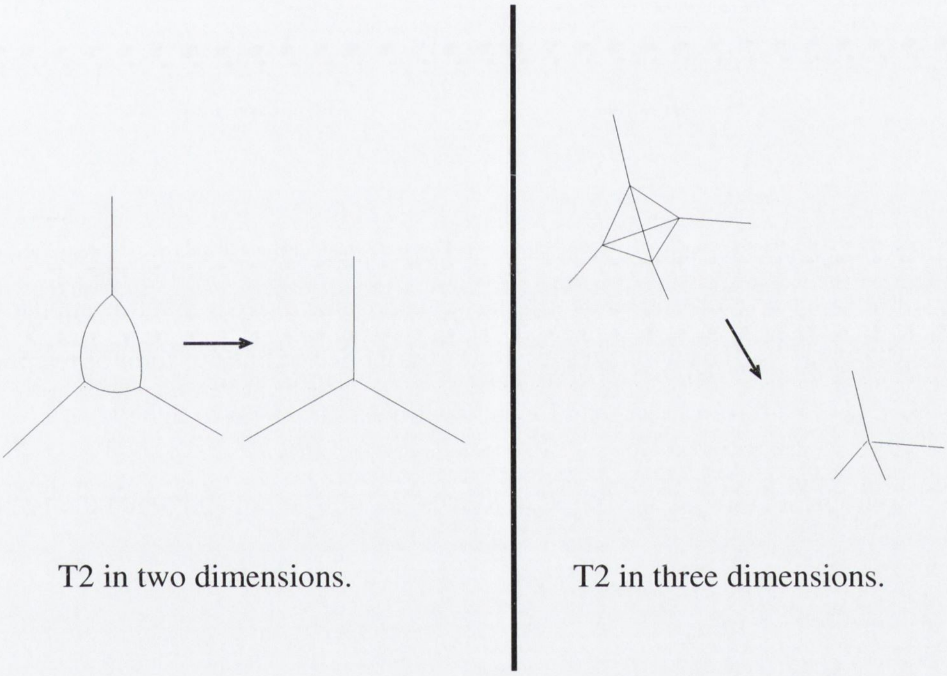

T2 in two dimensions.

T2 in three dimensions.

Figure 1-4: In the T2 process in 2D a three-sided cell vanishes. It is similar in 3D with tetragonal bubbles.

T1 changes are more complicated. A vertex can become unstable (by having more edges attached than the number allowed by Plateau rules) at some point in time. This may be due to evolution (coarsening), caused by internal (gas) pressures or external (shear) forces. This will lead to a change in the connectivity of the edges concerned. The unstable vertex dissociates in two and the relationships between neighbouring cells changes. A rough sketch of T1 changes is represented in Fig. 1-5.

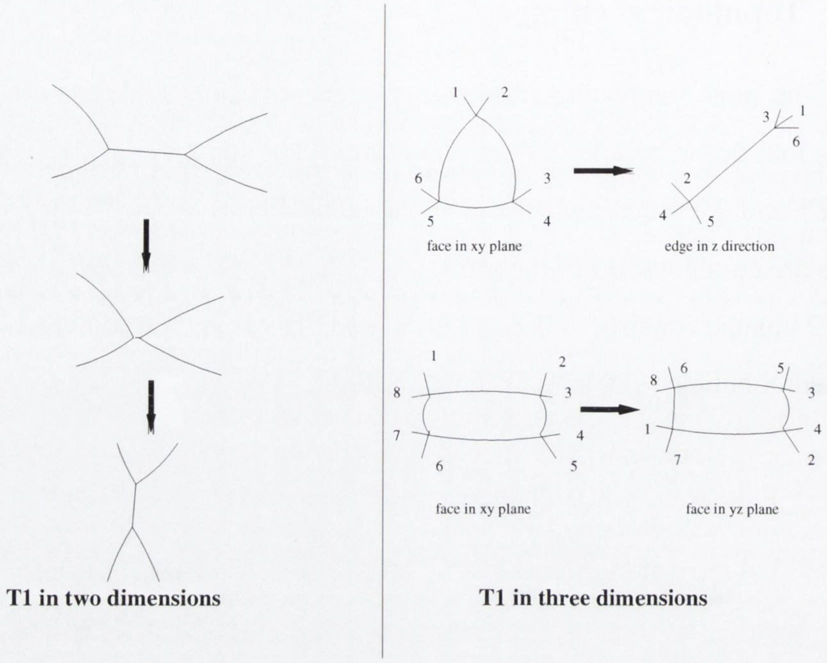

T1 in two dimensions

T1 in three dimensions

Figure 1-5: The T1 changes in 2D and 3D dry foams. In 2D foams, a four-fold unstable vertex is broken. For 3D foams an elementary rearrangement exists that it is similar to the T1 two-dimensional process (shown right up). However, the most common form of rearrangement that is observed in three-dimensional foams is the multiple process shown right down.

Topological changes are frequent in a coarsening foam and when the foam is subjected to shear.

1.3.5 Osmotic pressure

The *osmotic pressure* is analogous to the pressure that equilibrates the concentration of particles in solutions, hence the name. In a very wet foam, the bubbles are almost spherical and the contact between them is minimum. When the foam dries out, the bubbles are compressed together. They adopt polyhedral shapes that increase their surface energy. If liquid is free to enter or leave the system, the bubbles must be held in equilibrium by an external pressure - the osmotic pressure.

The osmotic pressure can be defined as the variation of the surface energy of the foam, F, in all the volume of the foam, V:

$$\pi = -\left(\frac{\partial F}{\partial V}\right)_{V_g}, \tag{1.3}$$

where it is assumed that the gas volume V_g does not vary.

The osmotic pressure depends on the liquid fraction. It goes from zero in a very wet foam to infinity in a dry foam. Simulations made on 2D polydisperse foams [1] have shown a good agreement with a quadratic dependence on liquid fraction, ϕ_l.

$$\pi = a(b - \phi_l)^2, \tag{1.4}$$

where a and b are constants.

The osmotic pressure also depends on state of the elastic deformation of the foam. This is a second order term that can be neglected in many cases but it may play an important role in the explanation of the convective instabilities in Chapter 3.

1.4 Drainage

The liquid content in a foam is quantified by the *liquid fraction* [3], ϕ_l, the ratio of the volume of liquid in the foam to the total volume of the foam. The experimental liquid fraction of a foam can often be estimated using the Archimedes principle (see Appendix D).

In our experimental work, we often add some liquid on top of the foam. This liquid is the same surfactant solution used to form the foam. The *flow rate*, Q, is the volume of fluid added per unit time. There is a simple relation between flow rate and liquid fraction in a uniformly draining foam [1]:

$$\phi_l \propto \sqrt{Q}. \tag{1.5}$$

The proportion of liquid or wetness of the foam determines many characteristics of the system: the Plateau borders thicken into channels; the vertices grow and, at a certain point, cannot be regarded as points any longer. Bubbles become more spherical in a wet foam.

---

[3] The *gas fraction* ϕ is defined as the ratio of the volume of gas in the foam to the total volume of the foam: $\phi = 1 - \phi_l$.

All these changes translate into different values for the physical parameters of the foam: elastic and rheological properties vary with the liquid content.

There is an equilibrium profile of liquid fraction under gravity in the vertical direction of the containers, with a dry foam at the top and wet foam at the bottom of the sample. The excess liquid is drained out of the foam.

In this thesis, drainage plays an important role: the instabilities described in Chapters 3 to 5 only appear at a certain liquid fraction.

We will describe first different ways to input liquid on top of a sample. Each of these will lead to a different vertical profile under gravity. Then, we will comment on the structure changes, which happen when there is an input of liquid in the foam. Drainage in a foam can be described mathematically by a nonlinear diffusion equation. There has been quite a debate regarding which form this equation should take. One of the forms of the equation is based in assumptions that concentrate all the flow dissipation in the channels (Plateau borders) and ignores node effects. The other one is node-dominated and neglects the channel contribution. The use of the channel-dominated form of the equation will be justified experimentally for the type of surfactant that we use in the experiments. The channel-dominated equation can be corrected to take the effect of the nodes to account

1.4.1 Free drainage, forced drainage and pulsed drainage

The most simple drainage experiment would occur when foam is left to drain on its own after formation, in what is known as *free drainage*. It is possible to measure the amount of liquid drained out from the foam as a function of time. Free drainage has fairly complicated mathematical solutions, but some recent work has been aimed at explaining some of their simplest features [7].

Forced drainage is established when an amount of liquid is input steadily into the foam. If we start the experiment with a dry foam, the liquid travels through the foam in the form of a *solitary wave*. An interface separates the wet part from the dry one. The solitary wave triggers local rearrangements in its way on the foam. When the input is constant, we can talk about *forced stationary drainage*. This is a very interesting case, as once the solitary wave has passed, the vertical liquid profile in the foam should be approximately homogeneous. This is a uniform wet foam, although not in equilibrium, in the usual sense.

Another way to study drainage in foam is *pulsed drainage*. A pulse of liquid is added on top of the foam and we can study how it spreads with time.

1.4.2 The growth of Plateau borders

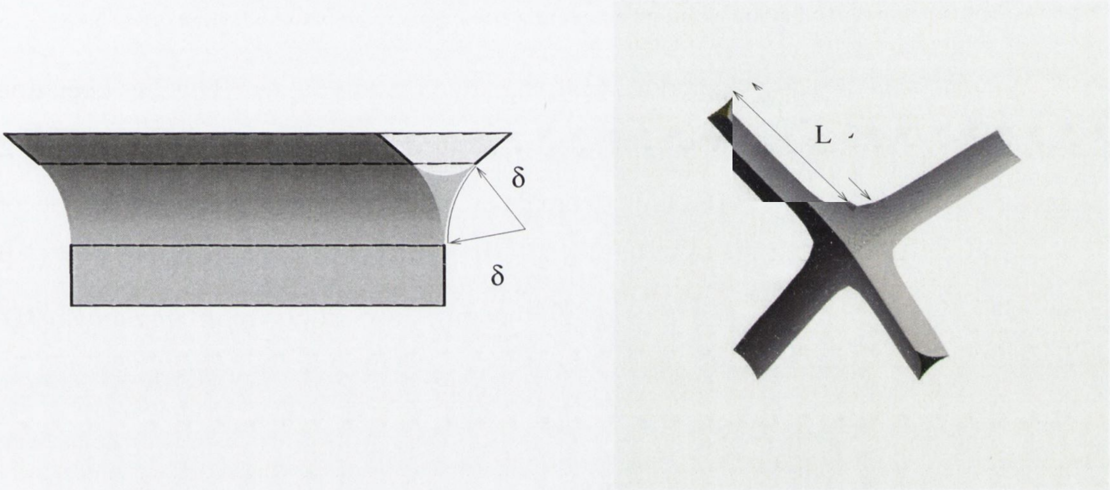

Figure 1-6: The Plateau Borders (left) increase their volume when the foam becomes wet. Four of them join in a junction (right), following the Plateau rules represented in Fig. 1-3, in the dry limit.

In wet foam, the bubbles become more spherical. The Plateau borders thicken and become channels in which the water percolates through the foam. The union between the Plateau borders is no longer a point-like vertex. The general case is that the three curvatures of the films that form the Plateau border are different. However, it is convenient to neglect the longitudinal curvature in many cases. In this way, the cross-section A_{PB} of the Plateau border can be written as:

$$A_{PB} = c_g \delta, \tag{1.6}$$

where δ is the width or radius of curvature of the Plateau border (see Fig. 1-6) and c_g a geometrical constant.

The volume of a Plateau Border in a dry foam is then:

$$V_{PB} = A_{PB}L. \tag{1.7}$$

A computation of a wet Plateau border and a *four-fold vertex* or *tetrahedral junction* (the junction of these channels together) made using the Surface Evolver [2] is shown in Fig. 1-6. For wet foams, the Surface Evolver calculates the shape of the junction, once given the width, δ, of the Plateau borders that join at it (related to the liquid fraction on the foam).

Plateau rules can be adapted to wet foams to a certain degree. This has been done successfully in 2D models [8] using the so-called 'decoration lemma'. It states that given a picture of a dry foam, it is possible to create an equilibrium wet foam just by 'decorating' each threefold vertex with Plateau borders. The Plateau borders have to follow Plateau rules and do not overlap. The 'decoration theorem' also works *approximately* in 3D [1].

1.4.3 The drainage equation

Several theoretical models have been described to predict the drainage behaviour in aqueous foam. All of them take the form of non-linear partial differential equations and neglect the contribution of films to drainage (which is minor compared to the flow of liquid through Plateau borders).

Goldfarb *et al.* [9], derived for the first time the channel- dominated form of drainage equation. The formulation we are going to use has been reproduced from the paper of Verbist and Weaire [10] in which this equation was independently derived and called as the *foam drainage equation* for the first time:

$$\frac{\partial \alpha}{\partial \tau} + \frac{\partial}{\partial \xi}\left(\alpha^2 - \frac{\sqrt{\alpha}}{2}\frac{\partial \alpha}{\partial \xi}\right) = 0. \tag{1.8}$$

Here α, ξ and τ are non-dimensional variables obtained from the cross-section of the Plateau border, the downward vertical coordinate and time, respectively. The main steps for the derivation of this form of the equation are included on Appendix C.

The equation described above only accounts for drainage in one dimension but it has been generalised to two and three [11]. Saint-Jalmes *et al.*, have attempted to apply it for an arbitrary container shape [12]. The effects of gravity in the drainage equation have received some interest in the last years [13, 14], linked in part to the possibility of performing experiments in microgravity conditions [15]. The microgravity experiments are often mentioned as a way to avoid the convective rolls described in this thesis.

The drainage equation (Eq. 1.8) has shown a great deal of accordance with experimental results. It has an exact solution in form of a solitary wave whose velocity V relates with the flow rate Q following the power law:

$$Q \propto V^2. \tag{1.9}$$

This result has been corroborated experimentally several times [16, 17, 18].

In 1999, new experimental results obtained by Koehler *et al.* [19] using improved methods were not in accordance with the dependence shown in Eq. 1.9. These experimental data show a solitary wave profile, but the dependence of flow rate Q with the velocity of the front V is found to be:

$$Q \propto V^3. \tag{1.10}$$

The authors explain their result writing a new form of the drainage equation, at which there is full-slip conditions at the walls of the channels, the opposite of the (Poiseuille) assumption previously used. The nodes viscous contribution becomes dominant and the result is a new equation which has a solution for the solitary wave follows the power law expected in Eq. 1.10. This approach is known as the *node-dominated foam drainage equation.*

The explanation to this dilemma came in the form of two different bottles of dishwashing liquid. Both equations seem to agree with experimental results obtained at different sides of the Atlantic. While Hutzler *et al.* [17] use the commercial dish-washing liquid Fairy for all the experimental work made in their group, the Harvard group [19] uses Dawn, a fairly more popular brand in the U.S.A. It seems that Fairy liquid produces a foam with different surface properties, a higher surface viscosity among them. This makes the assumption of Poiseuille flow a good one. Dawn produces a foam with comparatively low surface viscosity (so that dissipation has to be dominated by the existence of nodes in this case). Leonard and Lemlich had already noted that the rigid-wall hypothesis could fail in some cases [20].

Brannigan and de Alcantara Bonfim [21] suggest a dependence of the velocity of the solitary wave on the boundary of the tubes which contain the foam. And the dependence of drainage on the surface properties of the surfactant was corroborated recently by the data of Durand *et al.* [22]. They measured the velocity of the solitary wave for a single surfactant (SDS) with different amounts of dodecanol. Dodecanol forms rigid layers with SDS increasing the surface viscosity and the surface elasticity at the gas-water interface. An increase in the amount of dodecanol in the system gives results closer to the channel-dominated limit. Experiments carried out by Koehler *et al.* [23] seem to confirm further the idea of surface viscosity playing an important role in drainage. However, a theoretical model by Durand and Langevin [24] suggest that the surface elasticity is the main factor in drainage, neglecting the effect of surface viscosities. This has been contested, at least for slender Plateau borders, where the transverse shear viscous contribution is important [23], and surface elasticity now seems to be relatively insignificant in the standard experiments.

It seems plausible that all surfactants will flow with properties which lie between these two extreme behaviours. Efforts to join the effects of both equations in a single hybrid foam drainage equation, of which the channel-dominated form and the node-dominated form are extreme cases, are being undertaken at present [25, 24]. In this thesis, all our data are taken with Fairy Liquid and we accept the channel-dominated foam drainage equation as our standard flow equation, as it has been validated for our surfactant type in several occasions [17, 24].

1.5 Rheology

Some materials present a complicated type of flow, which makes them behave both as solids and as liquids depending on external conditions. There are many examples of this *plastic* behaviour (paint, cosmetics, spreads and so on). We can observe that in most cases the flow properties are fundamental for the good performance of these materials, especially in the ones developed as industrial products. A typical example is paint, which should flow when you coat the brush and stay on the wall as soon as you spread it. A good knowledge of the theoretical background of this flow allows to control the properties related to it.

Foam also shows this flow property: everybody who has played in a bubble bath as a child has tried to retain some water on their hands. We all know that it is extremely difficult because water escapes between your fingers. If we try to repeat this trick with foam, we discover that it stays in your hands and it only flows when we squeeze it. The yield stress, which determines the onset of flow is a key property.

1.5.1 Flow properties of materials

It is convenient at this point to introduce some terms of common use throughout the next chapters. These ideas are fundamental in order to understand and develop a theory of flow, and it is worthwhile to have a clear and rigorous definition of each of them. These definitions are taken from references [26, 27, 1, 28].

shear: In a two-dimension material we can define simple shear by:

$$\begin{aligned} x' &= x + \zeta y \\ y' &= y, \end{aligned} \tag{1.11}$$

while extensional shear can be defined by:

$$\begin{aligned} x' &= (1+\epsilon)x \\ y' &= (1+\epsilon)^{-1}y, \end{aligned} \tag{1.12}$$

In linear elasticity both types of shear are equivalent under a rotation by $\pi/4$ of axes with $\zeta = 2\epsilon$.

shear stress or stress: It is defined as the external force applied to the system per unit area. Its units are Pa (N/m^2) in I.S. It will be represented in this thesis by the symbol S.

strain: It is a relative displacement of the atoms of a solid $(\triangle l/l)$ for extensional shears and the angle of displacement for shear stress. The symbol used to represent strain in this thesis is ϵ.

shear modulus: The stress and strain can be represented by tensors and we can write their relation as follows:

$$S_i = G_{ij}\epsilon_j, \tag{1.13}$$

which is only valid when the material follows Hooke's law and the shear we are applying is into the elastic range. Using this formulation, it is easy to separate the three components of the equation in tensorial form and treat the effects of extensional and simple shear separately. G_{ij} is the stiffness matrix. G, the shear modulus is the ratio between the shear stress and the total shear strain on the plane at which we are considering the shear occurring.

shear rate: This is the rate of change (derivative) of shear strain in time. We will represent shear rate by the symbol $\dot{\epsilon}$

yield stress: Some materials do not start flowing apparently when a small shear stress is applied. In these cases, the yield stress is defined as the point at which the mechanical properties change dramatically and liquid-like behaviour starts.

creep Many solids and soft materials also experience a 'slow but continual steady deformation when stressed for a long time below this level' (for the yield stress) [26]. This phenomena is known as creep. However, the concept of yield stress previously defined can be applied because it remains valid in practice.

viscosity: Newton's law for viscous fluids gives a proportionality

$$S = \mu\frac{\partial v}{\partial x}, \tag{1.14}$$

where $\frac{\partial v}{\partial x}$ is the gradient of velocity (or shear rate) in the fluid and S is the stress. μ is the *coefficient of viscosity* of the fluid, often called just *viscosity*.

Viscosity is measured in $Pa\ s(N\ s/m^2)$ and it is represented by us using the symbol η. A quantity often used in experimental work is the *effective viscosity*, η_{eff}. It is defined as the ratio of shear stress and shear rate. This definition is related to that above, but the viscosity becomes a variable.

Another common term is the *kinematic viscosity*, η, that is defined as the ratio between viscosity and density in a fluid $\eta = \frac{\mu}{\rho}$.

For materials that present a yield stress a quantity called *plastic viscosity*, η_p, is defined in Section 1.5.2.

Newtonian and non-Newtonian flows: For certain fluids, the value of viscosity, η, is independent of time (or time derivatives) and does not change with the shear stress applied to the liquid. Under these conditions, η is just a constant of proportionality between shear stress and shear rate (it follows Newton's viscous law in Eq. 1.14) and this type of flow is what we use to call *Newtonian flow*. Other types of flow that do not have that simple behaviour are called by opposition *non-Newtonian*.

Under the denomination of non-Newtonian, is it possible to find many different types of flow. The rheological classification that follows is suggested in [29]:

1. Time independent fluids
   (a) Shear-thinning/Shear-thickening: Sometimes also called pseudo-plastic/dilatant [4] fluids. The effective viscosity decreases/increases with increasing shear rate. The process is reversible without time lag.
   (b) Viscoplastic fluids: A finite yield stress is required to start the flow.
2. Time dependent flows

---

[4] This is due to a traditional association between shear thickening and dilatancy [27]. Both effects are not connected, at least not in a simple way, and as we are going to use the dilatancy in the original sense given to the term later in this thesis, we will avoid this notation.

(a) Thixotropic fluids: These materials present a special kind of shear thinning dependent on time and followed by a recovery of the material. Changes in viscosity in this type of materials are not instantaneous. A typical example is non-drip paint.

(b) Viscoelastic fluids: They present both elastic and viscous properties.

Foam presents a combination of several of these properties, depending on time scale. There is a time variation of the viscosity due to the ageing of the foam. We will explain in Section 1.6 how coarsening is not an extreme concern to our experiments. If we neglect this coarsening variation, foam can be treated fairly as a viscoplastic material.

We can see a schematic representation of different types of time independent flows in Fig. 1-7.

1.5.2 Mathematical models for viscoplastic flows, including foam

The first model that we present includes a linear relationship between strain and stress above the yield stress:

$$S = S_y + \eta_p \, \dot{\epsilon}, \tag{1.15}$$

and it is called the Bingham model.

In this formulation S_y, the yield stress, and η_p, the plastic viscosity, are constants that depend on the fluid.

Some analytical exact solutions exists for the Bingham model fluid subject to boundary conditions, as in the case of tangential annular flow, thin slits or tubes [30] and a semi-infinite bulk fluid with a planar boundary [31]. Sekimoto [32] has also studied the motion of the yield surface at a Bingham fluid undergoing lateral shear.

The simplicity of this model makes it desirable to extend to some cases where a yield stress exists but linear fitting of the data above the yield stress is not possible. The Herschel-Bulkley model,

$$S = S_y + K_p \, \dot{\epsilon}^m, \tag{1.16}$$

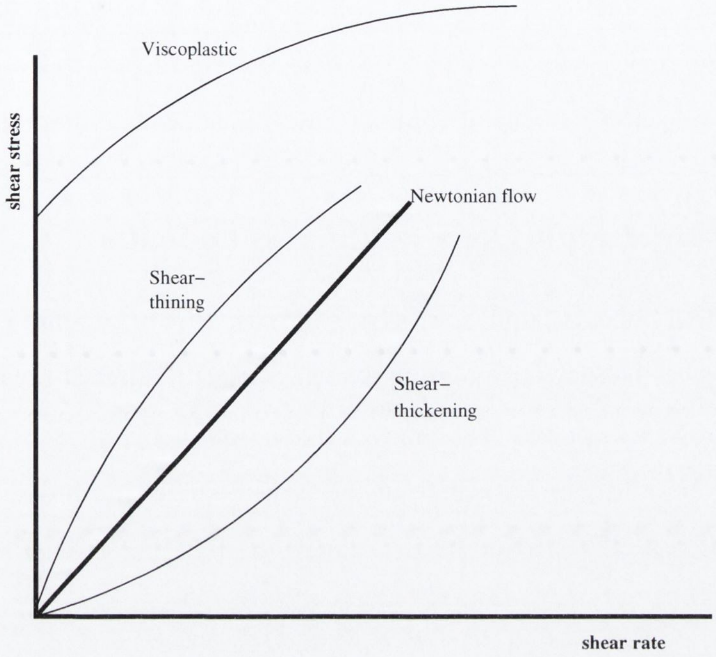

Figure 1-7: Different response under shear stress for some characteristic types of fluids in which viscosity is independent of time. A/Newtonian flow, viscosity (η) is a constant, corresponding with the slope of the line in this case. B,C/ Shear-thinning and shear-thickening fluids start flowing as soon as a shear stress is applied, but in both cases a change occurs in viscosity while the stress is acting. In shear-thinning fluids that change acts to decrease in the viscosity of the material. The case of shear-thickening fluids is the opposite one, there is an apparent increase in viscosity. D/ Viscoplastic fluids start flowing at a certain shear stress different to zero. This threshold is the yield stress.

provides a framework for these cases. K_p is a constant called the *plastic consistency*: its dimensions depend on the value of m. K_p becomes η_p when $m = 1$. Materials that follow the Herschel-Bulkley law (Eq. 1.16) are often referred as presenting shear-thinning ($m < 1$) or shear-thickening ($m > 1$) behaviour [27].

The validity and range of application of these models depend on shear rate. Bingham (Eq. 1.15) and Herschel-Bulkley (Eq. 1.16) describe quite well the behaviour of shear-thinning materials at very low shear rates but one has to be careful to work on a narrow range of shear rates [33].

The power law model:

$$\eta_{eff} = c_1 \dot{\epsilon}^{n-1}, \tag{1.17}$$

where c_1 is a constant that depends on viscosity and shear stress, increases in three times the range of shear rates in which it can be used accurately respect to Bingham, but fails at very high shear rates, where the local value of power is approaching to unity in experiments.

1.5.3 Shear modulus and yield stress on foam

The rheological behaviour of foam is still obscure to some extent [1]. But it is clear that foam belongs to the kind of materials known as soft matter: it presents a quite low yield stress beyond which it flows and behaves like a liquid. For stresses below this yield stress the response is solid-like. A sketch of the typical stress-strain diagram for a dry foam is shown in Fig. 1-8.

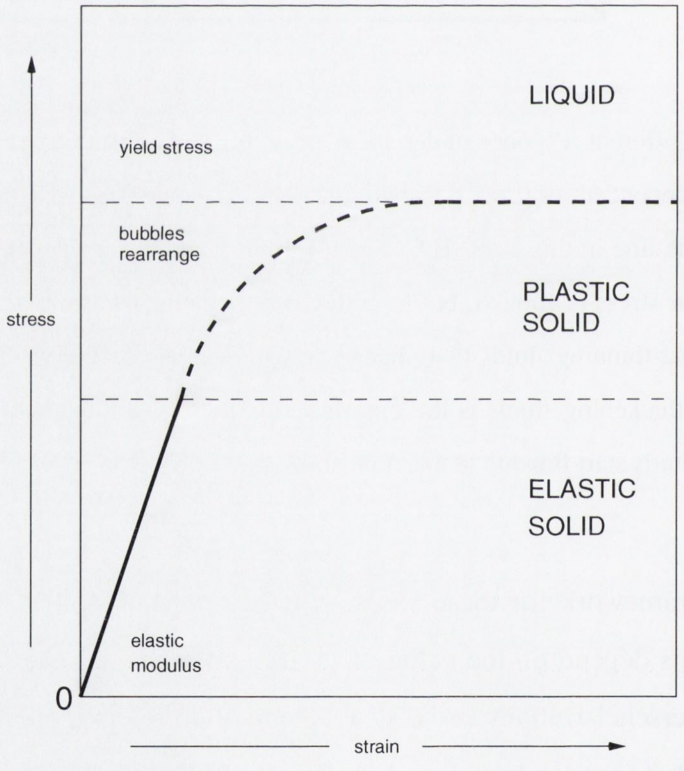

Figure 1-8: Sketched stress-strain relation for a liquid foam. Note the three different regions of behaviour (elastic solid, plastic solid and liquid). The diagrams of simulations in two-dimensional foams (which can be found in [34]) have a quite similar look. One can see a linear elastic relation for low stresses and a fluctuating behaviour of stress for larger strains, due to topological changes in a finite sample. Reproduced from [1].

The elastic modulus, G, of a foam depends only slightly on the geometry of the foam and more significantly on the bubble size and the liquid fraction. In the dry limit, G is found to be:

$$G = \frac{c\gamma}{\bar{d}}, \tag{1.18}$$

where c is a dimensionless parameter, dependent on the structure of the foam and $\bar{d}$ the average diameter of the cell or the bubble. This formula is valid for both two and three-dimensional foams. The parameter c is roughly of order unity [1]. For example, the ordered hexagonal two-dimensional structure (also known as honeycomb) gives the value $G = \frac{\gamma}{\sqrt{3}a}$, where a is the initial edge length and $c = \frac{2}{\sqrt{3}}$.

Unfortunately, there is no corresponding exact result for the foam in three dimensions, but some approximations lead to the Stamenovic estimate $\bar{G} = \frac{\gamma A_b}{6V_b}$, where the average of the elastic modulus is taken for generality (non-isotropic structures are included) and A_b and V_b are the surface area and the volume of the bubbles respectively.

If we add a small amount of liquid to the foam, applying the decoration theorem we can expect the change in the shear modulus G to be small. Overall, the modulus seems to have a roughly linear variation with ϕ_l [35, 36, 37] in 3D. Modest increases of liquid fraction lower the yield stress quite clearly, as some simulations carried out by Hutzler and co-workers [38] show. In this case a quadratic variation in the form $(\phi_l^c - \phi_l)^2$ is generally accepted. As we move closer to the rigidity loss transition, the difficulty of both, experimental and computational work is greatly increased [39] and we enter a regime for future research.

1.6 Coarsening and collapse

Whatever method we have used to prepare foam, the gas diffuses among the bubbles. The rate of diffusion is going to be dependent on the solubility of the gas in the fluid. Some general values for the solubility of the most common gases in water are reproduced in Appendix D.

The diffusion of gas depends mainly on the pressure differences between two bubbles. The smaller bubbles have higher gas pressure than the bigger ones (Eq. 1.1). The direction of gas diffusion is therefore from the small bubbles to the big ones. Eventually some of the small bubbles will collapse and disappear, causing the increase in the average diameter of the bubbles $\bar{d}$ [1], according to:

$$\bar{d} \propto (t - t_0)^{1/2}, \tag{1.19}$$

at least asymptotically.

We are not going to discuss this topic in full, as it is far from the subject of this thesis, but it is worth mentioning the measures taken to try to minimise this effect experimentally.

Part of the problem is tackled when we are using monodisperse foam (as in Chapters 3) to 5, for which the pressure of the gas is quite similar. Coarsening is also reduced by using relatively large bubbles.

It can be deduced from the data by Hutzler *et al.* [40] that the coarsening effect is small on time-scales shorter that around one hour in the experimental conditions that we use. All our experimental data are taken well below this time. We can neglect the effect of coarsening in the results presented in the thesis.

In the case of the bi-disperse bubbles in Appendix B, we are dealing with bubbles in contact with a pool of water. Coarsening depends also on the wetness of the foam [40]. When the foam is wet, the increase in the average bubble diameter is slower than it is in dry foam. This occurs because the Plateau borders reduce the surface of contact between bubbles, where the diffusion of gas takes place.

Part I

Rheological Properties

Chapter 2

The Stokes experiment in a foam

2.1 Motivation

This chapter reports the first (published) Stokes experiment in a foam [41]. This experiment gives an easy way to measure the viscosity of Newtonian fluids, by timing the fall of spheres in the fluid. Here we are applying it to a non-Newtonian fluid. Useful insight about the yield stress and the rheological character of a foam, which is a non-Newtonian fluid, can be gained by measuring the velocities of spheres falling through a column of foam.

The experimental aims of this work are:

- Find the terminal velocity of a sphere falling through a foam. This terminal velocity (defined in Section 2.2) is related to the drag force on the sphere.

- Investigate the variation of the terminal velocity of the spheres when different parameters of the experiment are changed. We vary the bubble radius of the foam B_r, the liquid fraction ϕ_l and the radii of the spheres a.

  Our results show a linear dependence of the velocity of the spheres with the bubble radius, at least up to the point when bubble radius and sphere radius become of comparable size. These is also a linear dependence of the terminal velocity with liquid fraction for spheres with different radii.

- Compare our results with a model and computations which consider the foam a continuum medium. Using spheres which will not fall initially through the foam, we perform a coarsening experiment. The yield stress of the foam will decrease when the bubble diameter increases and the sphere will start an accelerated motion through the foam. These experimental findings can be compared to a theoretical model and to calculations in order to characterise the foam as a Herschel-Bulkley fluid.

We have proposed a theoretical model for the forces acting on a sphere falling through foam, based on the results of the experiments. The model proposes the total drag force in a non-Newtonian fluid as a nonlinear function of the terminal velocity of the sphere. This is a reasonable first order approximation, in which the Newtonian fluids would be a particular case whose relation between total drag force and terminal velocity is linear and the yield stress is zero. We expect to obtain values for the exponent of the relationship from the experiment and to relate this theoretical model with the Herschel-Bulkley model used in the calculations. One of our goals is to estimate the value of the coefficient m in the Herschel-Bulkley equation (Eq. 1.16):

$$S = S_y + K_p\, \dot{\epsilon}^m, \tag{2.1}$$

where S is the shear stress, S_y the yield stress, K_p is the plastic consistency and $\dot{\epsilon}$ the shear rate. We will extend here the preliminary results included in our previous paper [41].

2.2 The Stokes experiment in a foam

2.2.1 Stokes experiment in Newtonian fluids

In the 19th century, G. G. Stokes described the drag force of a solid sphere in a Newtonian fluid [42, 43] (see Fig. 2-1). The result is the following equation:

$$F_{drag} = 6\pi\eta a v, \tag{2.2}$$

where η is the viscosity of the Newtonian fluid, a stands for the radius of the sphere and v for its velocity. However, the drag force is difficult to measure, so experiments usually concentrate on the terminal speed or terminal velocity [44].

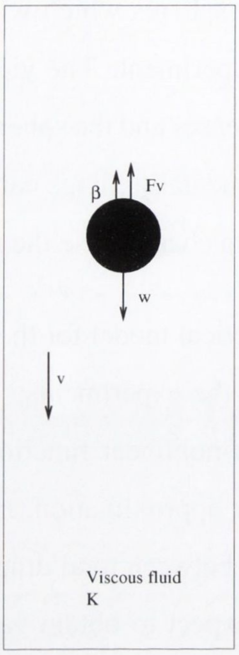

Figure 2-1: The Stokes experiment in a Newtonian fluid. w is the weight force and β the buoyancy. The drag force F_v is proportional to the velocity v of the falling sphere. Asymptotically, the equilibrium between forces causes the sphere to fall at constant velocity. This is what is known as terminal velocity. In our case the terminal velocity is reached almost immediately.

After an initial acceleration in the fluid, the sphere in free fall reaches a dynamic equilibrium. The sum of all the forces (buoyancy, drag force and weight of the sphere) is zero and the velocity of the sphere is constant,

$$\frac{4}{3}\pi a^3 \rho_{fluid} g + 6\pi\eta a v_t - \frac{4}{3}\pi a^3 \rho_{sphere} g = 0; \qquad (2.3)$$
$$v_t = \frac{2}{9}\frac{a^2 g}{\eta}(\rho_{sphere} - \rho_{fluid}).$$

The derivation of the formula can be found in any elementary physics text [45]. It provides an experimental way of measuring viscosity in Newtonian fluids (using the so-called ball viscometer).

2.2.2 Stokes experiment in a foam

The simple formula described in Equation 2.3 requires modification in the case of a non-Newtonian fluid. Calculating the contribution of the drag force in this case becomes non-trivial. Developing a heuristic theory, we can propose a relation between the drag force and the velocity and relate the results obtained this way with the Herschel-Bulkley model. Our final objective is to investigate the values of the exponent m in Eq. 2.1.

The idea of using falling spheres to get more information about non-Newtonian fluids is not new in itself. Boger fluids [1] [46] and Bingham fluids [47] can be mentioned as examples. The work of Mitsoulis' group, making numerical computations for the creeping motion of spheres in tubes filled with Bingham fluids [48] and Herschel-Bulkley fluids [49], provides very useful information about the procedure for a computational simulation of the experiment.

A list of different theoretical and computational rheological models for dry and wet foam and emulsions can be found in the first chapter of the thesis of Gardiner [50]. The choice of a Herschel-Bulkley model is supported by previous experiments in rheology of foams and emulsions [51, 52, 53, 54]. Experimental work supports the existence of a yield stress and shear-thinning behaviour in a foam (see Table 2.1). This makes the Herschel-Bulkley model (Eq. 2.1), of which the Bingham model (Eq.1.15 on page 18) is a particular case with m=1, a good candidate to describe dynamic flow of aqueous foam.

Recent simulations in 2D foams roughly fit to the Bingham model [58, 60] but experiments in emulsions and foams seem to be in accordance with the Herschel-Bulkley model with exponent $0 < m \leq 3/2$ [53, 54]. One of our aims in these experiments is to study the value of m in a three-dimensional aqueous foam.

---

[1] Boger fluids present shear thinning, but the drop in viscosity is quite small compared to the zero-shear value. Viscosity appears to be constant in these fluids for practical purposes.

Authors	*Type*	*Material*	*Model*	*Exponent value*
Brungraber *et al.* [51]	Ex - 3D	F	H-B	$m = 0.13$ to 0.69
Thondavadl and Lemlich [55]	Ex - 3D	F	PL	$n - 1 = -0.39$
Schwartz and Princen [56]	Ex - 3D	Em	H-B	$m = 3/2$
Reinelt and Kraynik [57]	C- 2D	-	H-B	$m = 3/2$
Khan *et al.* [52]	Ex - 2D	F	B	$m = 1$
Princen and Kiss [53]	Ex - 3D	Em	H-B	$m = 1/2$
Okuzono *et al.* [58]	C - 2D	–	B	$m = 1$
Rosa *et al.* [59]	Ex - 3D	F	PL	$n - 1 = -0.45$
Durian [60]	C - 2D	–	Bingham	$m = 1$
Bobert *et al.* [54]	Ex - 3D	FC	H-B	$m = 0.48$ to 0.53

Table 2.1: A table of different models used to fit experiments (Ex) and computations (C) in 2D and 3D systems on foam (F), Foam concentrates (FC) and emulsions (Em). The main models used are Power Law (PL) (Eq. 1.17, with exponent n), Bingham (B) (Eq. 1.15) and Herschel-Bulkley (H-B) model (Eq. 2.1 with exponent m). The Bingham model is a particular case of the Herschel-Bulkley model with exponent $m = 1$. The last two assume a finite yield stress of the foam.

2.2.3 Outlook of the chapter

We will describe first the materials and methods used in the experiments, in particular the size and weight of the spheres used in the experiments. Our experimental set-up imposes some limits in the accuracy that we could reach and these will be discussed as well. Afterwards, we describe the experiments. These can be divided into:

- Experiments on foam subjected to forced drainage in which we vary the bubble size of the foam and the flow rate. In these experiments the spheres move quite rapidly, involving velocities of the order of cm/s.

- Experiments on dry foam undergoing coarsening: in this case, we found two different regimes of motion, one of them interpreted as a slow continuous creep (of the order of mm/min) and a comparatively fast (order of cm/s) accelerated motion, once the yield stress of the foam has decreased sufficiently.

We have developed a heuristic model to relate the findings for the coarsening foam to the Herschel-Bulkley model in Eq. 2.1. Furthermore, calculations have been made using the fluid dynamics package Fluent (see Appendix E). These calculations represent the foam as a continuum, using the Herschel-Bulkley model. We relate the results of the calculations to the experimental findings through our theoretical model. The chapter concludes with a review of all the findings and possible future experiments.

2.3 Materials and methods

We have timed the descent of solid spheres of different sizes in a column of foam. For all the experiments described in this chapter, we use the same procedure to produce the foam, which is made following the method explained in Appendix D. A sparger attached to the gas line produces very fine polydisperse foam ($B_r \leq 0.5\ mm$) that is collected in tubes of $4\ cm$ diameter and typical lengths of $30\ cm$ for the forced drainage experiments and of $40\ cm$ for the foam coarsening experiments. These tubes are partially submerged into a pool of surfactant solution. We can pump liquid from the surfactant pool and add it at the top of the foam using a Watson-Marlow peristaltic pump. Varying the flow rate of liquid poured on top of the foam, we get an homogeneous liquid fraction in the column of foam. This is the forced drainage described in Section 1.4.1.

One of the limitations of the experiment lies in the type of the spheres that can be used (see Fig. 2-2). The spheres used in the experiments are made of different types of plastic with densities of the order of $\rho \approx 0.6 \times 10^3\ kg/m^3$. The density of the spheres that can be used for the rapid motion experiment are between $0.7 \times 10^3\ kg/m^3$ and $1.1 \times 10^3\ kg/m^3$. Plastic spheres whose densities are below those are not able to overcome the yield stress of the foam and will stay on top of the foam. We use these spheres for the experiments with coarsening foam. Some spheres with comparable densities made of wood and polystyrene were considered for the experiments and then rejected due to their tendency to absorb water. Other materials like metal or glass give much higher densities (of the order of $\rho \approx 5 \times 10^3\ kg/m^3$). The spheres become too heavy and it is very difficult to measure the time of the fall, especially when the foam is wet, leading to increased speed. Sometimes,

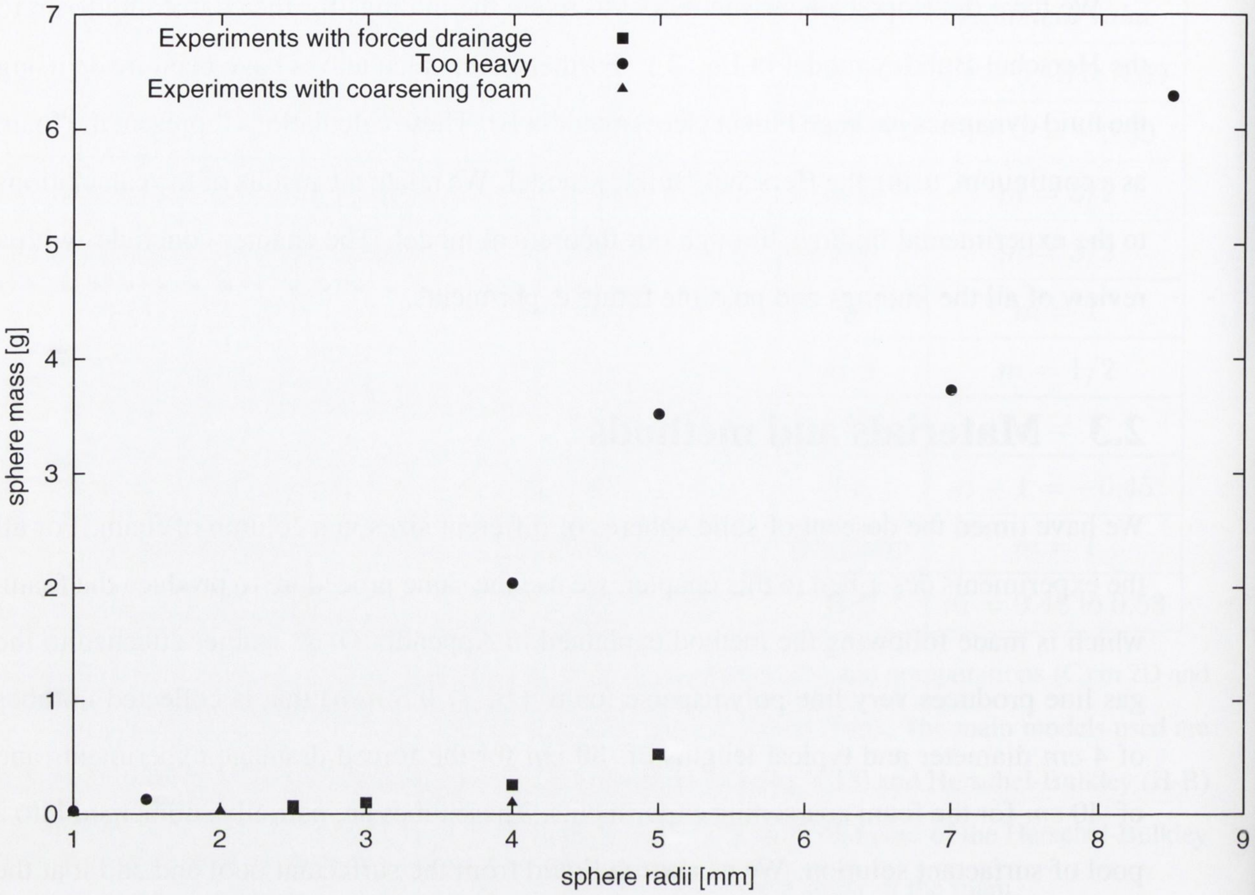

Figure 2-2: The density of the spheres is crucial in the Stokes experiment on a foam. We can vary two parameters to obtain the right density values: the sphere radius and weight. The radii of the spheres have to be chosen amongst those that make the continuum approach reasonable and minimise boundary effects. If the spheres are too heavy, it is difficult to time their descent and they can destroy the foam. On the contrary, when they are too light, their weight is not enough to overcome the initial force F_0 associated to yield stress S_y. The foam will not yield and the spheres will stay on top of the foam. The right densities of the spheres to perform forced drainage Stokes experiments are within a very narrow margin ($0.7 \times 10^3\ kg/m^3 \leq \rho \leq 0.9 \times 10^3\ kg/m^3$). With spheres made of plastic of densities smaller than $\rho = 0.6 \times 10^3\ kg/m^3$, we perform the experiments using coarsening foam. These values are taken for foams with a $B_r \leq 0.5\ mm$.

very heavy spheres rupture the foam films, causing the foam to collapse.

Using these ranges of densities in plastic, we can vary the diameter of our spheres to determine our choice. At least for a first approach, we want to compare the foam with a continuum model. To make this continuum assumption, the spheres have to be appreciably bigger than the bubble size of the foam. On the other hand, if the radius of the sphere is too large, the container walls will interfere with the results. This effect has been calculated to be significant in viscous flow at low Reynolds numbers (an error over 2% when the diameter of the container is a hundred times the diameter of the sphere is suggested in [43]).

In our case, the radius of the sphere has to accommodate both limits,

$$B_r \ll a \ll \frac{D}{2}, \tag{2.4}$$

where B_r is the bubble radius, a is the radius of the sphere and D the diameter of the tube.

The continuum approach is not extremely satisfactory, with a ratio of sphere diameter to bubble diameter from 2 to 8, but this is determined by the minimum bubble size that we can reach experimentally with our set-up. The ratio between the tube diameter and the sphere diameter varies from 5 to 10, so we can expect a significant wall effect. It is not possible to increase this ratio by making the tube diameter bigger, because of the time that it will take to fill it with foam: this would allow the foam on the top to coarsen. An estimation on the coarsening effects and times of foam formation is included in Appendix D.

2.4 Experimental results

Let us remind ourselves again that we have performed two series of experiments in the foam.

- Experiments in foam subjected to forced drainage.
- Experiments using coarsening foam.

2.4.1 Experiments in forced drainage

The terminal velocity is reached almost immediately and can be calculated by dividing the total length of the column of foam by the time the sphere takes to go through it (this is supported by visual observations of the motion of the coloured spheres that were close to the walls of the container). We further check the validity of the assumption of a terminal velocity using two tubes of $4\ cm$ diameter and lengths $15\ cm$ and $30\ cm$ respectively. We take some measurements using a single sphere ($4\ mm$ of radius and density $\rho = 0.9\ \times\ 10^3\ kg/m^3$) and a fixed value for the flow rate $Q = 0.13\ ml/s$. We time the descent of the sphere seven times on each tube under these conditions and calculate the velocity of each trial dividing by the respective length. Then we take the average values of the velocities for each tube. The values obtained in both tubes for the terminal velocity are $5.3\ \pm 0.6\ cm/s$ and $4.9\ \pm 0.7\ cm/s$ and they are close enough to proceed as above. However, in the remaining experiments, we have used tubes longer than $15\ cm$ to ensure that we remain within the limits of this approach.

We have repeated the experiment using a single sphere of radius $5\ mm$ and mass $0.53\ g$ ($\rho = (1.1 \pm 0.1)\ \times\ 10^3\ kg/m^3$). We use a low constant flow rate of $0.02\ ml/s$ in order to get an homogeneous liquid fraction in the foam and vary the bubble size of the foam. We have looked for the dependence of the velocity of the sphere with bubble radius B_r, at a constant low flow rate. We have a ratio $Q/A = 1.6\ \times\ 10^{-3}\ cm/s$, where A is the cross-sectional area of the tubes, for bubble sizes between $B_r\ =\ 0.6\ mm$ and $B_r = 2.8\ mm$.

As shown in Fig. 2-3 we find a linear relationship between the terminal velocity of the sphere and the bubble radius B_r of the foam. Except for the largest bubble radius, all the points in the graph are well described by this relationship. This bubble radius of $B_r\ =\ 2.8\ mm$ is about half the radius of the sphere used in this experiment. We thus attribute the deviation from linearity with a breakdown of the continuum approach (see Section 2.3). In view of these results, we estimate that using a bubble diameter lower than half the diameter of the sphere the terminal velocity can be interpreted using the continuum approach.

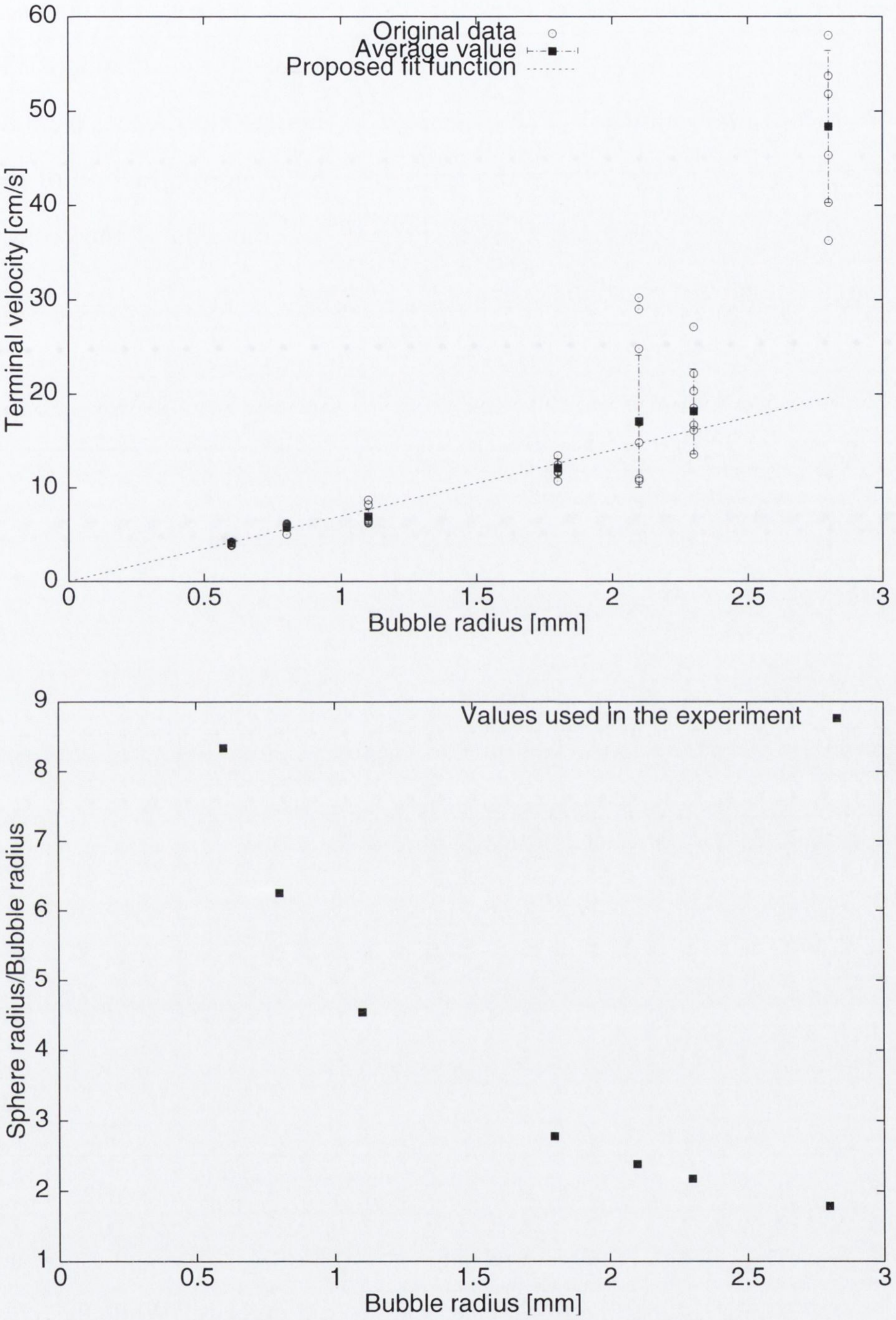

Figure 2-3: Stokes experiment using different bubble sizes. The graph at the top presents the terminal velocity of the spheres of different bubble sizes. The empty circles are experimental velocities obtained for each bubble size. We also include the average of velocities for each bubble size within a margin of confidence of 65%. The data are consistent with a linear fit, if we ignore the last point on the right (see text). The graph below shows the ratio of sphere radius to bubble radius for the different bubble radii used in this experiment. The breakdown is reached approximately when $B_r \approx a/2$ in this case ($a = 5\ mm$).

Finally, we have obtained values for the terminal velocity of spheres with different diameters within this range, varying also the flow rate for each sphere. The descent of the spheres is quite rapid (just a few seconds) in these experiments. We have investigated the dependence of the velocity of the spheres with the liquid fraction of the foam (Q/A between $0.510^{-3}cm/s$ and $210^{-2}cm/s$, where A is the area of the cross-section of the tubes, for a bubble radius of the order of $\leq 0.1mm$).

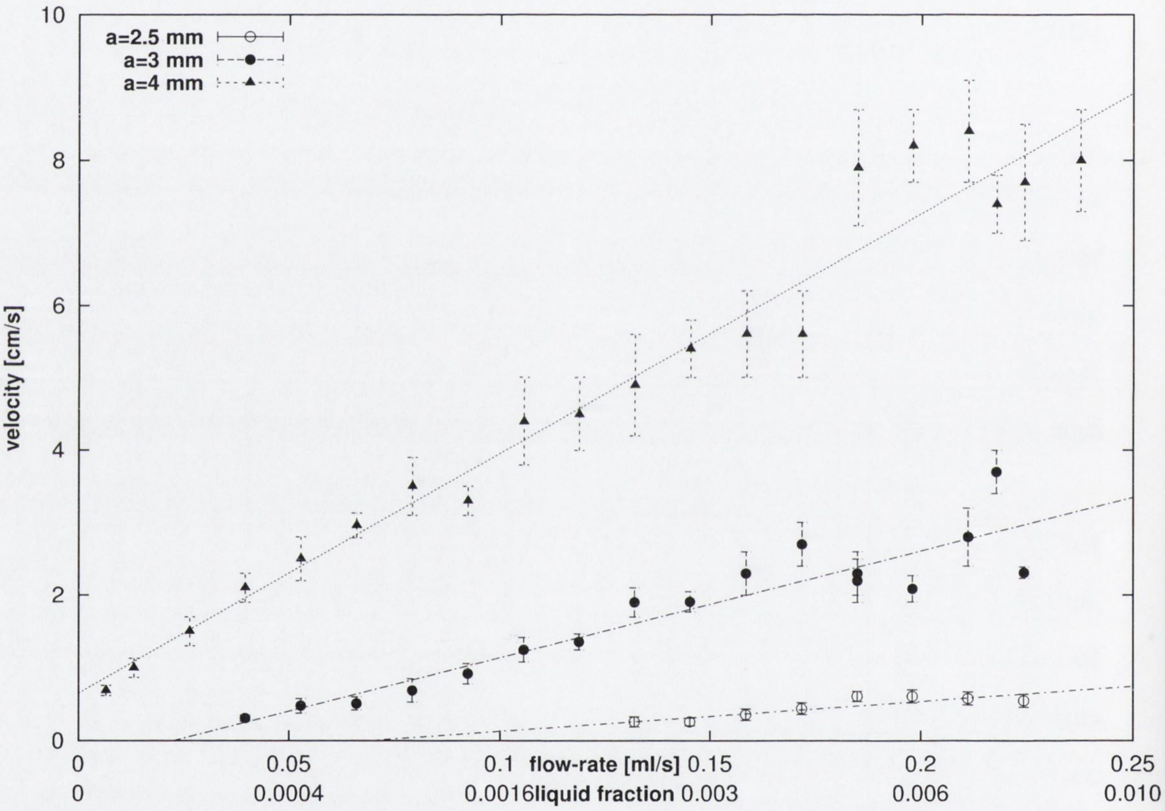

Figure 2-4: The velocity of spheres of radii $a = 2.5\ mm$, $3\ mm$ and $4\ mm$ and $\rho = (0.9 \pm 0.1) \times 10^3\ kg/m^3$ falling in a foam undergoing forced drainage. While the $a = 4\ mm$ sphere has a positive velocity for all the flow rates, the other ones do not move through the foam at low flow rates. This shows the existence of a yield stress in foams. The solid lines are linear fits to the data. The scale also includes the approximate values of average liquid fraction that correspond to the flow rates, estimated using Archimedes principle (Appendix D).

The velocity of spheres with the same density placed on top of a wet foam has a linear dependence with flow rate (Fig. 2-4), with a slope that depends on the radius of the sphere.

In the surfactant solution that we are using, the liquid fraction varies with the square root of flow rate [1], so the velocity has a quadratic dependence with liquid fraction:

$$v \propto Q \propto \phi_l^2. \tag{2.5}$$

The slope of the lines depends on the density of the spheres. However, the scattering in the experiment and the number of spheres available to compare are not sufficient to conclude anything from that dependence. Shown in Fig 2-4 are the results for spheres of density $\rho = (0.9 \pm 0.1) \times 10^3 kg/m^3$. Two to four more spheres of the same density would be needed to get the variation of the slope with the radius of the sphere a.

2.4.2 Experiments with coarsening foams

This experiment consists in measuring the position of a solid sphere placed on top of a dry foam while the foam is coarsening (see Chapter 1). We have used spheres whose weight is not sufficient to overcome the yield stress of the foam at first, so that the sphere initially remains "floating" at the top surface. Due to the coarsening of the foam, the value of the yield stress decreases steadily and after a time, the sphere will move through the foam. In this case, we have found two different types of motion: a very slow creeping descent at first and a later accelerated motion. We can plot the position of the sphere at different times (Fig. 2-5) in order to understand the character of the motion.

We see indeed that two different types of motion are involved in the fall of the sphere through the foam. In a first stage, the sphere moves downwards with a constant small velocity (of the order of mm/min). This can be identified as creep, a slow yielding of the foam due to local and topological rearrangements (see Section 1.3.4) which are the concomitant of the coarsening process. In the second, the sphere gains a much larger velocity (of the order of cm/min). This regime may be characterised by a power law:

$$x = c_1(t - t_0)^k, \qquad t > t_0 \tag{2.6}$$

where x is the position of the sphere, t the time and t_0 the time at which the change between the two regimes occurs.

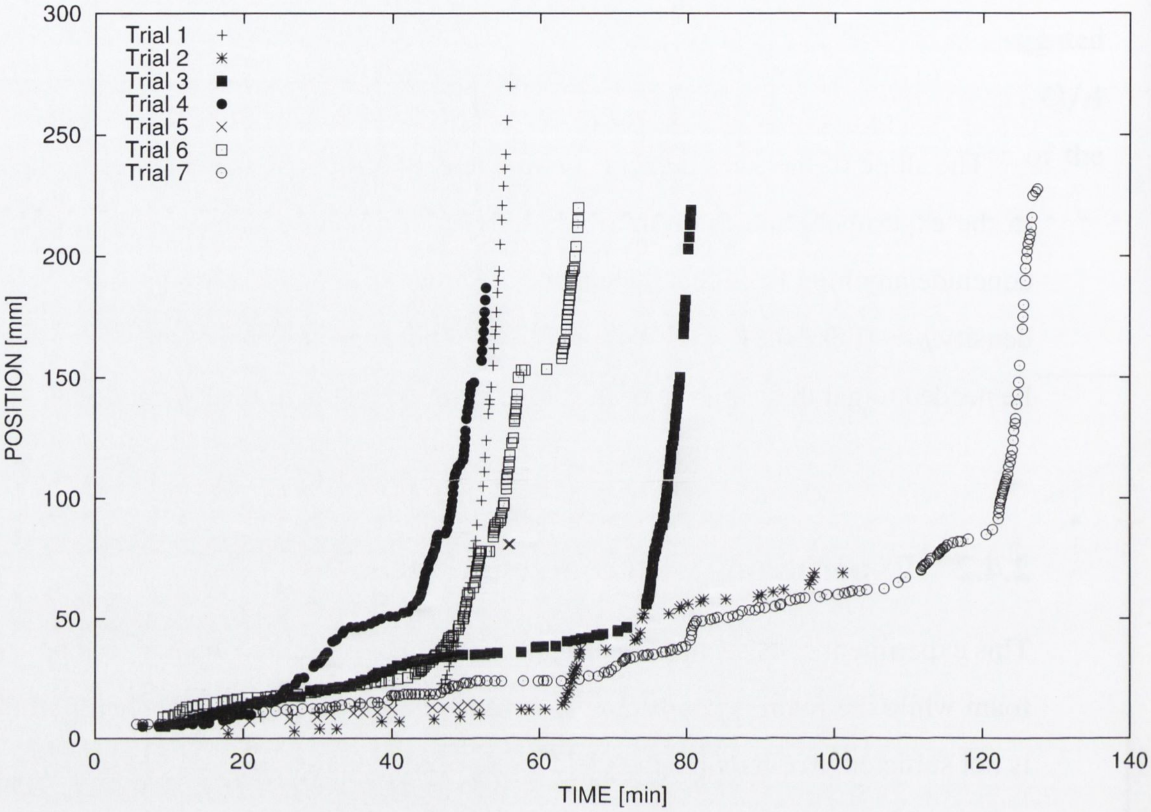

Figure 2-5: The sphere is dropped into a fairly dry foam compared with Fig. 2-4 (liquid fraction less than 0.01) at time zero and its position recorded. The radii of the spheres are between $2.5\ mm < a < 3.1\ mm$ and the cylindrical tube diameter is $40\ mm$. All the lines show a transition from creep (slow motion) to accelerated motion. Local inhomogeneities in the foam structure apparently cause the sphere to 'hesitate' in its descent during the accelerated motion, returning to the slow creep (Data in Trial 2 and Trial 6).

The transition to the more rapid descent is clearly attributable to the decrease of the yield stress of the foam, eventually reaching a critical value. The bubble size varies with the square root of time (Eq. 1.19) but it is possible to approximate this dependence as linear on the short time-scale that involves this experiment. The yield stress is related in turn to bubble radius on the sample [1]:

$$S_y \propto d^{-1} \tag{2.7}$$

where d is the mean bubble diameter, and hence varies at $t^{-1/2}$.

As the yield stress continues to decrease beyond the point at which it balances the gravitational force, the sphere accelerates. Since its velocity is always proportional to the net force acting on it (inertia being negligible) and this varies linearly with time, this acceleration may be expected to be approximately constant.

Such is the ideal behaviour to be expected. However, there are sections in the tube at which the velocity of the sphere falls dramatically (shown in Fig. 2-5) and the only measured change in position is due again to the creeping motion. We cannot avoid the presence of regions of local inhomogeneities, where the bubbles are smaller and therefore, the value of yield stress is higher locally. The sphere can get temporarily trapped in a high yield stress area. Furthermore, the frontier between the creep and the accelerated motion becomes difficult to define on these conditions.

It is possible to extract information on rheology in the foam using a theoretical model created for this task and described in the next section to compare with the accelerated motion due to the change of the yield stress of the foam. But first we have to prepare the data, excluding the effect of the creep from the experimental values.

2.5 Analysis of the results

2.5.1 Creep correction and data treatment

We need to prepare the data in Fig. 2-5 in order to relate them to the model selected to describe the foam, avoiding the effects of the creeping motion. To describe each step we will apply this correction in detail to the set marked as Trial 1 in Fig. 2-5.

1. We start with the original data from the experiment plotted using position versus time in Fig. 2-6.

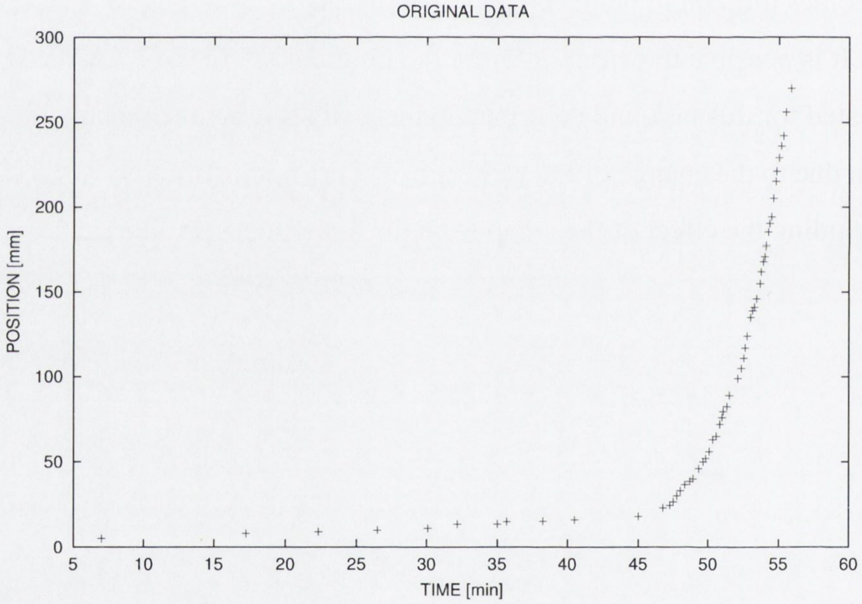

Figure 2-6: Original data for Trial 1. There is a transition between the motion produced by creep and the accelerated motion as the foam coarsens.

2. We apply a log plot to both time and position (Fig. 2-7). This is going to help to identify at what time t_0 we have a change between the slow motion (which follows a linear dependence) and the accelerated motion characterised by a power law. In the log-log plot the different regions appear roughly as straight lines with different slopes. Distinguishing the frontiers of the different regimes becomes more difficult if we do not use this type of plot.

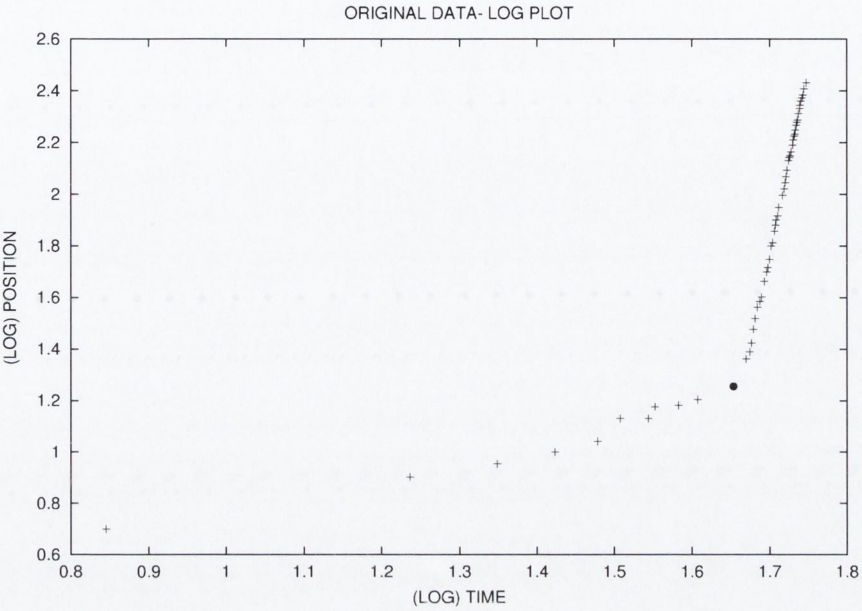

Figure 2-7: We convert the original data from Fig. 2-6 to a log plot. The log plot helps to difference the regions of slow creeping motion and fast accelerated motion, as they both have different dependences of position versus time. The full black dot represents t_0, the time at which the motion changes from creep to acceleration. In this case, we obtain $t_0 = 40.50\ min$.

3. Using the value of t_0 obtained in Fig. 2-7, we select the points in which only creep is present in Fig. 2-6. We fit these datapoints to a straight line. This line (in Fig. 2-8) will characterise the creep correction and must be subtracted from all the data (the creep motion remains after the sphere enters the accelerated motion regime).

4. The corrected data (Fig. 2-9) are obtained subtracting the creep line from the position and the value of t_0 from the time.

Applying these corrections (Figs. 2-6 to 2-9) to avoid the effect of creep in all the lines shown in Fig. 2-5, we obtain a new set of corrected data for all the experimental values, shown in Fig. 2-10.

The corrected values can be fitted using a log-log plot (Fig 2-11) to obtain the value of k:

$$log(x - x_{creep}) = k \log(t - t_0) + c_2, \qquad t > t_0, \tag{2.8}$$

and we obtain the values of k in Table 2.2.

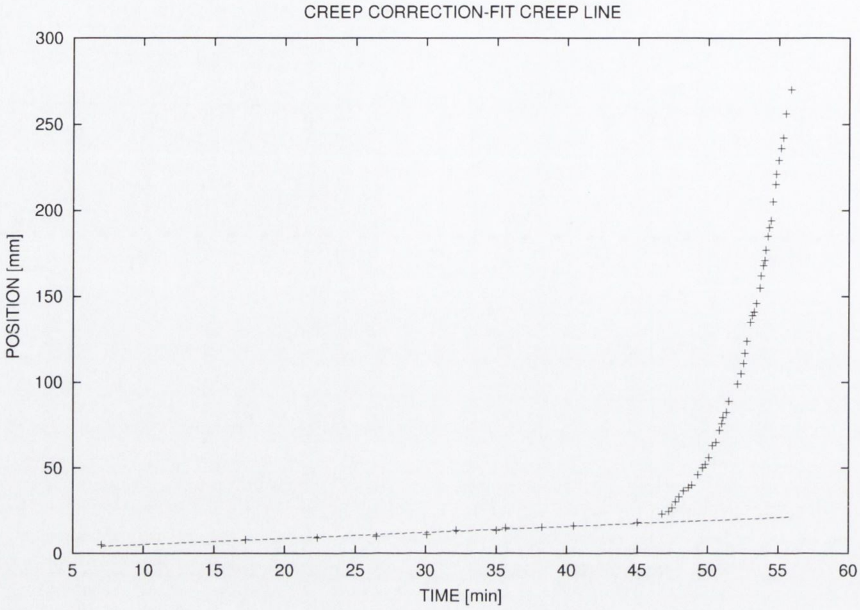

Figure 2-8: We use the value of t_0 obtained from Fig. 2-7 to fit all the data in Fig. 2-6 with $t \leq t_0$ to a straight line. The value obtained in this case for the creep correction is $0.34t + 2.0$. This line represents the creep motion.

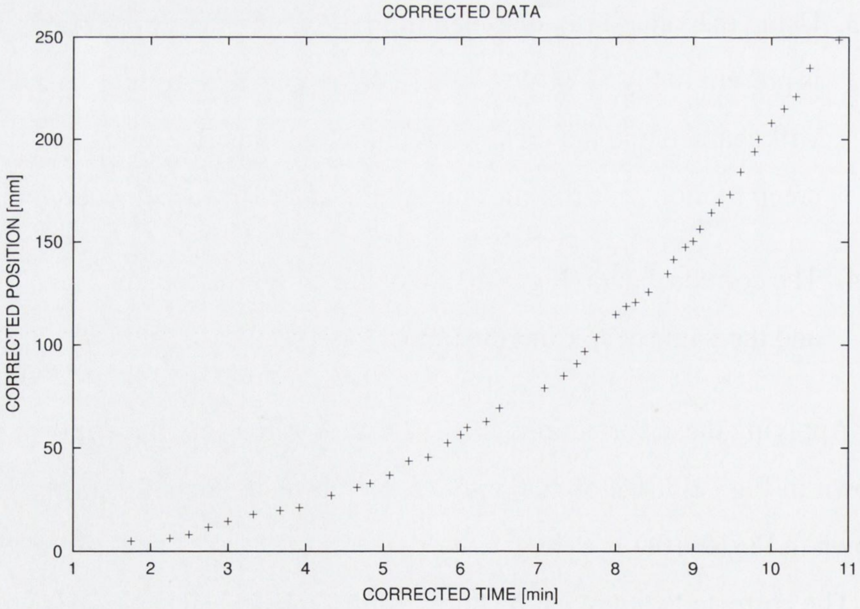

Figure 2-9: We obtain a corrected set of data from the original data in Fig. 2-6 by subtracting the creep correction (Fig. 2-8) from the position and the value of t_0 (Fig. 2-7) from the time.

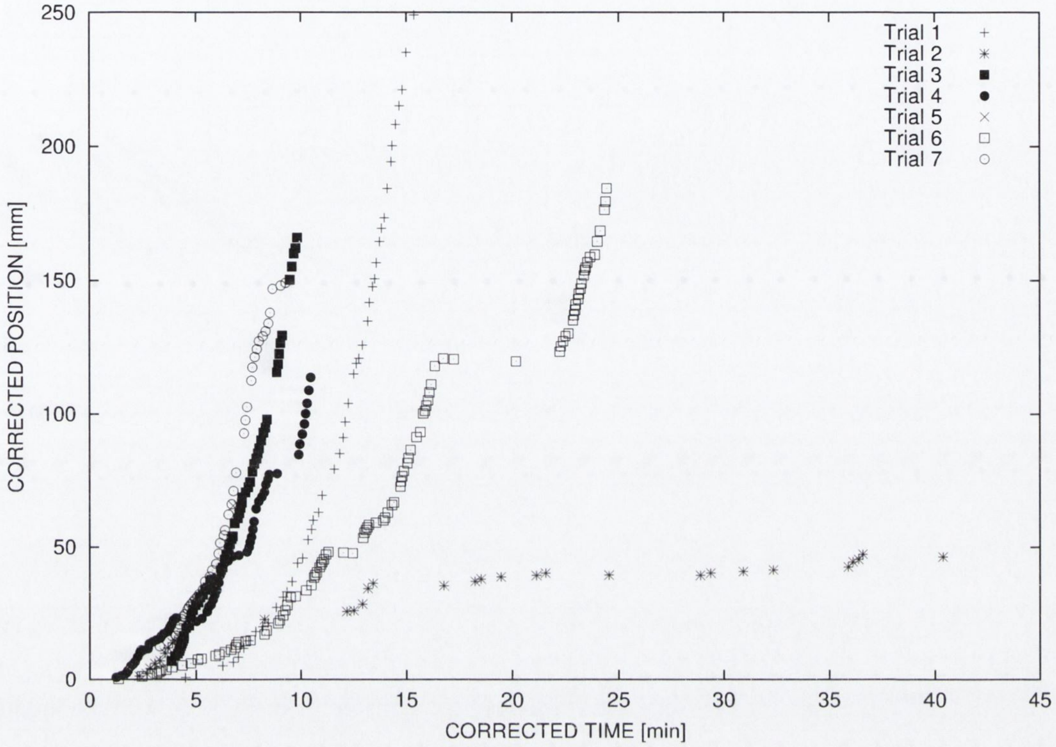

Figure 2-10: Using the correction described in Figs. 2-6 to 2-9 for the original data from the Stokes experiment on a coarsening foam, we obtain a set of different lines, described by the power law in Eq. 2.6.

The parameters used to correct each line and the individual final values for the constant k are given in Table 2.2. The values obtained are roughly consistent with $k = (3.1 \pm 0.9)$. The individual values of the exponent k are quite variable. We have already mentioned the flat regions found in the original data as a cause for this. It is difficult to get datapoints not affected by these 'hesitations' in the descent of the sphere, as the foam formation method used for this experiment produces an slightly polydisperse foam. We find that our value of k (see above) can be tentatively related to a Herschel-Bulkley model, using the following theoretical ideas.

2.5.2 A link to the rheology of the foam

In this section, we relate the experimentally determined exponent k of Eq. 2.6,

$$x = c_1(t - t_0)^k, \qquad t > t_0,$$

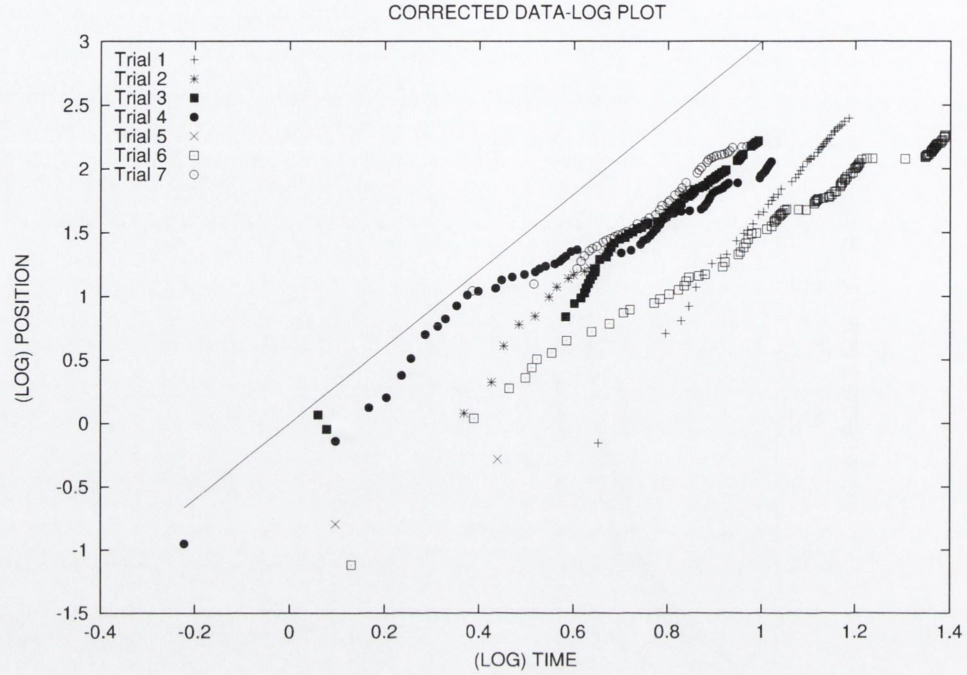

Figure 2-11: In order to obtain the values of the constant k in Eq. 2.6, we take logarithms on each side of the equation (Eq. 2.8). In this way, we obtain the values for k stated in Table 2.2. The line corresponds to the proposed value $k = 3.1$. Note that the second creep region on the data of Trial 2 (the flat part shown in Fig. 2-10) has been avoided when fitting this set of points.

where x is the position of the sphere, t the time and t_0 the time at which the change between regimes occurs, to the exponent m in the Herschel-Bulkey equation (Eq. 2.1):

$$S = S_y + K_p \, \dot{\epsilon}^m,$$

where S is the shear stress, S_y the yield stress, K_p is the plastic consistency and $\dot{\epsilon}$ the shear rate.

In order to do this we will introduce a model of the foam, based on the expected behaviour of the forces acting on the sphere (Eq. 2.9). We will assume that we can treat the foam as a continuum medium. As the sphere radii are significatively larger than the bubble radius, we can consider this choice as a reasonable first order approximation. This assumption was described when we explained the adequate size of the spheres for the experiments (Section 2.3).

First of all, let us introduce the balance of stresses in the foam in Fig.2-12.

Data set	t_0	Creep correction	k
Trial1	40.50	$0.34t + 2.0$	4.0
Trial2	60.75	$0.26t - 3.6$	3.9
Trial3	70.65	$0.65t + 0.7$	2.6
Trial4	42.20	$1.79t - 21$	3.0
Trial5	49.00	$0.24t + 2.1$	3.7
Trial6	40.75	$0.44t + 6.9$	2.2
Trial7	118.07	$0.68t - 8$	2.5

Table 2.2: Values for t_0 (Fig. 2-7) and the creep correction line (Fig. 2-8) applied to the experimental data in Fig. 2-5 to obtain the corrected values in Fig. 2-10. The last column gives the individual values of k obtained from the slopes on the log-log plot in Fig. 2-11.

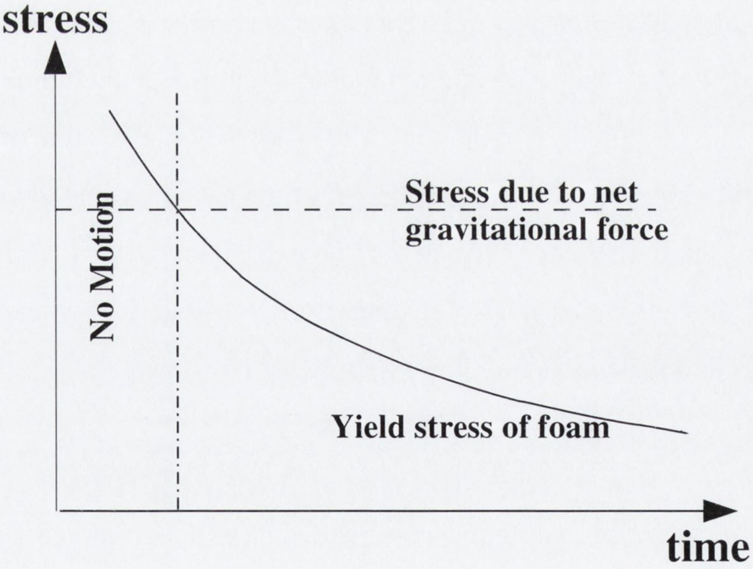
stress
No Motion
Stress due to net gravitational force
Yield stress of foam
time

Figure 2-12: The yield stress decreases due to coarsening (increase in bubble size with time) while the applied stress is roughly constant (neglecting the small change in buoyancy). Until the yield stress falls below the applied stress there is no motion, apart from that due to creep.

Our model is based on the idea that a foam has a finite yield stress. Therefore, a sphere moving through the foam may be expected to follow the equation:

$$\begin{aligned} F - F_0 &= \kappa v^n, \;\; F \geq F_0 \;\; \text{and} \\ v &= 0, \;\; F \leq F_0 \end{aligned} \tag{2.9}$$

where κ is a constant dependent on the radius a, the liquid fraction Φ_l of the foam and its rheological properties. F_0 is the minimum force required to move the sphere through this medium. At all points we neglect inertia and it is therefore assumed that the forces acting on the sphere (weight and drag) are in equilibrium.

The net force on the sphere, F, is constant while the minimum force required to move the sphere in the fluid, F_0, decreases with time; we assume this decrease to be linear over the duration of the experiment on a first order approximation. We can support this assumption because this minimum force F_0 and the yield stress S_y should follow the same dependence with time. Equivalently, consider the shear stress that the sphere exerts on the foam. In equilibrium the stress S is constant and less than the yield stress S_y which decreases with time. This is illustrated in Fig. 2-12. Since the falling of the sphere occurs in a short time just after the yield stress decreases below the value of the maximum stress in equilibrium, the yield stress variation with time is approximately linear.

We take the derivative of the fit for the experimental data (Eq. 2.6) to see that the velocity of the ball varies as t^{k-1}. Comparison with Eq. 2.9, where v^n varies linearly in time, shows that the exponent in the experiments is

$$n = \frac{1}{k-1}. \tag{2.10}$$

We define the *radius of yield*, δa, as the distance (in an average sense) from the surface of the sphere where the stress of the foam equals the value of the yield stress. When F_0 becomes equal to F the sphere acquires a non-zero velocity v. It is then contained within a small yielding region of radius $a + \delta a$. In all the points included in the yielded region $S \geq S_y$. Hence the distance δa will increase with the 'excess' stress $S - S_y$, by definition. We assume this increase to be linear on a first order approximation (as S_y

decreases also linearly with time approximately). Now, at the sphere's surface the rate of strain is approximately $v/\delta a$ so we find from Eq. 2.1 that

$$S - S_y \propto \left(\frac{v}{\delta a}\right)^m .$$

But since $\delta a \propto S - S_y$, we conclude that

$$\begin{aligned} S - S_y &\propto v^{m/(m+1)} \quad \text{and} \qquad (2.11)\\ \delta a &\propto v^{m/(m+1)} . \qquad (2.12)\end{aligned}$$

We wish to relate the stresses and forces around the ball, for which we need a length scale. The relevant length here is the radius of the sphere, so we can immediately equate the exponent of v in the stress equation, Eq. 2.11, with the exponent n in the force equation Eq. 2.9:

$$m = \frac{n}{1-n} . \qquad (2.13)$$

Using Fig. 2-11 and the data on Table 2.2 we found $k = (3.1 \pm 0.9)$, so that according to Eq. 2.10 we have $0.33 \leq n \leq 0.83$. When we introduce these values into Eq. 2.13 we obtain $0.5 \leq m \leq 4.8$. This conclusion is consistent only partly with previous theoretical and experimental values of m. We have to note again the dispersion of the values obtained in the experiments, which provides a large range of values for the exponent m. Foam has been largely found consistent with shear thinning behaviour before [50]. Part of our values include the possibility of shear thickening foam ($m > 1$). This could be due to the nature of the experimental shear, which does not encourage as many bubble rearrangements as other methods of shearing the foam produce [61]. However, the proposed value of $k = 3.1$ ($n = 0.48$, $m = 0.9$) suggests that the Bingham model is a good choice to represent the rheological character of aqueous foam and this result is in agreement with previous values for aqueous foam accounted in Table 2.1.

We now test if the hypothesis introduced to make our theory holds when compared to a numerical model of the experiments.

2.6 Numerical modelling

The main objectives of the use of computations at this point are to check the theoretical assumptions we have done and to obtain values of the drag force over the sphere, something that we have pointed out it is difficult to measure experimentally. Using a computer allows the variation of different parameters which would be very difficult to vary experimentally, such as the ratio of the diameter of the sphere versus the diameter of the tube. This will be helpful for future work on the subject.

We therefore model the flow of a yield stress fluid around a sphere confined within a cylinder, similar to the analysis of Mitsoulis and co-workers [48, 49]. Using an axisymmetric formulation, we hold the sphere fixed and allow the fluid to flow along the frictionless tube, see Fig. 2-13. We have also sketched in the figure δa, the radius of yield, defined in Section 2.5.2. As the yielded region around the sphere is not exactly spherical, the values of δa depend on the direction in which we take our measurements. We decide to measure the radius of yield, δa, in the radial direction across the tube. The boundary condition on the sphere is that of no-slip.

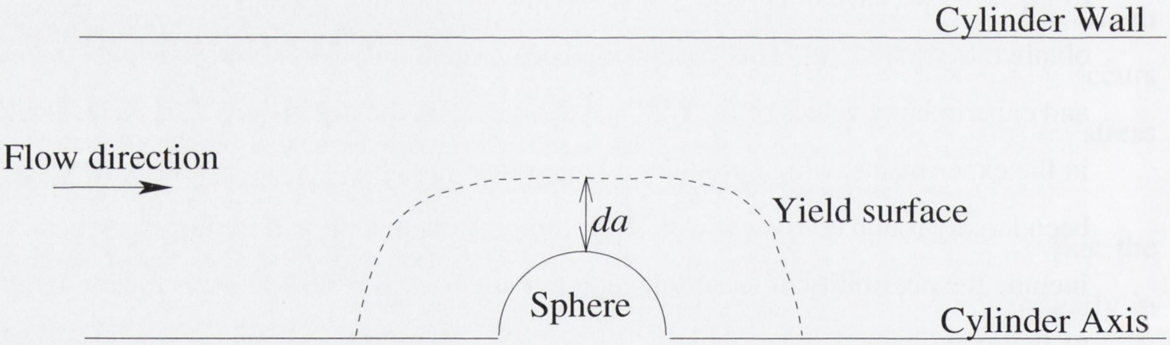

Figure 2-13: The foam flows past a stationary sphere. We sketch a cross-section showing the position of the yield surface (dotted line) around the sphere. The size of the yielded region between the yield surface and the sphere increases with velocity v and decreases with yield stress S_y. We measure this yielded region, δa, in the radial direction across the cylinder, as shown in the figure.

To measure the limits of the yielded region (the values of δa), we have used the values of the viscosity in the foam. Foam is a non-Newtonian fluid, whose viscosity depends on many structural factors and is also dependent on shear stress. In this type of material, it is possible to define the so-called effective viscosity η_{eff} (see Chapter 1). If we use the effective viscosity, we can write the stress-strain relation in a non-Newtonian material as if it followed from Newton's Viscous law, Eq. 1.14, with an effective viscosity which will vary with the shear rate.

Using the Herschel-Bulkley relation (Eq. 2.1) we define this effective viscosity in our case as:

$$\eta_{eff} = \frac{S}{\dot{\epsilon}} = \frac{S_y}{\dot{\epsilon}} + K_p \dot{\epsilon}^{m-1} \tag{2.14}$$

where K_p is the consistency at high strain rate. We instigate a cut-off for values of $\eta_{eff} > \eta_s$ (a 'solid' viscosity), after which η_{eff} is constant (at low strain-rate where the foam moves as a solid plug). Provided that η_s is sufficiently large, its value is not significant. We retain the foam density as $\rho = \rho_{water}\Phi_l \approx 10\ kg/m^3$ throughout (with $\Phi_l = 0.01$).

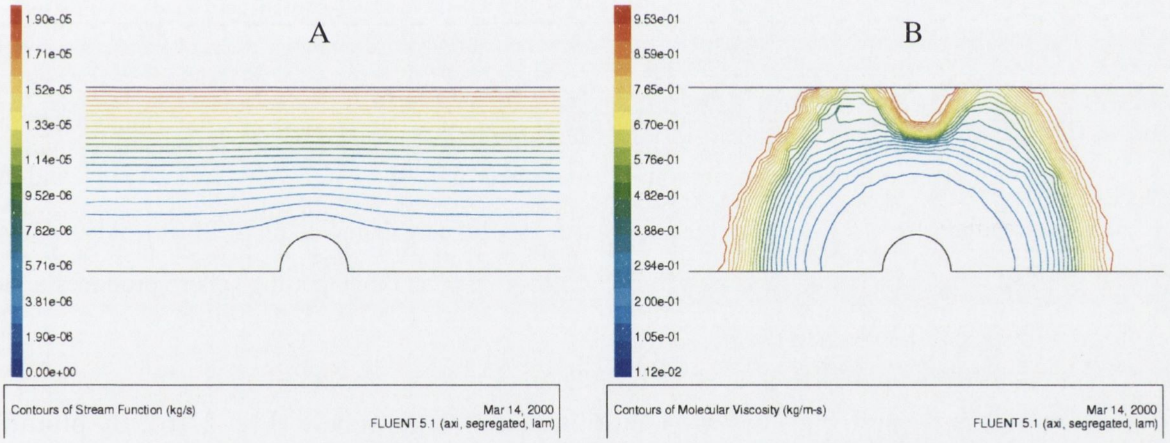

Figure 2-14: Streamlines (A) and viscosity values (B) for the Stokes experiment in a foam. The flow velocity is $v = 0.03\ cm/s$ Parameters are $m = 1, S_y = 0.01\ N/m^2$ and $K_p = 0.01\ Ns/m^2$ for a sphere of radius $a = 4mm$ in a tube of diameter $D = 40\ mm$. We attribute the non-spherical contour on the viscosity in (B) to the interaction with the boundary in the calculation.

Streamlines of the motion (Fig. 2-14-A) are easy to obtain but they prove of little value: they do not differ much while we vary the flow parameters. More interesting is the position of the yield surfaces (see the schematic in Fig. 2-13); this is taken as the contour at which the effective viscosity is no longer equal to the solid viscosity (Fig 2-14-B). As we show in Fig. 2-15, our computations in the case $m = 1$ are consistent with the theoretical estimate

(Eq. 2.12): the width of the yielded region, δa, does indeed increase with $\sqrt{v}$.

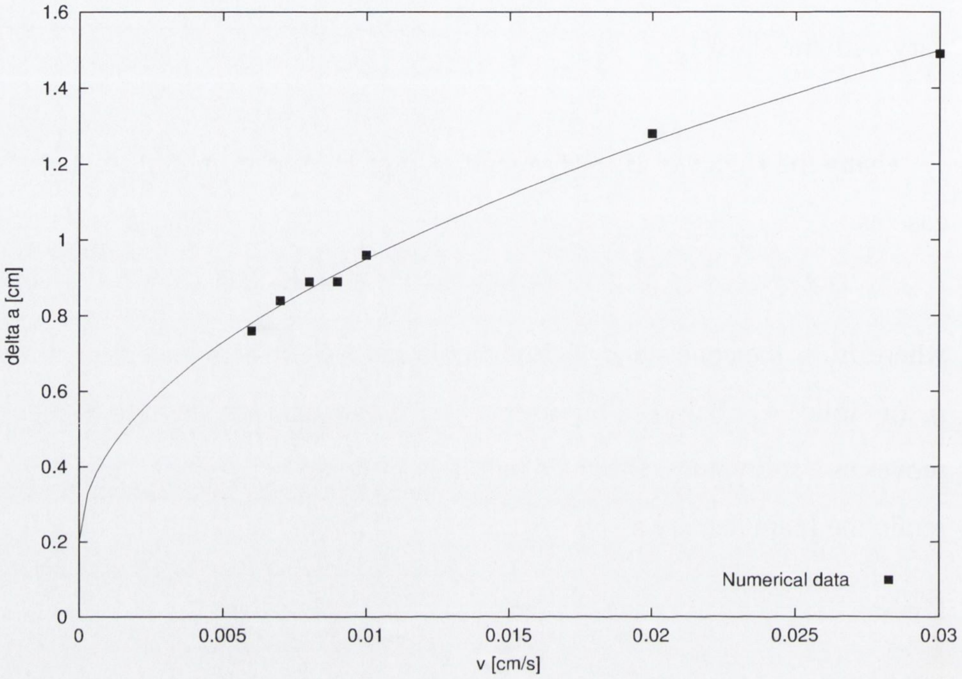

Figure 2-15: The numerically calculated width (across the cylinder) of the yielded region as a function of free stream foam velocity. Parameters are $m = 1, S_y = 0.01\ N/m^2$ and $K_p = 0.01\ Ns/m^2$ for a sphere of radius $a = 4mm$ in a tube of diameter $D = 40mm$. Also shown is a fit to $\delta a \sim \sqrt{v}$, the value predicted in Eq. 2.12 for $m = 1$. Note that the sphere produces a yielded region around it even at a zero velocity.

We finally perform a calculation of the force on the sphere (Fig. 2-16). By plotting the variation of this force with velocity at different values of the coefficient m we expect to check the values of the coefficient n obtained using the experimental values of k and Eq. 2.10. The results are compared in Table 2.3.

Our experiments, analysed using the theory developed in Section 2.5.2, include values of the exponent of velocity n (n_{theory}) in Eq. 2.9 between 0.33 and 0.83. However, most of the experimental values obtained lead to values of n_{theory} between 0.4 and 0.67 and therefore we decide to concentrate our efforts on this interval for the force calculation (Table 2.3). These values are related to the exponent in the Herschel-Bulkley equation (Eq. 2.1) by Eq. 2.13. We obtain values for m between 0.67 and 2.0. We use these values of m in the numerical calculations to verify the values of n (n_{numeric}) and obtain values between

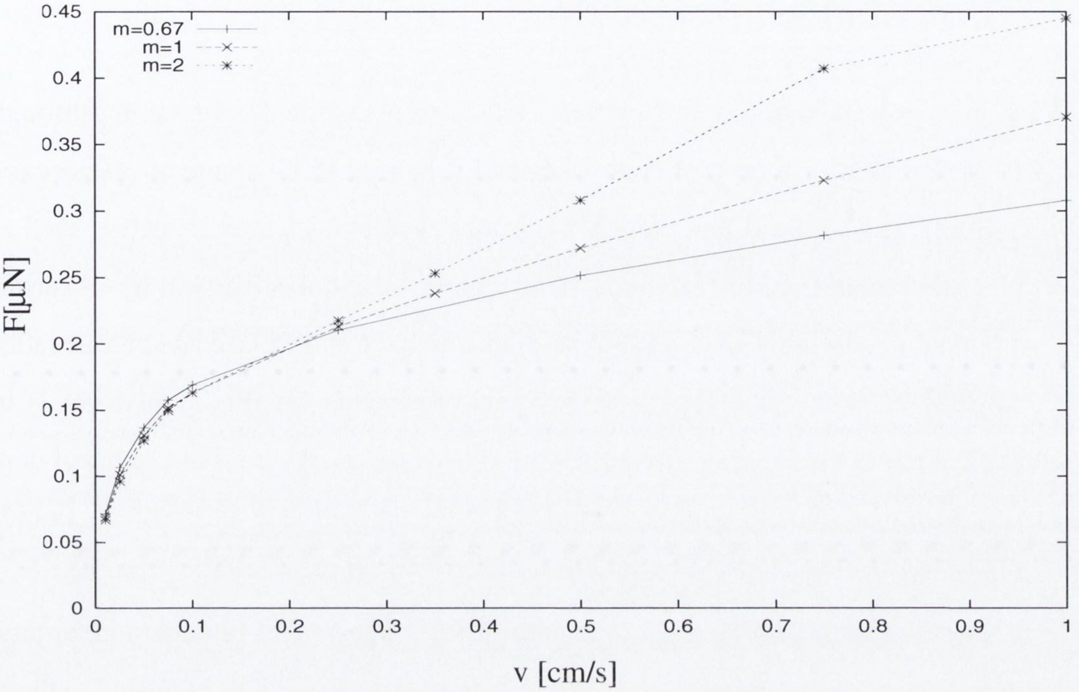

Figure 2-16: In a numerical calculation, we vary the exponent m in Eq.(2.1) to find the corresponding variation of the force on the sphere with the velocity. For $F \sim v^n$, we see that n is an increasing function of m; the values are given in Table 2.3. Parameters are $K_p = 0.01\ Ns/m^2$ and $S_y = 0.01\ N/m^2$ for a sphere of radius $a = 4mm$ in a tube of diameter $D = 40mm$.

n_{theory}	m	n_{numeric}
0.67	2.0	0.6
0.5	1.0	0.4
0.4	0.67	0.17

Table 2.3: Comparison of the theoretical and numerical estimates of the exponent of velocity, n, in the force equation (2.9). We also give the corresponding value of the exponent m in the Herschel-Bulkley relation, Eq.(2.1). We select values of n_{theory} between 0.4 and 0.67. The value of $m(n_{\text{theory}})$ is found from Eq. (2.13) and used in our numerical calculations to verify the value of n_{theory}. The values we find from the computations, n_{numeric}, are rather lower in all cases.

0.17 and 0.6. The numerical results are lower than the experimental ones in all the cases that we have calculated. In conclusion, the computation follows the qualitative predictions of the model but the quantitative results are lower than the expected ones.

2.7 Conclusion

We have described a range of new experiments on spherical balls falling through foams. We have shown that the concept of terminal velocity can be applied to these experiments and we have calculated the relation of terminal velocities with parameters such as bubble radius and liquid fraction. We have found that the terminal velocity of a ball varies linearly with bubble radius, at least up to the point in which the sphere size and bubble radii become comparable. The value suggested by our experiments for this breakdown is when the bubble diameter is equal or larger than the sphere radius. There is also a linear dependence of the terminal velocity with flow rate, and therefore with the square of the liquid fraction of the foam.

These experiments have also shown that the lighter spheres remain more or less static at dry foam and start gaining velocity at a finite liquid fraction. This is related to the existence of a yield stress of the foam, which decreases when we increase the liquid fraction. Further experimentation and theory needs to be undertaken to extract the exact dependence of the results on the bulk properties of the foam. In particular, it would be desirable to find a range of spheres with the adequate density and different radii to deduce the experimental change of the slope at the linear fits of velocity and flow rate with the sphere radius. This change is related to the drag force on the sphere.

Some spheres are too light to overcome the yield stress, even when its value decreases as we increase the liquid fraction. We have used these spheres to perform experiments in foam undergoing coarsening. When a light ball descends through a coarsening foam, it initially creeps (with position varying linearly with time) and then accelerates after the yield stress of the foam has been reduced by the coarsening process. We have found that in the latter part of the motion the velocity of a ball varies with the square of time. Unfortunately, the creep stage has been omitted from our simple analysis, but it may be eventually interesting in the view of new experiments with objects moving slowly through foam [61].

Our heuristic theoretical model is qualitatively and semi-quantitatively consistent with expectations based on the Herschel-Bulkley model, and also shows agreement with our experiments, within the wide uncertainties of the present results. These suggest that the exponent m in the Herschel-Bulkley relation lies between 0.5 and 4.8. Some of these values suggest foam as a shear-thickening fluid, which does not seem to agree with previous values reported in literature. We have to recall at this point the difficulty to fit the values due to the creep and 'hesitations' in our experiment. It is not yet possible to specify m more precisely at this stage. We have performed numerical calculations to identify the yield surfaces around a sphere and to obtain the variation of the force on a sphere with the free stream foam velocity. The results support the conclusions of our theoretical model. Further analysis is now required for larger parameter ranges.

Although the method is just starting to be developed, the Stokes experiment can be a useful way to measure rheological characteristics of the foam in a simple and inexpensive way. It allows measurements undergoing forced drainage, where it is easy to control that the foam has homogeneous liquid fraction. It measures the effective viscosity of the foam at low shear, where other methods used to measure viscosities (cone and plate, for example) have important slip corrections, due to the wall effects. Possibly, a better experimental set-up which will allow to use tubes of wider diameters, and further development of the theory will help to make progress towards such applications.

Chapter 3

Drainage induced convective motion in foam

3.1 Motivation

This chapter is devoted to the convective motion which appears in foams subjected to drainage at a high flow rate. Following on previous work at the TCD foam group, we have discovered that there are *two different kinds of convective patterns*. As far as we know, all previous reports of convective instabilities only mention one of these. We would like to understand the effect that several experimental parameters (bubble size, liquid fraction and the geometry of the container) have on both patterns. Accordingly we have produced the first systematic data on the effect.

Some hypotheses about the nature of the convective rolls will be introduced in an effort to explain the effect and character of the motion.

Firstly let us expose briefly some theoretical considerations about convective motions in foams. We will include a brief summary of results of previous papers on convective rolls. The following section is dedicated to the methods and materials used for the experiments. After this, we will examine in a purely empirical spirit the patterns of drainage driven instabilities found in a column of foam. We will report the two modes of motion found in a vertical column of foam and how they vary with bubble size and different geometries of the glass tubes. The speed of the convective motion of bubbles is studied in relation to liquid fraction. We report the finding of significant *hysteresis* associated to the convective motion. Until this was realised, we had considerable difficulty obtaining reproducible results, since the uniform state may persist metastably upon increasing the flow rate. Finally we will critically examine the form of a possible theory and reach some limited conclusions on this basis.

3.2 Theorical background of the convective motion

3.2.1 The nature of the transition to convective motion

We have already described how liquid drains through aqueous foam in Chapter 1. Here we concentrate our effort in *forced stationary drainage*. This means that a source of liquid is established at the top of the foam, delivering the fluid at a constant flow rate. One solution to the drainage equation under these conditions corresponds to a homogeneous liquid fraction profile and this corresponds closely to the observed profile. There is a small departure from uniformity at the bottom, also derivable from the drainage equation.

If the flow rate is increased, a wet front moves downwards in the form of a *solitary wave*, incidentally triggering local rearrangements [1]. After this solitary wave has gone through the foam a new dynamic equilibrium state, with a homogeneous higher liquid fraction, is reached. Theoretically, this could be carried on, increasing the flow rate step-by-step up to the point in which the foam loses rigidity and becomes a bubbly liquid. This rigidity loss transition is also referred to in literature as the *wet limit* [1] or *melting*. The value of liquid fraction at the transition has been calculated and measured experimentally in emulsions as ${\phi_l}^c = 0.36$ for a 3D monodisperse foam or emulsion [62, 36].

However, *flow instability* appears in foams at high liquid fractions well before this wet limit. Hutzler *et al.* [63] investigated foams at high flow rates and report a range of liquid fractions, below the *rigidity loss transition*, where convective instabilities are present. These instabilities take the form of convective rolls where some bubbles move upwards while other bubbles move downwards in the foam (see Fig. 3-1).

Even when we may occasionally use the term “convective instability” when we refer to the motions we have investigated, it may be slightly misleading. The data (in as much

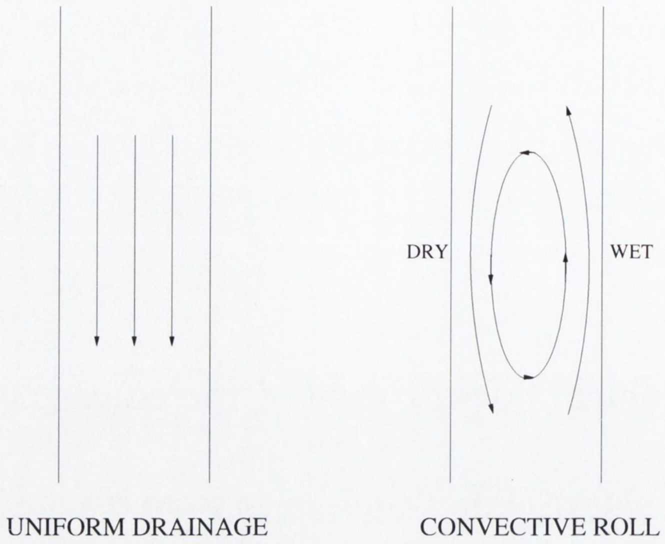
DRY
WET
UNIFORM DRAINAGE
CONVECTIVE ROLL

Figure 3-1: At some critical liquid fraction (or flow rate) uniform drainage is unstable. Convective rolls occur either "side-by-side" as shown, or in a cylindrical form.

as there is substantial *hysteresis*) do not point to a simple instability of uniform flow with respect to small perturbations. In this scenario, it would seem that the convective state should be regarded as an alternative stable state. In Fig. 3-2 we have sketched a mechanical analogy.

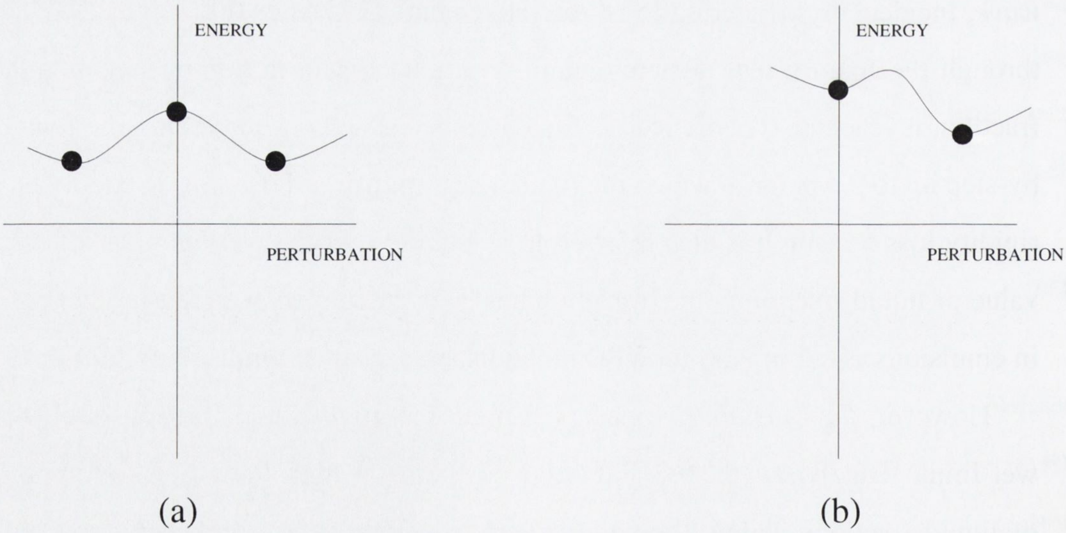
ENERGY
PERTURBATION
ENERGY
PERTURBATION

(a) (b)

Figure 3-2: Schematic mechanical analogy: the observation of hysteresis suggests that the system is more analogous to the one represented in (b) than to (a), close to the threshold of convection.

The phenomenon of convective instability is surely closely related to the *viscoplastic* character (see Chapter 1) of the foam: it behaves as an elastic solid when low forces are exerted, but can flow as a liquid when the force is increased. Flow must occur in practice when the yield stress is exceeded somewhere in the system. We will pursue this idea later, as we are going to introduce a semi-phenomenological theory and therefore we will need to introduce first the experimental findings that motivate the theory.

3.2.2 Previous results on convective motion

In the preliminary observations of the TCD group, which first announced the convective effect in drainage, Hutzler et al. [63] have used cylinders of circular cross-section, filled in with monodisperse foam. Vera et al. [39] at UCLA have used a wide rectangular box with a very small depth and filled with polydisperse foam. Forced drainage is used to increase the liquid fraction after foam formation in both cases. The results that have been reported by both groups are quite different and we will not attempt to explain the effects seen by Vera and their co-workers in their very different geometry (see Fig. 3-3).

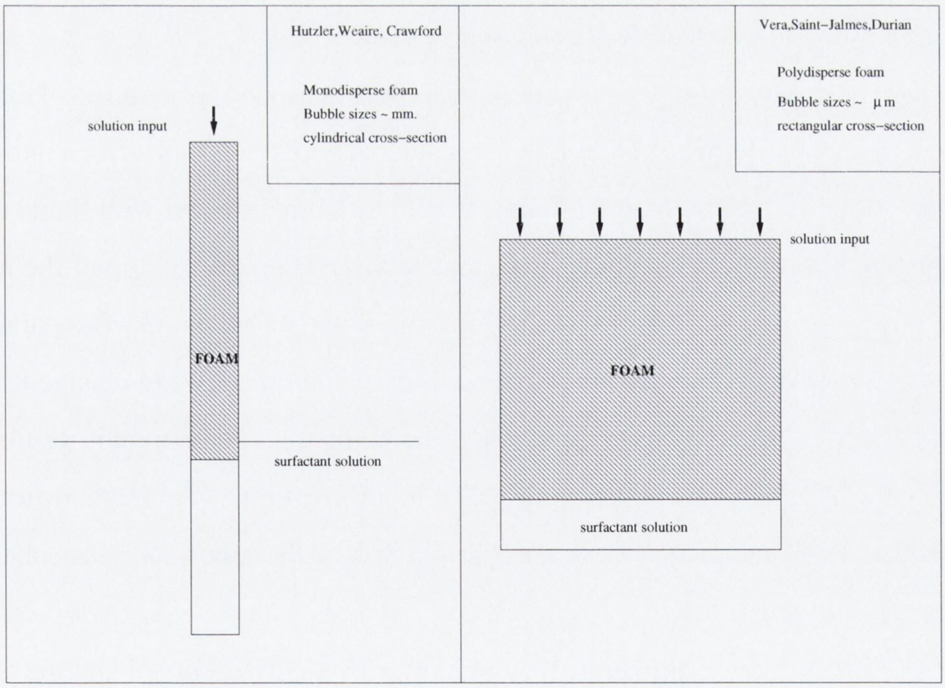
Hutzler,Weaire, Crawford
Monodisperse foam
Bubble sizes ~ mm.
cylindrical cross-section
solution input
FOAM
surfactant solution
Vera,Saint-Jalmes,Durian
Polydisperse foam
Bubble sizes ~ μm
rectangular cross-section
solution input
FOAM
surfactant solution

Figure 3-3: The setups for Hutzler *et al.* and Vera *et al.* experiments. A list of the principal differences is included.

Hutzler et al. [63] have reported the existence of a single convective roll in which all the bubbles on one side of the tube move upwards while the bubbles on the other side of the tube move downwards in a convective roll. Hutzler et al. observed that the motion has a clear onset, corresponding to a critical liquid fraction. The variation of this critical liquid fraction was measured in relation to inverse bubble radius. They have reported that the critical liquid fraction shows a linear increase with inverse bubble radius, ${B_r}^{-1}$, at first and levels off to around $\phi_l = 0.20$ for bubbles smaller than $1.25\,mm^3$.

The authors noted some dependence of the data on the length of the foam columns, but this dependence was not discussed in depth. They attempted to explain the onset of the motion in terms of yield stress, but the argument given is inadequate. As we see it now, it lacks several essential ingredients and it is in any case illogical.

3.3 Materials and methods

This section gives a description of the different apparatus and experimental tools that we use for the experiments described in the chapter. We study in particular the convective motion found in vertical 3D glass cylindrical tubes.

Monodisperse foam (see Appendix D), is introduced into glass tubes of different lengths and diameters. All the different foam containers are partially introduced into a pool of surfactant solution, so the foam has contact with air at the top and with liquid at the bottom, as shown in Fig. 3-4. Then, the surfactant solution is poured on top of the foam at different flow rates using a Watson-Marlow © 505S peristaltic pump. The parameter that we control in the experiments is the flow rate, as our pump allows to change it in increments of $0.03\ ml/s$. But it is more convenient for comparison of different results and for preliminary interpretations to use the average liquid fraction of the foam, estimated by using Archimedes formula (Eq D.1). The straightness of the tubes and glass plates is checked using a spirit level.

In some of the experiments, the bubbles are visually observed and the velocity of the bubbles is timed with a stopwatch. The 3D convective motions are also filmed using a Nikon © Coolpix 990 camera. This photo-camera can record short films (up to 40 seconds) at a speed of 30 frames per second.

3.4 Drainage driven convective motion in a vertical tube

3.4.1 Description of the drainage driven convective rolls

There are several parameters that may play a role in the drainage driven convective motions in a foam. The main ones are the flow rate, Q, at which liquid is added (related to the average liquid fraction in the foam, ϕ_l by Eq. 1.5), the bubble radius and the container geometry. The convective roll that has been reported by Hutzler *et al.* [63] has a clear onset at a certain liquid fraction. In the same work, dependence on the length of the tube has been suggested. Therefore, the aim at the start of the experiments undertaken here was to study systematically that dependence for the diameter and length of the tube in glass cylinders. But the results of the first experiments were quite surprising: a second type of instability, not previously reported, was discovered.

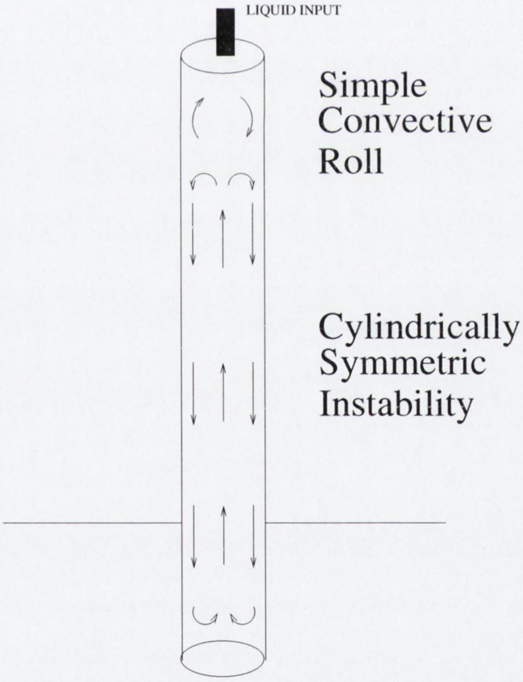

Figure 3-4: This sketch shows co-existence of both types of convective instabilities in a column of foam: the one that does not have cylindrical symmetry on top and the cylindrically symmetric at the lower part. In some cases, only the symmetry-breaking instability is observed. This happens when the tube is short or the bubble size of the foam is relatively big. The cylindrically symmetric instability has not been found on its own during any of the experiments.

Both types of instability can sometimes co-exist in the same tube, as is sketched in Fig 3-4. Eventually we came to regard the second cylindrically symmetric convective roll as the one of primary importance.

We will refer from now on to the convective motions shown in Fig. 3-4 as *Simple Convective Roll* or **SCR** and *Cylindrically Symmetric Instability* or **CSI**.

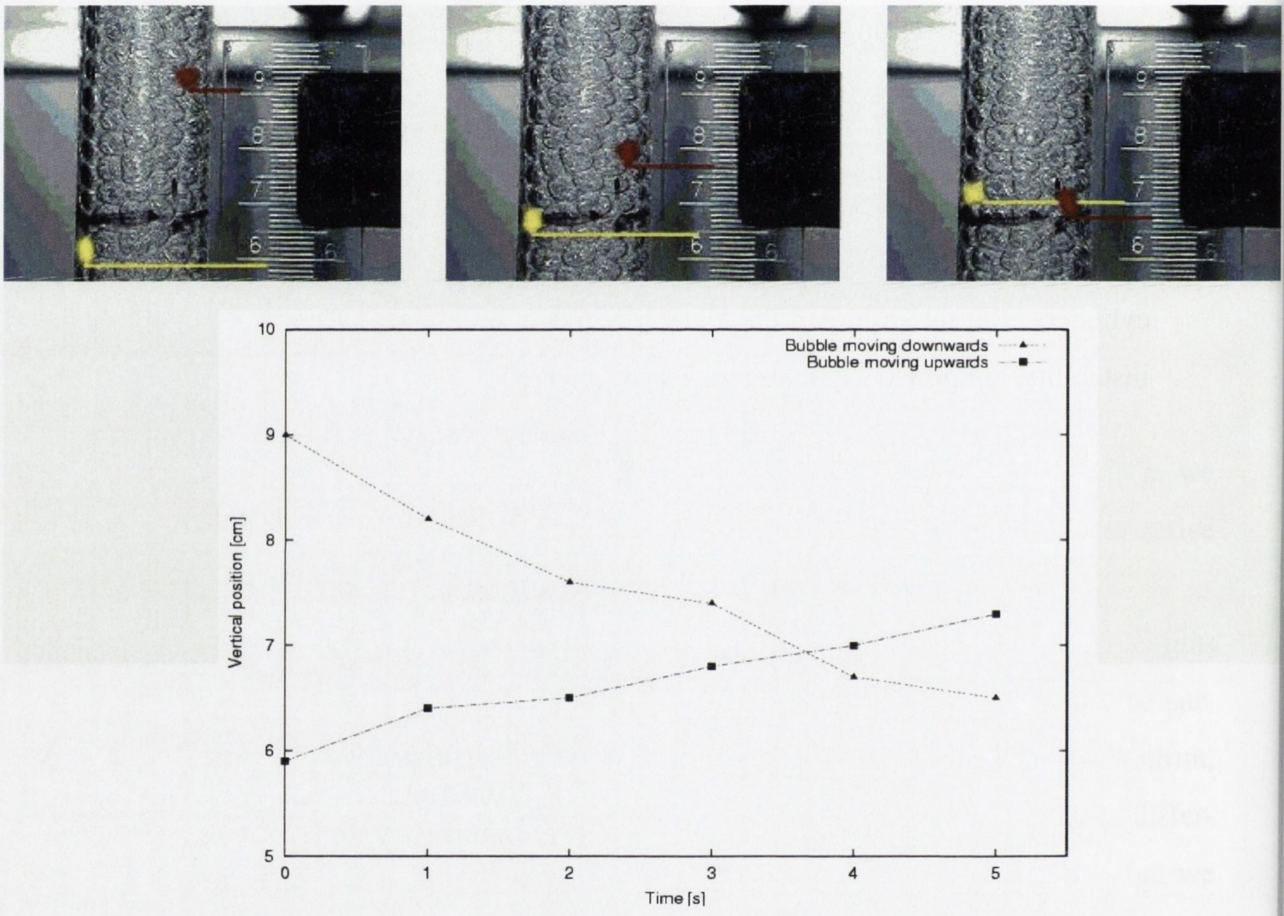

Figure 3-5: Three consecutive snapshots of the **SCR**. The pictures are separated by 2 seconds. The positions of two particular bubbles are marked to indicate the motion, one in yellow, moving upwards and the other in red, moving downwards. If we plot the position of the bubbles in relation to time, the velocity of the motion is approximately uniform. Downward motion is faster than upward motion. This is due to the different relative volumes of wet and dry foam. N.B.: The tubes are accurately vertical but the camera was slightly misaligned.

In the **SCR** (Fig. 3-5), bubbles move downwards along one side of the tube and upwards along the opposite side, as described previously in the paper by Hutzler *et al.* [63]. A video of the **SCR**, `SCR.mpg`, is provided on the CD that accompanies this thesis. The bubbles on one side of the tube move downwards while the ones at the opposite side of the tube move upwards. Visually following the motion of an individual bubble, one can see that after about several centimetres (4 to 16, depending on bubble size) it slowly moves towards the side, marking the end of this convective roll.

The plot of the position of the bubbles versus time for the **SCR** in Fig. 3-5 shows a difference in velocities between the bubbles moving upwards and the ones moving downwards. The mass of the system is conserved and we can write then:

$$\rho_{up} A_{up} v_{up} = \rho_{down} A_{down} v_{down}, \tag{3.1}$$

where ρ_{up} and ρ_{down} are the density of the foam moving upwards or downwards, A_{up} and A_{down} are the areas of the tube where the bubbles move upwards or downwards and v the velocity of the motion.

We can express the density of the foam in terms of the density of the liquid that it contains, neglecting the contribution of the gas phase. Therefore, $\rho_{foam} = \rho_{liquid}\phi_l$ and Eq. 3.1 becomes:

$$\phi_l^{up} A_{up} v_{up} = \phi_l^{down} A_{down} v_{down}. \tag{3.2}$$

We have mentioned in Chapter 1 that when the foam is static and at low flow rate, the liquid fraction is homogeneous all over the tube [1]. This is not the case when the convective rolls appear. But as we will mention later (Section 3.5), the difference in liquid fraction between the foam moving upwards and downwards is small. Therefore the change in velocities between the foam moving upwards and downwards implies a difference also in the relative volumes of foam moving upwards or downwards. Unfortunately, we do not know the behaviour of the bubbles in the bulk of the foam. Our observation is limited to the bubbles in contact with the walls of the tube, but within this limit the fraction of bubbles moving downwards is quite smaller than the one moving upwards.

The second type of motion, **(CSI)** is shown in Fig. 3-4. In this pattern all surface bubbles move downwards, implying that bubbles in the bulk move upwards. Playing with the depth of field of the microscope it is possible to get a focused image of the bulk bubbles but the image is not clear enough to get any quantitative information about the velocity of

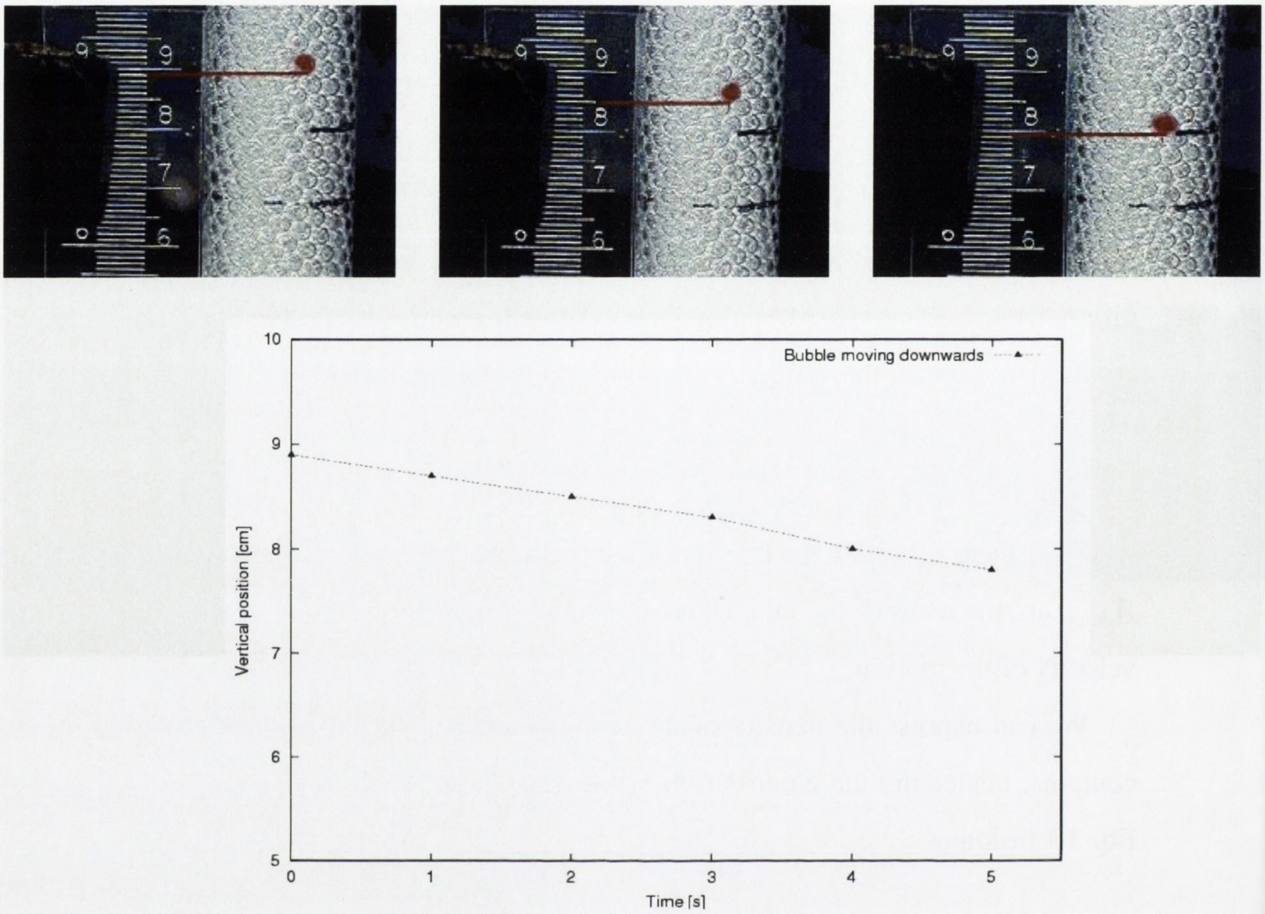

Figure 3-6: Three consecutive snapshots of the continuous motion stage for **CSI**. The pictures are separated by 2 seconds. The coloured bubble indicates the motion. Again, a plot of the position of the bubble in relation to time, shows a quite uniform velocity of the motion.

internal bubbles. Therefore, we track only the position of individual surface bubbles. Once they reach the bottom of the tube, they are drawn towards the centre of the base of the foam. Then, they disappear upwards into the bulk. **CSI** is the dominant bubble motion, meaning by this that it covers a bigger region of the tubes, in most of the cases.

For the **CSI**, it is possible to distinguish several subtypes of motion, depending on flow rate values. At higher flow rates, the video `CSI-C.mpg` shows a continuous regular motion, with all the bubbles moving downwards (Fig. 3-6). The bubbles tend to move in ordered layers, but some of them jump from one row to another.

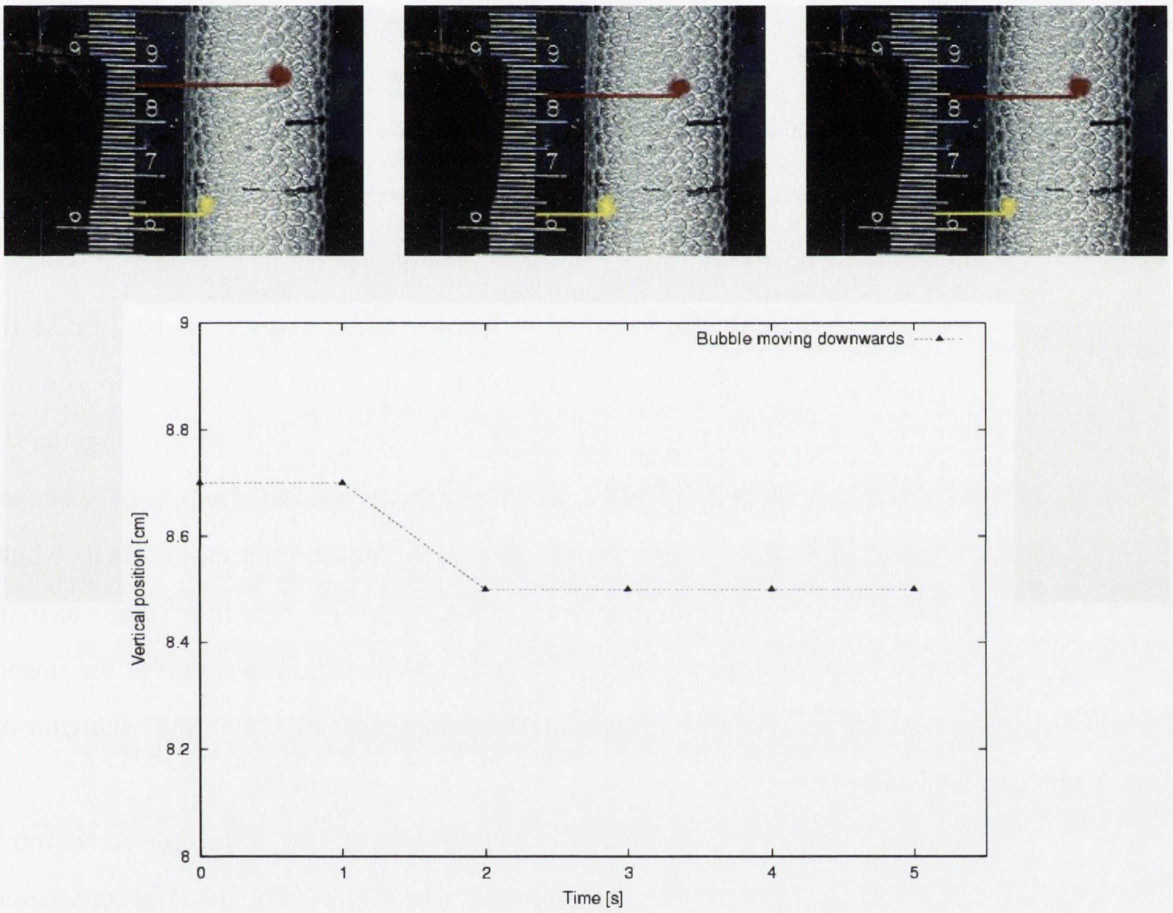

Figure 3-7: Three consecutive snapshots of **CSI** for the non-continuous motion. The pictures are separated by 2 seconds. The red bubble moves downwards but then seems to stop for a while, as we can deduce by the plot of position versus time. The yellow bubble does not move at all during the making of the film.

When the liquid fraction is decreased, the velocity of the motion becomes discontinuous, as we can see in the following pictures and in the film `CSI-A.mpg`. The motion seems to be limited to some bubbles, with the subsequent collapse of the bubbles that are on top of them (Fig. 3-7). These series of motions occur at random times, giving sometimes the impression that the foam has stopped completely. This behaviour remind us of the creep regime observed in the Stokes experiments (Chapter 2) which may well have some correspondence here. In what follows we will not distinguish between these subclasses of the motion unless stated otherwise.

3.4.2 General description of results for the convective rolls

So far, we have described the two instability types, Simple Convective Roll or **SCR** and Cylindrically Symmetric Instability or **CSI**, which can be found and co-exist in a column of foam at high flow rates. From the description of the motions in Section 3.4.1 and the sketch in Fig. 3-4, we can establish that these convective rolls have clear *domains* of existence: at a certain height of the tube and at a given value of the liquid fraction the surface bubbles will either not move or move in one of these convective rolls. Our intention is to map out these domains of occurrence, together with values of the liquid fraction at the onset and velocity of the two kinds of instability with different values of flow input, diameter of the tube and bubble size.

We will have a look first at the general pattern of appearance of the convective motions, shown in Fig. 3-8: we indicate the fraction of the tube occupied by the convective motions at different liquid fractions.

A major feature of these results not previously recorded is *hysteresis*, that is, the uniform state may persist above the threshold value for the convective rolls. This is mainly observed for the **CSI** and the effect varies to a greater or lesser extent in different experiments (Fig. 3-9).

Measuring by increasing the flow rate can lead to a value for critical average liquid fraction that is higher than that presented by data for decreasing flow rate. Unless stated otherwise, the experimental values in this the chapter are taken by increasing the flow rate to a value in which both convective motions are fully developed, and then decreasing the

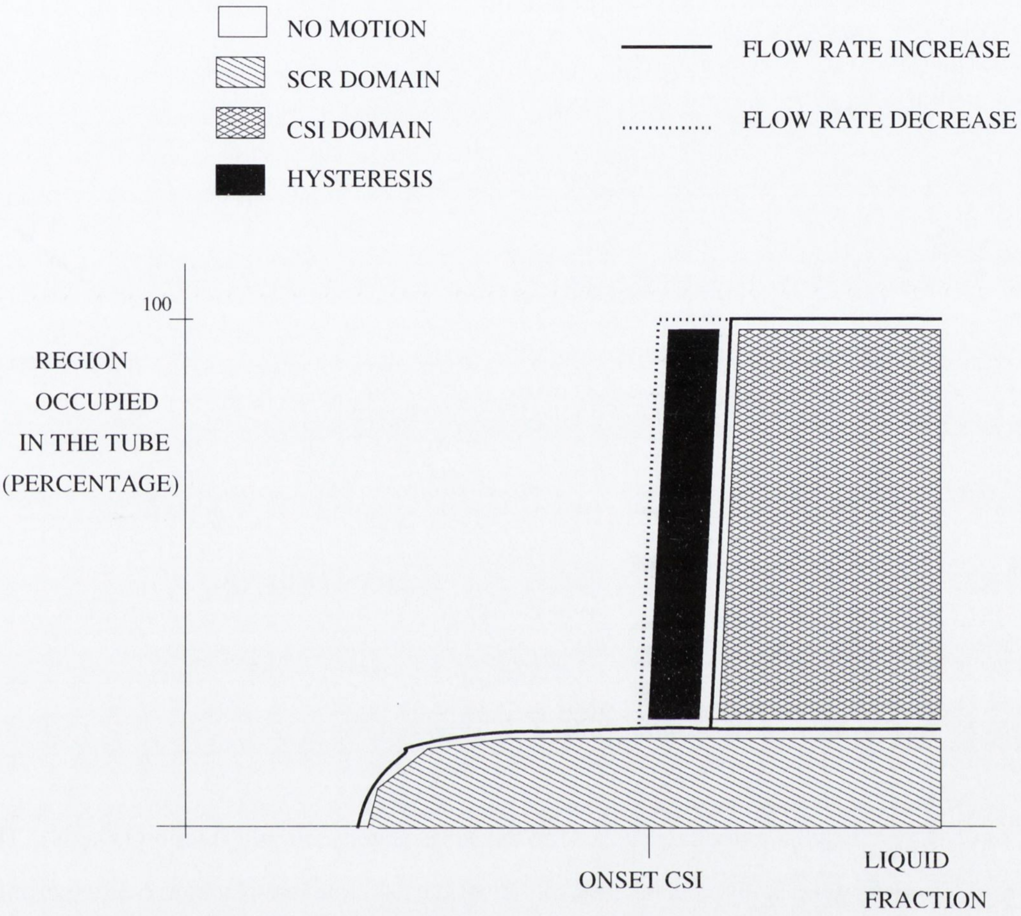
NO MOTION
SCR DOMAIN
CSI DOMAIN
HYSTERESIS
FLOW RATE INCREASE
FLOW RATE DECREASE
100
REGION OCCUPIED IN THE TUBE (PERCENTAGE)
ONSET CSI
LIQUID FRACTION

Figure 3-8: Typical domain of co-existence for the two types of instability in the same tube. The x-axis shows liquid fraction values and the y-axis the fraction of the length of tube occupied by the convective flows. Let us recall that **SCR** develops at the top of the tube and **CSI** in the rest of it, as seen in Fig. 3-4. The different regions of existence of **SCR** and **CSI** appear shaded. **SCR** develops at the top of the tube, increasing in length until **CSI** appears in the rest of the tube. Data is taken increasing the flow rate (solid line) until both motions are fully developed on the tube. After that, we decrease the flow rate (dotted line). This shows hysteresis (the area shaded in black) in the onset of **CSI**. An example of the experimental data is shown in Fig. 3-11, where the shaded regions have been omitted. For most of the experimental data, we have only measured values decreasing the flow.

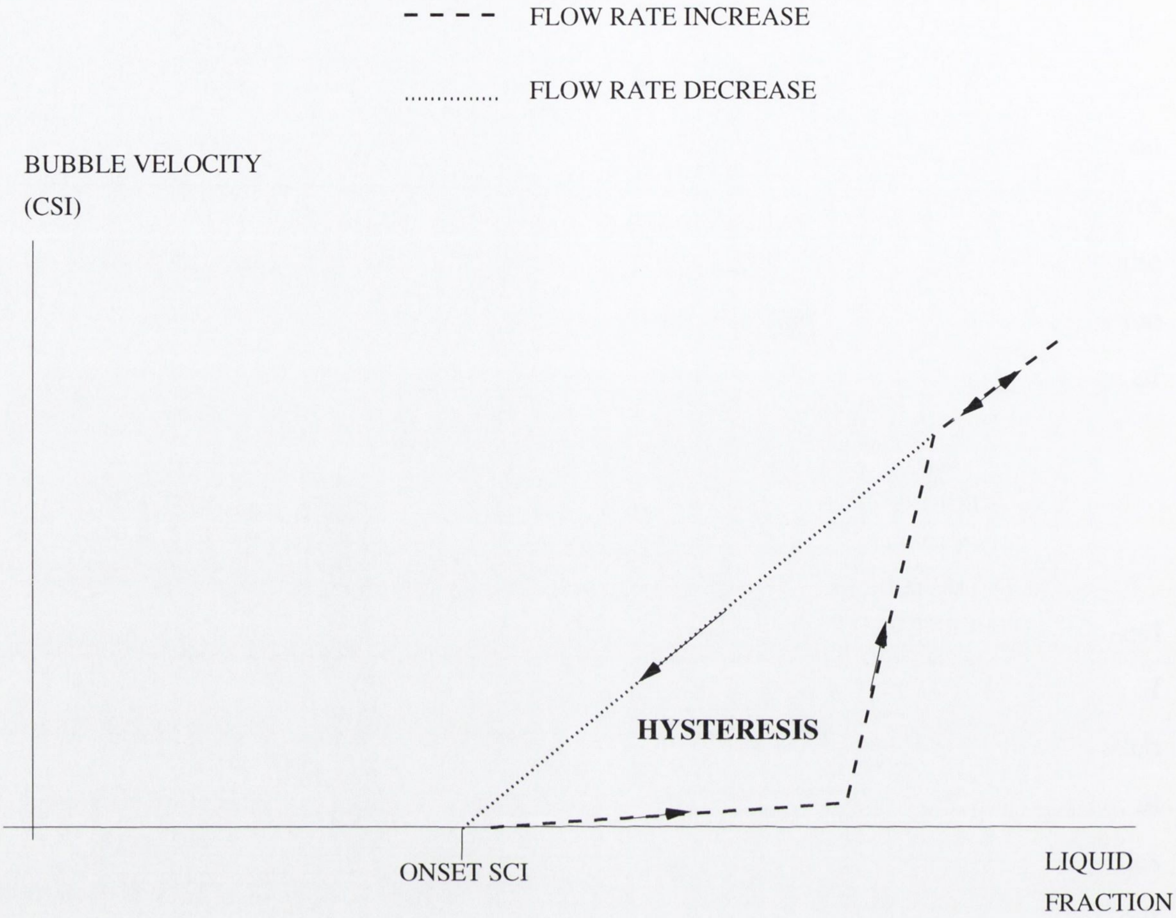
FLOW RATE INCREASE
FLOW RATE DECREASE
BUBBLE VELOCITY (CSI)
HYSTERESIS
ONSET SCI
LIQUID FRACTION

Figure 3-9: Bubble velocities (y-axis) in the **CSI** related to liquid fraction (x-axis). This diagram also shows hysteresis in the behaviour of the bubbles as flow rate is varied (see experimental values in Fig. 3-20).

flow rate while performing the measurements. In this way, we determine the critical liquid fraction at the point at which the velocity v goes to zero. Note also that the shaded regions at Fig. 3-8 will be omitted when showing experimental data, for the sake of clarity.

3.4.3 Influence of the liquid input in the convective rolls

The convective rolls that we have just described in Section 3.4.1 depend strongly on the liquid fraction. We have already mentioned that obtaining reproducible values for the onset of the convective rolls is not straightforward. At low liquid fractions the dry foam theories postulate that small inhomogeneities in the input of flow in forced drainage situation will be compensated by the diffusion of the liquid through the foam. But this is not necessarily true at higher liquid fractions. Therefore, we have decided to investigate the effect of off-centring the input of surfactant solution (Fig. 3-10). We use three different wetting conditions: data labeled as "Centred" correspond to a wetting input carefully centred in relation to the cross-section of the tube, using a ruler; "Off-centred" means that the input has been slightly misplaced from the centred position; the "Extreme off-centred" values stand for data taken placing the wetting input touching the walls of the tube.

Off-centring the input produces an increase in the height of the tube covered by **SCR**, at the expense of the length of **CSI**, but it does not seem to have a large effect on other characteristics of the motion. For the wider tube, the one with diameter of $3.2\ cm$, this effect is more pronounced than for the other tubes. Extreme off-centring produces lower values for the onset of both convective motions. Our results show that the influence of the wetting input is very important at the time of taking systematic values for the onset of the convective rolls or to establish the domains of the two instabilities. The rest of the experiments are done taking precautions to assure a centred input [1].

3.4.4 Examples of hysteresis on the convective rolls

Hysteresis can be appreciated in the onset of the Cylindrically Symmetric Instability (**CSI**) pattern in the data shown in Fig. 3-11 (as sketched in Fig. 3-9).

---

[1] N.B.: The next two sections contain a lot of detailed results: the reader who is concerned mainly with the onset of convection and the present state of relevant theory may disregard these details and proceed to Section 3.4.6.

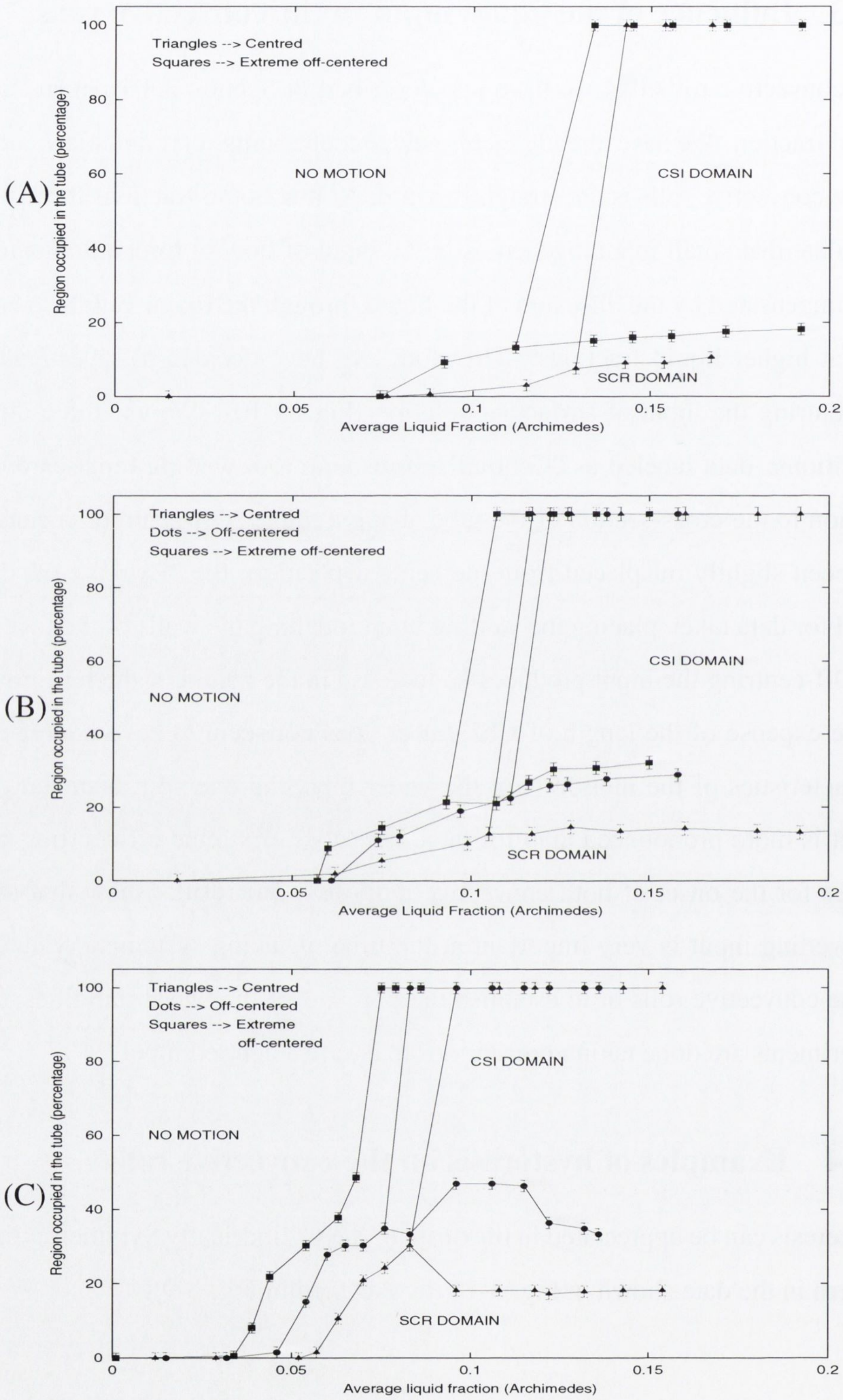

Figure 3-10: The figure shows the influence of the three different positions available for the wetting input in the convective rolls. We compare tubes with foam length 30 *cm* and (A) 1.6 *cm* diameter, (B) 2.0 *cm* diameter and (C) 3.2 *cm* diameter. The bubble radius is $B_r = 0.16\ cm$. We increase the flow rate to obtain domains of the convective rolls (explained in Fig. 3-8) but the shading of the different regions is omitted for clarity. The tube with 1.6 *cm* diameter was too narrow to allow us to take data of the "Off-centred" position. The values for the centred input cannot be compared with further experiments due to the hysteresis, explained in Section 3.4.4 (see Fig. 3-11).

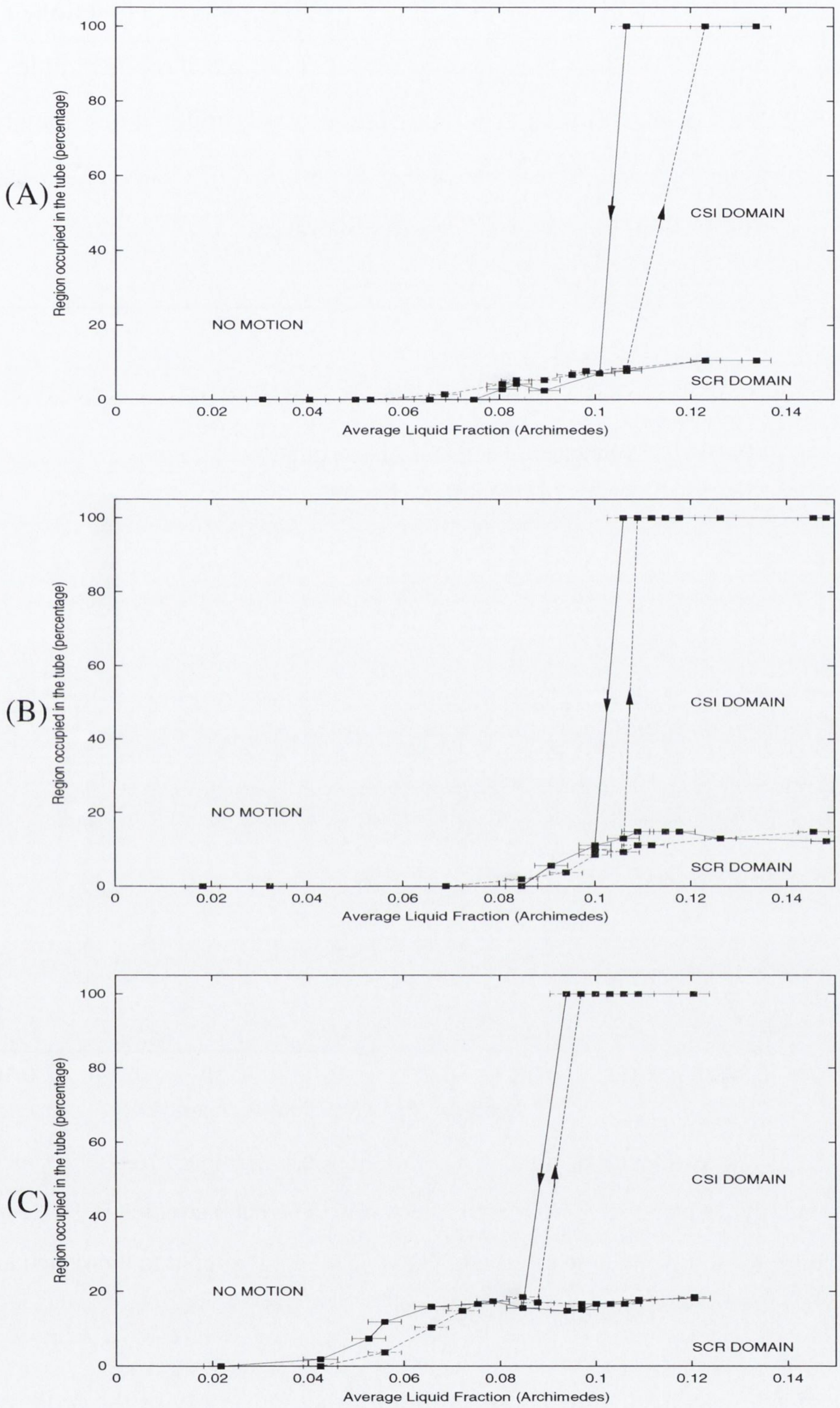

Figure 3-11: Typical co-existence pattern for the two types of instability in cylindrical tubes. The input of surfactant solution is centred for tubes (A) 1.6 cm diameter, (B) 2.0 cm diameter and (C) 3.2 cm diameter and foam length 30 cm. The bubble radius is $B_r = 0.13\ cm$ in the three samples. **SCR** first develops at the top of the tube, increasing in length until **CSI** appears in the rest of the tube. We have increased the flow rate first and decreased it afterwards. This shows the hysteresis (the area shaded in black at Fig. 3-8) in the onset of **CSI**. The values for the onset critical liquid fractions are in accordance with the values obtained in Fig. 3-15.

A typical hysteresis cycle of velocities of the **CSI** motion as a function of average liquid fraction, shown in Fig. 3-12, presents a lower but finite speed of the bubbles when the flow rate is increased starting from a dry foam. These small, finite values, may be due to some sort of *creep* analogous to that in the Stokes experiment of Chapter 2. We shall disregard them in our discussion, treating them as effectively zero.

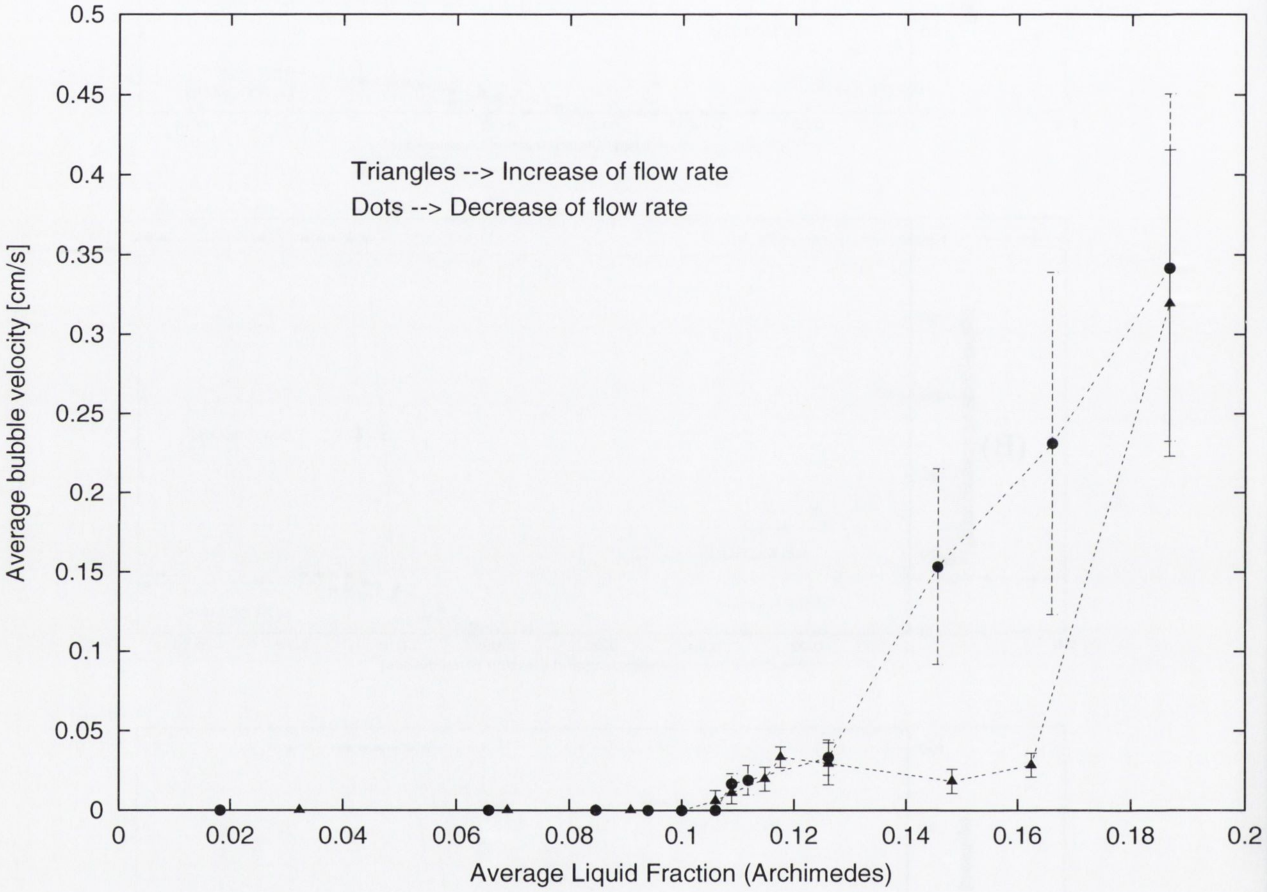

Figure 3-12: The velocity of the bubbles in **CSI** when the liquid fraction is increased until the motion is fully developed and decreased afterwards. The bubble radius is $B_r = 0.15\ cm$ and the tube diameter is 2.0 cm with foam length 30 cm. The plot is similar to the sketch in Fig. 3-9. Each velocity point is the average of six measurements.

The hysteresis for the onset critical liquid fraction is only of the order of 10% when it appears (it is easier to appreciate the hysteresis in the velocity plots as in Fig. 3-12). But the effect of hysteresis has to be taken in account when we do experiments. All the data presented from this point will be taken in the way just explained (using a *centred input* and *decreasing the flow rate*) unless explicitly mentioned.

3.4.5 Domains of the drainage driven convective motions in a foam

In the last two sections, Sections 3.4.3 and 3.4.4, we have presented the necessary procedure to obtain systematic data for the convective rolls. Now we are ready to determine the domains of existence of each of the convective motions for different tube diameters and bubble sizes.

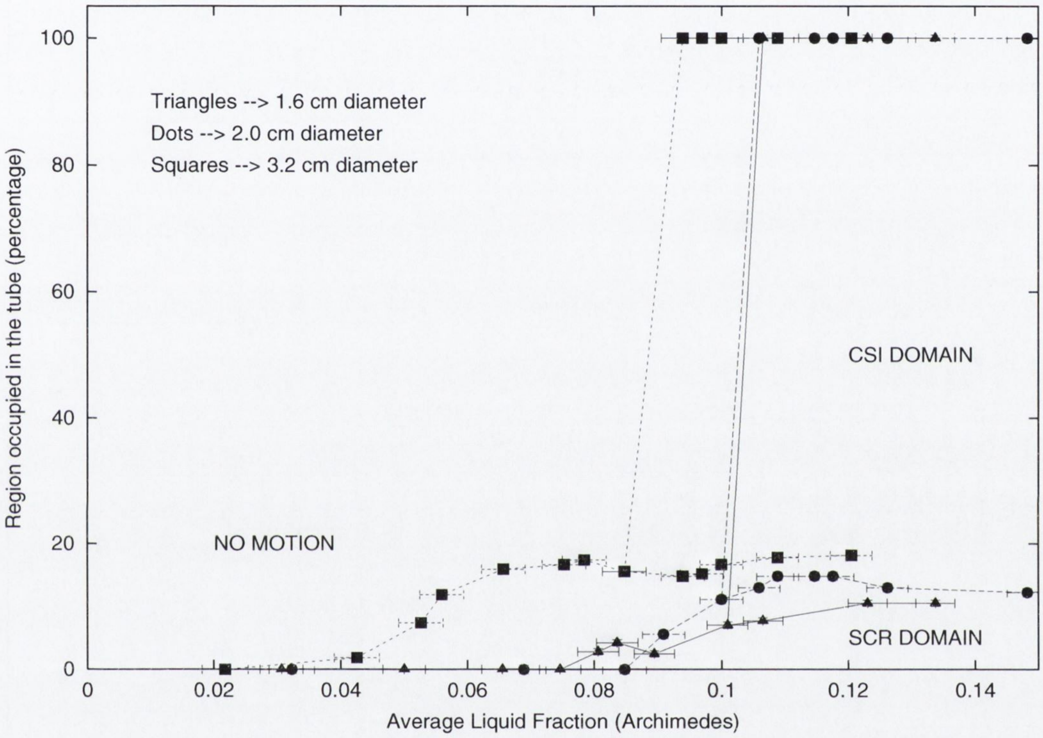

Figure 3-13: A plot of the values of the domains of the two convective rolls (see Fig. 3-8) for a centred input. The same tube diameters used in Fig. 3-11 are shown together to compare them when we decrease the flow rate. These diameters are 1.6 cm, 2.0 cm and 3.2 cm with foam length 30 cm. The bubble radius is $B_r = 0.13\ cm$ Relatively wide tubes present a bigger **SCR** domain. There is also a tendency to get lower onset values for **CSI** with higher tube diameter. This dependence of critical onset liquid fraction with tube diameter will be confirmed later (see Fig. 3-17). Again, the domain regions (Fig. 3-8) are not shaded for the sake of clarity.

A comparison of three different tube diameters using a centred input (Fig. 3-13) shows that the diameter of the tube has an effect in the height of the tube covered by **SCR**. Wider tubes present a longer **SCR** domain and lower liquid fraction values for the onset of the **CSI**.

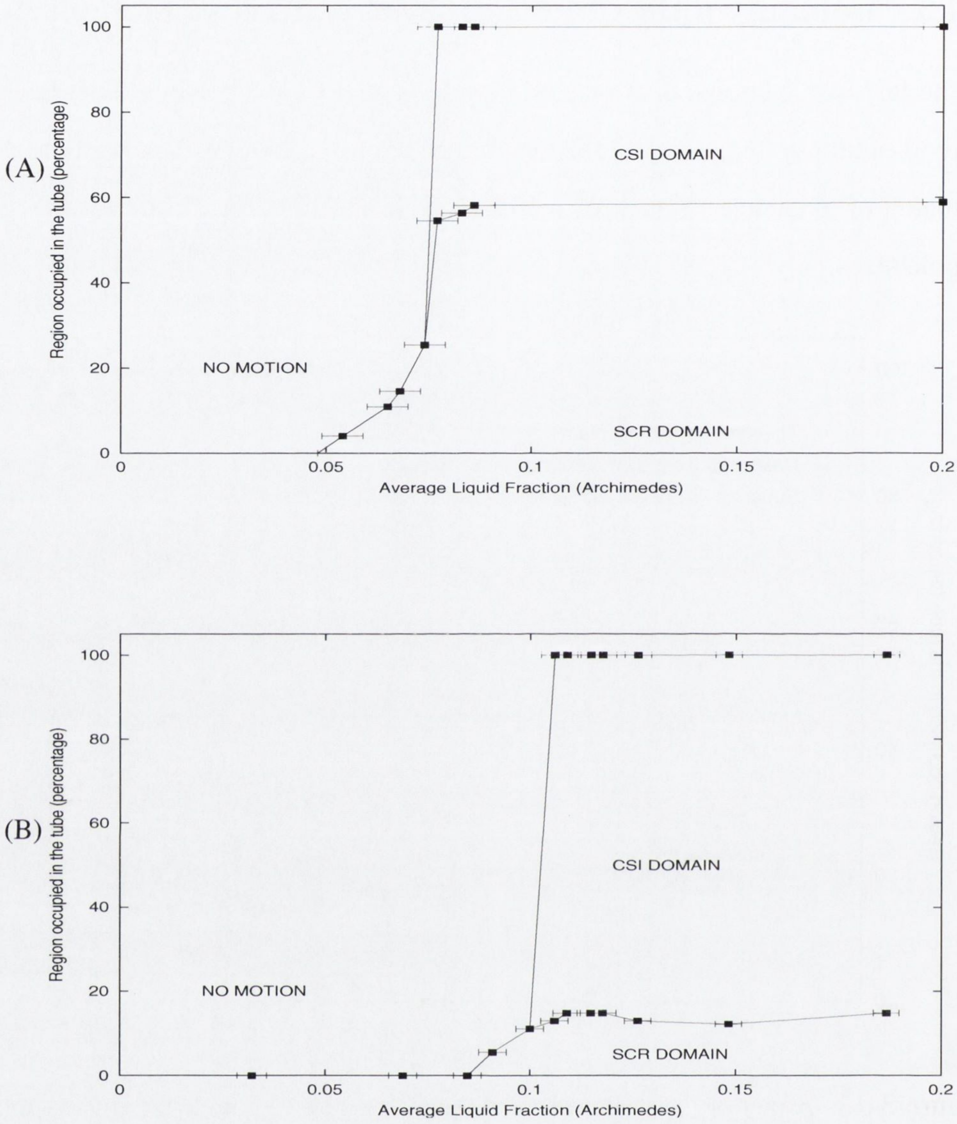

Figure 3-14: The domain of existence of the convective motions (see Fig. 3-8 for interpretation of this diagram) is also dependent on bubble size. The graphs correspond to a tube of 2.0 cm diameter and foam length 30 cm. The bubble radii are (A) 0.27 cm and (B) 0.15 cm. An increase in the bubble size leads to an increase in the domain of **SCR**, with the subsequent decrease of **CSI**. Therefore, for big bubble sizes or relatively short tubes, **SCR** is the only instability that would be observed. This affirmation has been checked several times during the experiments and will affect the way in which we investigate the dependence of the onset of the rolls with bubble size. The onset critical liquid fraction values seem to be lower at bigger bubbles attending to the preliminary result in this plot. We can confirm this from extended data in Figs. 3-15 and 3-20.

In Fig. 3-14 we compare the domains for **CSI** and **SCR** in the same tube using two different bubble sizes. An increase of the bubble size produces a longer **SCR** domain. It is also clear that the liquid fraction at the onset of the **CSI** is lower when the bubble size increases. This trend is more clearly shown in the next section (Section 3.4.6), that investigates the liquid fraction values at the onset of the motion.

3.4.6 Onset of the convective rolls

In this section we present results for the onset of convective motion and gather many of them together in the last figure (Fig. 3-18).

Given what has gone before, it seems best to disregard the Simple Convective Roll (**SCR**) for present purposes, since it occupies only the top of the tube at onset and is somewhat sensitive to centring the liquid input (see the video `input.mpg`.). The newly discovered Cylindrically Symmetric Instability (**CSI**) offers a better object for study, particularly as its symmetry is amenable to relatively simple theoretical treatment.

Accordingly, the onset of **CSI** motion is investigated below for different bubble sizes. There is an exception for bubble radii $B_r \geq 2\ mm$, at the extreme lower range of our data. The **SCR** reaches a longer distance at these bubble sizes (see Fig. 3-14) and it appears into the region where we are measuring the onset of **CSI**. We take the values of liquid fraction at which there is a convection occupying the whole tube (even if it is **SCR**) for these bubble sizes. At even larger bubble radii $B_r \geq 3.5\ mm$ it becomes impossible to get data. Ordered cylindrical structures of foam [64] form in the tubes. These structures do not present convective motion. They rotate at twist boundaries described previously by Hutzler *et al.* [65].

First we show our main results in Figs. 3-15 and 3-16. Recall that values of the critical liquid fraction at the onset are taken by decreasing carefully the flow rate at the foam. Every time that we decrease the flow rate, we wait for some minutes before taking the measurements to allow the system to reach a stable average liquid fraction. To determine the critical liquid fraction, we just observe visually the foam after this waiting period.

We have chosen arbitrarily to fit the data on Figs. 3-15 and 3-16 to a line of the type:

$$f(x) = \frac{a * x}{1 + b * x}, \tag{3.3}$$

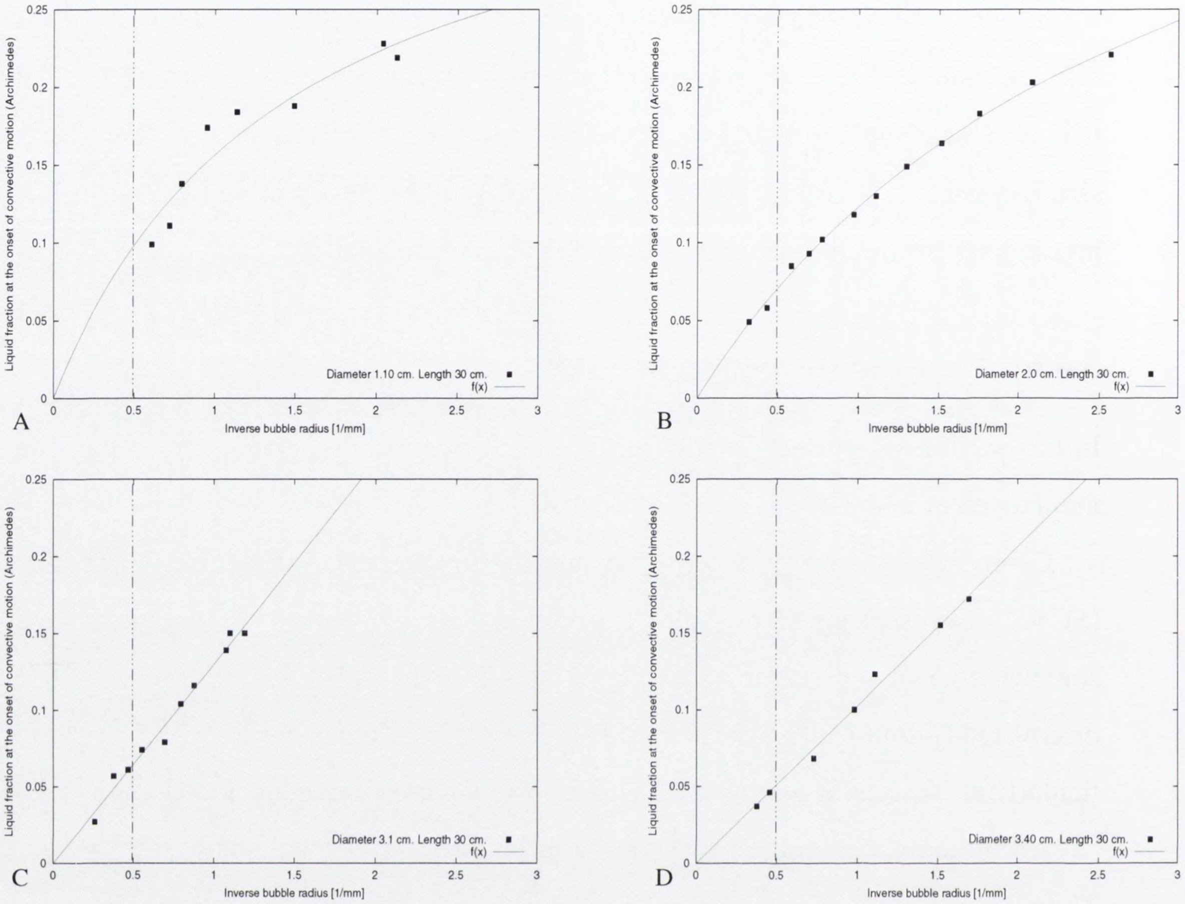

Figure 3-15: Dependence of the critical liquid fraction for the onset of the convective rolls upon inverse bubble radius. Values for four different tube *diameters* (A 1.1 cm, B 2.0 cm, C 3.1 cm and D 3.4 cm) are shown. The length of the tubes is 30 cm. The dashed-dotted line marks the inverse bubble radius below which the motion observed at the tube is **SCR**. The solid lines are fits to Eq. 3.3.

where $x = \frac{1}{B_r}$ and a, b are free parameters. Here we assume that the data should level off as it happened in the previous work of Hutzler et al. [63]. The tubes with bigger diameters in Fig. 3-15-(C,D) do not show this tendency to level off, but note that ϕ_l does not reach the same high values as it does in the narrower tubes. Due to the difficulty to fill in these tubes with small bubbles, we have very few data for the range of values at small bubble radius.

We can conclude from Fig. 3-16 than the shorter the tube, the easier to get a convective roll. To confirm these qualitative impressions, we can compare the slope of the lines fitted to the tubes. In Fig. 3-17 we show the values for the slope at the big bubble size range

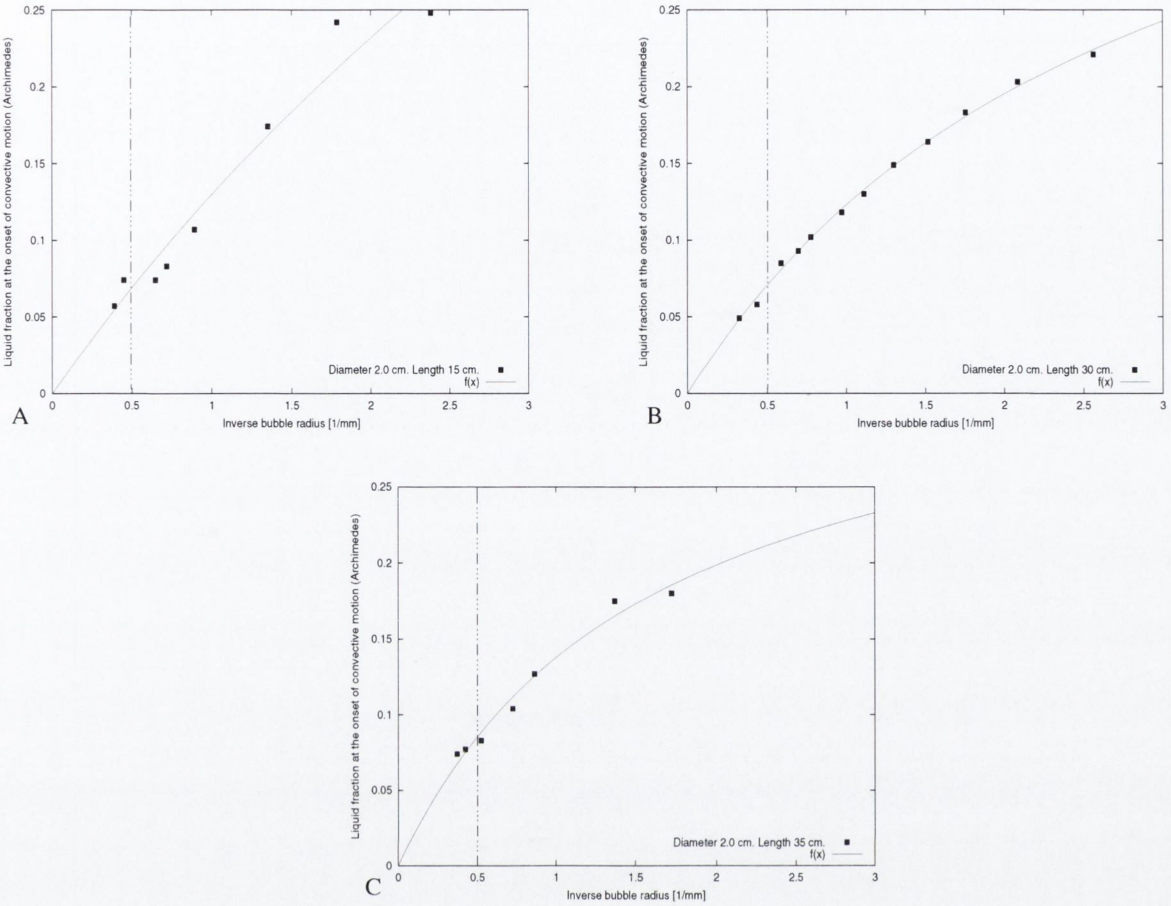

Figure 3-16: Dependence of the critical liquid fraction at the onset of the convective rolls with inverse bubble radius. Values for three different tube *lengths* (A 15 cm, B 30 cm and C 35 cm) are shown. The diameter of the tubes is 2.0 cm. The graph marked as B is the same graph shown in Fig. 3-15-B. The dashed-dotted line marks the inverse bubble radius below which the motion observed at the tube is **SCR**. The solid lines are fits to Eq. 3.3.

(parameter a in Eq. 3.3). This parameter gives an idea of how does the critical liquid fraction grow with inverse bubble size. We can compare the evolution of the slope for all the tubes with the same length Fig. 3-17-(A) and all the tubes with the same diameter Fig. 3-17-(B). As we expected, the wider and shorter tubes are more likely to present convective rolls at lower liquid fractions

Finally (Fig. 3-18), we will show a comparison of our data to those of Hutzler et al. [63].

Various consistent features emerge from all of these measurements, particularly the average liquid fraction needed for the onset of the motion in the whole length of a tube is

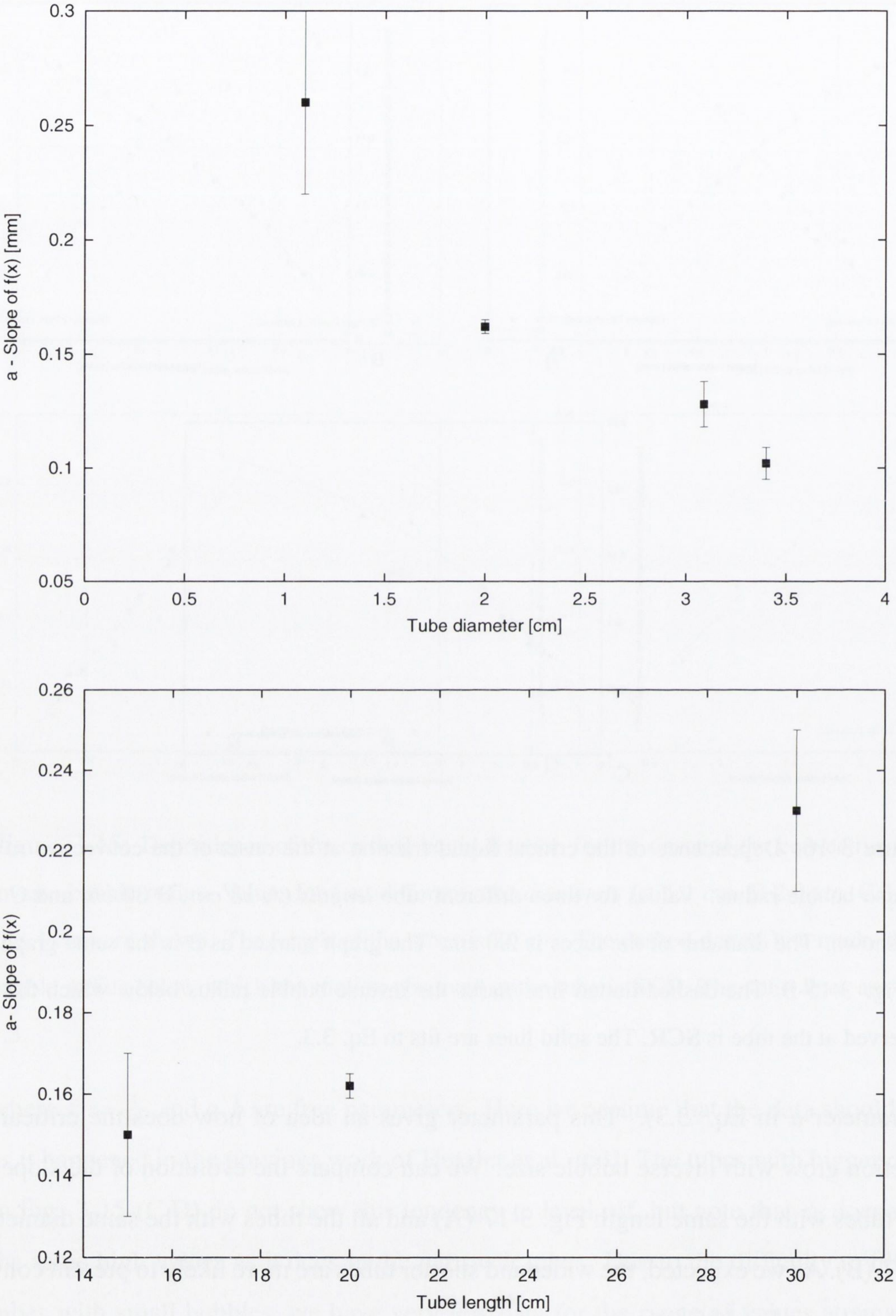

Figure 3-17: A comparison of the slopes for all the tubes (A) in Fig. 3-15 and (B) in Fig. 3-16. The slope a decreases with tube diameter and increases with tube length. This corresponds with the qualitative observations deduced from these figures.

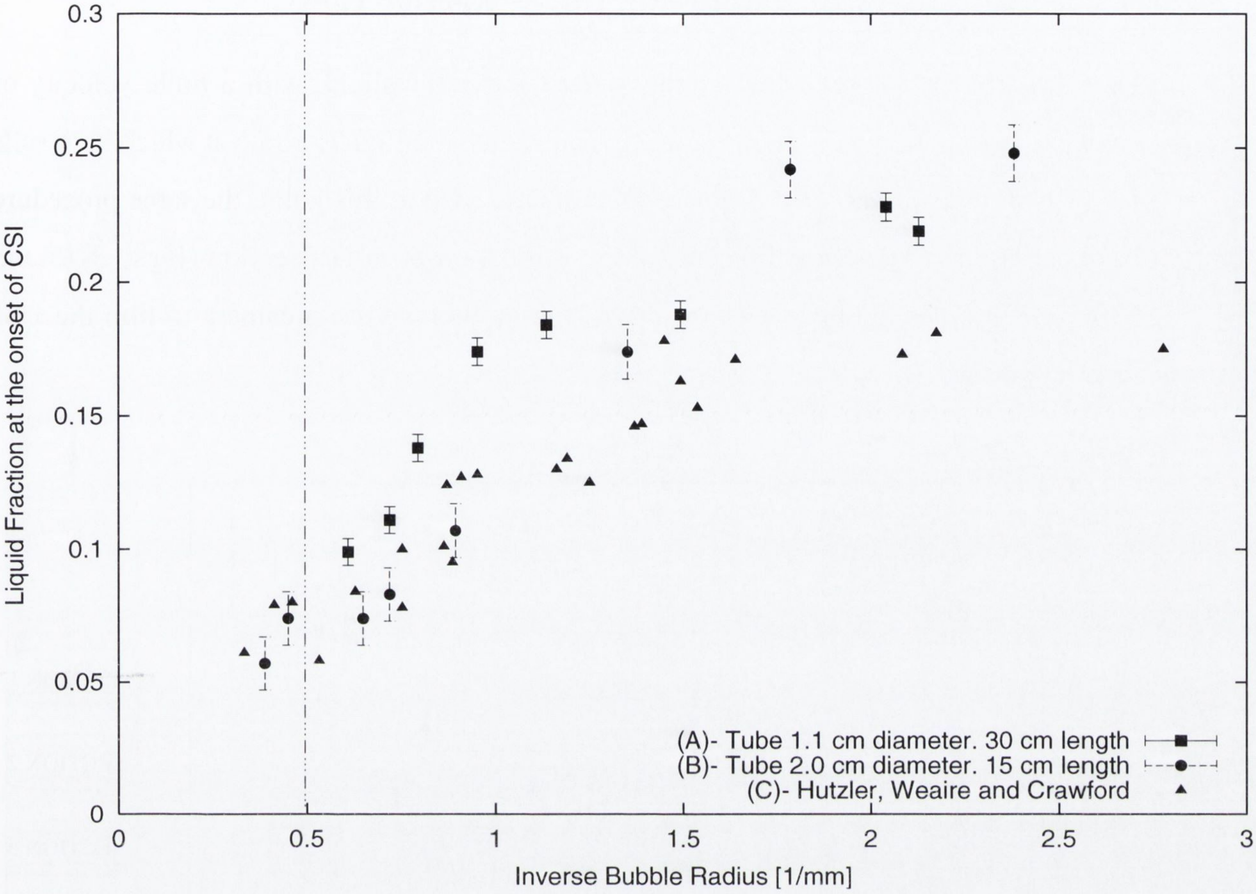

Figure 3-18: Comparison of the data obtained for **CSI** to the values reported by Hutzler et al. [63] for the onset of **SCR**. We compare tubes with (A)-1.1 cm diameter and (B)-15 cm length to (C)-the original data (1.5 cm diameter and length 12 cm). Our results are in accordance to the previous ones for larger bubbles (as both measure the onset of **SCR** at that range) but there is a departure of the points for smaller bubbles. The data from Hutzler et al. appears to level off at a value around $\phi_l = 0.2$, which is lower than the values obtained in Figs. 3-15 and 3-16.

roughly equal for both convective motions in the case of large bubble sizes. The critical liquid fraction goes to zero as $B_r \to \infty$ and levels off somewhat as $B_r \to 0$, with no clear limiting value, in general [2].

---

[2] N.B. In the next section, we proceed to describe measurements of the velocity of convective motions above threshold. Again, the reader may wish to set aside and consider the present attempts to understand the threshold itself in Section 3.5

3.4.7 Velocity of the bubbles in the convective rolls

Here we address the behaviour of the system above threshold, with a finite velocity of convective motion. Again we start our experiment at an initial flow rate at which both rolls are fully developed and then decrease the flow rate. Up to this point, the same procedure has been used to take measurements of the critical onset in last section (Figs. 3-15 and 3-16) but in order to obtain the velocity of the motion we use a camera to film the **CSI** convective roll.

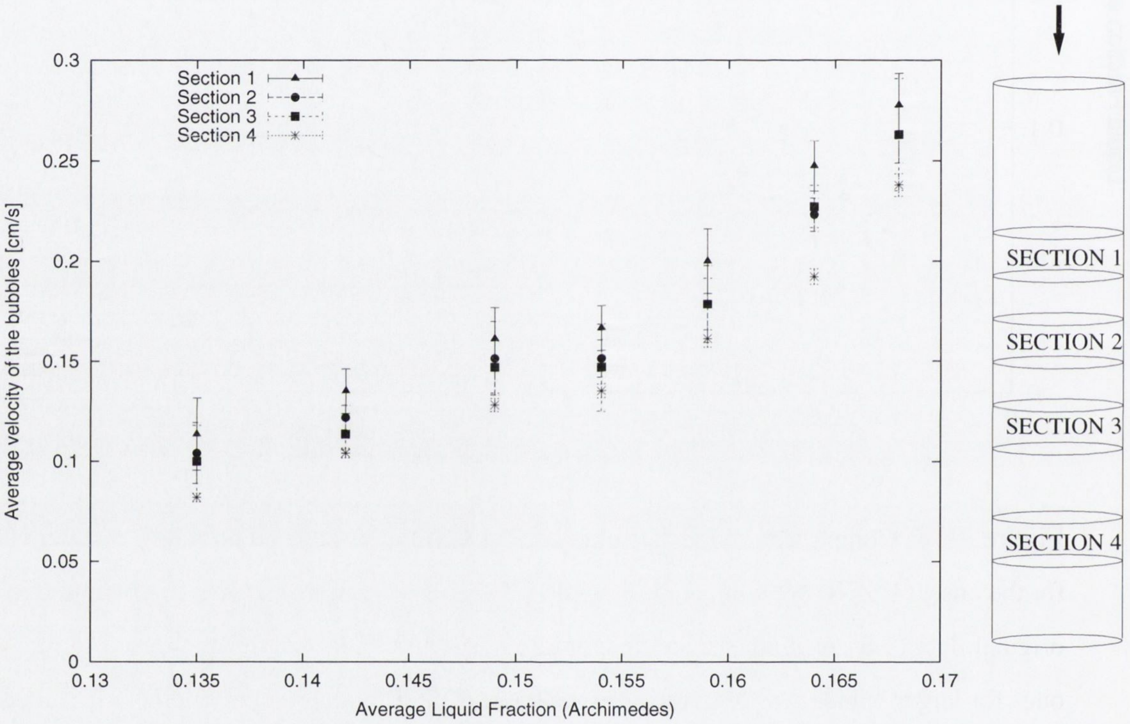

Figure 3-19: This diagram shows the average velocities of the **CSI** bubble motion for four sections of a relatively long tube, over a narrow range of liquid fractions above threshold. The tube has 2.0 cm diameter and 52 cm length and the bubble radius is 0.13 cm. Each of the sections covers 5 cm in the tube. Section 1 is at the top of the tube, close to the area where **SCR** ends. Sections 2 and 3 are at the middle part of the tube (as sketched in the graphic). Section 4 is at the bottom part of the tube. The values at the middle sections are similar (each data point is the average of seven measurements).

We will use the speed of the bubbles at the central part of the tube (see Fig. 3-19) to characterise the velocity of bubble motion associated with **CSI** convective rolls. Fig. 3-20 shows such data.

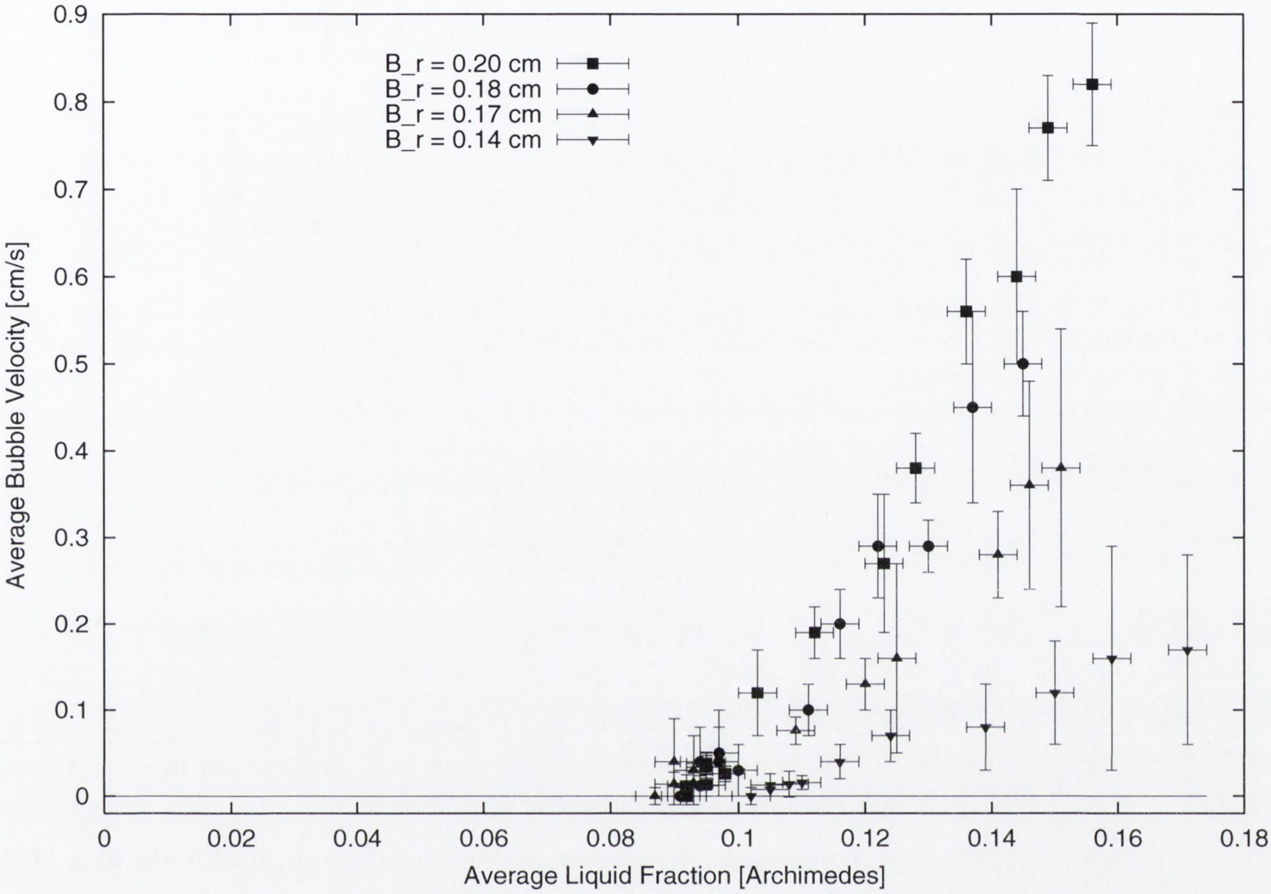

Figure 3-20: Velocity of the bubbles in **CSI**. We found there is linear dependence on the excess liquid fraction over its critical value. This dependence is found for several bubble radius B_r using a tube 2.0 cm diameter and 35 cm long.

In order to proceed in a systematic manner, we have chosen to fit the data in Fig. 3-20 using the function:

$$g(x) = \frac{c * (x - d)}{1 + \exp\left(\frac{d-x}{e}\right)}, \tag{3.4}$$

where c, d are free parameters and e is a constant lower than 0.0001 (to obtain the steep step expected). The function gives a velocity close to zero up to the point at which we reach the critical liquid fraction (parameter d) and a linear increase of velocity with the excess liquid fraction above this point. In this way we can identify the threshold in a well-defined way.

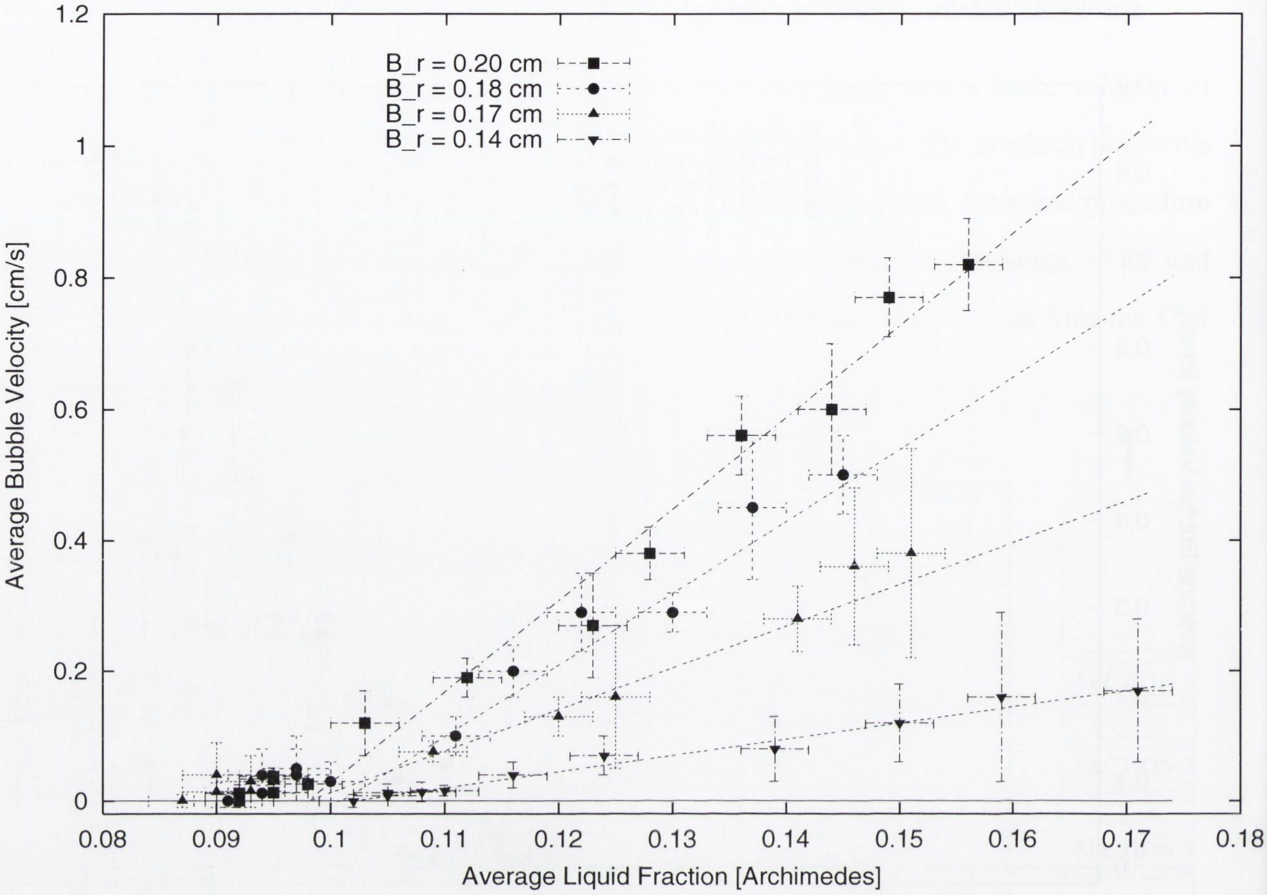

Figure 3-21: A blow up of Fig. 3-20 showing the detail of the lines fitted to the data. This graphs also allow to determine values for the critical liquid fraction at the onset of the motion in an alternative way to the values obtained in Figs. 3-15 and 3-16.

3.5 Interpretation of the results: towards a model

Convective motion has been observed in the draining foam since 1998 [63], and probably much earlier without being clearly identified and reported. It has grown in importance, as it has been repeatedly described by Durian and others, as an impediment to research aimed at understanding wet foams. It is frequently mentioned in the justification for microgravity experiments [15], since it excludes the uniform draining wet foam from study for large liquid fractions. In the microgravity environment, uniform wet foam of any liquid fraction may be made and analysed in equilibrium.

There is no satisfactory published theory. In this section we shall attempt to lay the foundations of one, based on ideas discussed in the Foams Group over several years and constrained by the facts presented by the data on this thesis.

Those facts are:

1. The critical value of liquid fraction for the onset of convective motion depends strongly on bubble diameter d, tending to zero for large bubble radius, B_r.
2. There is some tendency for the critical value to saturate as the bubble size decreases, but this is not as clear as in the previous data from Hutzler et al. [63].
3. There is substantial hysteresis, in that the uniform state can persist above the threshold, upon *increasing* flow rate.
4. The hysteresis region described in (3) as having uniform flow nevertheless shows a slow ”creeping” convective motion.
5. Velocity of convection is roughly linear in the excess liquid fraction, relative to its threshold value.

The ideas which we shall present here will address only points (1) and (2), and invite further elaboration to confront (3)-(5).

3.5.1 The ingredients of the theory

A theory successful in embracing the main facts presented seems a modest objective but it has proved difficult to attain. In a sense this is not surprising, because we have become accustomed to theories for dry foams (as presented in the book by Weaire and Hutzler [1]). They perform miraculously well for liquid fractions up to, say, ten percent. In the present case we confront a problem that has to do with wet foams. Perhaps unfamiliar factors operate, as trusted approximations (which are not always explicit) fail?

That is our understanding, that the conventional descriptions of drainage and rheology cannot simply be pasted together to obtain the required theory. They need to be reconsidered. This reconsideration may bring into play several ingredients of theory that have been disregarded until now. Three of these are *dilatancy*, *gas pressure variation* and *wall effects*.

- *Dilatancy.* This is the coupling between *expansion* and *shear*. It has been introduced into foam physics by Hutzler and Weaire [66]. We need to make a distinction here between *elastic* or *static* and *dynamic* dilatancy.

  Elastic dilatancy has been treated by Weaire and Hutzler in his paper [66]. The osmotic pressure defined in Chapter 1 at Eq. 1.3 is a function of the liquid fraction. But it has also a dependence, of second order, on the shear strain on the foam. Therefore, the dilatancy coefficient, χ can be defined as a function of liquid fraction ϕ_l:

  $$\chi(\phi_l) = \frac{\partial^2 \Pi(\phi_l)}{\partial \epsilon^2}. \tag{3.5}$$

  If a foam is partially sheared, the consequence of dilatancy is that the sheared part will increase its liquid fraction. Even if the foam remains in equilibrium, two liquid fractions can thus co-exist in the same foam. A useful measure of the dilatancy effect is the difference $\Delta\phi_l(\phi_l)$ between the liquid fractions of sheared and unsheared foam:

  $$\Delta\phi_l(\phi_l) = -\frac{1}{2}\frac{\partial \phi_l}{\partial \Pi}\chi(\phi_l)\epsilon^2. \tag{3.6}$$

  The magnitude of this effect has been calculated at a foam sheared beyond the yield strain [66]. Using a computer simulation program called PLAT [8, 67] in 2D, they observe differences in liquid fraction of 1.5%-2.0% between the sheared and unsheared foam when the liquid fraction of the unsheared foam is around 0.08. There is reason to think that this effect should be equally appreciable at a 3D foam and therefore, relevant to the onset of convective motions.

  In granular materials, dynamic dilatancy is more important than its static counterpart. The effect of both in foams is probably significant but we do not have a theory for dynamic dilatancy.

- *Gas pressure variation.* In the successful theory of drainage for dry foams this is completely disregarded. The conventional theory of foam drainage contains the approximation that there is no gas pressure variation (other than the local variation between small and large cells if the foam is polydisperse): we speak of average gas pressure. This is justified by noting that, in a dry foam, the pressure variation between cells is bounded (because the curvature, related to pressure difference by Laplace law (Eq. 1.1), cannot exceed the inverse radius of the cell) and is restricted to values small compared with the liquid pressure variation. It was always obvious that this was questionable for large liquid fractions.

Weaire et al. [68] have discussed the possibility of gas pressure variation in equilibrium dry foams recently, noting that an external force is required to balance them and giving some examples. A mathematical treatment of this gas pressure gradients has been also presented by Weaire et al. [69]. In the present case, if we assume a completely uniform drainage, that external force can be identified simply with the gravitational force on the liquid. Since liquid pressure cannot vary (with such assumptions) the external force of gravity must be balanced by a gradient of gas pressure, in the absence of shear stress. This argument indicates that the gradient may be of the order of $\phi_l\ g$.

- *Wall effects* It proves to be difficult to write even a tentative theory without some drag effects at the wall. Physically, this may be associated with the motion of Plateau borders along the wall. This has been discussed recently in other contexts [70], with a general acceptance of the Bretherton law [71] for the force, $F \propto v^{2/3}$. At first glance this appears to be the only boundary force, and it is opposed to the motion. We believe that something further is missing and the missing ingredient is the force associated to the surface drainage through the surface Plateau Borders [72].

  Whenever a system with internal structure is described by a continuum approach there is always a problem with the boundary conditions [73]. In this case, in addition, the surface is different from the bulk, with a greater liquid flow through its Plateau borders. Therefore, let us assume that this flow exerts a downwards force on the bulk and supplies a surface force in the continuum approximation.

  In summary, there is a *driving* force due to the flow at the surface and a *drag* force for $v \neq 0$

3.5.2 The driving force at the wall

No calculation has yet been performed to evaluate the force on the interior faces (see Fig. 3-22) of a surface Plateau border (the force exerted on the outer surface is irrelevant here).

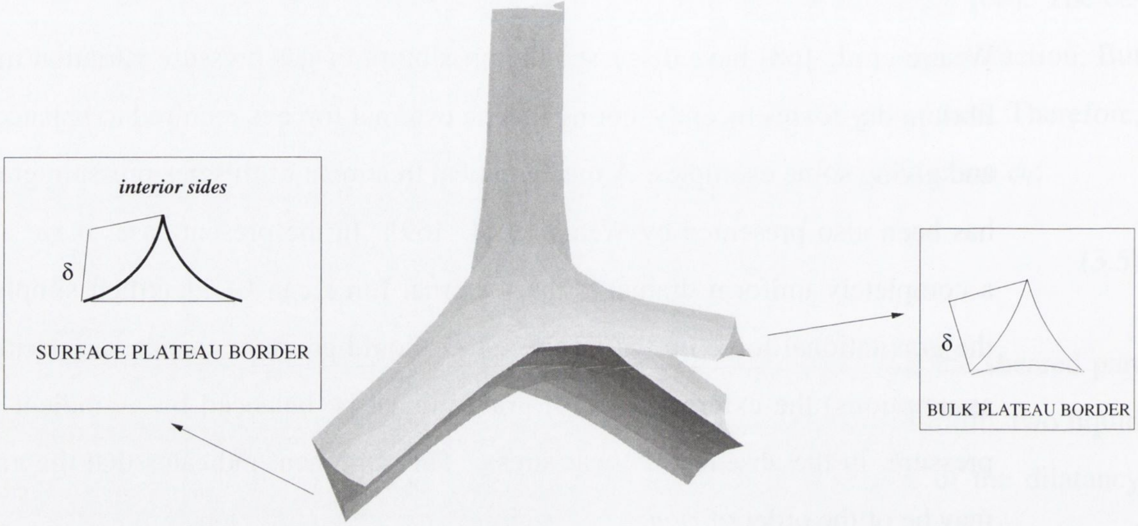

Figure 3-22: A four-fold vertex at the surface of the container, reproduced from [74].

However, one may estimate the required force (and stress) roughly for present purposes as a half of the total force on these faces (recall that we have chosen to work within the Poiseuille approximation for all sides). With this rough approximation one may proceed as follows to work out the total stress at the outer surface, due to Poiseuille flow at the Plateau borders.

For any shape of channel, the average velocity is related to the driving force for flow, according to:

$$u = C\,\frac{G\,A}{\mu}, \tag{3.7}$$

where G is the pressure gradient in the absence of gravity (with gravity we must replace this term with a contribution of both pressure gradient and gravitational body force and A is the cross-section of the channel. The constant C is dimensionless and depends on the *shape* of the Plateau border. Peters [75] and Bradley [76] have calculated the value of C for a Plateau border using different methods. Their results place this value around $1/50$ which can be used in both cases, surface and bulk Plateau borders.

Under steady flow, the drag force at the boundary, F per unit length, must balance the driving force. Therefore $F = G\ A$ and by simple geometry:

$$F_{P.B.bulk} = G(\sqrt{3} - \frac{\pi}{2})\delta^2; \tag{3.8}$$

$$F_{P.B.surface} = G(\frac{1}{2})(4 - \pi)\delta^2; \tag{3.9}$$

in terms of the Plateau border surface curvature δ, which is the same in bulk and surface Plateau borders within our approximation.

Then, we can also write the flow rate in a single Plateau border as $Q = A\ u$:

$$Q_{P.B.bulk} = \frac{C\ G}{\mu} \approx \frac{G}{50\ \mu}(\sqrt{3} - \frac{\pi}{2})\delta^4; \tag{3.10}$$

$$Q_{P.B.surface} = \frac{C\ G}{\mu} \approx \frac{G}{50\ \mu}(\frac{1}{2})(4 - \pi)\delta^4; \tag{3.11}$$

These equations should be sufficient to build the required theory in which the driving force for convective motion is provided by the force exerted by the Surface Plateau borders. Eq. 3.10 can be used to assemble a method of evaluating the total flow rate, Q, as a sum of surface and bulk contributions, but we shall not pursue this here.

3.5.3 The threshold condition

So long as our preoccupation is only with the threshold condition for onset of convective motion, we may proceed very simply as follows. The threshold is identified with the point at which the stress in the foam at the wall (Fig. 3-23) has increased a value *equal to the yield stress*, $S_{wall} = S_y$.

In what follows immediately, we shall implicitly neglect dilatancy and hence speak of a liquid fraction which is uniform in the bulk.

In Section 3.5.2 we have estimated the force at the surface Plateau borders (Eq. 3.8). We can write $G = \rho\ g$ for a vertical Plateau border, since there is considered to be no vertical liquid pressure gradient. Therefore, we can write the surface driving force exerted on the static foam as:

$$S = \frac{1}{2}\frac{1}{2}\rho\ g(\frac{1}{2})(4 - \pi)\delta^2 l_S, \tag{3.12}$$

where the l_S is the length per unit area in the surface (an analogous parameter l is used by Weaire and Hutzler [1] in the bulk). The $1/2$ factor in front of the estimate comes from

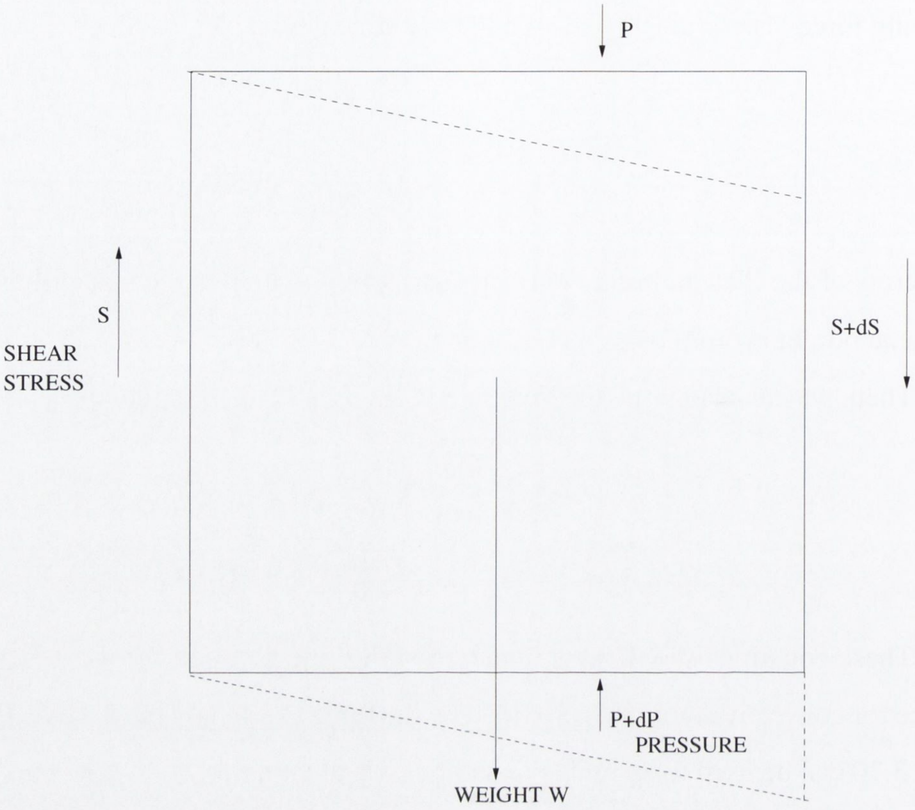

Figure 3-23: Schematic illustration of forces/stresses involved in the equilibrium of a small element of foam under steady drainage. Dashed lines indicate the direction of shear strain or strain rate, for positive S.

averaging the space orientation of the Plateau borders (this factor is $1/3$ in the bulk as seen in [1]) and the second $1/2$ comes from the estimation made on the last section that the stress required has to be roughly half of the total force on the faces.

Note also that for the bulk of the foam (Weaire and Hutzler [1] page 29):

$$\phi_l \approx \frac{1}{3}\frac{\delta^2}{(d/2)^2}, \tag{3.13}$$

and the surface length parameter can be crudely estimated using the bubble diameter as $l_S \approx 2/d$ ($d = 2B_r$ in relation to the previous notation). The stress may be rewritten as:

$$S = \frac{(4-\pi)}{8}\frac{3}{4}\rho g \phi_l d^2 \frac{2}{d} \approx 0.15 \rho g \phi_l d. \tag{3.14}$$

We want to equate this shear on the wall to the yield stress, which is given by:

$$S_y = S_y^0 \frac{(\phi_l^0 - \phi_l)^2}{(\phi_l^0)^2}, \tag{3.15}$$

where ϕ_l^0 is the value for the wet limit, that is, $\phi_l^0 \approx 0.36$ and $S_y^0 \approx \frac{\gamma}{d}$ is the value of yield stress on the dry limit [62, 37].

Equating S and S_y and using $l_0^2 = \frac{\gamma}{\rho g}$, the familiar definition of a length characteristic of capillarity [1]:

$$l_0{}^2 \frac{(0.36 - \phi_l)^2}{0.36^2} \approx 0.15\phi_l d^2. \tag{3.16}$$

Eq. 3.16 is an estimation of the threshold liquid fraction ϕ_l^c. For large bubbles it gives approximately:

$$\phi_l \approx \frac{l_0{}^2}{d^2}, \tag{3.17}$$

which goes to zero as bubble diameter goes to infinity in accord with the data. But this is quadratic rather than linear in d^{-1} (as shown in Fig. 3-25).

In the opposite limit (d tends to zero), $\phi_l^c \rightarrow 0.36$, which is the value of liquid fraction on the wet limit. There is no upper bound to ϕ_l^c. Figure 3-24 shows the form of the dependence of Eq. 3.16, to be compared with experimental data from Fig. 3-18. The critical liquid fraction, $\phi_l^c(d^{-1})$, shows a downward curvature in accord with the data

At first sight these results look promising, in terms of their qualitative form, but they imply values of critical liquid fraction which are at least one order of magnitude high. The surface driving force is not, on its own, sufficiently large to explain the experiments quantitatively.

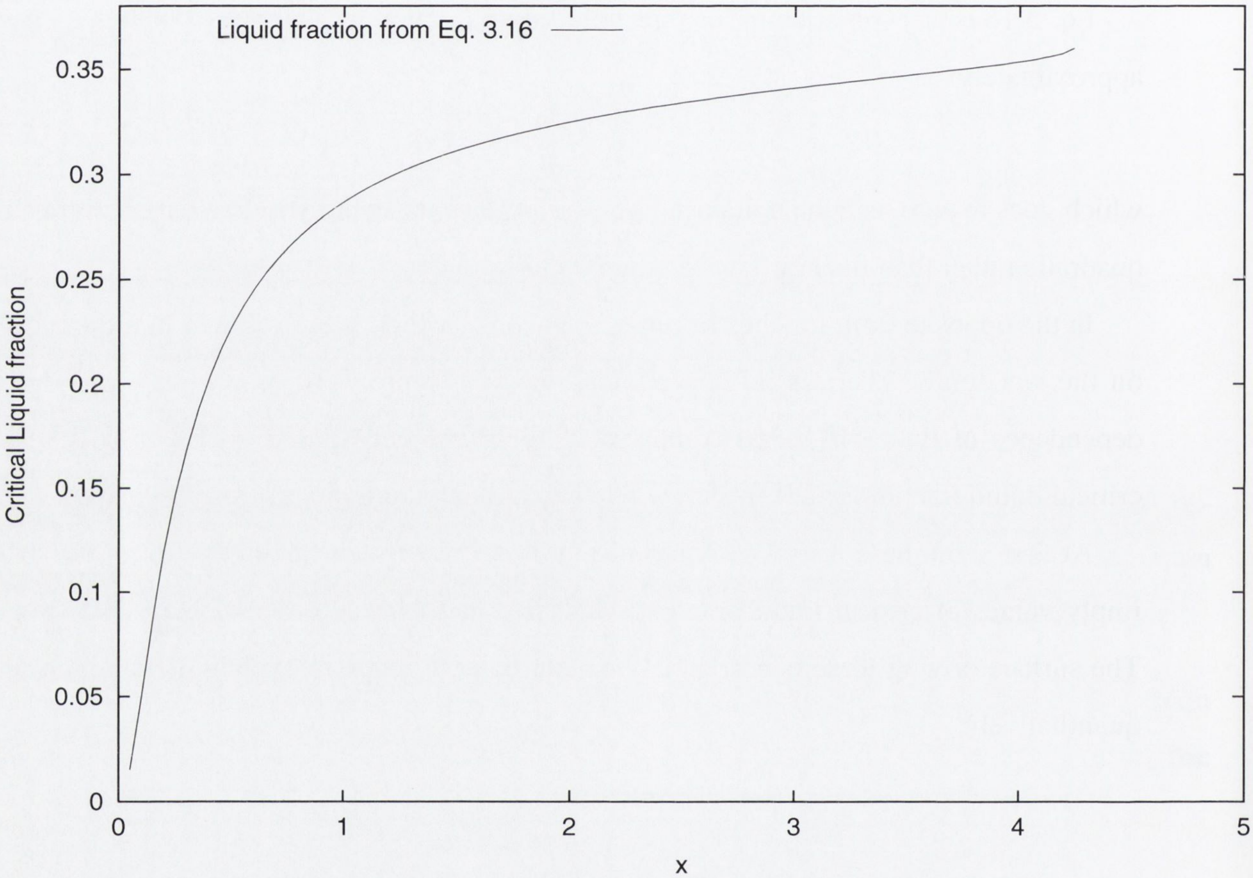

Figure 3-24: Estimated values of the threshold for the convective motion from the "surface-driven" theory. We plot $\phi_l^c(x)$ with $x = \frac{l_0}{d}$. The theory gives a critical liquid fraction, ϕ_l^c, much higher than the experimental values shown in Fig. 3-18, but with a very similar overall shape.

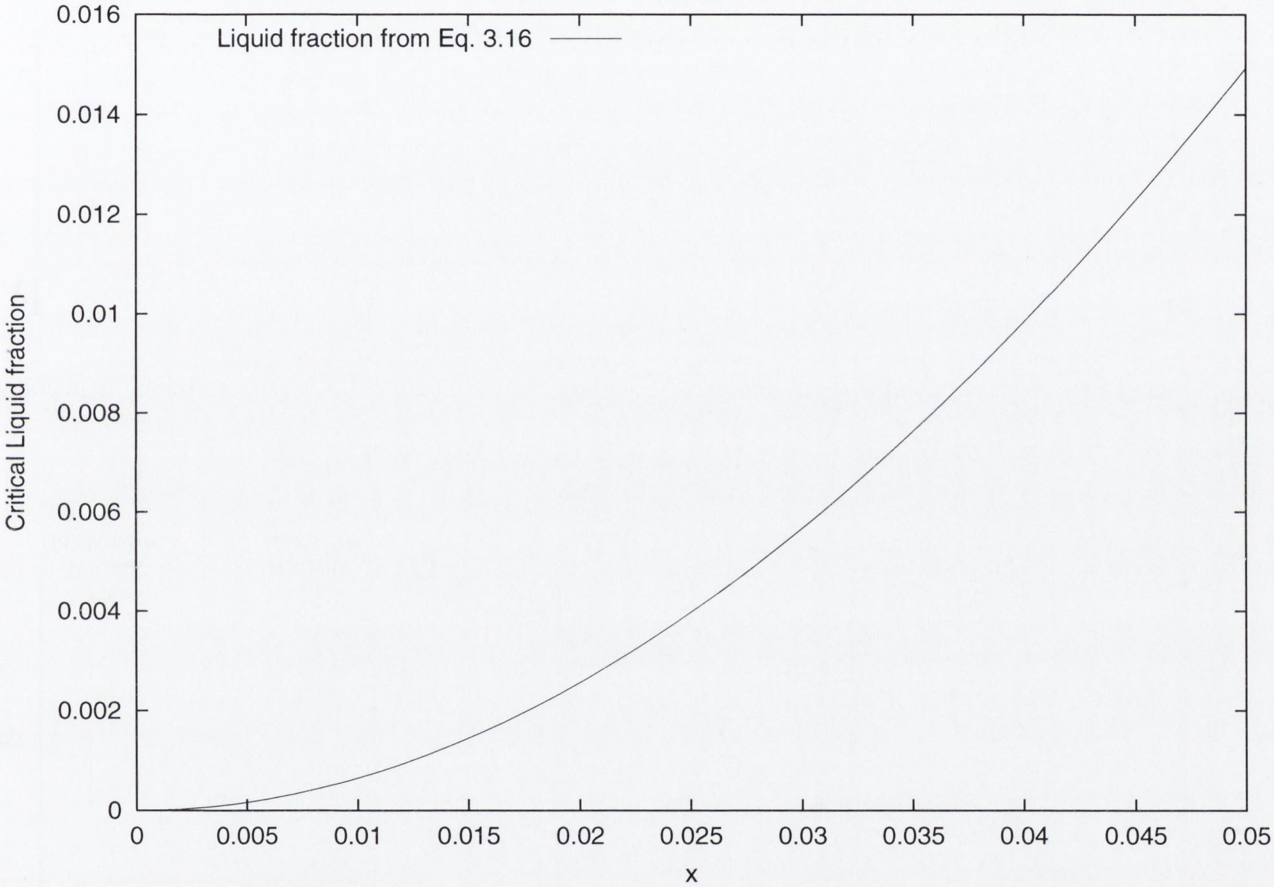

Figure 3-25: A blow up from Fig. 3-24 showing the quadratic dependence when $d \to \infty$ (Eq. 3.17).

3.5.4 Towards a more complete theory

Here we address the details of the radial dependence of S and ϕ_l (Figs. 3-26 and 3-27). We consider the various forces acting on it, which must balance (see Fig. 3-23). The resulting differential equation, proposed by Weaire [72] will be solved numerically and analytically.

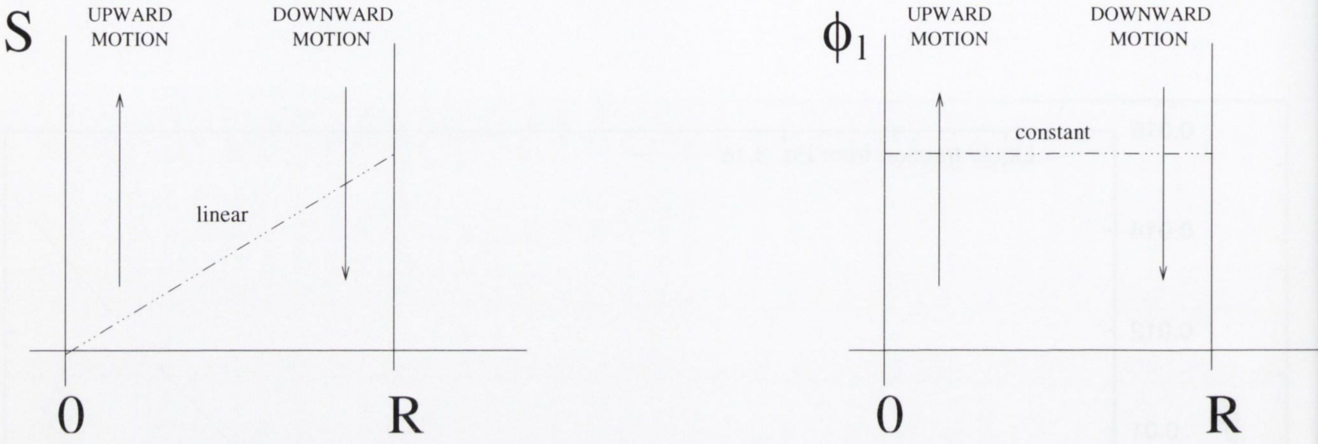
S
UPWARD MOTION
DOWNWARD MOTION
linear
0
R
ϕ_1
UPWARD MOTION
DOWNWARD MOTION
constant
0
R

Figure 3-26: The radial dependences of S and ϕ_l^c as from Section 3.5.3, without taking in account the elastic dilatancy.

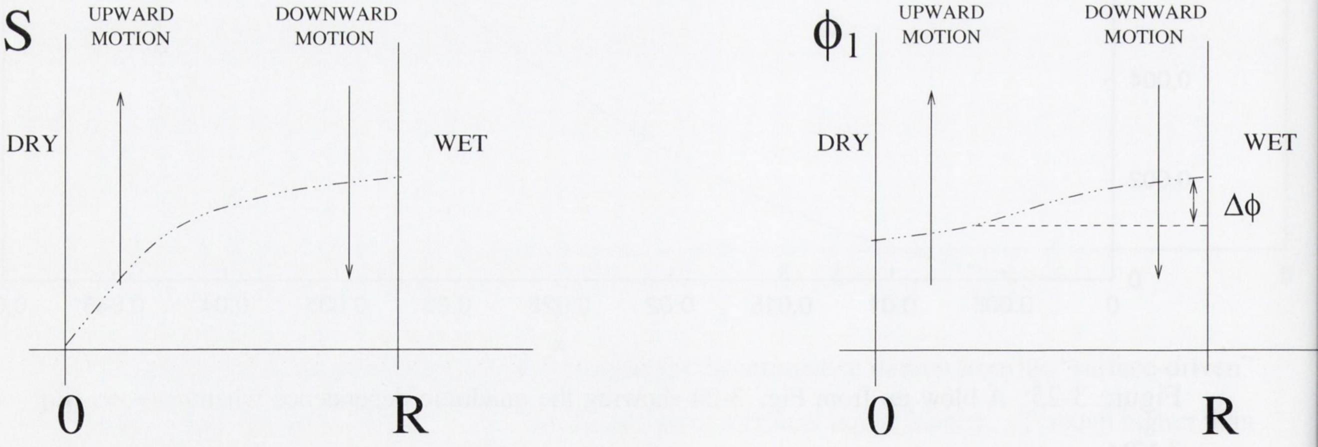
S
UPWARD MOTION
DOWNWARD MOTION
DRY
WET
0
R
ϕ_1
UPWARD MOTION
DOWNWARD MOTION
DRY
WET
$\Delta\phi$
0
R

Figure 3-27: The solutions sketched in Fig. 3-26 change when we introduce the effect of elastic dilatancy in our considerations. Recall that dilantacy predicts $\Delta\phi_l \propto S^2$

The arguments of the previous sections establish a critical value of ϕ_l (Fig. 3-26). This may be viewed more generally as applying only at the surface. That is, we can introduce static dilatancy and still equate S and S_y as a boundary condition. The full theory will in principle give the detailed variation of stress and liquid fraction with r.

With dilatancy (Fig. 3-27, the scheme of solution is a bit more complicated: we can solve the differential equation as before, with two adjustable parameters, ϕ_l^0 the liquid fraction at $r = 0$ and the pressure gradient P'. We have two required boundary conditions at $r = R$ (see Fig. 3-28) which can be used (by an iterative process) to fix the parameters:

1. $S(R) = S_y(\phi_l(R))$, yield stress.
2. $S(R) \propto \phi_l d$, driving force at the wall.

Our experiments suggest that the end effects at the top and the bottom of the tube are not large (as seen in Fig. 3-19) and so we may hope that the convective motion can be analysed without their inclusion. That is, we propose to consider only a thin horizontal slice of the system (Fig. 3-28), and assume that it is similar everywhere (this is not quite correct but it may serve as a first approximation). We seek solutions for the equations of drainage and rheology for this slice. We can therefore ignore the azimuthal variable and deal only with the radius r to describe position (see Fig. 3-28).

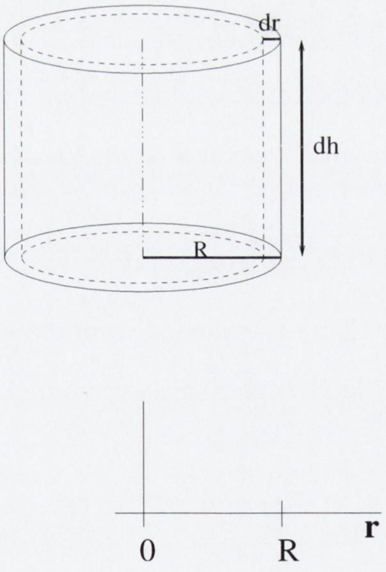

Figure 3-28: A slice of the tube is represented by a cylindrical shell of thickness dr and height dh. Position is represented by the radial coordinate r. Liquid fraction and other variables are functions of r.

We proceed to identify the forces on the element, taking positive forces upwards (therefore, gravity will go on the negative direction).

1. Gravity contribution:

$$F_g = -\phi_l(r)\rho g 2\pi r dr dh, \tag{3.18}$$

   where the liquid fraction, $\phi_l(r)$, is a function of r, ρ is the density of the foam and g is the gravity constant.

2. Force due to pressure gradient:

$$F_P = P' \, 2\pi r dr dh, \tag{3.19}$$

   where $P' = -\partial P/\partial z$ is the upwards pressure gradient.

3. Shear stress:

$$F_S = -\frac{d}{dr}(rS(r)) \, 2\pi dr dh, \tag{3.20}$$

   where $S(r)$ is the shear stress, a function also of r. We assume this force to be in the same direction of gravity

If we assume that the osmotic pressure is constant along the radius, then the variation of ϕ_l with r is tied to shear and shear rate, via elastic and dynamic dilatancy. For the moment, let us confine ourselves to the steady state equation for the onset of convective motion, so that we set aside the dynamic aspect and write, so long as the foam is static:

$$\phi_l = \phi_l^0 + aS^2, \tag{3.21}$$

where a is a constant that can be evaluated from the work of Weaire and Hutzler [66]. ϕ_l^0 is the liquid fraction at $r = 0$ where $S = 0$ by symmetry. In this way we arrive to the force balance equation:

$$\frac{d}{dr}(rS(r)) = r[P' - (\phi_l^0 + aS^2(r)\rho g], \tag{3.22}$$

where P',ϕ_l^0,a and ρg are constants.

This is a differential equation which gives us two solutions as expected. By setting $S = 0$ we have a uniform solution with the pressure gradient being the value required to support the mass of the foam. We have solved Eq. 3.22 using Maple [3] and obtained the following solution in terms of Bessel functions:

---

[3] A standard math software package.

$$S(r) = -\frac{\sqrt{\rho g a(-P' + \rho g \phi_l^0)} Bessel_J(1, \sqrt{\rho g a(-P' + \rho g \phi_l^0)} r)}{\rho g a Bessel_J(0, \sqrt{\rho g a(-P' + \rho g \phi_l^0)} r)} \tag{3.23}$$

Eq. 3.23 presents solution of the type sketched in Fig. 3-27, as shown in Fig. 3-29.

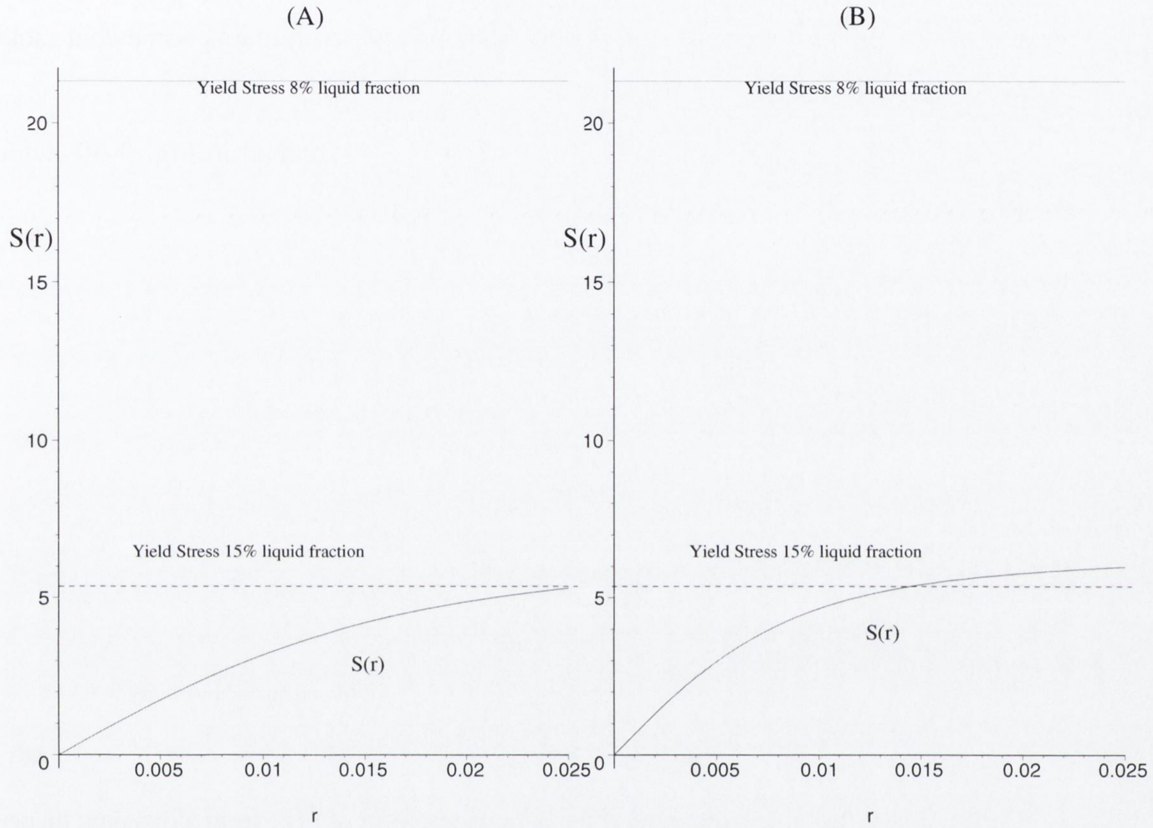

Figure 3-29: Examples of solutions of Eq. 3.23 for (A)-$\phi_l^0 \approx 0.08$; (B)-$\phi_l^0 \approx 0.15$. We approach $\rho = \rho_w \phi_l^0$. The values of the constants are estimated using [37, 68, 66, 53]

3.5.5 Discussion

Although we have exhibited some solutions of the differential equation for $S(r)$ (and $\phi_l(r)$), we have not pursued this work to its final conclusion, which would be a rather elaborate calculation. Let us sketch a possible *modus operandi*.

The condition $S = 0$ is the boundary condition at $r = 0$ in all cases. As above, the equation may be integrated with an assumed value of P' and the liquid fraction at $r = 0$. These may be considered free parameters, to be eventually adjusted by some iterative process to establish an acceptable solution. The conditions which will determine this parameters have already been stated in Section 3.5.4. It seems intuitively clear that static dilatancy favours instability, moving the threshold value of flow rate to a significant lower value, but this remains to be confirmed. Perhaps will be better to concentrate on the consequences for $\phi_l(r)$ which should eventually be measurable. Indeed this might present one of the best measures of elastic dilatancy, which remains somewhat lacking in experimental confirmation.

A full theory will also make predictions for $v(r)$, as sketched in Fig. 3-30 (which are far from obvious).

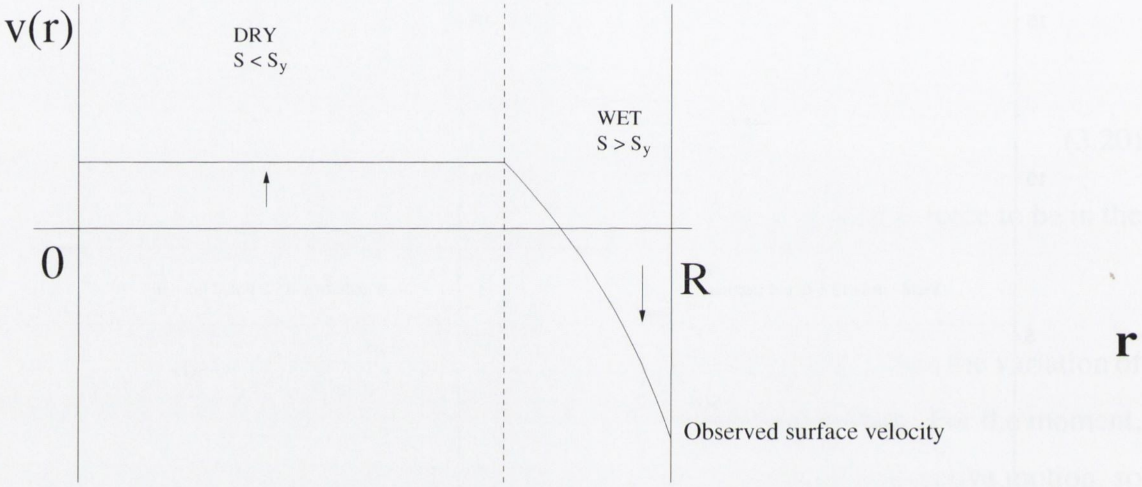

Figure 3-30: Schematic diagram of the anticipated form of $v(r)$ from a dynamic theory.

To make detailed predictions of $v(r)$, particularly $v(R)$, will require a calculation of a different type of solution, in which the same general form of differential equation as that above is used to determine $S(r)$. The additional features in its formulation and interpretation will be:

1. Introduction of the Bretherton drag force [71] opposing the motion at the surface, hence a different boundary condition, determining v at the surface.

2. Introduction of dynamic dilatancy, of which little is known yet.

3. Identification of a region of continuous deformation (finite shear rate $\dot{\epsilon}$), where S exceeds the yield stress.

4. Calculation of $\dot{\epsilon}(r)$ by integration from the Herschel-Bulkley or Bingham model (as suggested from Stokes experiment in Chapter 2).

5. Imposition of mass conservation: the final $v(r)$ must satisfy $\int_0^R drr\phi(r) = 0$.

In broad terms, the calculation seems tractable, but it is not practical at the present time in terms of the programming involved and some uncertainties in the ingredients to be added.

3.6 Summary

Two patterns of convective convective motions, Simple Convective Roll **SCR** and Convective Symmetric Instability or **CSI** are found in cylinders subjected to forced drainage, as shown in Fig. 3-4. These convective motions present a finite onset in liquid fraction (Section 3.4.6) related to bubble size. We conclude a inverse linear relationship with bubble radius for large bubble sizes.

We are still far from a complete dynamical theory of the effect. Nevertheless we have built up a reasonably coherent theoretical scenario, with the following features, which should be amenable to test, in due course:

- The cylindrically convective roll consists of a shearing wet outer shell with shear rate, hence velocity, increasing close to the wall

- The interior undergoes plug flow.

- There is an small ($\approx 1\%$) difference in liquid fraction (at threshold) between these two regions, due to dilatancy.

- Theoretic critical values of ϕ_l^0 (hence Q) are in very rough agreement with existing experiments, except that $\phi_l^c \sim \frac{1}{d^2}$ at large values of d. Comparison with experiments in this region is complicated by the fact that as d increases the bubble size becomes comparable to the tube diameter, so the experiments may not be reliable on this point in relation to the present crude theory.

- ϕ_l^c tends to zero for large d and to the wet foam limit ϕ_l^0 when d tends to zero. This behaviour appears clear and consistent with the experiments and suggest that earlier references of a lower limit are probably erroneous.

Further experiments that give new information to test the above assertions would be valuable. For example, a non-destructive method that might permit to obtain local values of liquid fraction with precision, even in the bulk of the foam, would be desirable. This seems attainable with MRI or x-ray tomography in the near future. If this is done (and it is under consideration) it will incidentally be an excellent test of foam dilatancy, which is as yet a theoretical prediction with little validation.

More modestly, we have tried to determine external local liquid fractions using the width of the wall Plateau borders as a reference, but the error in the measurements is quite big and we are not able to conclude much from our data. We include our measurements (Appendix A), hoping that future improvements on the technique might indeed allow one to obtain more conclusive results.

One exciting possibility is the performance of experiments in microgravity, or reduced gravity, which is under active consideration. In the elementary theory for onset, gravity enters only through l_0, so its predictions are clear. For a given surfactant system critical liquid fractions should scale as $\phi_l^c = f(\frac{1}{d\ g^{1/2}})$. The conclusion although drawn for from the above theory, may have a much more general validity in terms of scale arguments.

To pursue such questions experimentally an alternative is to pursue experiments on emulsion systems, for which the effective gravity is reduced due to the small density difference of the components. In this case, some preliminary experiments have already been performed [77] but more systematic work needs to be done.

Chapter 4

Convective instabilities in 2D

4.1 Motivation

Given our inability to look inside the specimens of the 3D convective experiments (Chapter 3), the possibility of a 2D analogy presents itself. This is a familiar strategy in the physics of foam and has often proved fruitful.

In this chapter we present the first results for convective motion in 2D forced drainage. This requires further analysis, on which developing understanding of 2D foam dynamics [78] can be brought to bear. Experimental work in flow of two-dimensional foam due to shear has been recently carried out by Debregeas et al. [79] and Lauridsen et al. [80].

Is it possible to have a convective motion on 2D? That question was posed during one of the meetings covered to discuss the 3D motion. The answer is yes. It is possible to reproduce the patterns found in the 3D corresponding experiments, and observation of the internal bubbles is easier in this kind of setup. However, we have to be cautious before we compare the results between 2D and 3D experiments, as the geometries are quite different, with large surface effects intervining in 2D [70]. The study of the motion in 2D geometries (Hele-Shaw cells) is introduced and some empirical observations are described.

We also expect to find an easier way to measure liquid fraction locally in two-dimensional foam. All these reasons will allow a much better picture of the phenomena occurring in the foam undergoing forced drainage.

4.2 Experimental set-up

We use a Hele-Shaw cell filled up with foam. Our system (Fig. 4-1) is quasi two-dimensional, as the separation between the plates is small compared to the bubble size. We also find a way of minimising the effect of the off-centring input of liquid and spread more evenly the surfactant solution.

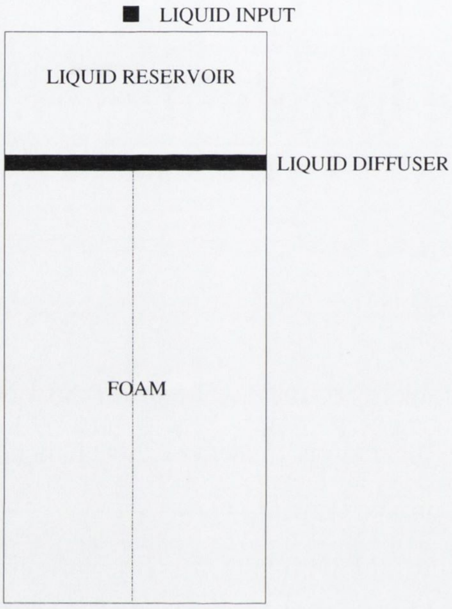

Figure 4-1: An sketch of the 2D experimental setup. The separation between the plates is around 0.5 mm. The reservoir is refilled constantly with surfactant solution and spread evenly with the help of a piece of porous material. The foam undergoes convective motions similar to the ones described on the 3D case. The symmetry axis in the convections is marked by the dot-dashed line.

Monodisperse foam (see Appendix D), is introduced between parallel glass plates with a separation of half a millimetre (very small compared with the length and width of the foam, which are 200 mm and 50 mm respectively). Then, the foam containers is partially introduced into a pool of surfactant solution, so the foam has contact with air at the top and with liquid at the bottom, as shown in Fig. 4-1. We can pour surfactant solution on top of the foam at different flow rates using a Watson-Marlow © 505 S peristaltic pump.

We observe the bubbles using a Sony © DCR TRV 30E video camera to get a continuous film. The taped film is digitalised using Ulead Video Studio © 5.0 DV, a frame grabber that allows digital capture at a speed of 25 frames per second.

4.2.1 Results

We have been able to reproduce the patterns of convective motion found in a cylindrical tube using this bi-dimensional system (see Fig. 4-2). However, we do not find coexistence of the two patterns as it happened in the 3D experiments. **CSI** (Convective Symmetric Instability, see Section 3.4.1) is the dominant bubble motion and appears on its own at all times (see video `2D.mpg`). We were only able to reproduce the **SCR** (Simple Convective Roll instability, as shown in Section 3.4.1) by chance, due to an accidental asymmetry (a hole pierced in the material used as a sponge) in our liquid diffusion system. The symmetry axis in these experiments is parallel to the plates and equidistant on the two walls, as sketched in Fig. 4-1.

As the 2D setup allows us to watch the interior of the foam, there are some particular aspects of the 2D motion that were not observable in the 3D experiment. One of such particularities a pulsing (see video `pulse2D.mpg`), in which there is a brief passage of a relatively large amount of liquid through the channels of the foam, Fig 4-3, as if a liquid channel opens suddenly. The rows of bubbles open to allow this amount of liquid to make its way to the bottom and then return to their initial positions after the liquid has made its way. This occurs seldom and at relatively high liquid fractions.

The second observation, in Fig. 4-4, is that the last layer of bubbles (the ones closer to the sides of the Hele-Shaw cell) adopt a distorted shape at high flow rates or liquid fractions. In the 2D case, we can appreciate that the content of liquid at the sides is much higher than it is in the interior of the foam. A layer of fluid forms close to the walls of the Hele-Shaw cell at high liquid fractions.

We consider that the 2D system presents an interesting future opportunity because it allows us to observe clearly the motion of all the bubbles in the system. It offers a beautiful demonstration of the qualitative effect, but one must be careful in making any detailed comparison with 3D, as the physics is quite different in some respects (drag forces on the glass plates).

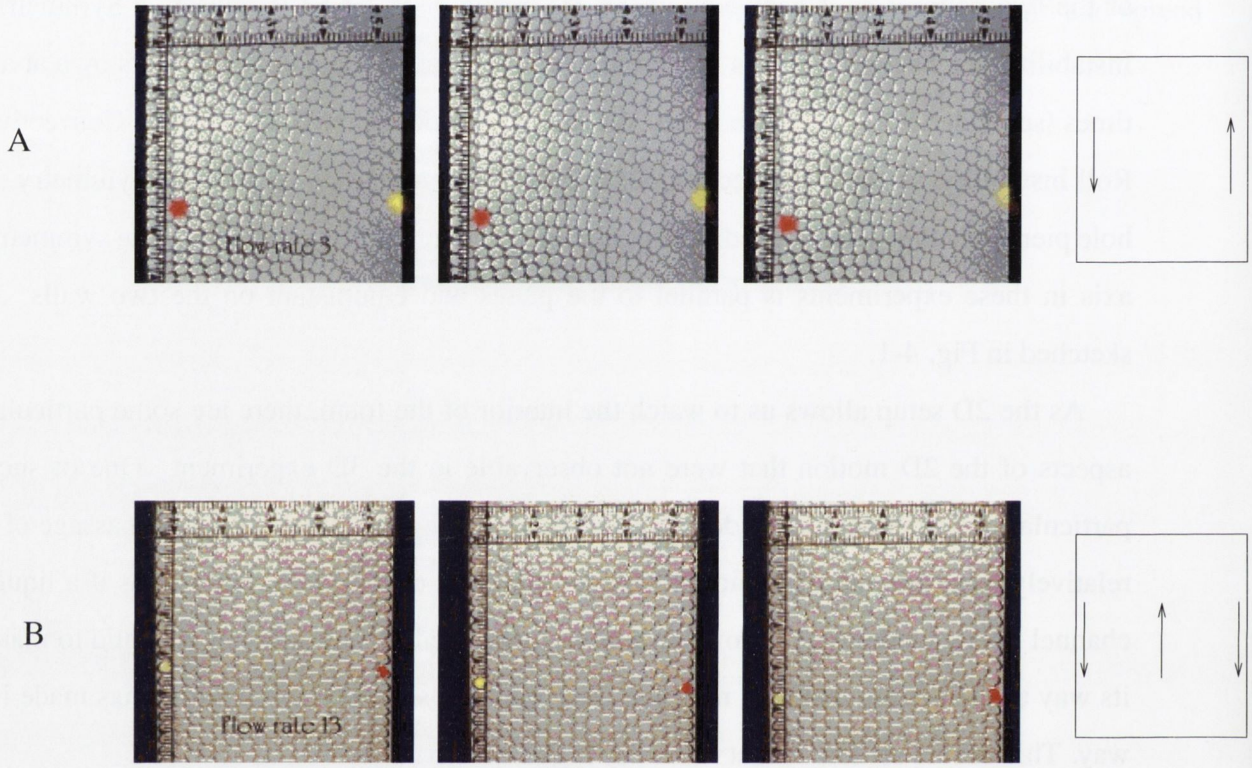

Figure 4-2: The patterns found for the 3D convective motions can be reproduced in the 2D experiment. There are some differences between the 2D and the 3D case. A - **CSI**, in which bubbles move downwards at the wall and upwards in the rest of the foam appears in all the experiments with homogeneous wetting conditions. B - However, to reproduce the **SCR**, in which bubbles on one side move downwards and the ones at the opposite side move upwards, we need to force an inhomogeneous input. We do not find coexistence of the different convective patterns in the 2D setup.

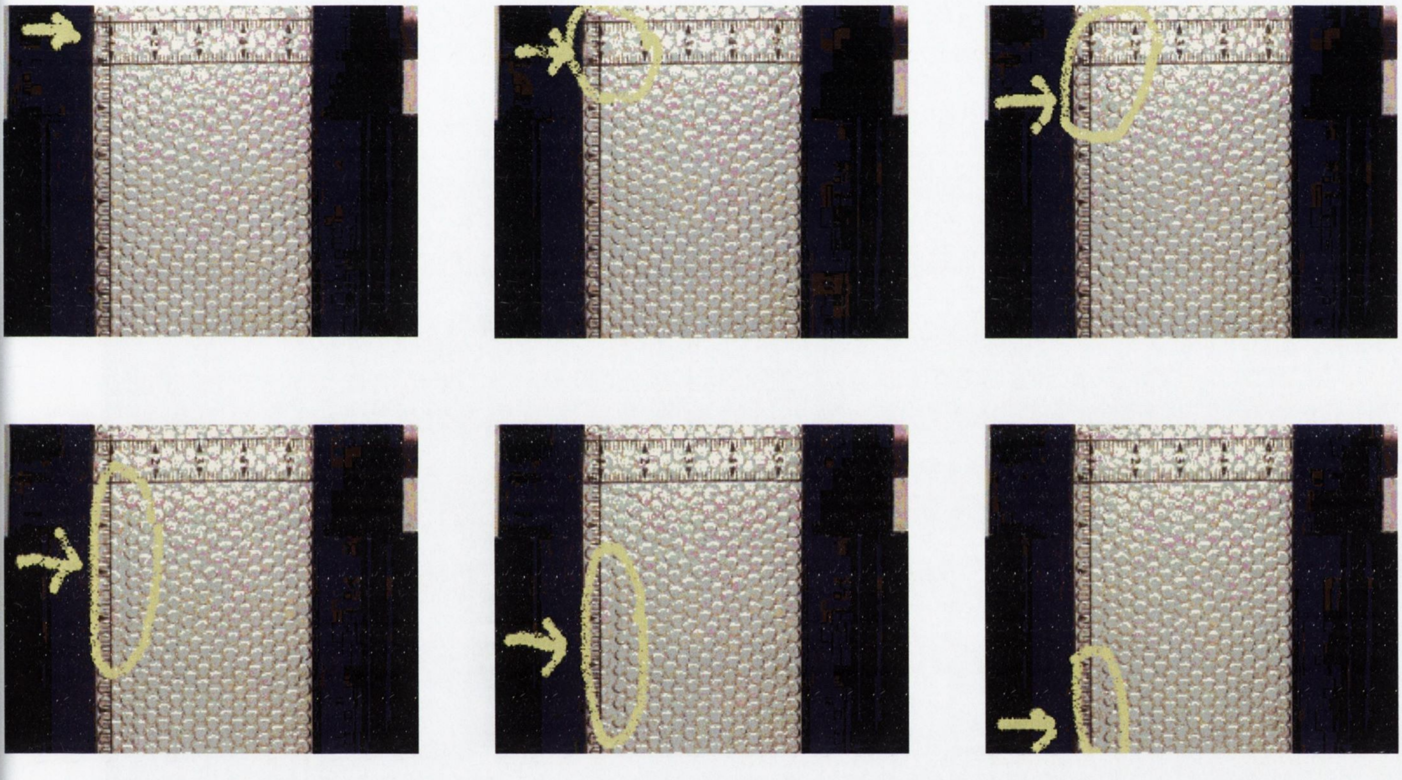

Figure 4-3: A liquid channel a 2D foam. The snapshots are separated by 0.02 seconds. Two adjacent columns of bubbles separate to allow a great amount of water passing through. After the water has drained through the bubbles, the foam returns to its original equilibrium state. This occurs very seldom.

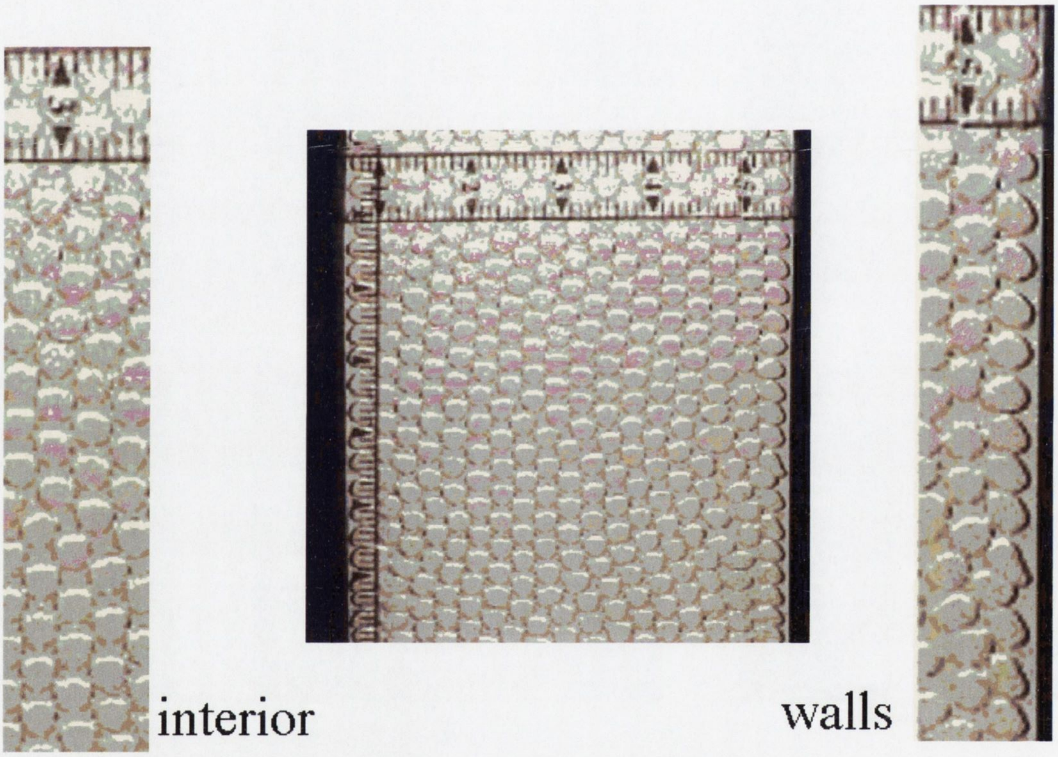

Figure 4-4: There is a clear layer of fluid in contact with the wall at high liquid fractions. The bubbles are deformed in a quite particular way that reminds us of an 'S'.

Chapter 5

Convective motion in a tilted tube

5.1 Motivation

There is another experimental variation of the convective motion [81] that we have explored, which results more amenable to theory than much of the above. Its successful analysis, using some of the same ideas that we have presented already, must offer some confidence in future progress. In this series of experiments in drainage driven instabilities,we use cylinders tilted at an angle from the vertical (see Fig. 5-1). When subjected to forced drainage, the bubbles in these tubes present a pattern of motion very similar to the Simple Convective Roll or **SCR** in the vertical tube.

In Fig. 5-1, consider the line that marks the axis of the tube. As we tilt the tube, the bubbles below this axis become wetter and the ones above the axis become dryer. This will impose a shear stress which must exceed the yield stress, dependent on the liquid fraction ϕ_l. The wetter part eventually undergoes shear and a convective motion is produced, much as the vertically aligned case. In the present case the essential driving force is very evident (see Fig. 5-2). It is possible to adapt the homogeneous drainage equation to include this case and interpret the onset of the motion in terms of yield stress.

The behaviour of the foam in the tilted tube is analogous to the Boycott effect [82], which describes how the sedimentation of particles suspended in a fluid is five to ten times faster in a tilted tube than in a vertical one. The explanation of this phenomenon [83] is that in the vertical tube, the particles have to move against the static fluid. When the tube

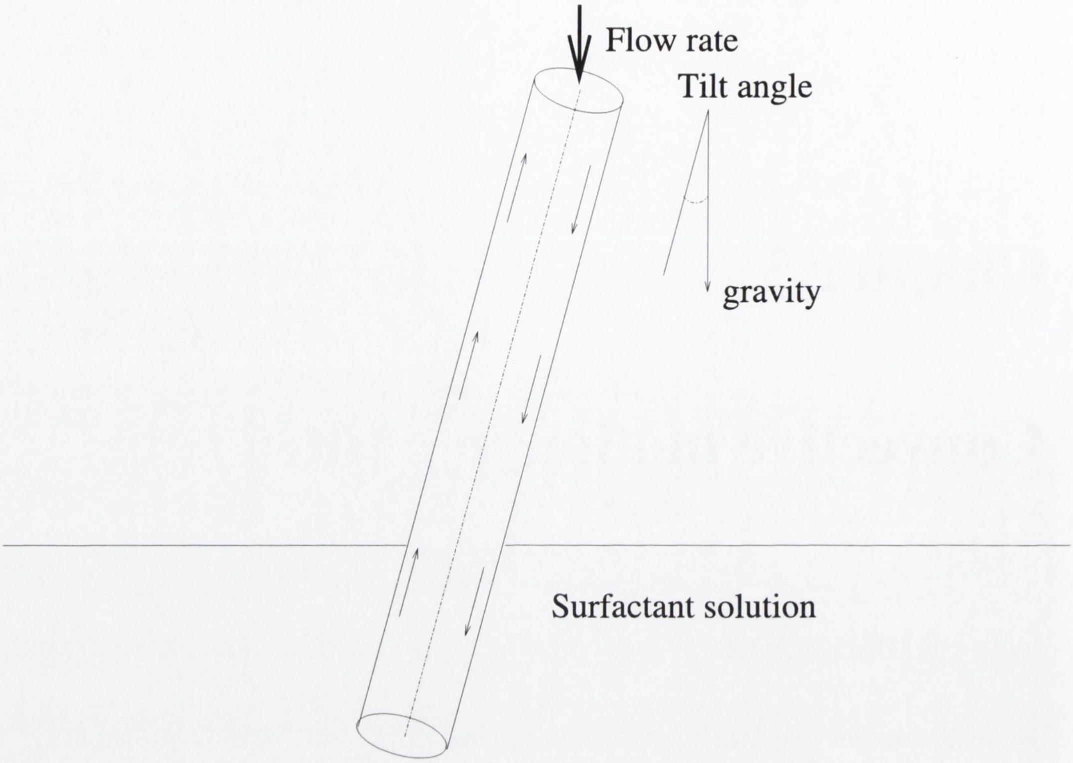

Figure 5-1: A sketch of the convective roll in a tilted tube. The dashed central line is a reference showing the central axis of the tube. The black arrows show the sense of the motion of the bubbles. Fluid draining on the foam moves preferably in the vertical direction, due to the gravity force attraction.

is tilted, the concentration of particles below the axis of the tube grows and the fluid rises above the axis. The convection produced helps to the particles to sediment faster. An analogous situation has been found in granular materials falling out of a tube [84]. Duran and Mazozi have used the complementary angle to the one we are using in our work (they measure the inclination from the horizontal). The flow of grains out of the tube is faster at angles between 30^o and 45^o degrees from the vertical.

5.2 Materials and methods

We introduce monodisperse foam produced as detailed in Appendix D into glass tubes of different lengths and diameters. The tubes are partially introduced into a pool of surfactant solution, so the foam has contact with air at the top and with liquid at the bottom. We make sure that the tubes are perfectly vertical and establish forced drainage by adding surfactant

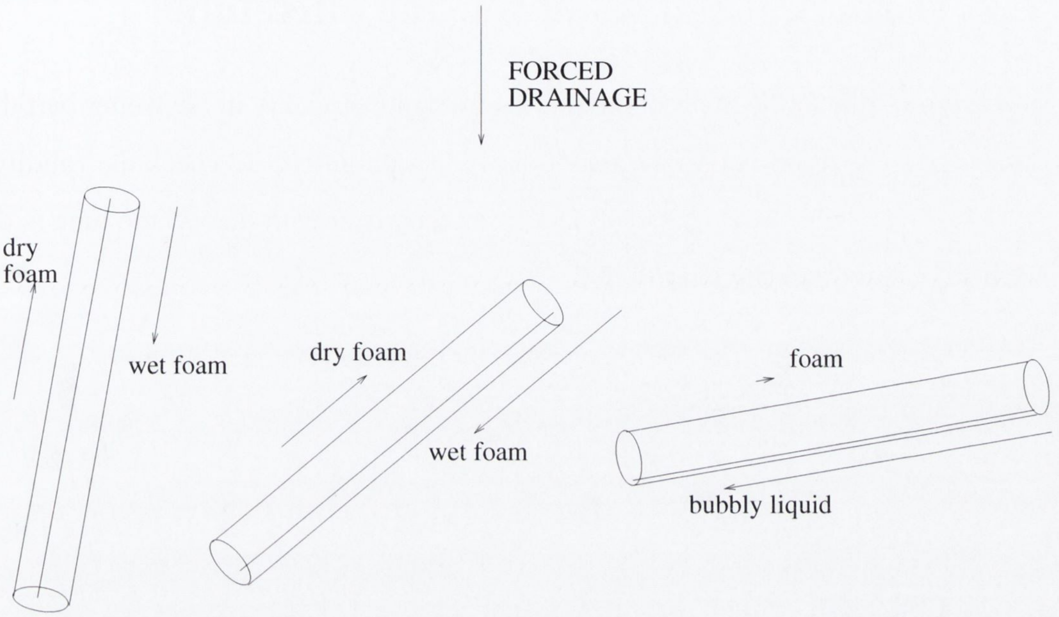

Figure 5-2: As the angle is tilted in the tube, the water is driven to the wall. The width of the wet region reduces. It may be possible that eventually, an angle would be reached at which the dry foam will float on a thin layer of bubbly liquid. In practice, it is impossible to do the experiment at angles close to the horizontal orientation.

solution at the top of the tube using a Watson-Marlow © 505S peristaltic pump which allows increments of $0.03\ ml/s$ in flow rate. Then we tilt the tubes to specified angles (see Fig. 5-1).

In these experiments, the bubbles are visually observed and the velocity of the bubbles is timed with a stopwatch. We have also filmed the convective rolls using a Nikon © Coolpix 990 camera. This photo-camera can record short films (up to 40 seconds) at a speed of 30 frames per second.

The velocity of the surface bubbles can be measured as a function of the angle of tilt and physical parameters of the motion can be obtained and compared to theoretical results. A short film of the evolution of the motion when we increase the tilt angle is in the CD that comes with the thesis (video `tilted.mpg`).

5.3 Experimental results for the tilted tube

It is appreciable to the eye that the foam moves more quickly in the wetter part than in the drier part. The drier part seems also to move in a plug flow. To check the validity of these observations and provide detailed data for comparison with theory, the tube is divided in five sections as indicated in Fig. 5-3.

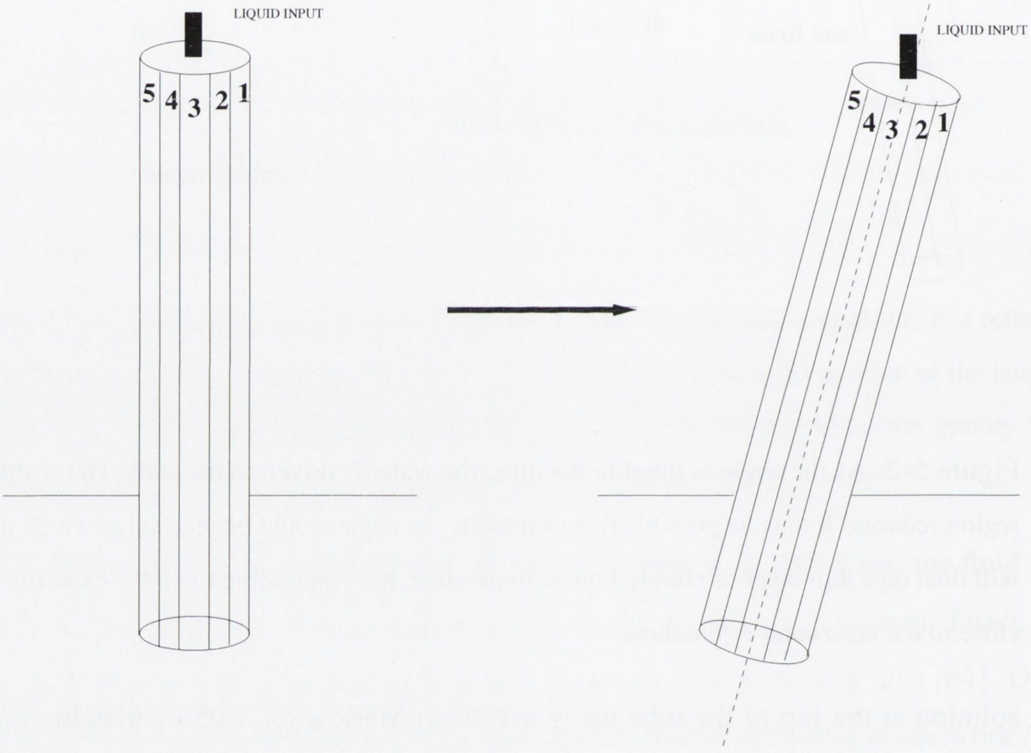

Figure 5-3: Division of the sections in the tube. As we tilt the tube to the right, sections 1 and 2 will fall below the axis (wet foam) and sections 4 and 5 above it (dry foam).

We measure the velocity of surface bubbles for different tilt angles. A positive velocity here means that the bubbles move on average upwards and a negative velocity means that they move downwards. The results are shown in Fig 5-4.

Bubbles in position 1 and 2 move clearly downwards and bubbles in positions 4 and 5 move clearly upwards. The bubbles at position number 3 change their behaviour when the tube is tilted away from the vertical. Thus, when the tilt angle is low, roughly half of

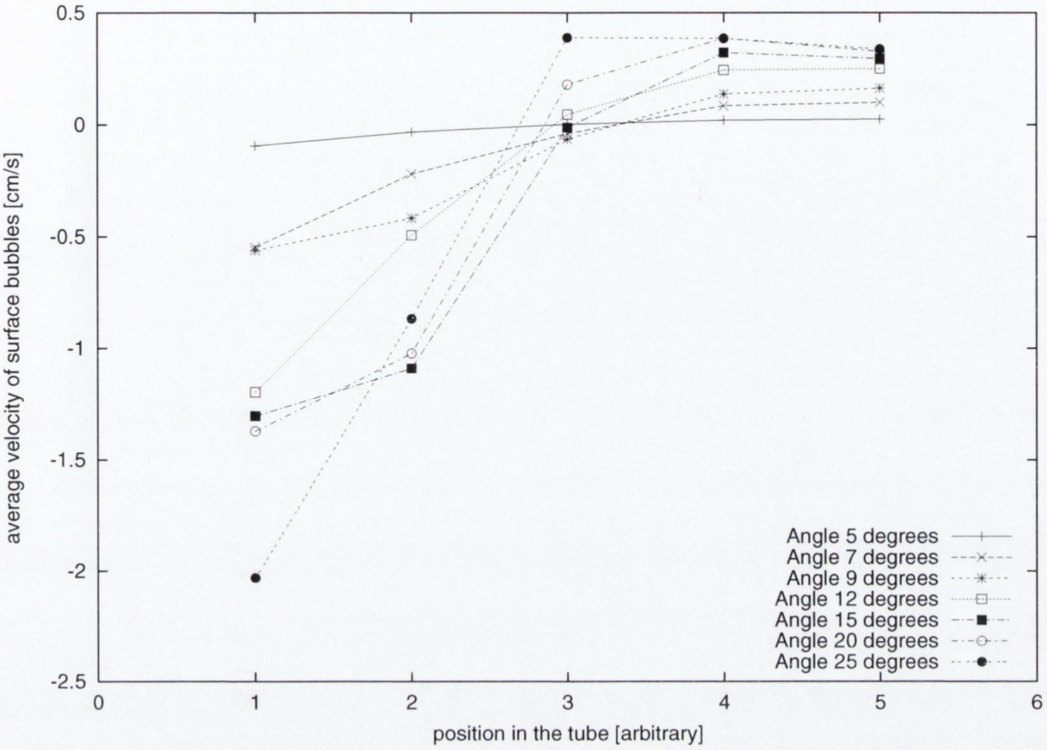

Figure 5-4: Average velocity of surface bubbles (six per point) at five different sections of the tube sketched in Fig. 5-3. Each set of data is for a different angle of inclination. Flow rate is fixed at 0.408 ml/s and the bubble radius is 1.79 mm. The change of sign in velocity in section 3 start at angles $\approx 15^o$. Bubbles in position 2, slow their downwards motion as well at those angles. The width of the wet side decreases when the tube is tilted, as it is marked by the solid lines. The speed of bubbles in sections 4 and 5 is fairly constant at each angle, which is consistent with the plug flow observed visually. Error bars have been omitted for clarity.

the bubbles move in each direction and these gives on average a small velocity. But as the tilt angle increases, the bubbles on section 3 move clearly upwards. These results support our visual impression that the wet bubbles move faster than the dryer side and the dry side moves more or less in plug flow, as expected.

We choose the velocity of this plug flow to primarily characterise the motion. This is recorded for different angles of tilt at fixed liquid fractions (see Fig. 5-5). It is not possible to consider an experimental average liquid fraction in these experiments (the tilting of the tube does not allow us to use Archimedes principle in Eq. D.1). The lines are fitted to a function $f(\theta) = a\ tanh(b\theta - c)$, chosen because it reproduces the sharp rise and plateau observed in the data.

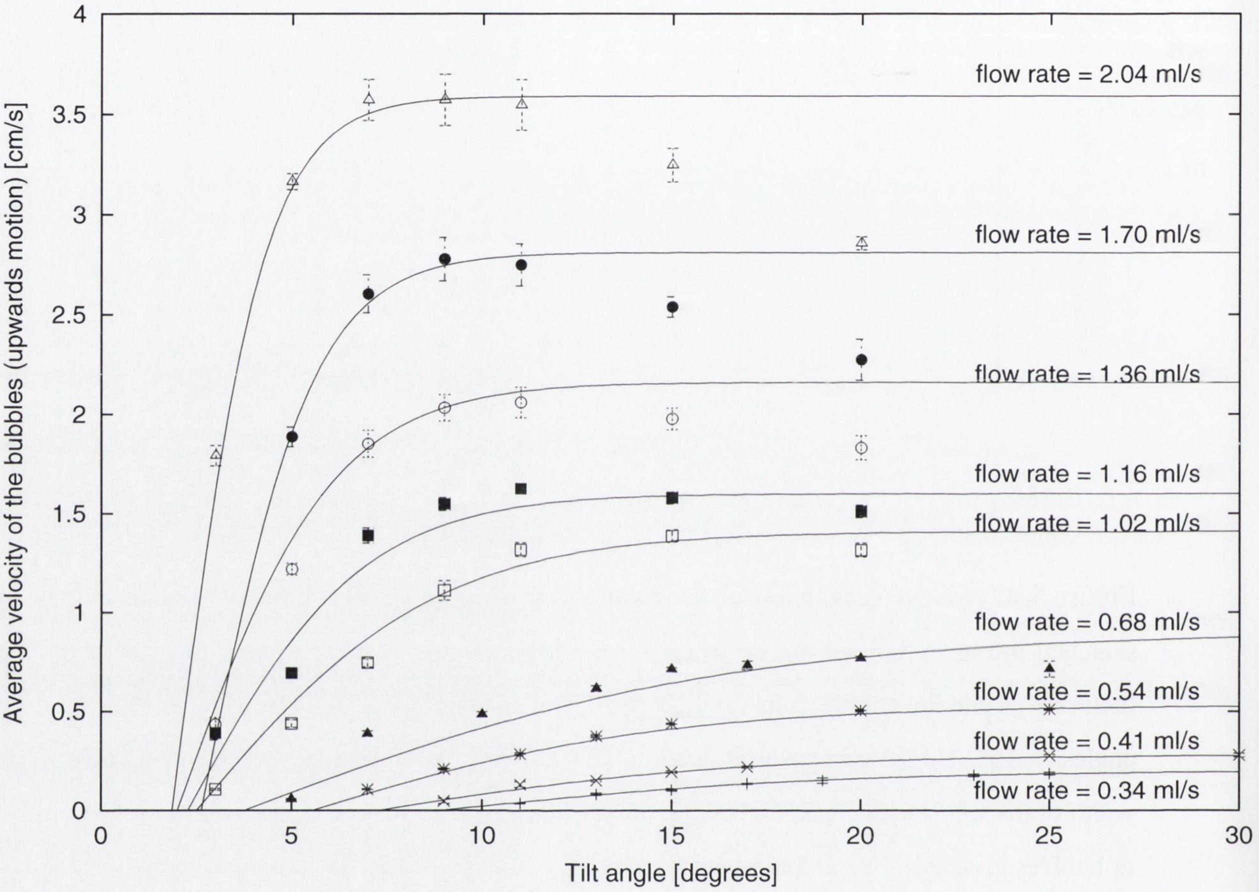

Figure 5-5: The figure shows the velocity of the bubbles that move upwards in relation to the angle of tilt. Every curve is labeled with the fixed flow rate at which it was taken. Small increases in the tilt angle lead to an increase in the speed of the bubbles at first. This effect levels off. At low flow rates, the velocity reaches a stable level and at higher flow rates, the bubbles moving upwards start to slow down showing non-continuous motion. We ignore the points after this slow down deliberately to fit the motion (this only affects to the data at flow rates higher than $1.16\ ml/s$. For the other sets, all the data up to 25^o is considered). The points for each different flow rate can be fitted to the function $f(\theta) = a\ tanh(b\theta - c)$. This set of data is for foam with a bubble radius $r = 1.56\ mm$ in a $2\ cm$ diameter tube.

Increasing the tilt angle beyond a certain point leads to a rapid increase of velocity in all cases. The slope depends on the flow rate. For flow rates lower than $0.68\ ml/s$ the velocity reaches a plateau and stays at the same value when the tube is tilted further. Flow rates bigger than that value result in a decrease of velocity of the surface bubbles, for tilted angles above 12^o. In some cases, for the higher flow rates and angles above 20^o, the slow down is associated with non-continuous motion of the bubbles moving upwards. Foam moves in short lapses, rather than continuous plug motion (video `catter.mpg`). This may be due to the character of the motion at high tilted angles (sketched in Fig. 5-2). We have neglected these points at the fitting in Fig. 5-5.

5.4 Analysis of results

Here, we relate the parameters a,b,c of the fittings for the velocity of the motion at different flow rates in Fig. 5-5 to physical quantities. The parameter a is the limit value of velocity at high flow rate.

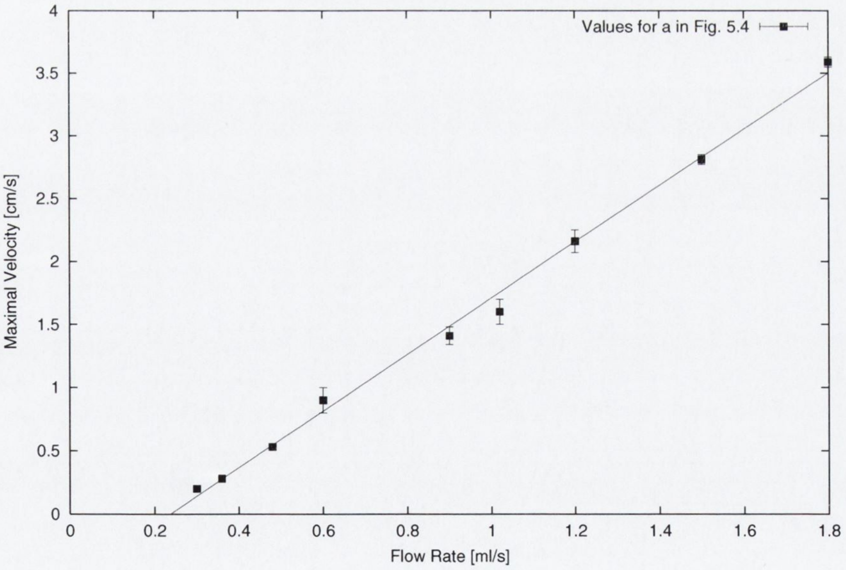

Figure 5-6: The values for the limit velocity reached by the convective roll in a tilted tube (parameter a in Fig. 5-5). vary linearly with flow rate. This set of data is for foam with a bubble radius $r = 1.56\ mm$ in a $2\ cm$ diameter tube.

In terms of these fitted parameters, the tilt angle for onset of motion is $\theta_c = c/b$.

The results on Fig. 5-5 may thus be reduced to $\theta_c = c/b$ and a for many purposes. Figs.5-6 and 5-7 use this procedure:

- The first relates the limit velocity a to flow rate. It varies linearly with respect to flow rate. At the moment we cannot offer an explanation for this behaviour.
- The second relates the critical angle to flow rate. We will discuss now how this flow rate varies respect to the critical tilt angle in Section 5.5.

The tilted experiment is repeated for different tube diameters and lengths using the same bubble size ($B_r = 1.56\ mm$). All the results are consistent with the results described so far for one tube.

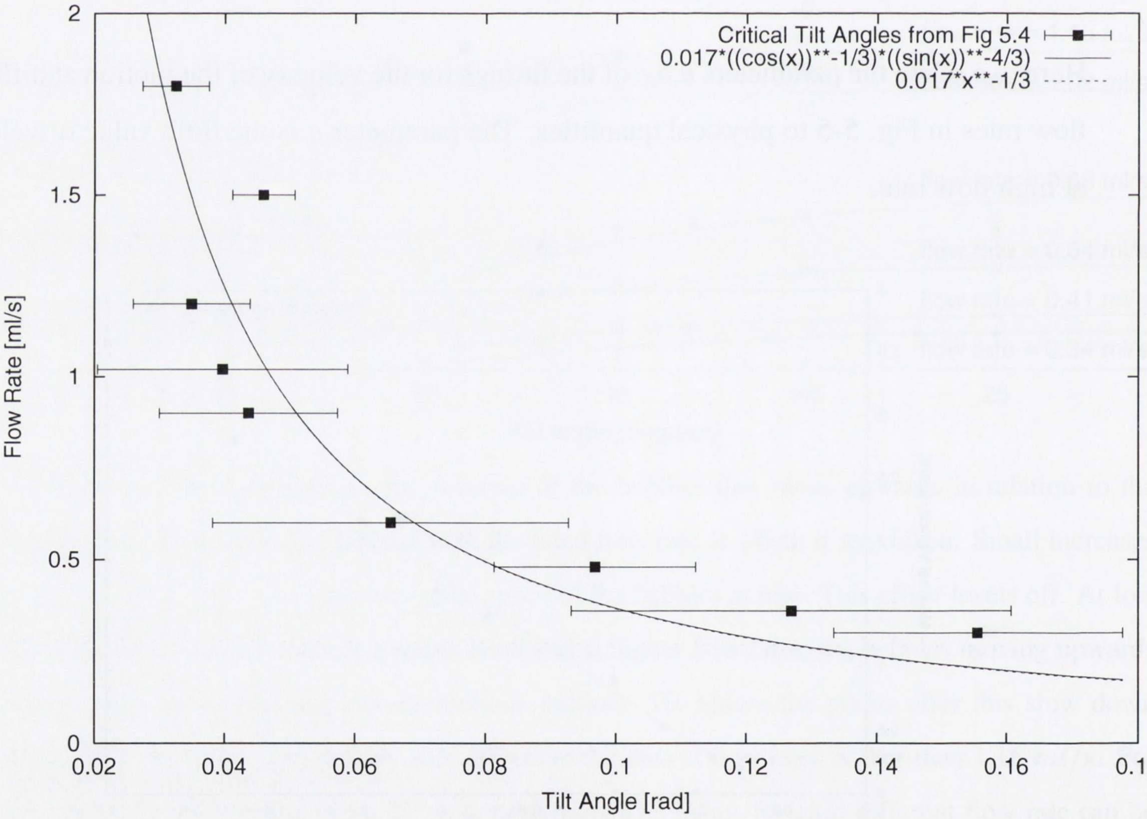

Figure 5-7: The values for the flow rate related to critical angle at the onset of the tilt convective motion in radians ($\theta_c = \frac{c}{b} * \frac{2\pi}{360^o}$ see Fig. 5-5 for clarification.). This set of data is for foam with a bubble radius $r = 1.56\ mm$ in a 2 cm diameter tube. The data fits to Eqs. 5.2 and 5.3 (the approximation for small angles) in Section 5.5.

5.5 Theoretical Comparison

The drainage equation 1.8 on page 12 has been solved [81, 85] for the tilted tube using a change of coordinates. A full derivation of the solution appears in Appendix G.

The shear stress, S, in a foam is a function of liquid fraction. The dependence of S with flow rate can be obtained as (Appendix G):

$$S \sim 2g^{5/4} \cos^{1/4}\theta \sin\theta \, Q_Z^{3/4}. \tag{5.1}$$

Foam flows when the value of shear stress equals the yield stress value $S = S_y$. The yield stress S_y is taken as a fixed constant. We equate the right hand term in Eq. 5.1 to S_y and obtain the following expression for the flow rate in the gravity direction, Q_Z, under the critical condition for onset of convection:

$$Q_Z \sim \frac{S_y^{4/3}}{2^{4/3} g^{5/3} \cos^{1/3}\theta_c \, \sin^{4/3}\theta_c}. \tag{5.2}$$

This can be approximated for small angles using $\cos\theta_c \approx 1$; $\sin\theta_c \approx \theta_c$:

$$Q_Z \sim \theta_c^{-4/3}. \tag{5.3}$$

The values obtained in Fig 5-7 fit well to both Eqs. 5.2 and 5.3 as seen in Fig 5-7. It is possible to evaluate the error committed in using Eq. 5.3 as the larger critical angles are around $10^o \approx 0.175 rad$. In this case $\sin 10^o \approx 0.173$ and $\cos 10^o \approx 0.985$ and introducing these values in the formula we estimate an error about 2%.

5.6 Conclusions for the tilted tube

Our empirical conclusions are:

- the limit velocity of the bubbles grows linearly with flow rate.
- the critical angle at the onset of the motion, is related to the flow rate in the gravity direction assuming a constant yield stress S_y. The dependence is found to be $Q_Z \sim \theta_c^{-4/3}$.

These results are consistent for several tubes with different diameters and lengths. The theoretical formula proposed in Appendix G provides a good fit for the data of the critical angle at the onset of the motion, deduced from experiments. In this way we see a clear demonstration of what was anticipated at the outset, that the requirement of a certain finite tilt angle to induce convective motion is related to a finite yield stress S_y, which must be overcome.

Appendices

Appendix A

Measurements of local liquid fraction related to convective motions in foam

A.1 Motivation

In Chapter 3) we have reported convective patterns of motion in foams at high flow rates and we have described a phenomenological theory which should give solutions compatible with those expected by the experiments.

As we have explained, it would be useful to have local measurements of the liquid fraction. We will describe some attempts to estimate local surface liquid fractions with a microscope. We try to relate the width of the Plateau borders in the surface of the sample to the average liquid fractions calculated using the Archimedes method (see Appendix D). The result is still uncertain, as such estimates involve considerable experimental errors and the variations of liquid fraction entailed by convective motion do not appear to be large. In the end, the purely optical method described here does not seem to be the solution to the problem of finding precise liquid fractions at local level.

A.2 Surface liquid fraction measurements

To observe the foam at a closer level, in an attempt to determine local liquid fraction, we use a Euromex © optical microscope with a trinocular head. It has ×3 and ×10 magnification and allows us to take pictures of the magnified foam when used in conjunction with the Nikon © camera. In order to examine in detail the growth of the wall Plateau borders, we have taken some pictures of a column of foam using the microscope at the highest magnification available (×10). Fig. A-1 shows some of the pictures.

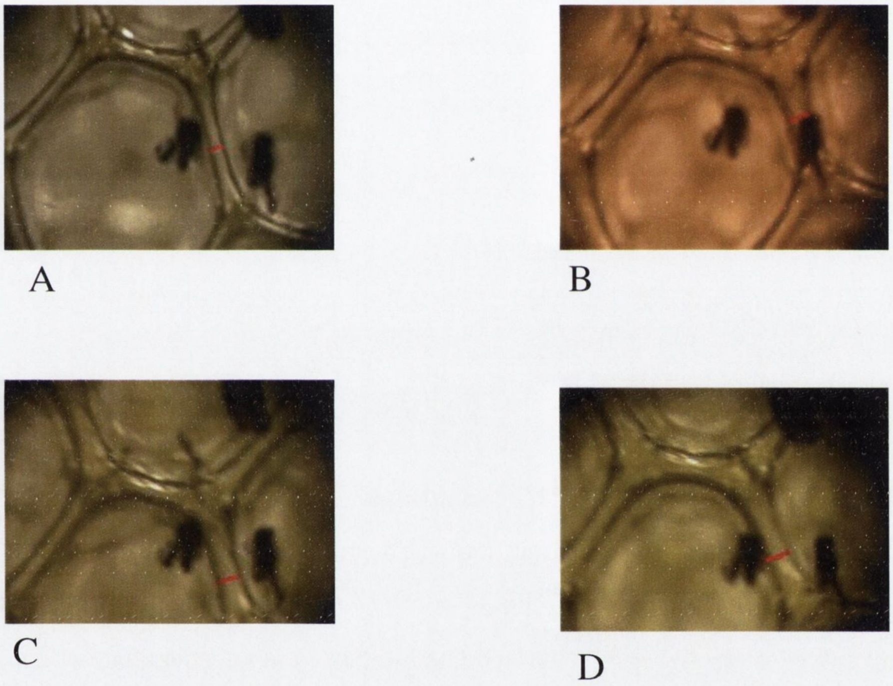

Figure A-1: Four pictures of the same bubble showing the growth of the Plateau borders when the liquid fraction is increased. The values of liquid fraction are, respectively (A)-$\phi_l = 0.048$; (B)-$\phi_l = 0.075$; (C)-$\phi_l = 0.089$ and (D)- $\phi_l = 0.097$ for a bubble radius 1.3 mm. The convective instability, **CSI**, is triggered at a slow velocity in picture (D) (see movie `wallmotion.mpg` in CD). Two black dots at the bottom of the pictures are one millimetre apart and serve also as a check for the camera focus. We have measured only the evolution of the Plateau Border width marked by the red line. Results are shown in Fig. A-2.

We measure the evolution of a single Plateau border using a computer graphics program (Adobe © Photoshop 5.0). The same bubble is pictured at different liquid fractions. The liquid fraction is an average on the foam, calculated using Archimedes principle in

Appendix D. We mark the width of one of the Plateau borders surrounding the bubble and measure this line in pixels, calibrating this with a known distance in millimetres. The errors are calculated considering propagation of error from the original pixel measurements. Results are shown in Fig. A-2.

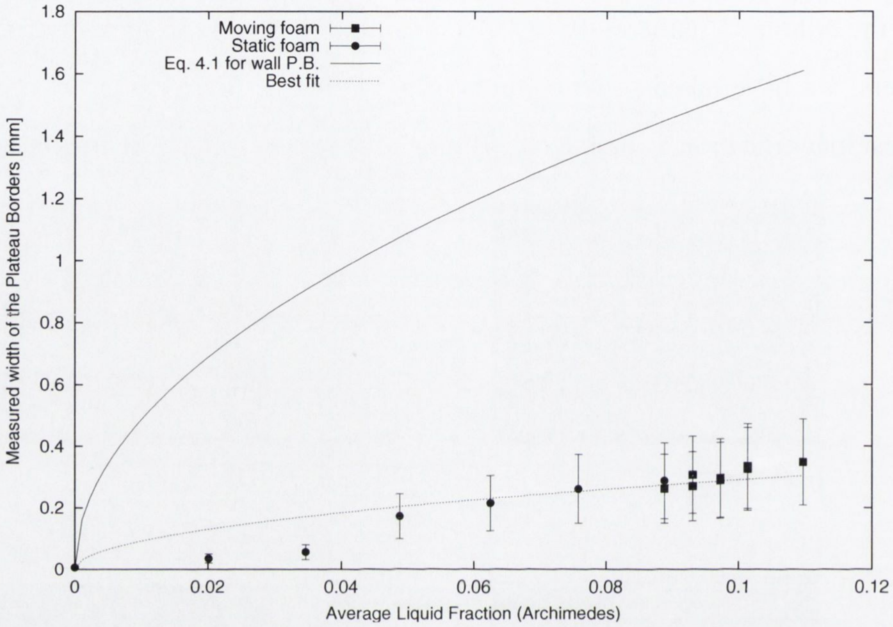

Figure A-2: Apparent width of the Plateau Borders at the surface of the foam. The bubble radius is $1.3\ mm$. The foam is static when the liquid fraction is lower than 0.09 (dots) and moves in convective motion (**CSI**) at higher liquid fractions (squares). The solid line represent the values corresponding to Eq. A.1 and the dashed line is a best fit to the equation $\delta = constant * \phi_l^{1/2}$

The error in the measurements is large. We have tried to minimise this error by averaging different Plateau borders, but this method in fact increases the error when the foam is in motion. We believe that this is due to the deformation that the bubbles suffer during convective motion (see video `wallmotion.mpg`).

The results for one single Plateau border can be related to the theoretical formula that relates liquid fraction, ϕ_l, to the ratio between bulk Plateau border area and bubble volume in a dry foam [1].

$$\phi_l \approx c_K \frac{A_{PB}}{V_b^{2/3}} = 5.35 \frac{c_g \delta^2}{V_b^{2/3}}, \tag{A.1}$$

where c_K is a geometrical factor (calculated assuming that the foam is a Kelvin structure),

A_{PB} is the cross-section of the Plateau border, c_g is a geometrical constant whose value is 0.161 [1], δ is the width of a Plateau border in the bulk of the foam and V_b is the bubble volume. This formula gives a value of the bulk Plateau Border width $\delta \approx 0.32\ mm$ for a liquid fraction of 0.02. The result is even more discouraging when we take in account that the Plateau borders at the wall of the container are twice the width of the interior ones according to corrections of the theory calculated using Surface Evolver (Fig. A-3). We should have got a value $\delta_w \approx 0.62\ mm$ and our measured value is $\delta_{exp} \approx 0.03\ mm$.

Even if we can appreciate the growth of the Plateau border width on the bubbles at the wall, the method we have used is not good enough. The error is quite large, but even taking this in account, the values that we obtain seem to be lower than the ones expected theoretically by one order of magnitude in the dry foam case. We believe that this is due to optical considerations and lack of contrast in the images. Our understanding is that the δ_{exp} that we are measuring is not the real width of the Plateau Border (Fig. A-4), but an apparent length that would need to be related to other parameters of the foam in order to get an interpretation of these results.

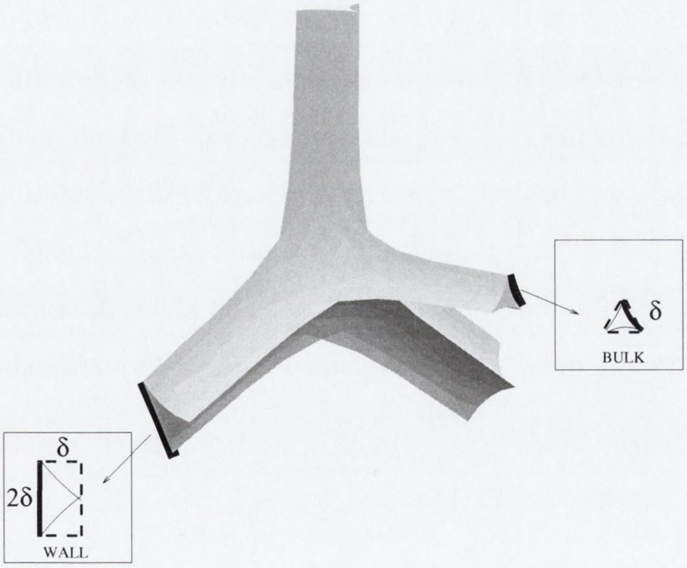

Figure A-3: A four-fold vertex at the surface of the container. The width of the Plateau border at the container wall is twice the width of an internal Plateau border. Reproduced from [74].

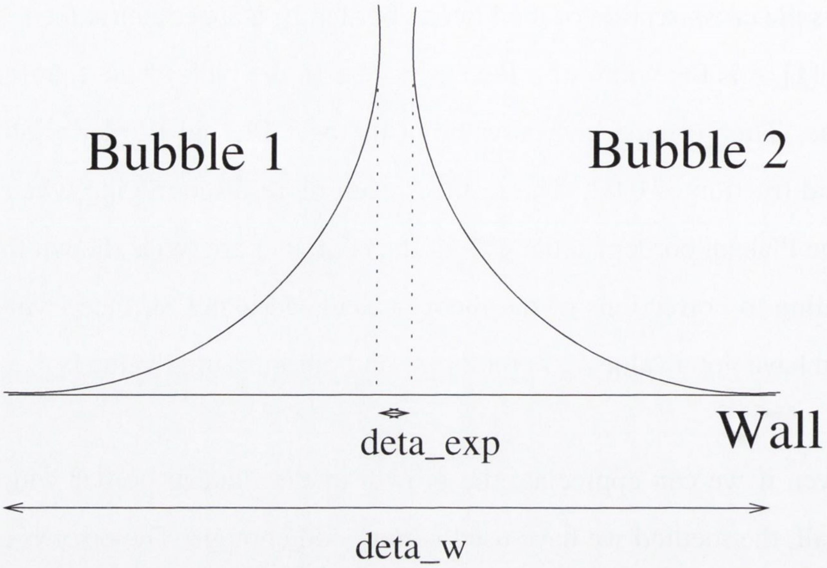

Figure A-4: The experimental results in Fig. A-2 are sensibly lower than the ones expected from Eq. A.1. We attribute this difference in the measurements to optical reasons. The values we measure δ_{exp} are different to the real width of the Plateau borders δ_w.

Several techniques have been considered to obtain precise measurements of local liquid fraction values, even in the bulk of the foam. MRI (magnetic resonance image) [86] or NMR (nuclear magnetic resonance) [87, 88] have already been tried on aqueous foam or porous materials. CT (computer tomography) scanning [89, 90], using X-ray radiation is another option that has rendered precise images of the bulk of foam. Real time confocal microscopy was another option available [91, 23]. This possibility was considered in our experiment but rejected, as the only confocal microscope available could only acquire static data at several μm in the bulk of the sample. But real time confocal microscopy could be able to produce micro-slices of the foam up to several mm into the sample [92].

Appendix B

Minimal configurations of bidisperse bubble clusters

B.1 Motivation

In this Appendix we present a study of 2D foam clusters [93], undertaken in the course of our evaluation of 2D foam systems for experiments. Is it possible to determine the minimum energy configuration for a 2D bidisperse foam cluster, such as the one in Fig. B-1?

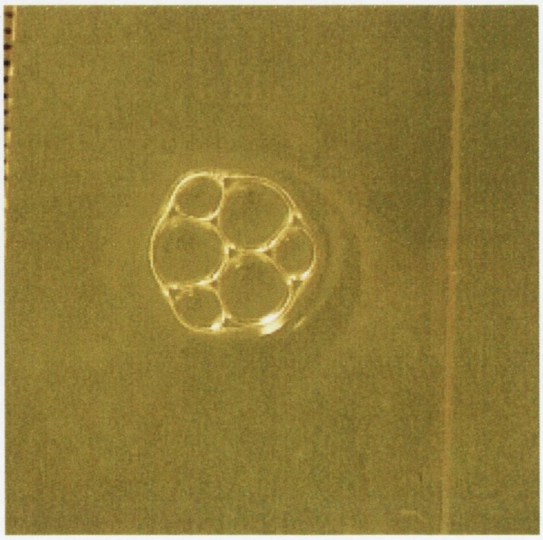

Figure B-1: A bidisperse bubble cluster has bubbles of two different areas.

Maybe this question will sound more familiar if we ask another one more general: given a collection of planar regions with fixed areas, which is the arrangement with a minimum perimeter?

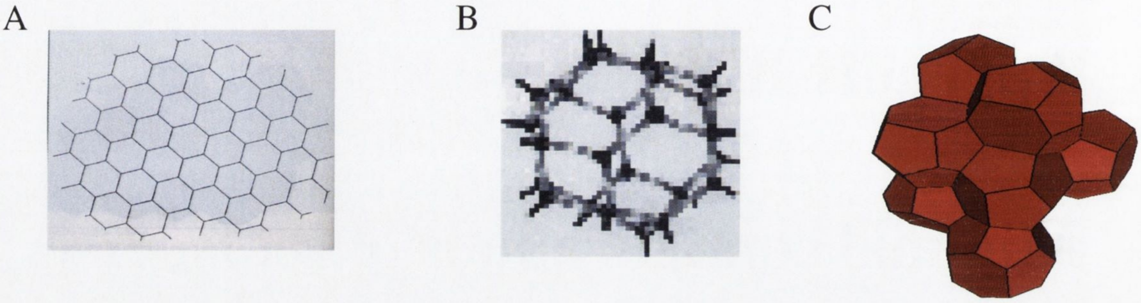

Figure B-2: What is the minimum perimeter that can enclose cells of a given area or volume? A/ For an infinite plane, the best option available has been proved to be the honeycomb. In 3D the problem is known as the Kelvin problem and space partition remains debatable. B/ Kelvin conjectured a solution with a unit cell composed by two equal cells (tetrakaidecahedrons), which are truncated octahedra slightly deformed. C/ Weaire and Phelan have calculated that the structure shown in the picture has lower energy than the Kelvin partition of space. The Weaire-Phelan unit cell is composed of eight bubbles of two different shapes but equal volume.

The statement of the problem sounds simple but solving it is not. In 2D, the so-called 'honeycomb conjecture' (see Fig. B-2), was enunciated about 2000 years ago. Fejes Tóth produced a partial proof in 1943, assuming convex cells. It has only been proved without any assumption very recently by Hales [94]. It states that the minimum perimeter configuration for the packing of tiles with the same area is one in which all the tiles are regular hexagons. But this is only relevant when the 2D cluster is infinite or repeated periodically. For finite clusters, the boundary of the cluster (understood as the cluster's external perimeter) has to be taken in account. Finite bubble clusters of N bubbles have been investigated in search of the minimum perimeter solution. In a very few cases, the cluster minimum has been exactly solved ($N = 2$ by Alfaro et al. [95, 96] and $N = 3$ by Wichiramala [97]). However, in the rest of cases progress has been limited to making conjectures about the minimal perimeter configurations. Estimates have been suggested for clusters with N between 1 and 42 and for $N = 50$, $N = 100$ and $N = 200$ [98, 99, 95, 100]. The partition of the space in 3D cells, known as the Kelvin problem, is also complicated although a structure has been proposed as a candidate: the Weaire-Phelan [3] in Fig. B-2. Configurations of 3D clusters have been analysed only for $N = 2$ to 4 bubbles [101]. For a large number of bubbles the problem becomes complicated and difficult to analyse.

Recent works [102, 99, 98] that study the minimum configuration on equal size bubble clusters are described here. We will pay special attention to the work by Vaz et al. [103], as they propose approximate formulas for bubble clusters with different bubble areas (particularly bidisperse clusters). They calculate precisely the surface energy for bidisperse clusters composed of a central cell surrounded by one or two shells of cells.

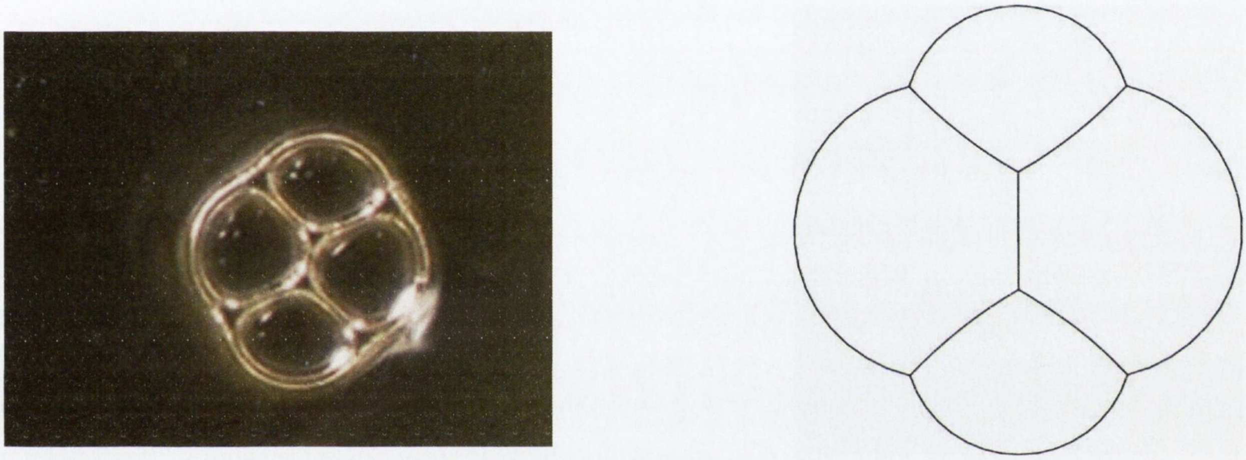

Figure B-3: One candidate for minimum energy in (2-2) clusters. Experimental picture of the cluster (left). Simulations can be done the Surface Evolver (right).

We will describe in detail our experiments undertaken in collaboration with Vaz, as well as numerical simulations done using the Surface Evolver (see Appendix F). We have produced clusters of N bubbles with two different areas.Our candidates that appear experimentally are supposed to be the most energetically favourable (see Fig. B-3.) Therefore, we have used their topologies to calculate their energy using the Surface Evolver [2] and have compared the values obtained to theoretical lower bounds for the energy of clusters and statistics on the frequency of occurrence of a cluster, made on the experimental clusters. The results show agreement between the Evolver calculations and the theoretical formulas, but poor correlation with the statistical values. This can be attributed to the low energy differences among the different candidate clusters and the neglected contribution of the Plateau borders.

B.2 The minimal problem in 2D bubble clusters

When two or more bubbles join (Fig. B-4) the film length of the aggregate is less than the sum of the films of the individual bubbles. This happens because the intervening film is shared by the two bubbles.

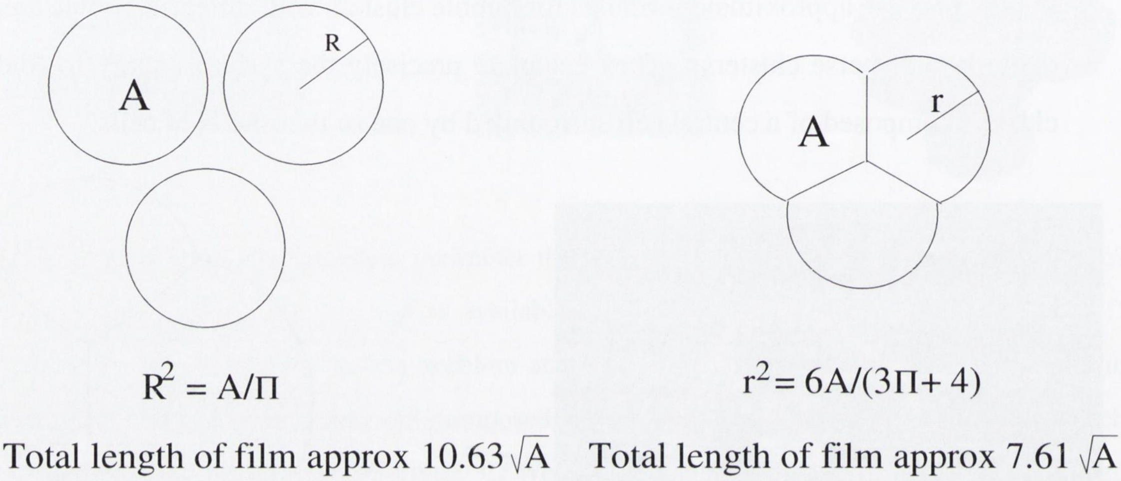
R
A
A
r
R² = A/Π
r² = 6A/(3Π+ 4)
Total length of film approx 10.63 √A
Total length of film approx 7.61 √A

Figure B-4: Bubbles come together because sharing a common film lowers their surface energy. This energy is proportional to the total length of the film that encloses the bubbles. The bubbles are supposed to keep a constant area A.

Within a very good first approximation, the energy of the clusters is defined by the surface tension of the soap films that form them, that is:

$$E = \gamma_{foam} L, \tag{B.1}$$

where E represents the free energy of the bubble cluster, γ_{foam} the surface tension and L the total length (total area in 3D) of the films that separate the bubbles. We are neglecting several contributions to the total energy in this approximation. The main ones are the contribution of the liquid content of the foam and considering the gas to be incompressible in the cells. But we are also neglecting the effect of coarsening, any elastic contributions to the energy and local changes in the surface tension of the films. Experimentally, all these contributions are much lower than the main term that we are using in Eq. B.1. Studying the minimum energy configuration of bubbles is equivalent to studying isoperimetrical problems within this approximation.

B.2.1 Contributions to the energy in 2D clusters

Graner et al. [102] discuss in detail minimal 2D clusters of different bubble areas. They refer to the minimum energy for a given topology as the ground state. Graner et al. show that all the stable states of the clusters have an energy that is quite close to that minimum and describe the physical causes that raise the energy of a real cluster of foam: great differences in the areas of the bubbles (area mismatch), topological charges [1] and the effect of the boundaries at free clusters (boundary conditions).

- Two bubbles share a film that has to accommodate a length that suits both (optimal edge length). The effect of area mismatch grows when the difference between the areas of the bubbles is bigger.
- The coordination number is the number of bubbles surrounding another bubble. In an infinite 2D dry foam, one cell will have an average of 6 neighbours. Graner et al. introduce a topological charge that measures how the topology deviates from the honeycomb topology. Using this topological charge, they show that a single topological charge is not favourable in energy (i.e. defects will appear in pairs at the real foam).
- The contribution of the boundary comes from the fact that straight lines have to relax to arcs of circle in free boundary conditions. This is especially important in small clusters, as the one we describe in this chapter. For a small cluster $N < 15$, most of the bubbles on the cluster are peripheral. Therefore, the contribution of the topology will be more noticeable for small clusters [102, 99].

Graner et al. also conjectured that for a fixed topology with given bubble areas, the shape of the cluster should be unique. This has been proved wrong by counter-example on a given topology and fixed bubble areas by Weaire et al. [104], where several minimal configurations were found. However, it is clear now that all these configurations all share the same energy [105].

---

[1] The topological charge of a bubble is a deviation in the coordination number of the bubbles from that of the hexagonal honeycomb

We have to find a method to quantify the energy of the clusters, as we want to compare different candidates for the minimum. In the following sections, we will describe the different attempts to estimate and compare the energy of 2D bubble clusters. Most of these energies are calculated for monodisperse clusters (clusters in which the bubbles have all the same area), but the ideas underlying can be useful in our evaluation of the energy of bidisperse clusters.

B.2.2 The broken bond method

The free energy of a 2D cluster can be estimated using the excess energy [99] of the bubbles in the boundary:

$$E_b = E - E_o, \tag{B.2}$$

where E is the free energy of the whole cluster and E_o is the energy associated with the internal bubbles. $E_o = 3Na\gamma_{foam}$ is the energy of a regular honeycomb of N bubbles and a is the edge length of an hexagon of area $A = \frac{3\sqrt{3}}{2}a^2$.

The perimeter cells have in general less than six bubbles surrounding them and therefore, have an excess energy compared to the internal bubbles. It is possible to estimate this excess energy by counting the broken bonds of the peripheral cells (the missing cells that will complete six neighbours). The number of broken bonds, B, in a cluster with P peripheral bubbles is defined by [106, 107]:

$$B = 6 + 2P. \tag{B.3}$$

Each broken bond gives a 'penalty energy', $\epsilon(N, n)$, that depends on the number of bubbles of the cluster N and the average number of neighbours, n, of the internal bubbles. The sum of all these energies, is the excess energy of the boundary.

$$E_b = B\epsilon(N, n). \tag{B.4}$$

B.2.3 Estimates of the energy on monodisperse clusters

An analytical estimation of the energy of the clusters, using the broken bond method, has been compared recently with calculations made by Cox et al. [98] for equal area clusters. They estimate the number of perimeter bubbles, $P \approx -3 + \sqrt{3(4N-1)}$ [2], assuming that the minimal configuration is close to a round shape. They suggest the expression:

$$E \approx E_o + 2\epsilon\sqrt{3(4N-1)}L\gamma_{foam}, \tag{B.5}$$

where ϵ is obtained by fitting Eq. B.5 to the values obtained in Surface Evolver simulations. This parameter is always close to 0.45.

They obtained an initial cluster by cutting a circular section of the honeycomb with N bubbles. Some elongated initial configurations were tried for testing with the same final result (but longer computing time). They have allowed the clusters to shuffle by performing neighbour swapping events ($T1s$) at each iteration. Their results suggest that minimum clusters have circular perimeters and few defects (the number of neighbours of each internal cell is as close to six as possible).

B.2.4 Estimates of the energy on polydisperse clusters

Vaz et al. [103] have made exact calculations of symmetrical 2D clusters formed by a central cell and surrounded by one or two shells of bidisperse bubbles, *i.e.* with two different cell areas. They propose an estimate for the surface energy, taking the equation:

$$\frac{E}{\gamma_{foam}} \approx \frac{3.722}{2}\sum_i {A_i}^{1/2}, \tag{B.6}$$

used by Graner et al. [102] as an estimate for the surface energy of a polydisperse cluster, where A_i is the area of the i^{th}-bubble of the cluster and 3.722 is the perimeter of a regular hexagon of area 1. This is a lower bound that considers that bubbles are going to be as round as their constraints (other bubbles in the cluster) permit them to be.

The coefficient in Eq. B.6 can be changed to 3.692 if the space is divided in clusters with two different bubble areas (bidisperse clusters), as proposed by Teixeira et al. [108].

---

[2] They have presumed this value exact for 6-fold symmetric clusters.

$$\frac{E}{\gamma_{foam}} \approx \frac{3.692}{2} \sum_i {A_i}^{1/2}, \tag{B.7}$$

In both cases, in Eq. B.6 and Eq. B.7, we can add the contribution of the boundary for real finite clusters. This contribution is calculated using a broken bond approach, with the values for the perimeter energy of a monodisperse cluster found by Fortes and Rosa [109]. The equation suggested for the surface energy of a round cluster is:

$$\frac{E}{\gamma_{foam}} \approx \frac{3.722}{2} \sum_i {A_i}^{1/2} + 2.042(\sum_i A_i)^{1/2}. \tag{B.8}$$

Vaz et al. [103] deduce a possible lower bound considering that in a cluster of regular hexagons of the same area with regular hexagonal boundary the factor 2.042 reduces to 1.934:

$$\frac{E}{\gamma_{foam}} \approx \frac{3.692}{2} \sum_i {A_i}^{1/2} + 1.934(\sum_i A_i)^{1/2}. \tag{B.9}$$

Both equations, Eq. B.8 and Eq. B.9, work better for clusters with a fairly large number of bubbles [103], but which is the best approach for the boundary of a cluster with a large number of bubbles is still open to question [110].

The aim of our experiments is to obtain some information about the minimum energy configurations for clusters with two different bubble sizes. In particular, the energy found for the clusters in Surface Evolver can be compared to Eq. B.8 and Eq. B.9. We will achieve this aim of producing experimental clusters and reproducing their topology in the Surface Evolver to get an estimate on their energy.

B.3 Experimental methods

When we introduce the possibility of varying bubble sizes, the number of candidates available for a minimal cluster is much higher than in monodisperse clusters (see Fig. B-5). These clusters have N bubbles and can be represented by the pair, (M, m), where M is the number of bubbles of one size and m is the number of bubbles of the other size. One idea to reduce the number of configurations to compare is using clusters with only two different bubble sizes and equal number of bubbles of each size $M = m$. But this reduction still leaves a great number of possibilities to be studied.

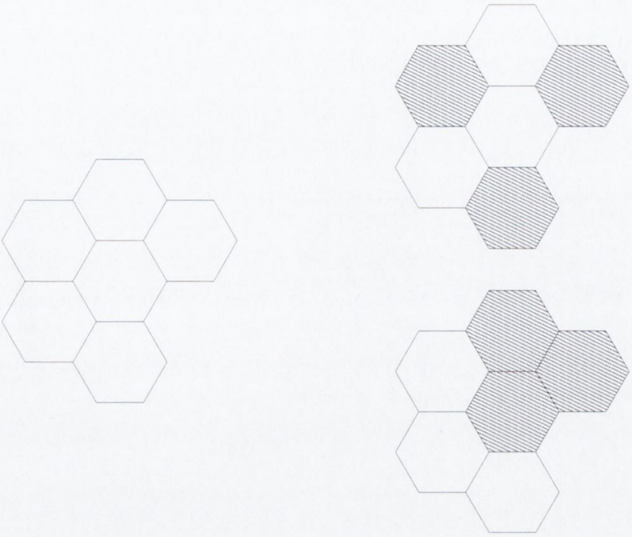

Figure B-5: When the bubbles sizes are different, the number of configurations that a cluster with the same topology can access grows. We can see on the sketch that the configuration on the left, does not change if we swap the elements between them. The ones at the right, that have different tiles, are not the same, even if all share the same topology. Greater polydispersity leads to a greater number of configurations.

To reduce even further the number of candidates we use a heuristic approach. We are searching for the clusters with minimum energy and we want to simulate them using Surface Evolver. One way of reducing the number of candidates is to make experiments in order to identify minimum energy candidates. We are not really sure that we have studied all the possible bubble clusters for a given number of bubbles (M,m), but it is quite probable that the ones with minimum energy will show in the experiments. We believe this because the number of experimental trials is fairly large and we encourage new configurations by perturbing the cluster. Even using this simple approach, we have plenty of configurations to choose. For a $N = 4$ bubble cluster, which we denote as $(2, 2)$, only two candidates are found, even if some metastable states (clusters that change their topology without any external perturbation) were photographed. But the number grows to fifteen in the $(3, 3)$ clusters. Although the final number of configurations will eventually grow as we made more experiments, in the $(4, 4)$ and $(5, 5)$ preliminary trials, we have found 15 and 31 configurations respectively. We decide to concentrate on the $(2, 2)$ and $(3, 3)$ clusters to study the effect of varying the relative size of the two different bubble areas in the cluster.

B.3.1 Materials and methods

The 2D bubble cluster production is similar to the one described in Vaz et al. [99].

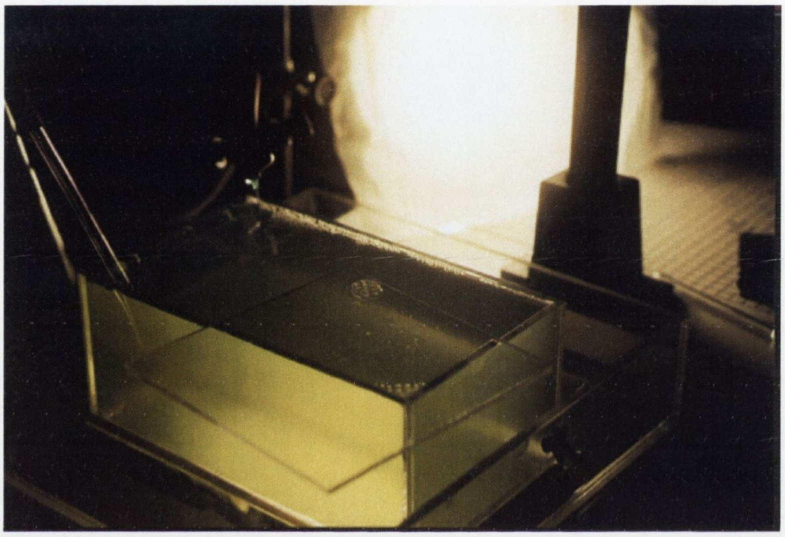

Figure B-6: A picture of the experimental set-up. A Plexiglas top plate covers the bottom left part of the vessel. It can be tilted to separate the bubbles by submerging them into the pool. One of the nozzles used for foam production (described in Appendix D) can be seen at the top left. The top plate is covering a cluster in the centre of the vessel.

A rectangular Plexiglas vessel (Fig. B-6) is filled with surfactant solution. Foam is produced by blowing air through different size nozzles in a similar way to the method described in Appendix D. When the two bubble sizes desired have been produced, bubbles can be picked with a fine nozzle and assembled to construct a monolayer, using a plate to cover the top of the tank. The air gap between the top plate and the surfactant solution of is approximately $3.0\ mm$.

The clusters produced are stable to small perturbations (caused by shaking gently the Plexiglas top cover and pushing individual bubbles with a nozzle). However, large perturbations can induce topological changes (see Chapter 1) in some configurations. The cluster topology appears in free conditions (i.e. not attached to other surfaces) and we take pictures of the configurations, that are numbered as they appear experimentally. In some cases, the clusters have been photographed near the border of the plate. This can lead to a change in the experimental energy of the clusters. However, these clusters have the same topology when they are obtained apart from the border and we estimate the energy from the Surface Evolver calculation.

B.3.2 Experimental results

We have produced clusters of three different area ratios to study the effect of dispersity in the bubbles sizes. We have decided to study bidisperse clusters with computational area ratios of $A_M/A_m = \frac{4}{3}$, $A_M/A_m = 2$ and $A_M/A_m = 4$, where M refers to the big bubbles and m to the smaller. These ratios have been chosen in order to facilitate future comparison with our work. The experimental bubble diameters are chosen to facilitate qualitative comparison with the Evolver calculations that follow in Section B.4, but they are also dependent on the facilities available.

We can see that the experimental candidates to be the minimum cluster are the same topological configurations for different dispersion of the areas (Figs. B-7, B-8, B-9, B-10, B-11 and B-12). We found two stable $(2, 2)$ experimental clusters and fifteen in the $(3, 3)$ case. The photographs show that the majority of them are rounded clusters. Elongated configurations are less likely to be found experimentally. These are the configurations that we will reproduce in Surface Evolver in order to get an estimation of their energy.

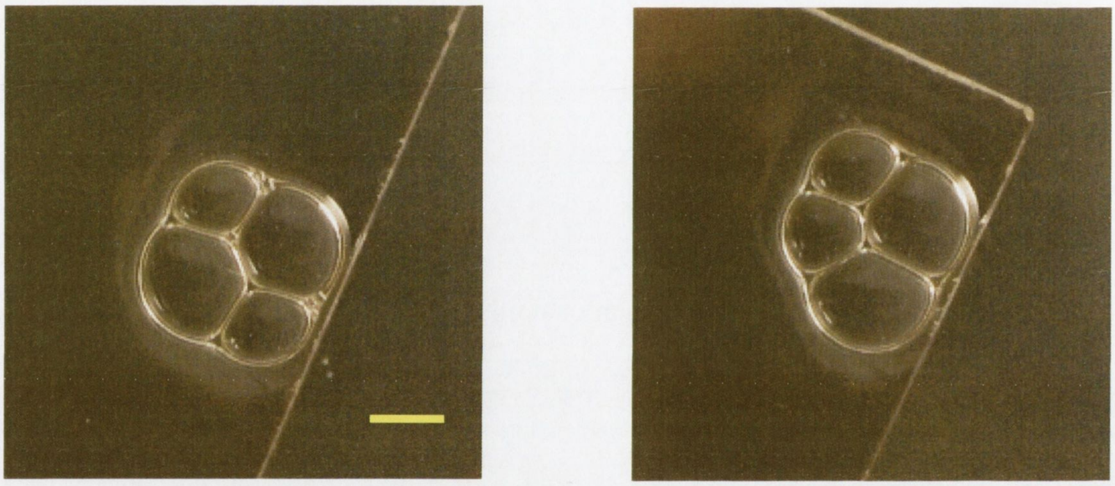

CLUSTER 1 **CLUSTER 2**

Figure B-7: Stable experimental clusters formed by 4 bubbles. $A_M/A_m \approx \frac{4}{3}$. The reference line corresponds to $5\ mm$ in real size. Two different clusters are found. The statistics of the two clusters occurrence (see Fig. B-13) show a preference for the second configuration experimentally. This configuration is not symmetrical (the two small bubbles are in contact).

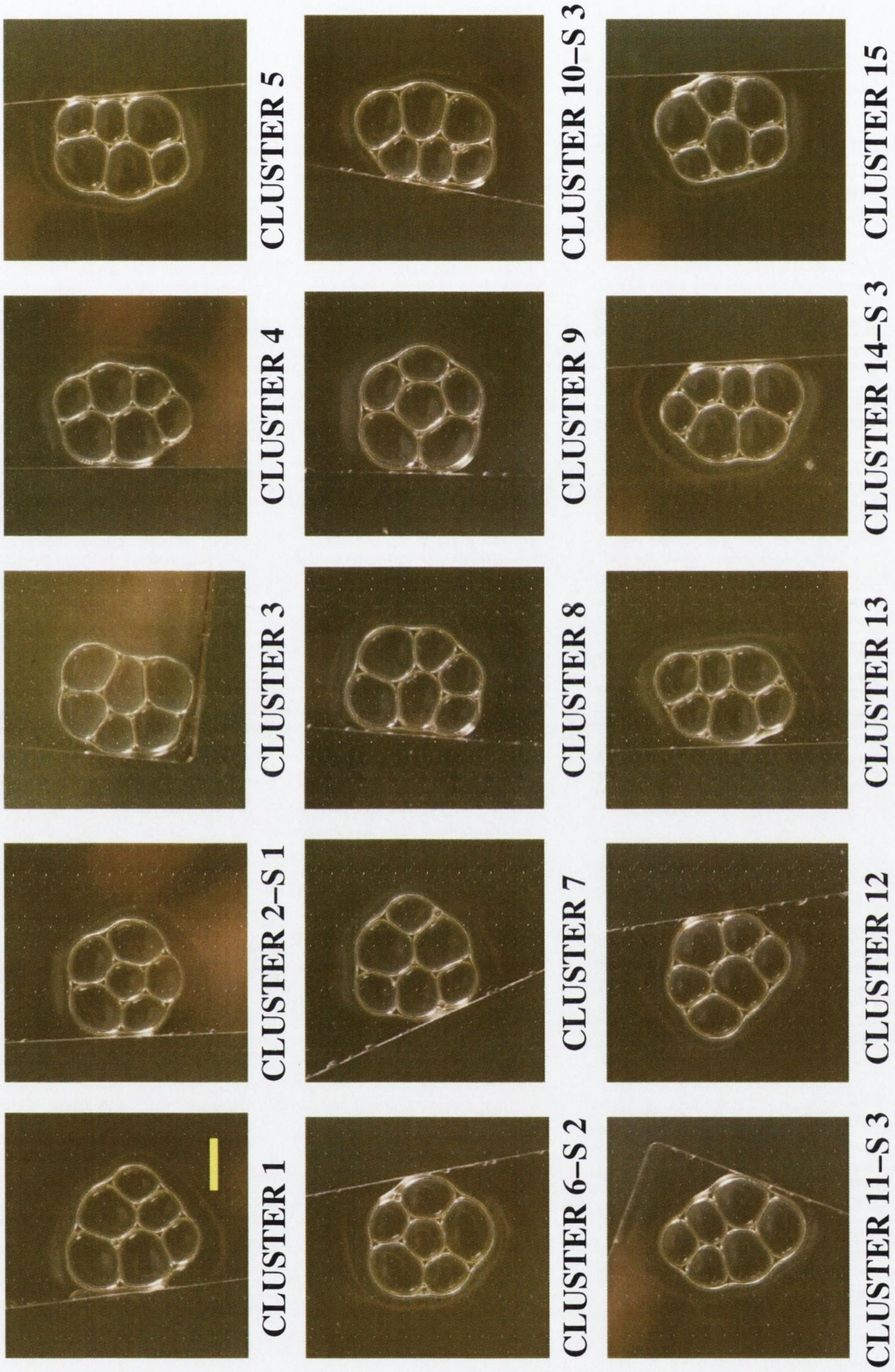
CLUSTER 1
CLUSTER 2–S 1
CLUSTER 3
CLUSTER 4
CLUSTER 5
CLUSTER 6–S 2
CLUSTER 7
CLUSTER 8
CLUSTER 9
CLUSTER 10–S 3
CLUSTER 11–S 3
CLUSTER 12
CLUSTER 13
CLUSTER 14–S 3
CLUSTER 15

Figure B-8: Stable experimental clusters formed by 6 bubbles where $A_M/A_m \approx \frac{4}{3}$. The reference line corresponds to 5 mm in real size. Fifteen candidates are found. The ones that appear more often experimentally (see Fig. B-13 for the complete statistical values) are marked in the picture as S1, S2 and S3.

The relation $A_M/A_m = \frac{4}{3}$ is approximated experimentally using bubbles of radius $r_M = 8\ mm$ and $r_m = 7\ mm$. The real area relation for these clusters is $A_M/A_m = 1.30$. That is, we have an error of 2%, when we compare the experimental and the computational ratio between areas. With the available experimental set-up is difficult to produce bubbles with an exact radius $r_m = 6.93\ mm$ for $r_M = 8\ mm$, which would have given an exact area ratio.

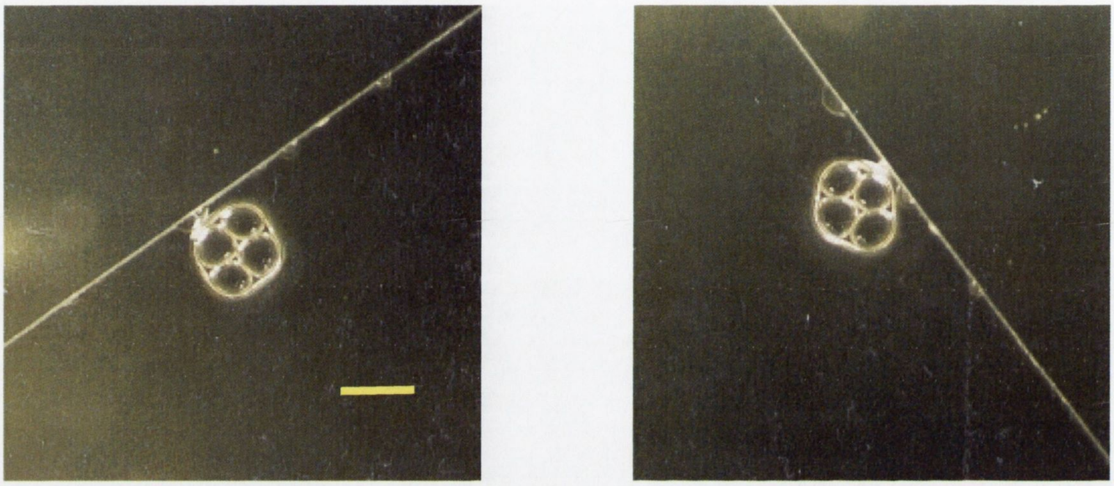

CLUSTER 1 **CLUSTER 2**

Figure B-9: Stable experimental clusters where $A_M/A_m = 2$. The reference line corresponds to 5 mm in real size. Two different clusters are found. The statistic study of occurrence of these clusters (see Fig. B-14) shows a preference to the symmetrical configuration (number 1), where the two small bubbles are separated.

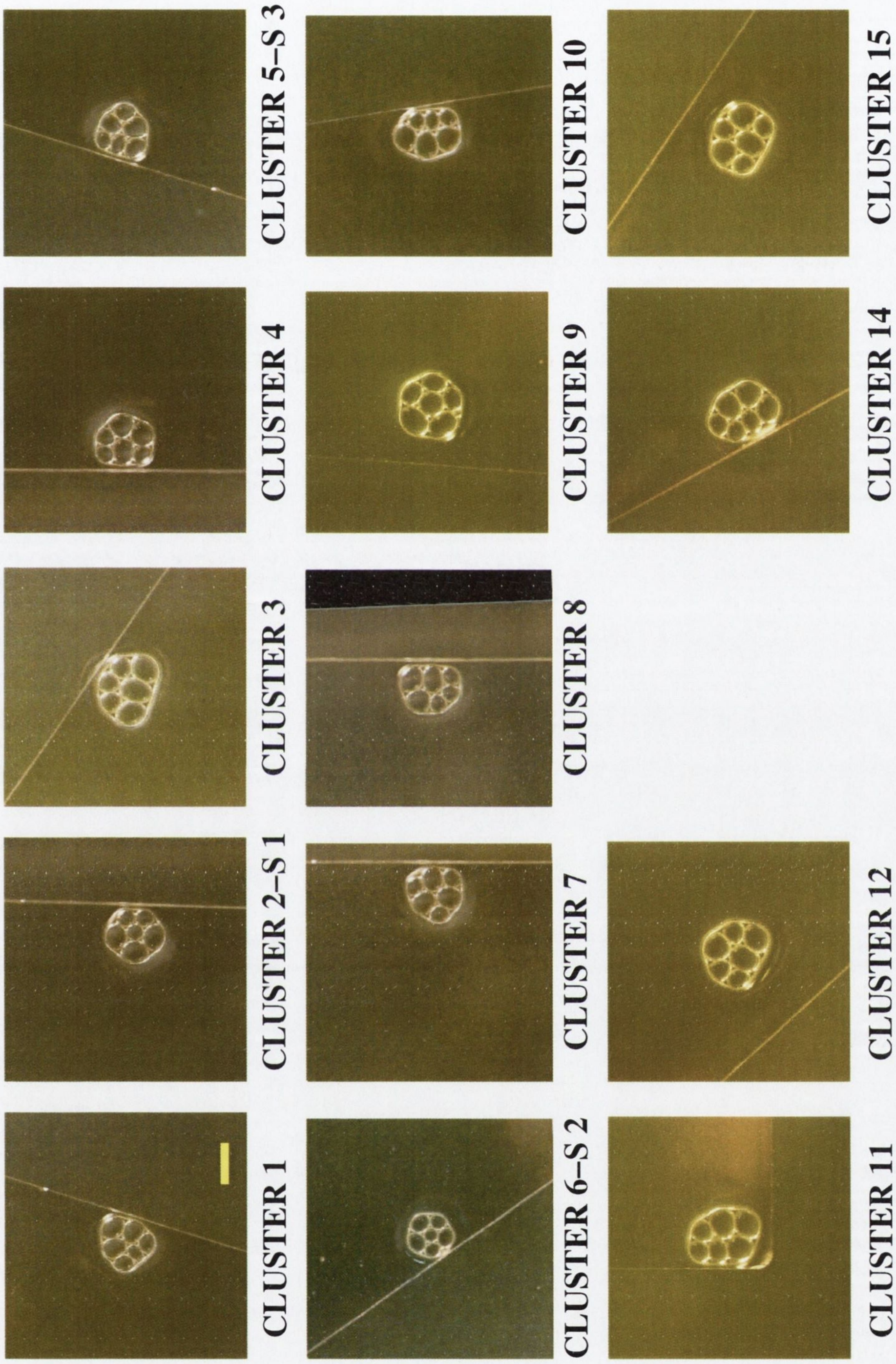
CLUSTER 1
CLUSTER 2–S 1
CLUSTER 3
CLUSTER 4
CLUSTER 5–S 3
CLUSTER 6–S 2
CLUSTER 7
CLUSTER 8
CLUSTER 9
CLUSTER 10
CLUSTER 11
CLUSTER 12
CLUSTER 14
CLUSTER 15

Figure B-10: Stable experimental clusters for 6 bubbles where $A_M/A_m = 2$. The reference line corresponds to 5 mm in real size. We find the same candidates as for $A_M/A_m = \frac{4}{3}$ (Fig. B-8) , except cluster 13. A statistical study of the clusters shows that the most frequent ones are numbers 2, 6 and 5.

The experimental radius for the clusters in Figs.B-9 and B-10 are $r_M = 4\ mm$ and $r_m = 3\ mm$. This gives an area ratio of $A_M/A_m = 1.78$. The error in the approximation to $A_M/A_m = 2$ is around 10%.

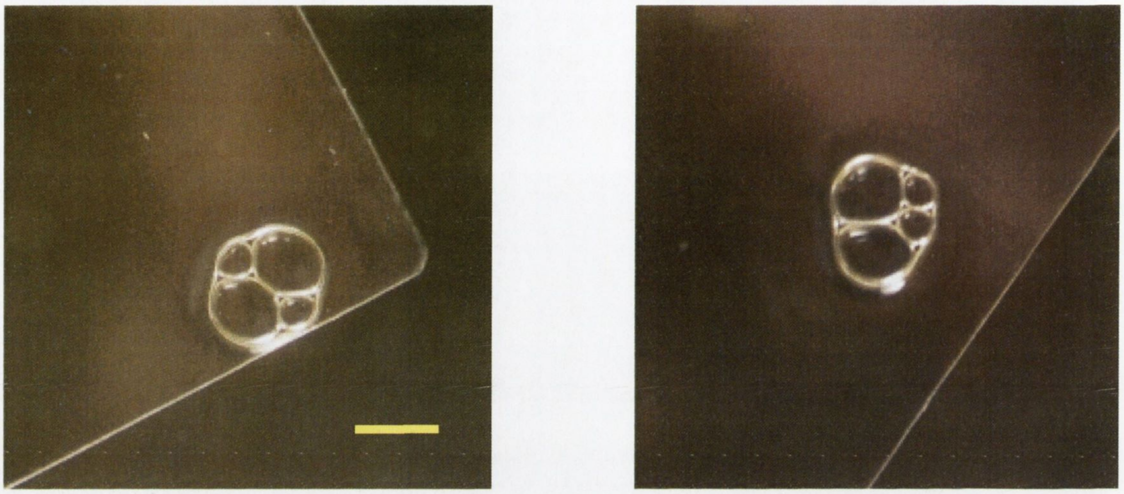

CLUSTER 1 **CLUSTER 2**

Figure B-11: The two stable experimental clusters for 4 bubbles where $A_M/A_m = 4$. The reference line corresponds to $5\ mm$ in real size. The cluster labelled number 1 is statistically more probable than number 2 (see Fig. B-15).

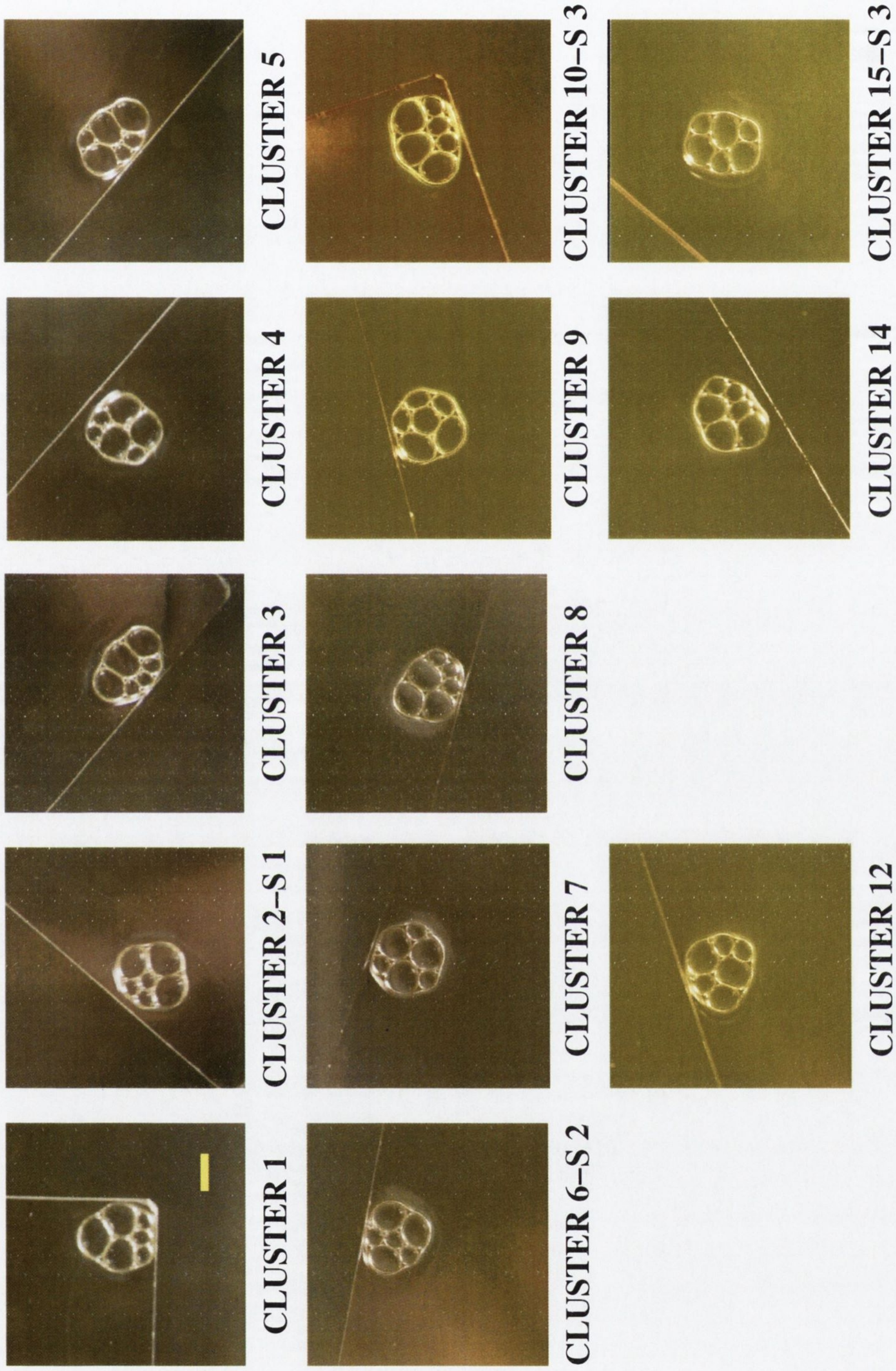
CLUSTER 1
CLUSTER 2–S 1
CLUSTER 3
CLUSTER 4
CLUSTER 5
CLUSTER 6–S 2
CLUSTER 7
CLUSTER 8
CLUSTER 9
CLUSTER 10–S 3
CLUSTER 12
CLUSTER 14
CLUSTER 15–S 3

Figure B-12: Stable experimental clusters with six bubbles with area ratio $A_M/A_m = 4$. The reference line corresponds to 5 mm in real size. The three statistically most favourable clusters (see Fig. B-15) are marked in the picture.

For the last series of experiments, we used bubbles of radius $r_M = 6\ mm$ and $r_m = 3\ mm$. The real area relation for these clusters is exactly $A_M/A_m = 4$. We find again similar candidates to the ones found in other ratios, with a few exceptions.

In order to gain some information about the experimental energy of the clusters, we acquire statistics for the probability of occurrence of the candidate clusters. We start the process with a given set of bubbles and tilt the upper plate until the bubbles separate immersed in the water. The plate is returned to the original position, allowing the bubbles to rearrange in a new configuration. The value of the configuration is noted and the process is repeated around sixty times. Results are in Figs. B-13, B-14 and B-15.

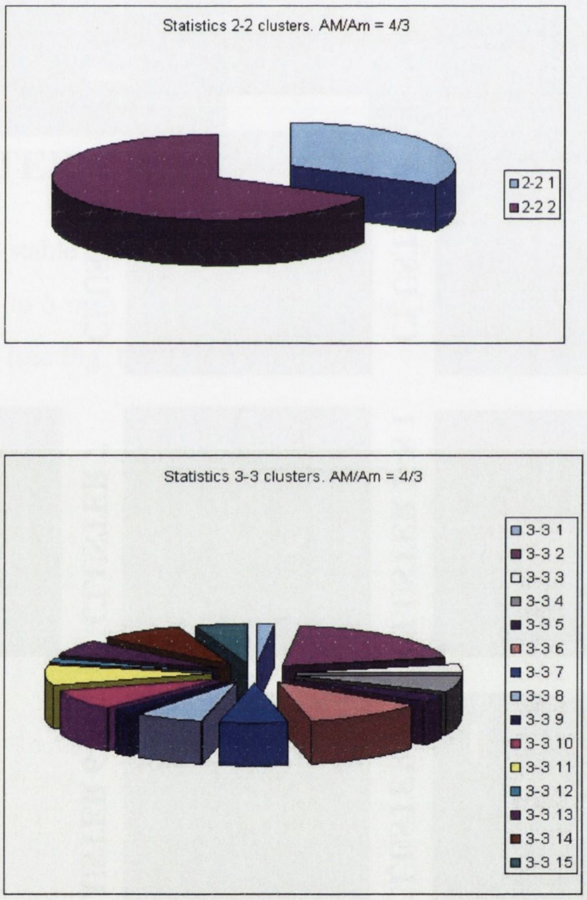

Figure B-13: Statistics that show the probability to find the clusters on experimental trials. In this case, $A_M/A_m = \frac{4}{3}$.

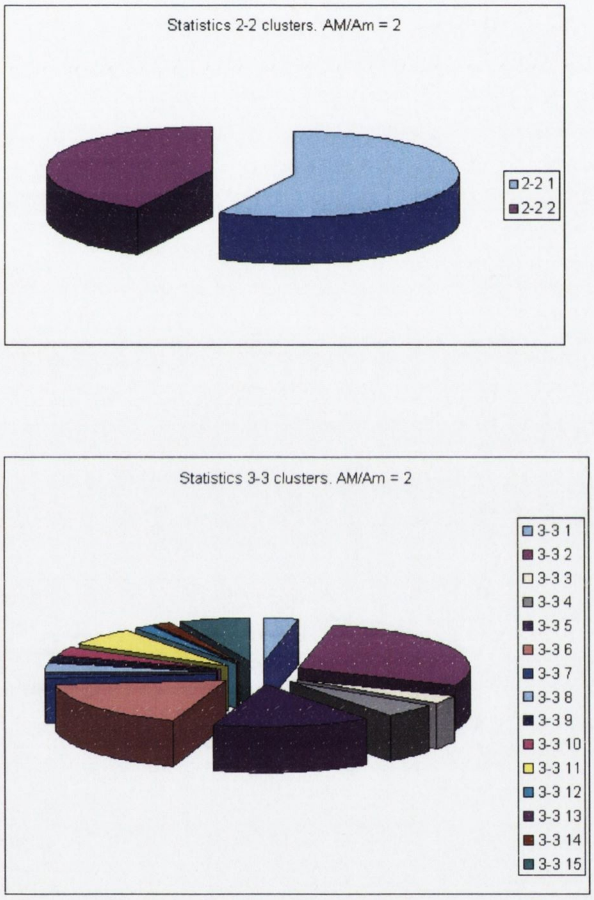

Figure B-14: Statistics that show the probability to find the clusters on experimental trials, when $A_M/A_m = 2$.

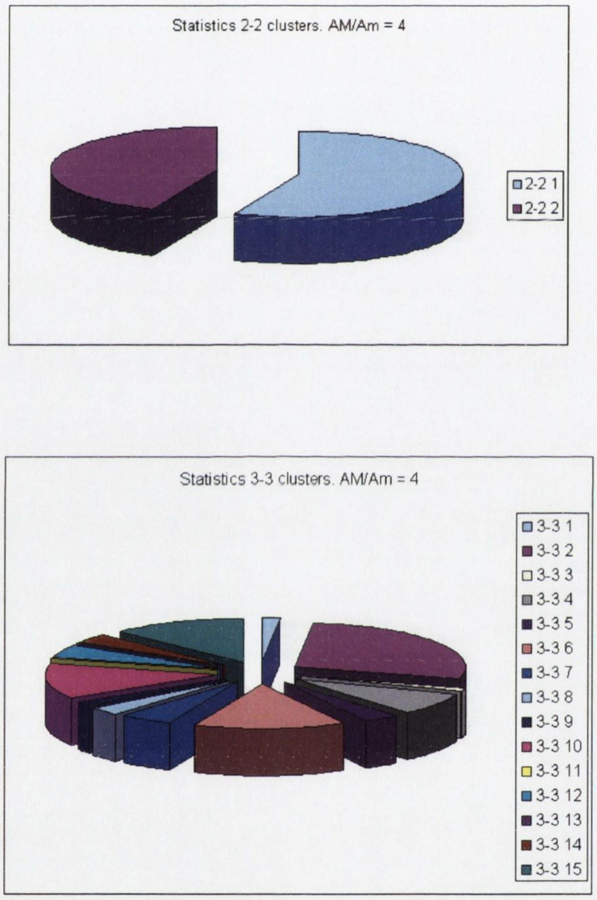

Figure B-15: Statistics that show the probability to find the clusters on experimental trials. In this case, $A_M/A_m = 4$.

The statistics show a change in the occurrence of the $(2, 2)$ clusters when the ratio of the areas approaches 1. The second candidate that was less probable for the higher ratios of areas becomes more probable at $A_M/A_m = \frac{4}{3}$. We do not notice significant differences in the statistics for the three ratios on the $(3, 3)$ clusters. Clusters numbered 2 and 6 are the most frequent in all cases. A look at the experimental pictures reveals that they are both almost circular and have one internal bubble. But this cannot be the only reason that makes them so favourable, as cluster 9, for example, shares the same features. We notice that these two are the only clusters with one internal bubble of area A_m. They adopt the same configuration than the clusters surrounded by a single shell of bubbles calculated by Vaz *et al.* [103], but the bubble sizes are different, making the comparison with the exact calculations on this paper quite difficult. A small central bubble leads to a more circular configuration of the bubbles at the periphery of the cluster and therefore, implies a lower boundary energy.

We have identified so far possible experimental candidates to the minimum configuration in bidisperse clusters with different area ratios. This experimental configurations are reproduced in Surface Evolver, to estimate the energy computationally. We will compare the values of Evolver energies with the statistical values of occurrence of the clusters.

B.4 Evolver calculations

To calculate an estimate of the energy of the clusters found experimentally, we use the Surface Evolver [2]. The calculation process is as follows (see Appendix F for details):

- A basic file reproducing the number of bubbles and a target area for each of the bubbles is written for the Surface Evolver.
- The cluster is forced to the topology found experimentally, forcing $T1's$ (Chapter 1) in some edges until the bubbles have the desired number of neighbours.
- We refine the mesh twice and iterate the minimisation routine until energy converges to within a value of 10^{-6}.

Cluster number	E_{SE}/γ_{foam} *for* $A_M/A_m = \frac{4}{3}$	E_{SE}/γ_{foam} *for* $A_M/A_m = 2$	E_{SE}/γ_{foam} *for* $A_M/A_m = 4$
(2-2) 1	**10.426758**	**9.555029**	**8.483212**
(2-2) 2	10.446446	9.591514	8.529406
(3,3) 1	14.828815	13.582943	12.027617
(3,3) 2	**14.699001**	**13.470386**	11.972402
(3,3) 3	14.858968	13.651651	12.155985
(3,3) 4	14.820343	13.553717	11.985299
(3,3) 5	14.832435	13.601391	12.086763
(3,3) 6	14.701568	13.485487	12.031970
(3,3) 7	14.788875	13.509879	**11.934931**
(3,3) 8	14.833716	13.590822	12.037172
(3,3) 9	14.774599	13.638529	12.275611
(3,3) 10	14.867307	13.654013	12.152186
(3,3) 11	14.863695	13.635199	12.090376
(3,3) 12	14.835380	13.605980	12.093257
(3,3) 13	14.871687	13.677043	12.230237
(3,3) 14	14.873046	13.651222	12.143695
(3,3) 15	14.816419	13.570611	12.048122

Table B.1: Surface Evolver energies for the area ratios $A_M/A_m = \frac{4}{3}$, $A_M/A_m = 2$ and $A_M/A_m = 4$.

- We activate quadratic mode and iterate again until energy converges within the same value.

The results for all the clusters are in table B.1. The minimum energies in each area ratio are set in bold.

The more favourable cluster in the Evolver estimation for the $(2,2)$ is the symmetric one, where the two small bubbles are not neighbours (number 1). In the $(3,3)$ case, the minimum candidate changes from the cluster with rotational trigonal symmetry (number

7) in the $A_M/A_m = 2$ ratio to the one in which all the small bubbles are neighbours, with one of them in the centre of the cluster (number 2) in the other ratios.
However, we can see that the energies are quite close between them. The difference between the lowest and the highest energies for the (2,2) clusters is less than 0.18% in the $A_M/A_m = \frac{4}{3}$. This difference increases when the ratio of areas of the bubbles A_M/A_m increases (0.38% for an area ratio of $A_M/A_m = 2$ and 0.54% for an area ratio of $A_M/A_m = 4$). An increase in the area mismatch increases the difference between the energies of the configurations. Graner et al. [102] expect this, as we have mentioned in subsection B.2.1. The same tendency happens in the (3,3) clusters which go from a difference of less than 1.2% in the $A_M/A_m = \frac{4}{3}$ to 2.85% for an area ratio of $A_M/A_m = 4$.

We would expect that the clusters that have lower energy would appear more often experimentally. However, comparison of the statistics made for the experimental clusters with their calculated energies show a weak correlation, as in Vaz and Fortes [99].

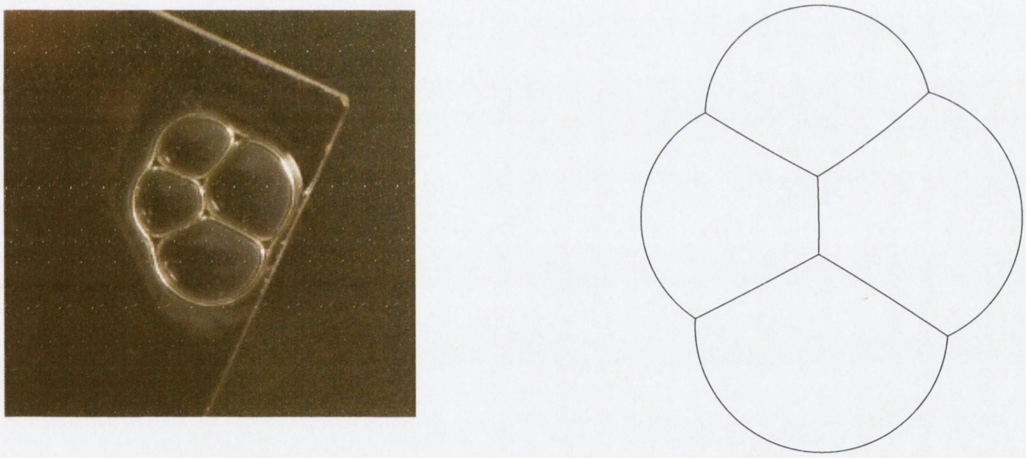

Figure B-16: The $(2,2)$ cluster number 2 for the area ratio $A_M/A_m = \frac{4}{3}$. The experimental picture is shown together with the Evolver simulated shape. This cluster appears experimentally more often than expected, giving its calculated energy.

For the $(3,3)$ clusters, even if the candidates that appear more often experimentally have a low Evolver energy, clusters with very high evolver energy also occur very often (Figs. B-13, B-14 and B-15). In the $(2,2)$ clusters, at a ratio $A_M/A_m = \frac{4}{3}$, number 2 appears more often experimentally than it would be expected by its energy estimation in Evolver (Fig. B-16). This may be due to close energy values, an insufficient number of cases in the statistics or other energy contributions, which have been neglected. The neglected terms include the Plateau border contribution. It can be appreciated in any photograph of the clusters that the film edges do not join in a single vertex, but form Plateau channels (see Section 1.4.2). Our experimental clusters are in contact with a pool of surfactant and they are not dry (this is not so important to obtain the candidate topologies but has to be considered when comparing the energies).

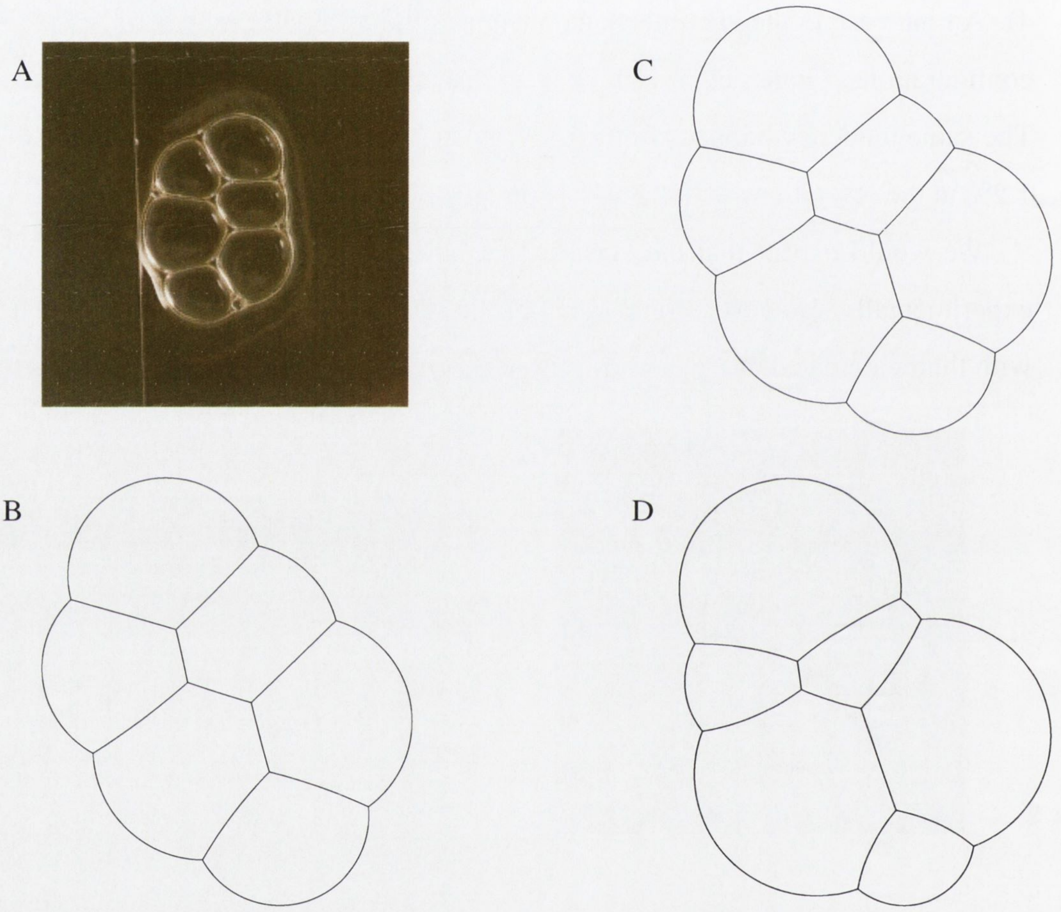

Figure B-17: The $(3, 3)$ cluster number 13. A/ Experimental picture at a ratio $A_M/A_m = \frac{4}{3}$. B/ Evolver calculated shape for the same ratio and topology. C and D/ Evolver calculated shapes for the same topology and ratios $A_M/A_m = 2$ (C) and $A_M/A_m = 4$ (D). The cluster does not appear experimentally for these ratios. The length of the edges at the small bubbles at the calculated shape (D) suggest that the cluster may be prone to have a $T1$ and become a new configuration.

Clusters that do not appear experimentally at certain area ratios can be reproduced and studied with the Surface Evolver (Fig. B-17). These clusters have a high energy and the calculated shapes may not be very favourable at some of the area ratios.

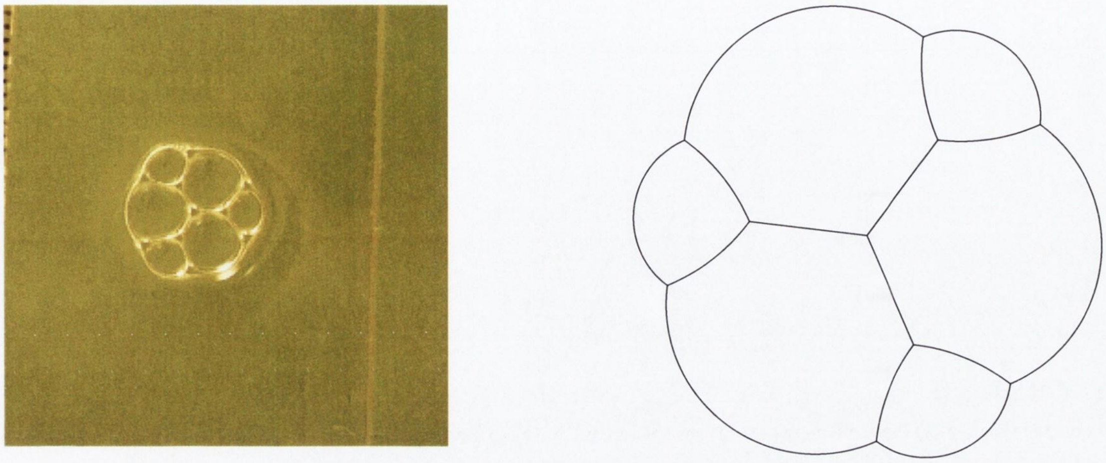

Figure B-18: Cluster $(3, 3)$ number 7 becomes the one with less calculated energy at an area ratio $A_M/A_m = 4$.

The cluster with rotational trigonal symmetry becomes more favourable for the area ratio $A_M/A_m = 4$. This is interesting, as the cluster shape (Fig. B-18) remind us of the partition proposed by Teixeira *et al.* [108] to calculate the lower bound in Eq. B.7.

B.5 Analysis of results

We can compare the energies calculated in the Surface Evolver, which we denote as E_{SE}/γ_{foam}, with the possible theoretical lower bounds suggested in Eq. B.8 and Eq. B.9 (Fig. B-19).

The energy of all the bidisperse candidate clusters lies close to both theoretical lines, so we can consider them as good estimates of the energy of polydisperse 2D clusters. These equations were both suggested as lower bounds for the energy, but it is clear that the calculated energies of some of our clusters lie below the proposed lower bound. This can be attributed, as in Vaz et al [103], to the low number of bubbles studied in the clusters ($N \leq 10$) in the work described here.

An interesting observation when A_M/A_m changes is that some configurations that had an elongated perimeter for the lower area ratios, such as $(3, 3)$ number 4 and $(3, 3)$ number 12, become more rounded in the higher area ratio. This has an effect in their calculated energy (that becomes lower in relation with the energies of the other candidates) and their statistical performance. The results are still partial, as the number of bubbles N studied is

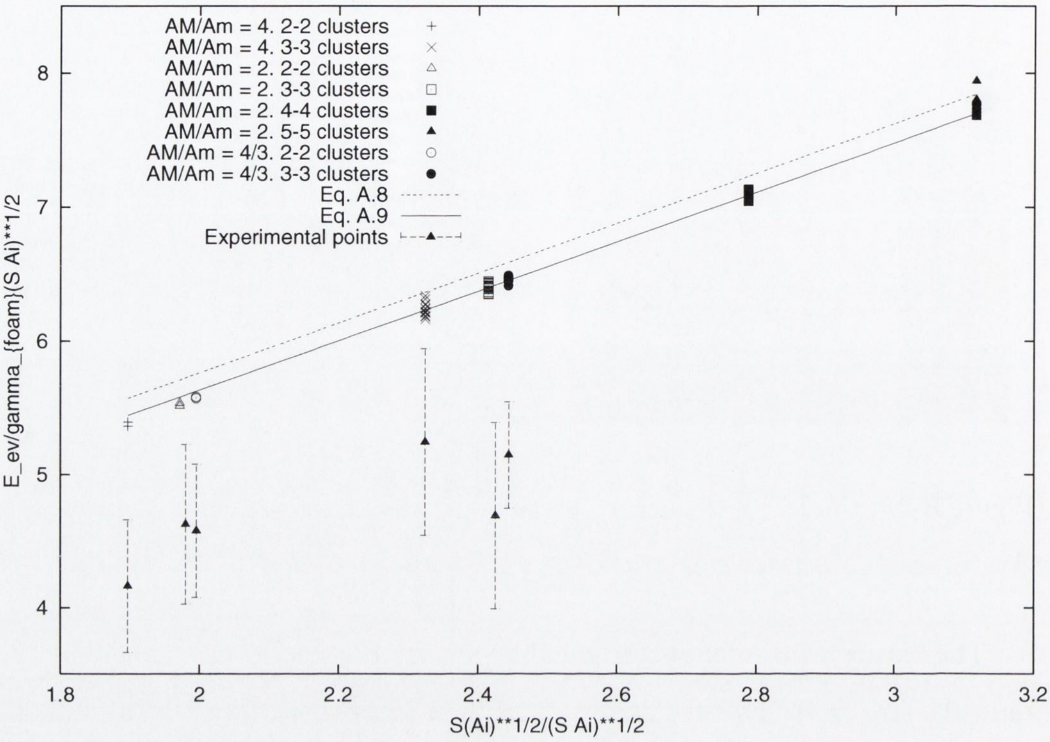

Figure B-19: The calculated energy of all clusters is presented here and compared with the lower bound calculated for polydisperse clusters and round boundary, Eq. B.8, and the lower bound calculated for bidisperse clusters and hexagonal boundary, Eq. B.9. The values are close to the theoretical equations, even if the number of bubbles N is quite small. However, some of the calculated energies of our clusters are below the possible lower bounds. This was expected, as Eq. B.8 and Eq. B.9 are deduced for clusters with a large number of bubbles. The experimental values included correspond to the minimum energy clusters obtained in Table B.1. The experimental values for $E/\gamma_{foam}\sqrt(SA_i)$ are around 10% below the energies predicted by the theoretical lines. These lower energies can be attributed to the experimental set-up, in which the bubbles are in contact to the surfactant liquid pool.

very low this time. But this still suggests that the idea of the rounded or hexagonal bounded clusters being the minimal ones is quite reasonable, as it was suggested in Section B.2.

The energy for the minimum experimental clusters (in bold at table B.1) has been estimated by taking the skeleton of the bubble clusters in the pictures and measuring their perimeters with Adobe © Photoshop. The areas of the bubbles are calculated using the values of the bubble diameters measured in the lab. The values are clearly below the expected theoretical values. This is partly due to the error attached to the digital handling of the images, but also reflects the fact that our clusters are floating in a pool of surfactant liquid during the experiment and therefore, their liquid fraction is non-zero, making the estimate of the energy more difficult to achieve.

It is noted that the difference in energy between the lowest and the highest configuration increases with area mismatch. As A_m approaches the value of A_M, we are getting closer to the monodisperse cluster situation and therefore, the difference in energies between the configurations becomes less wide, as expected.

B.6 Conclusions and Outlook

As we have seen, the theoretical formulas predicted in Vaz *et al.* [103] give a very good approach for the energy of dry 2D bidisperse clusters. These formulas were derived for round symmetrical clusters and were expected to work better with clusters with a high number of bubbles N.

Even though we have not studied all the possible clusters with our method, our examples suggest that the candidates obtained from experiments contain indeed the lowest energy cluster. Our partial results show that, for the surface Evolver energies, the agreement is good in the dry limit even for clusters with a limited number of bubbles. A more exhaustive investigation that includes clusters with $N > 10$ will establish if these preliminary results are correct. Area mismatch in the clusters (a bigger A_M/A_m ratio) increases the energy gaps between configurations. However, the difference in energy between the clusters is quite low and the Plateau border contribution seems to be fundamental in the case of experimental clusters. The Surface Evolver can calculate the Plateau border contribution if we provide the Plateau border area. The problem lies in the difficulty to determine the Plateau border size from the pictures, as we have seen in Appendix A.

Anyway, it would be interesting to try to estimate the experimental cluster energies, even if it is in a dry limit approach. We can see in some of our pictures that the films shared by two bubbles of the same area are not straight lines, as it would be if their pressures were equal. This aim can be achieved by using two programs developed by MacLeod [111] and Foley [112]. Foley has produced a program that allows to minimise a 2D foam. It uses as an input the vertices and the connectivity between them (easy to deduce from the photographs that we have taken) and calculates the film final geometry, represented by circular arcs and the internal pressure of the bubbles. This is equivalent to calculate the real areas of the experimental cluster. MacLeod's code reproduces graphically the cluster from the topology and the areas given by Foley's program. We hope that this can explain further the variations in energy between the experimental and the theoretical case.

Appendix C

The channel-dominated form of the foam drainage equation

We neglect the flow through the films and accept that most of the liquid drains through the Plateau borders. The channels are reduced to a net of N independent pipes. Treating the liquid as incompressible, it is possible to obtain the equation of continuity for a single Plateau border vertically oriented,

$$\frac{\partial A(x,t)}{\partial t} + \frac{\partial}{\partial x}[A(x,t)u(x,t)] = 0, \tag{C.1}$$

where $A(x,t)$ is the cross-section of the Plateau border and $u(x,t)$ is the velocity of the fluid averaged over the cross-section. Both magnitudes depend on a downward vertical coordinate x and time t.

In a Plateau border, there is a dissipative (viscous) force due to flow which is balanced by gravity and the pressure gradient. Here comes the most controversial assumption of this calculation: that dissipation of flow occurs by shear at the channel walls and the dissipation at the nodes is not significant. This is known as flow of Poiseuille type. In the element $A(x,t)dx$ the balance of forces gives the equation,

$$\rho g - \frac{\partial}{\partial x}p_{liquid} - \frac{\eta_{liquid} f u(x,t)}{A(x,t)} = 0, \tag{C.2}$$

where ρ is the density of the foam, g the gravity constant, p_{liquid} the pressure on the fluid,

η_{liquid} the viscosity and f a factor that depends only on the shape of the channel.

For a monodisperse foam we can write the Young-Laplace equation, that relates the gas pressure difference inside and outside the bubble with the radius of the bubble, in terms of $A(x,t)$,

$$p_{liquid} = p_{gas} - \frac{C\gamma}{\sqrt{A(x,t)}}, \tag{C.3}$$

where $C = \sqrt{\sqrt{3} - \pi/2}$ and γ is the surface tension.

Introducing the value of p_{liquid} obtained from Eq. C.3 into Eq. C.2, $u(x,t)$ can be written as a function of $A(x,t)$. It is therefore possible to write Eq. C.1 as a function only of A.

Although derived for a single vertical Plateau border, the equation can be adapted to the case of a network, by the incorporation of various constants. Weaire *et al.* consider the foam to be isotropic, average over the different orientations of the Plateau borders, and use a change of variables to achieve the final result in Eq 1.8:

$$\frac{\partial \alpha}{\partial \tau} + \frac{\partial}{\partial \xi}\left(\alpha^2 - \frac{\sqrt{\alpha}}{2}\frac{\partial \alpha}{\partial \xi}\right) = 0. \tag{C.4}$$

The solutions of the equation are of various kinds of which the very simplest is just $A = constant$, the steady drainage case.

In work that deals with very *wet* foam, as in much of this thesis, many of the approximations inherent in the above equation must be treated with scepticism. One of their more interesting failings (because it may introduce extremely new effects) is the lack of any allowance for deformation of the structure due to fluid flow. Indeed the deformation may even proceed to the point of local structure instability. This has been observed in wire frames [1] but it is not usually seen in foams: we suspect it takes over as the primary instability of steady drainage for very large bubbles. In Appendix F we sketch a possible approach to this problem.

Appendix D

Experimental foam production

There are many procedures to obtain a foam, but not all are suitable for the same purposes. We reproduce in Fig. D-1 a picture of the results of different foam production methods from Hutzler et al. [113]. Normally, blending and whisking methods lead to highly polydisperse foam and blowing gas in a controlled manner, produces more regular foams.

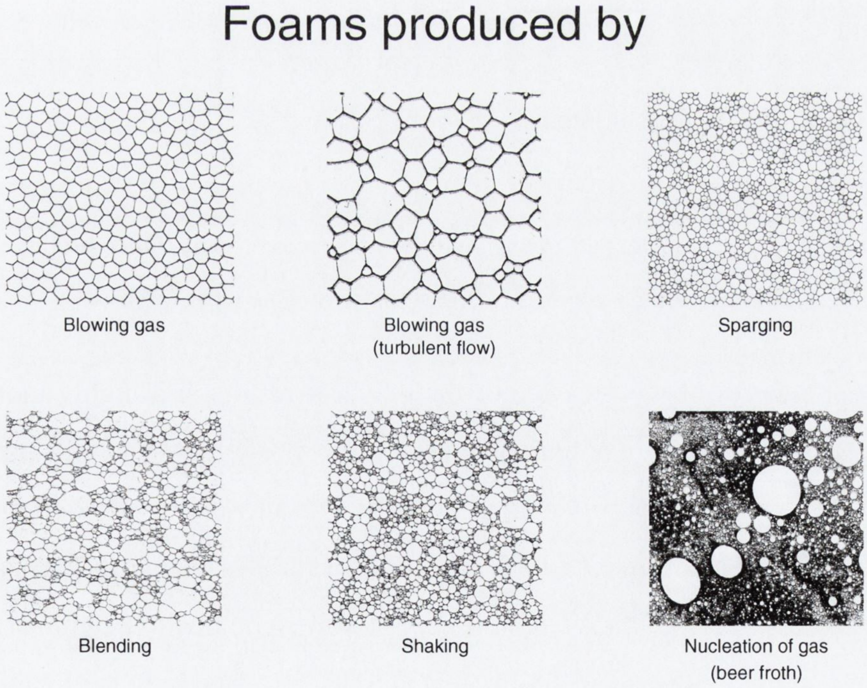
Foams produced by
Blowing gas
Blowing gas (turbulent flow)
Sparging
Blending
Shaking
Nucleation of gas (beer froth)

Figure D-1: Foam produced by several different methods. The dispersion in bubble size is less for the blowing production methods. Reproduced from [1, 113].

Much of the work done for this thesis involves producing monodisperse aqueous foam at different bubble sizes. This excludes the foam formed for the experiments described in Chapter 2, in which the main interest was to get a bubble size small enough to consider the foam a continuous medium.

The procedure we use to obtain monodisperse bubbles is to blow gas (air or nitrogen) through a nozzle or a syringe needle into surfactant solution. The surfactant solution is Fairy Liquid in water at approximately 2% in volume. A sketch of the experimental set-up is shown in Fig. D-2.

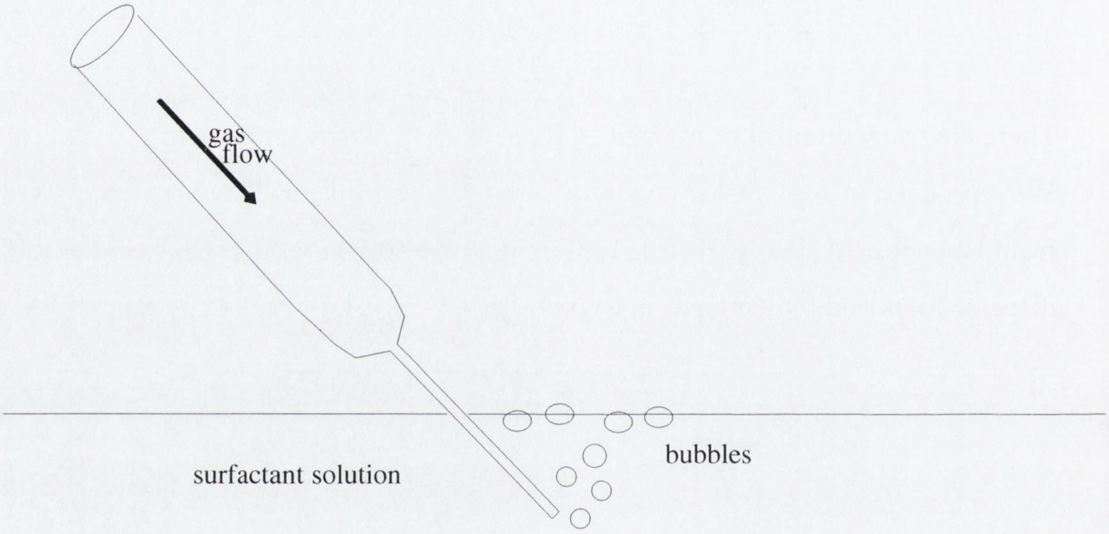

Figure D-2: Experimental set-up to obtain monodisperse foams. Once produced, the foam can be introduced into different geometries to carry out 3D or 2D experiments.

Good control of the pressure of the gas flow results in a highly monodisperse foam. The gas tap provides a maximum gauge pressure of 3 N/m^2, [1] but this pressure results in a turbulent flow that gives polydisperse foam as a result, very close to a bimodal distribution, as pictured in Hutzler et al. (see Fig. D-1). The best range in pressures to produce a monodisperse foam is 0.5 N/m^2 to 1 N/m^2, corresponding to a laminar flow. This allows to grow ordered columns of foams that can be introduced in small capillary tubes. It is possible to grow up to several tens of centimeter without defects.

Bubble size can be controlled primarily by using nozzles with different cross-sections. For the smaller bubbles (0.5 mm to 0.8 mm in radius), we use special nozzles with a small circular cross-section of less than 1 mm in diameter. In some cases, the nozzle has to touch the bottom of the basin. The result is a partial block at the opening of the nozzle that allows us to obtain smaller bubble sizes. Intermediate and big bubble sizes (0.8 mm to 4.0 mm) are produced with syringe needles of elliptical cross-section. Polydisperse foam with a very small bubble size, as the one we use in Chapter 2, is produced by attaching a sparger to the gas source.

---

[1] $1\,N/m^2 = 1Pa$

The bubble size is measured with the aid of small capillary tubes when we are using monodisperse foam. An ordered structure, as the ones described in Chapter 13 of [1], is grown on a tube of known diameter. The volume of a section of the tube is divided by the number of bubbles contained in that section. The measurement is extended to a large number of bubbles to minimise the errors. We have not quantified polydispersity in all the experiments, but it is possible to estimate it from the bubble size measurements. In the worst cases, only one every twenty fifth bubbles introduces a small defect in the ordered structures we grow on the capillary tubes. The bubble size of this defects is quite close to the one of the regular bubbles. This gives less than 5% defects in our foam, which can be taken as quite monodisperse.

Another effect that can affect the bubble size is the coarsening of the foam. The diffusion of the gas through the films causes an enlargement of the average size of the bubbles. Bigger bubbles have a lower gas pressure than smaller bubbles. The gas diffuses to the area of lower pressure and big bubbles tend to coarsen at the expense of the small ones. This diffusion is related with the gas solubility, as mentioned in [1]. We can compare the values of solubility of pure gas at 1 atm and 20^oC for $N_2 = 7.0\ 10^{-4}\ molL^{-1}$, air = $7.9\ 10^{-4}\ molL^{-1}$, $O_2 = 1.3\ 10^{-3}\ molL^{-1}$, and $CO_2 = 2.3\ 10^{-2}\ molL^{-1}$ [114]. The values of N_2 are the best to minimise coarsening in the experiments. Results of the effects of coarsening of air foams under forced drainage, show that this coarsening is neglectable over a time scale of thirty minutes [40]. All the experiments described here are well below this time, including the stage of foam formation. The growth of the column depends on the tube length and diameter and the bubble size we are producing. The rates of growth vary quite a lot, but a rough idea of the time-scale can be inferred from the following extreme examples:

- in a $1.5\ cm$ diameter and $20\ cm$ length tube, using $4\ mm$ radius bubbles, it will take a few seconds to fill in the tube,
- using the sparger (small bubbles with a radius less than $0.5\ mm$) with in the tube of $4\ cm$ diameter, it takes around thirty minutes to fill in the tube.

In most of our experiments we have worked with wet foam. Once we have produced the foam, we will measure its experimental liquid fraction. In simple geometries, like rectangular or cylindrical containers, where the foam is in contact with the surfactant solution, the average liquid fraction of a foam can be estimated experimentally using the Archimedes principle [115]:

$$\phi_l = \frac{h}{H}, \tag{D.1}$$

where h is the depth which the foam reaches below the surface of the liquid and H is the total length of the foam (Fig. D-3).

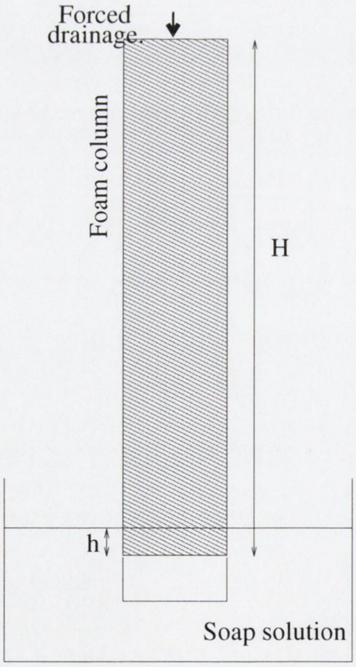

Figure D-3: Experimental set-up to obtain monodisperse foams. Once produced, the foam can be introduced into different geometries to carry out 3D or 2D experiments.

Appendix E

Fluent

We have used FLUENT, a flow dynamics software package, in order to make computations of the Stokes experiment in Chapter 2. FLUENT allows to model fluid flow and heat transfer in complex geometries. These geometries can be meshed in a very flexible way, allowing even to adapt the refining of the mesh based on the flow solution. These can be useful to determine which regions require a more refined mesh and therefore, can save computational effort. As FLUENT is written in C computer language, it is possible to write scripts to handle particular flow types, such as the Bingham model (Eq 1.15) or the Herschel-Bulkley model (Eq 1.16).

FLUENT solves the general conservation equations for mass and momentum for inviscid flows, with the appropriate boundary conditions. Depending on the solver formulation chosen the equations will be solved segregated, first the momentum equation, and once solved this, the continuity equation, or coupled (simultaneously solving both flow equations). In both cases, the solver divides the geometry into discrete control volumes (computational grid) and integrates the flow equations on the individual control volumes to get algebraic equations of magnitudes such as velocities, pressure and temperature. These algebraic equations, once linearised, constitute a linear equation system whose variables are the values of the magnitudes. The results are the same, regardless of the type of solver formulation chosen. The only advantage of using one or the other, is to obtain a speedier convergence in the values of flow.

After determining the features of the problem that we want to solve, the procedure of the FLUENT calculations is the following:

1. Create the mesh using the preprocessor package, GAMBIT.
2. Start the program for 2D or 3D models.
3. Import and check the grid. It is possible to scale the grid in this step, to allow a change of units.
4. Select the solver formulation if desired. Segregated is the default.
5. Create or select the fluid properties from the database.
6. Specify the boundary conditions.
7. Adjust the value of the residuals to control the accuracy of the solution.
8. Initialise the flow field and iterate until convergence.
9. Examine and save the results.
10. If necessary, refine the mesh or the parameters of convergence and repeat the calculation from step 8.

Appendix F

Surface Evolver

The Surface Evolver [1] is used to perform calculations minimising bubble clusters in Appendix B in this thesis. It is a computer program that minimises the energy of a surface subject to constraints [2]. It was developed by Professor Kenneth Brake [2] during his participation in the Geometry Center Project [3] at the University of Minnesota. The capacities of this piece of software include many possibilities, the main being:

- the capacity to perform calculations on N-dimensional surfaces, using the different surface modes;
- it deals with any energy that can be represented as an integral over the surface;
- different constraints and boundaries at the surface can be imposed;
- it is possible to refine and change the surface during iteration;
- it can be used with or without graphics. Compatible with Geomview [4].
- the output can be easily dumped in several image formats.

Thus, the Surface Evolver has been widely used in various environments and problems, as computing capillary forces at non-cylindrical geometries, simulating grain growth and studying the shape of molten solder on microcircuits. One of the problems tackled with the Surface Evolver is the equilibrium structure of soap films (foam) [116].

---

[1] The Surface Evolver is available free of charge at www.susqu.edu/facstaff/b/brakke/evolver/evolver.html

[2] www.susqu.edu/facstaff/b/brakke/

[3] www.geom.umn.edu

[4] Geomview is an interactive graphic viewer that allows, among any other capacities, direct rotation of the surface on screen. It can be found at www.geom.umn.edu/locate/geomview/

The Surface Evolver uses a finite-element approach to represent a surface. We can reduce a complex figure to a compound of small triangulated surfaces or facets. The Surface Evolver will work from a simple approximation to the surface provided, if they have the same topology. This simple topology is defined using vertices (points), edges that connect the vertices and faces enclosed by a series of edges. The Surface Evolver will triangulate automatically any face that has not this shape. A closed group of facets can form a body.

The Surface Evolver deals with different models of surfaces during calculations. The different models available, attending to the surface representation are:

- **String model**: For one dimensional surfaces.
- **Soapfilm model**: For two dimensional surfaces.
- **Simplex model**: For n-dimensional surfaces with $n \geq 3$.

There are also different models of representing the surface elements:

- **Linear model**: The elements that join the vertices are lines and the facets are flat.
- **Quadratic model**: Lines and flat facets are substituted by quadratic curves and patches, by interpolating a middle point between two vertices.

Default calculations in the Surface Evolver use Soapfilm model and Linear model. At some stages in our calculations we have made use of the String model and Quadratic model.

Surface Evolver performs calculations in iterative steps. The surface evolution uses a gradient-descent method. Each step will:

1. Calculate the force at each vertex.
2. Projects the forces to be tangent to the constraints for the elements if necessary.
3. Save the current vertex positions.
4. Moves the vertex in accordance with the force calculated in step 1.

5. Projection of the elements out of place to the constraints.
6. Recalculates the new energy values.
7. Performs a check in the increase of energy, when this option is activated.
8. Prints the new values and re-displays the surface if graphics are on.

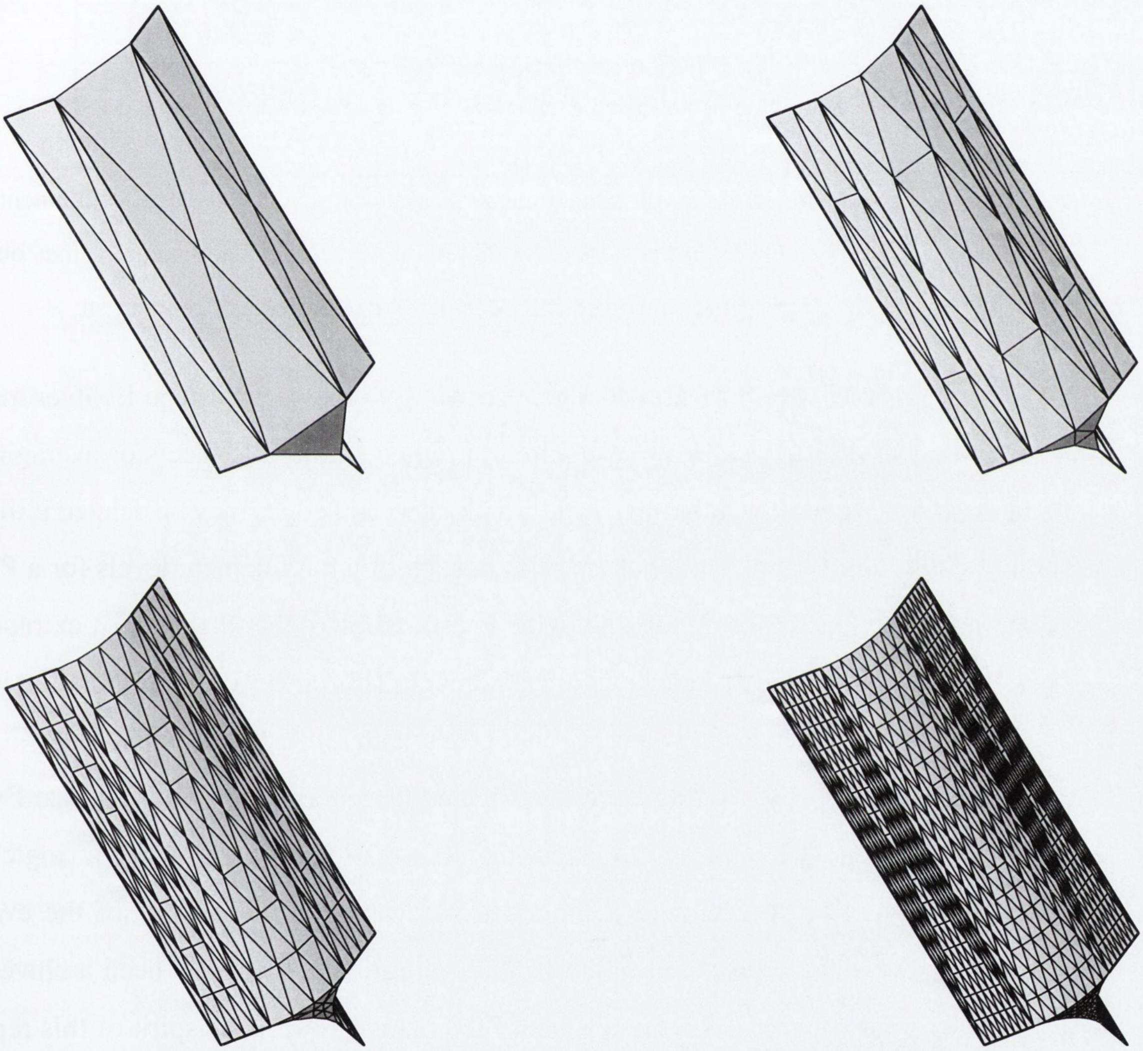

Figure F-1: Images of a Plateau border at different stages of an Evolver calculation. A- Starting topology for the Plateau border. B- One level of refinement after 500 iterations. C- Two levels of refinement after 500 iterations. D- Three levels of refinement after 500 iterations.

The Surface Evolver allows to refine the surface, *i.e.*, interpolate new vertices to get a finer mesh, while there is memory available in the computer. Fig. F-1 shows a Plateau border at different levels of refinement.

Refinement level	Final energy	Extrapolated energy
0	1.37942	
1	1.35594	
2	1.35405	1.35388
3	1.35356	1.35339
4	1.35344	1.35340
5	1.35341	1.35340

Table F.1: Final energies for the iterated Plateau border for several levels of refinement. The column on the right is a power law extrapolation based on the previous and actual values obtained for the energy. The energy value converges to 1.35340 at the sixth level of refinement.

Convergence is very difficult to judge, according to the own Surface Evolver manual. Hand tuning of the surface is often required. Equiangulating the facets or averaging the vertices provides a more regular mesh and small facets and edges may be deleted if they are stalling the minimisation. The final energies at each of the refinement levels for a Plateau border are shown in Table F.1, together with an estimation of the final energy, extrapolated from the values obtained at each level of refinement. This power law extrapolation is very useful for complex structures, where it is not possible to refine to this extent.

As noted in Appendix C, we have investigated the interfacing of the Surface Evolver and Fluen (Appendix E) in order to assess the deformation due to flow for a single tetrahedral junction. While extensive technical work was done, the results of the eventual calculations were not considered reliable. Accordingly this work has been archived in a separate internal Technical Report for the TCD Foams Group. The spirit of this report is contained in Fig. F-2.

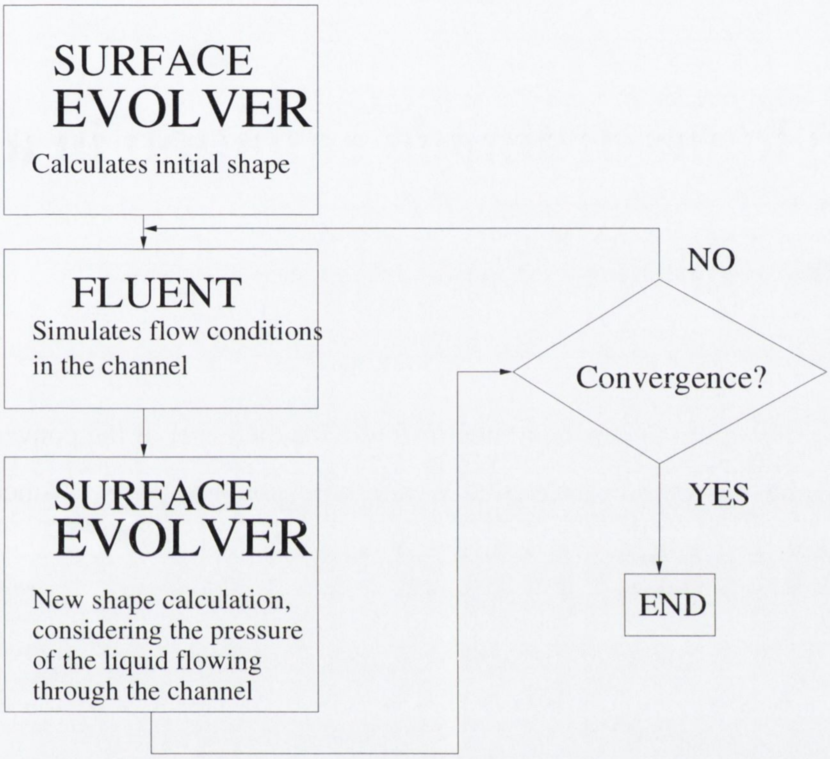
SURFACE
EVOLVER
Calculates initial shape
FLUENT
Simulates flow conditions
in the channel
SURFACE
EVOLVER
New shape calculation,
considering the pressure
of the liquid flowing
through the channel
NO
Convergence?
YES
END

Figure F-2: The diagram shows the method followed in our calculations of flow induced deformation in tetrahedral junctions. First, the channel shape is calculated using the Surface Evolver. The surface is meshed using the preprocessor included in the Fluent package, Gambit and we simulate flow conditions inside the channel. The flow produces a force at the walls of the channels which can be introduced as a new boundary condition in the Surface Evolver. At that point, we compare the result of our calculation with the surface obtained at the previous step. If their energies differ by less than 0.01%, we consider the result converged.

Appendix G

The foam drainage equation in a tilted tube

This is a derivation of the theoretical formula for the onset of the convective instability in a tilted tube, developed by Cox and Weaire in response to the experimental results of this thesis [85].

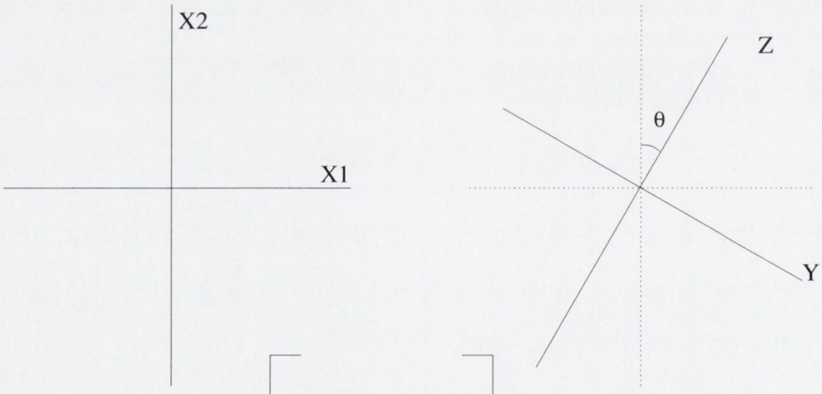

$$M = \begin{bmatrix} -\sin\theta & \cos\theta \\ \cos\theta & \sin\theta \end{bmatrix}$$

Figure G-1: The tilted tube changes its orientation with respect to gravity. The axis X1 and X2 are tilted an angle θ to get the new set of axis in which Z is parallel to the axis of the tube. M is the matrix that rotates the system X1-X2 into the new system Y-Z.

We will employ the channel-dominated two-dimensional form of the drainage equation, as it appears in Cox et al. [11],

$$\frac{\partial \alpha}{\partial \tau}+\frac{\partial}{\partial \xi}\left(g\alpha^2-\frac{\sqrt{\alpha}}{2}\frac{\partial \alpha}{\partial \xi}\right)-\frac{\partial}{\partial \eta}\left(\frac{\sqrt{\alpha}}{2}\frac{\partial \alpha}{\partial \eta}\right)=0, \tag{G.1}$$

where α is the cross-section of the Plateau border and (ξ, η) its position (see Fig. G-1) at a time τ. The acceleration due to gravity g has been included explicitly.

The tube that contains the foam is tilted an angle θ. We can define a new coordinate system, with the two new coordinates along and perpendicular to the axis of the tube, as in Fig. G-1:

$$Z=\xi\cos\theta+\eta\sin\theta \quad \text{and} \quad Y=-\xi\sin\theta+\eta\cos\theta.$$

When this change of coordinates is applied to Eq. G.1, it becomes:

$$\frac{\partial \alpha}{\partial \tau}+\frac{\partial}{\partial Z}\left(g\cos\theta\,\alpha^2-\frac{\sqrt{\alpha}}{2}\frac{\partial \alpha}{\partial Z}\right)-\frac{\partial}{\partial Y}\left(g\sin\theta\,\alpha^2+\frac{\sqrt{\alpha}}{2}\frac{\partial \alpha}{\partial Y}\right)=0. \tag{G.2}$$

If the flow rate is constant (steady drainage), then the time derivative in the equation $\frac{\partial\alpha}{\partial\tau}$ can be neglected. These conditions lead to two separate equations that relate the balance of flow in the Y and Z directions. The boundary conditions on the flow are constant flow rate Q in the Z direction, and zero flow at the walls in the Y direction.

The condition of zero flow at the walls leads to the absence of flow in the Y direction. Under these hypothesis, $\alpha=\alpha(Y)$ and it has to satisfy

$$g\sin\theta\,\alpha^2+\frac{\sqrt{\alpha}}{2}\frac{\partial \alpha}{\partial Y}=0. \tag{G.3}$$

One solution of Eq. G.3 is

$$\alpha(Y)=\left[g\sin\theta(Y+C)\right]^{-2} \tag{G.4}$$

where the constant C is evaluated from the total amount of liquid input into the foam Q_{tot} [1]:

$$Q_{tot}=\int_0^W \mathrm{dY}\frac{\mathrm{g}\cos\theta}{[\mathrm{g}\sin\theta\ (\mathrm{Y}+\mathrm{C})]^4}=\frac{\cos\theta}{3\mathrm{g}^3\sin^4\theta}\left[\frac{1}{\mathrm{C}^3}-\frac{1}{(\mathrm{C}+\mathrm{W})^3}\right]. \tag{G.5}$$

to find $C(Q_{tot})$ implicitly.

---

[1] $Q_{tot}=\int_0^W Q_z \mathrm{dY}$ where $Q_z=g\cos\theta\alpha^2$.

The liquid velocity in the foam is given by the flow rate divided by the Plateau border area α. The shear stress S scales with the derivative of the velocity, so that we have

$$S \sim \frac{\partial}{\partial Y}\left(\frac{g\cos\theta}{[g\sin\theta(Y+C)]^2}\right) = -\frac{2\cos\theta}{g\sin^2\theta}\frac{1}{(Y+C)^3} = -2g^{5/4}\cos^{1/4}\theta\sin\theta Q_Z^{3/4}.$$

Now, consider the foam to have a yield stress S_y. The critical angle at which flow first occurs, θ_c, is given by the condition that $S = S_y$. At this point the variation of flow rate with angle is

$$Q_Z \sim \frac{S_y^{4/3}}{2^{4/3}g^{5/3}\cos^{1/3}\theta_c\,\sin^{4/3}\theta_c}. \tag{G.6}$$

For small angles $\theta_c \ll 1$ we find that

$$Q_Z \sim \theta_c^{-4/3}. \tag{G.7}$$

Bibliography

[1] Weaire D. and Hutzler S. *The Physics of foams.* Oxford Univ. Press ISBN 0-198-50551-5, 246 pages (1999)

[2] Brakke K. *Exp. Math.* **1 (2)**, 141-165 (1992)

[3] Weaire D. and Phelan R. *Phil. Mag. Lett.* **69 (2)**, 107-110 (1994)

[4] Weaire D. , Bradley. G. and Phelan R. *Soft Condens. Matter: Configurations, Dynamics and Functionality.* , 247-268 (2000)

[5] Bikerman J. J. *Foams.* Springer-Verlag ISBN 0387061088, 337 pages (1973)

[6] Weaire D. and Kermode J. P. *Philos. Mag. B.* **48 (3)**, 245-259 (1983)

[7] Kraynik A. M. *Sandia Report SAND 83-0844* , (1983)

[8] Bolton F. and Weaire D. *Philos. Mag. B.* **63 (4)**, 795-809 (1991)

[9] Goldfarb I. I. , Kann K. B. and Shreiber I. R. . *Izvestiya an Sssr. Mekhanika Zhidkosti i Gaza* **23 (2)**, 103-108 (1988) *Fluid Dynamics (Official English translation of USSR Academy of Science, series Mechanics of Liquids and Gases)* **23**, 244-249 (1988)

[10] Verbist G. and Weaire D. *Europhys. Lett.* **26 (8)**, 631-634 (1994)

[11] Cox S. J. , Weaire D. , Hutzler S. , Murphy J. , Phelan R. and Verbist G. *P. Roy. Soc. Lond. A Mat.* **456**, 2441-2464 (2002)

[12] Saint-Jalmes A. , Vera M. U. and Durian D. J. *Europhys. Lett.* **50 (5)**, 695-701 (2000)

[13] Noever D. A. and Cronise R. J. *Phys. Fluids.* **6 (7)**, 2493-2500 (1994)

[14] Cox S. J. and Verbist G. *Eurofoams 2002.* Poster presentation, Manchester (2002)

[15] Weaire D. , Cox. S. J. , Hutzler S. and Bradley. G. *J. Phys. IV France* **11 (Pr6)**, 213-220 (2002)

[16] Weaire D. , Pittet N. , Hutzler S. and Pardal D. *Phys. Rev. Lett.* **71 (16)**, 2670-2673 (1993)

[17] Hutzler S. , Verbist G. , Weaire D. and van der Steen J. A. *Europhys. Lett.* **31 (8)**, 497-502 (1995)

[18] Stoyanov S. , Dushkin C. , Langevin D. , Weaire D. and Verbist G . *Langmuir* **14 (16)**, 4663-4665 (1998)

[19] Koehler S. A. , Hilgenfeldt S. and Stone H. A. *Phys. Rev. Lett.* **82 (21)**, 4232-4235 (1999)

[20] Leonard R. A. and Lemlich R. *AIChEJ..* **11**, 18-25 (1965)

[21] Brannigan G. and de Alcantara Bonfim O . F . *Phil. Mag. Lett.* **81 (3)**, 197-201 (2001)

[22] Durand M. , Martinoty G. and Langevin D. *Phys. Rev. E* **60 (6)**, R6307-R6308 (1999)

[23] Koehler S. A. , Hilgenfeldt S. Weeks E. R. and Stone H. A. *Phys. Rev. E* **66 (4)**, art. no. 040601 (2001)

[24] Durand M. and Langevin D. *Eur. Phys. J. E* **7 (1)**, 35-44 (2002)

[25] Koehler S. A. , Hilgenfeldt S. and Stone H. A. *Langmuir* **16 (15)**, 6327-6340 (2000)

[26] Barnes H. A. *J. of Non-Newtonian Fluid Mech.* **81 (1-2)**, 133-178 (1999)

[27] Larson R. G. *The structure and rheology of complex fluids.* Oxford Univ. Press ISBN 019512197X, 663 pages (1999)

[28] IFSCC Monograph no 3. *An Introduction to Rheology*. Published on behalf of the International Federation of Societies of Cosmetic Chemists by Micelle ISBN 1870228162, 35 pages (1997)

[29] Harris J. *Rheology and non-Newtonian flow.* Longman Group Limited ISBN 0582463319, 333 pages (1977)

[30] Bird R. B., Armstrong R. C. and Hassager O. . *Dynamics of polymeric liquids Vol. 1: fluid mechanics.* 2^{nd} *Ed.*. John Wiley & Sons ISBN 047180245X, 672 pages (1989) [(1977 first edition)]

[31] Sekimoto K. *J. of Non-Newtonian Fluid Mech.* **39 (1)**, 107-113 (1991)

[32] Sekimoto K. *J. of Non-Newtonian Fluid Mech.* **46 (2-3)**, 219-227 (1993)

[33] Barnes H. A. , Hutton J. F. and Walters K. *An introduction to rheology*. Elsevier Science Publishers ISBN 0444871403, 199 pages (1989)

[34] Hutzler S. PhD. Thesis, *University of Dublin* , (1997)

[35] Princen H. M. and Kiss A. D. *J. of Colloid and Interface Science.* **112 (2)**, 427-437 (1986)

[36] Lacasse M. D. , Grest G. S. , Levine D. , Mason T. G. and Weitz D. A. *Phys. Rev. Lett.*. **76 (18)**, 3448-3451 (1996)

[37] Saint-Jalmes A. and Durian D. J. *J. Rheol.* **43 (6)**, 1411-1422 (1999)

[38] Hutzler S. , Bolton F. and Weaire D. *Philos. Mag. B.* **71 (3)**, 277-289 (1995)

[39] Vera M. U. , Saint-Jalmes A. and Durian D. J. *Phys. Rev. Lett.* **84 (13)**, 3001-3004 (2000)

[40] Hutzler S. and Weaire D. *Phil. Mag. Lett.* **80 (6)**, 41-48 (2000)

[41] Cox S. J. , Alonso M. D. , Hutzler S. and Weaire D. *Foams, Emilsions and their Applications* Proceedings Eurofoam 2000 MIT Publishing Bremen ISBN 398057489X, (2000)

[42] Paterson A. R. *A first course in fluid dynamics.* Cambridge Univ. Press ISBN 0521254167, 528 pages (1983)

[43] Tritton D. J. *Physical Fluid Dynamics.* 2^{nd} *Ed.* Oxford Science Publications ISBN 0198544936, 430 pages (1988)

[44] Acheson D. J. *Elementary fluid dynamics.* . Oxford Applied Mathematics and computing Science series ISBN 0198596790, 397 pages (1990)

[45] Young H. D. and Freedman R. A. *Sears and Zemansky's University Physics* 10^{th} *Ed.* Addison-Wesley ISBN 0-201-60336-5, 1513 pages (2000)

[46] Bot E. T. G. , Hulsen M. A. and van den Brule B. H. A. A. *J. of Non-Newtonian Fluid Mech.* **79** **(2-3)**, 191-212 (1998)

[47] Briscoe B. J., Glaese M. , Luckham P. F. and Ren S. . *Colloids and Surfaces* **65** **(1)**, 69-75 (1992)

[48] Blakery J. and Mitsoulis E. *J. of Non-Newtonian Fluid Mech.* **70** **(1-2)**, 59-77 (1997)

[49] Beaulne M. and Mitsoulis E. *J. of Non-Newtonian Fluid Mech.* **72** **(1)**, 55-71 (1997)

[50] Gardiner B. S. PhD. Thesis, *University of Newcastle* , (1999)

[51] Brungraber R. J. , Wenzel H. G. , and Stelson T. E. *J. Materials* **5** **(2)**, 396-412 (1970)

[52] Khan S. A. , Schnepper C. A. and Armstrong R. C. *J. Rheol.* **32** **(1)**, 69-92 (1988)

[53] Princen H. M. and Kiss A. D. *J. of Colloid and Interface Science.* **128** **(1)**, 176-187 (1989)

[54] Bobert M. , Persson H. and Persson B. *Fire technology.* **33** **(4)**, 336-355 (1997)

[55] Thondavadl N. N. and Lemlich R. *Ind. Eng. Chem. Process Des. Dev.* **24** **(3)**, 748-753 (1970)

[56] Schwartz L. W. and Princen H. M. *J. Coll. Interf. Sci.* **118**, 201-211 (1987)

[57] Reinelt D. A. and Kraynik A. M. *J. Fluid Mechanics.* **215** , 431-455 (1990)

[58] Okuzono T. , Kawasaki K. and Nagai T. *J. Rheol.* **37 (4)**, 571-586 (1993)

[59] Rosa M. E. , Diogo A. C. and Fortes M. A. *Langmuir* **11 (7)**, 2329-2333 (1995)

[60] Durian D. J. *Phys. Rev. E.* **55 (2)**, 1739-1751 (1997)

[61] Cox S. J. , Hutzler S. and Sun Q. *To be published* , (2004)

[62] Mason T. G. , Bibette J. and Weitz D. A. *Phys. Rev. Lett.* **75 (10)**, 2051-2054 (1995)

[63] Hutzler S. , Weaire D. and Crawford R. *Europhys. Lett.* **41 (4)**, 461-465 (1998)

[64] Pittet N. , Rivier N. and Weaire D. *Forma* **10 (1)**, 65-73 (1995)

[65] Hutzler S. , Weaire D. and Crawford R. *Phil. Mag. B* **75 (6)**, 845-857 (1997)

[66] Weaire D. and Hutzler S. *Phil. Mag.* **83 (23)**, 2747-2760 (2003)

[67] Bolton F. and Weaire D. *Philos. Mag. B.* **65 (3)**, 473-487 (1992)

[68] Weaire D. , Kern N. and Verbist G. *Phil. Mag. Lett.* **84 (2)**, 117-125 (2004)

[69] Weaire D. , Kern N. , Cox S. J. , Sullivan J. M. and Morgan F. *P. Roy. Soc. Lond. A* **460**, 569-579 (2004)

[70] Cantat I. , Kern N. and Delannay R. *Europhys. Lett.* **65 (5)**, 726-732 (2004)

[71] Bretherton F. P. *J. Fluid Mech..* **10**, 166-188 (1961)

[72] Weaire D. , Alonso M. D. , Cox S. J. , Rioual F. , and Hutzler S. *To be published* , (2004)

[73] Weaire D. *Private communication* , (2004)

[74] Weaire D. , Hutzler S. , Cox S. J. , Kern N. , Alonso M. D. and Drenckhan. W. *J. Phys.:Condens. Matter* **15**, S65 (2003)

[75] Peters E. A. J. F. MSc. Thesis, *Eindhoven University of Technology* , (1995)

[76] Bradley K. G. PhD. Thesis, *University of Dublin* , (2000)

[77] Hutzler S. , Péron N., Weaire D. and Drenckhan W. *Eur. Phys. J. E* **14** (), 381-386 (2004)

[78] Kern N. , Weaire D. , Martin A. , Hutzler S. and Cox S. J. *accepted for publication in Phys. Rev. E* ,(2004)

[79] Debregeas G. , Tabuteau H. and di Meglio J. M. *Phys. Rev. Lett.* **87 (17)**, 178305/1-4 (2001)

[80] Lauridsen J. , Twardos M. and Dennin M. *Phys. Rev. Lett.* **89 (9)**, 098303/1-4 (2002)

[81] Alonso M. D. , Cox S. J. , Hutzler S. and Weaire D. *To be published* , (2004)

[82] Boycott A. E. *Nature.* **104** , 532 (1920)

[83] Guyon E. , Hulin J. P. and Petit L. *Hydrodynamique physique.* InterEditions ISBN 2868835023, 674 pages (1991)

[84] Duran J. and Mazozi T. *Phys. Rev. E* **60 (5)**, 6199-6201 (1999)

[85] Cox S. J. and Weaire D. Private communication.

[86] Prause B. A. , Glazier J. A. , Gravina S. J. and Montemagno C. D. *J. Phys. Condens. Matt.* **7 (4)**, L511-L516 (1995)

[87] Assink R. A. , Caprihan A. and Fukushima E. *AIChEJ.*. **34 (12)**, 2077-2079 (1988)

[88] Kopinga K. and Pel L. *Rev. Sci. Instrum.* **65 (12)**, 3673-3681 (1994)

[89] Banhart J. , Stanzick H. , Helfen L. , Baumbach T. *App. Phys. Lett.*. **78 (8)**, 1152-1154 (2001)

[90] Seidler G. T. , Atkins L. J. , Behne E. A. , Noomnarm U. , Koehler S. A. , Gustafson R. R. and McKean W. T. *Advances in Complex Systems* **4 (4)**, 481-490 (2001)

[91] Brujić J. , Edwards S. F. , Grinev D. V. , Hopkinson I. , Brujić D. and Makse H. A. *Faraday Discuss* **123** , 207-220 (2002)

[92] McCabe E. *Private communication* , (2002)

[93] Vaz M. F. , Cox S. J. and Alonso M. D. *J. Phys.:Condens. Matter* **16 (23)**, 4165-4175 (2004)

[94] Hales T. C. *Discrete & Computational Geometry* **25 (1)**, 1-22 (2001)

[95] Alfaro M. , Brock J. , Foisy J. , Hodges N. , Zimba J. and Morgan F. *Geometry Group. Williams College* SMALL Undergraduate Research Project, (1990)

[96] Morgan F. *Geometric measure theory: a beginner's guide.* Boston Academic. Press ISBN 0125068557, 145 pages (2000)

[97] Wichiramala W. PhD. Thesis, *University of Illinois* , (2002)

[98] Cox S. J. , Graner F. , Vaz M. F. , Monnereau-Pittet C. and Pittet N. *Phil. Mag.* **83 (11)**, 1393-1406 (2003)

[99] Vaz M. F. and Fortes M. A. *J. Phys. Condens. Mat.* **13 (7)**, 1395-1411 (2000)

[100] Morgan F. *Amer. Math. Mon.* **101 (4)**, 343-351 (1994)

[101] Herdtle T. and Aref H. *P. Roy. Soc. Lond. A Mat.* **434 (1891)**, 441-447 (1991)

[102] Graner F. , Jiang Y. , Janiaud E. and Flament C. *Phys. Rev. E* **63 (1)**, art.no. 011402 (2001)

[103] Vaz M. F. , Fortes M. A. and Graner F. *Phil. Mag. Lett.* **82 (10)**, 575-579 (2000)

[104] Weaire D. , Cox. S. J. and Graner F. *Eur. Phys. J. E* **7 (2)**, 123-127 (2002)

[105] Cox S. J. Private communication.

[106] Smith C. S. *Metal interfaces.* **ASM**, (1952)

[107] Aste T. , Boose D. and Rivier N. *Phys. Rev. E.* **53 (6)**, 6181-6191 (1996)

[108] Teixeira P. I. C. , Graner F. and Fortes M. A. *Eur. Phys. J. E* **9 (5)**, 447-452 (2002)

[109] Fortes M. A. and Rosa M. E. *J. Colloid Interface Sci.* **241 (1)**, 205-214 (2001)

[110] Morgan F. *Private communication to S. J. Cox.*

[111] MacLeod F. MSc. Thesis, *University of Dublin* , (2002)

[112] Foley B. TP. Project, Physics Dept. *University of Dublin* , (2002)

[113] Hutzler S. , Weaire D. and Shah S. *Phil. Mag. Lett.* **80 (1)**, 41-48 (2000)

[114] Atkins P. and Jones L. *Chemical Principles.* W. H. Freeman and Company ISBN 0716735962, 908 pages (1999)

[115] Pittet N. MSc. Thesis, *University of Dublin* , (1993)

[116] Phelan R. , Weaire D. and Brakke K. *Exp. Math.* **4 (3)**, 181-192 (1995)